Ion Irradiation and Carbon Radical Exposure of Graphene and Hexagonal Boron Nitride on Iridium(111)

I n a u g u r a l - D i s s e r t a t i o n

zur

Erlangung des Doktorgrades

der Mathematisch-Naturwissenschaftlichen Fakultät

der Universität zu Köln

vorgelegt von

M. Sc. Charlotte Herbig

aus Göttingen

Köln 2017

Erster Berichterstatter:	Prof. Dr. Thomas Michely
Zweiter Berichterstatter:	Prof. Dr. Marika Schleberger

Tag der mündlichen Prüfung: 26.01.2017

Abstract

In the recent years, two-dimensional materials such as graphene and monolayers of hexagonal boron nitride have moved increasingly into the spotlight of science and research due to their extraordinary properties. This thesis is devoted to the investigation of the phenomena that occur during ion irradiation and carbon radical exposure of graphene and monolayer hexagonal boron nitride resting on a metal substrate. The resulting surface morphologies are studied by scanning tunneling microscopy and low-energy electron diffraction, whereas X-ray photoelectron spectroscopy and temperature programmed desorption provide chemical information. The experimental data is corroborated by molecular dynamics simulations and density functional theory calculations shedding light on the microscopic mechanisms.

In the first part, we study the response of graphene and monolayer hexagonal boron nitride resting on an Ir(111) substrate to ion irradiation. We show that over a broad parameter space ion irradiation of graphene and monolayer hexagonal boron nitride results in noble gas trapping at the interface of the two-dimensional layers and their metal supports. The two-dimensional layers act as one-way valves which upon annealing seal the trapped species in highly pressurized blisters. We find that the one-way valve effect results from the fact that the energetic particles can easily penetrate the two-dimensional sheet, then lose most of their energy to the substrate, making a return through the covering layer virtually impossible. Moreover, even though the two-dimensional layers are highly perforated, the edges of the holes bind strongly to the metal substrate and thereby prevent the escape from underneath. Since the phenomenon holds for ion exposure of graphene and monolayers of hexagonal boron nitride it must be assumed to take place for a broad range of materials out of the zoo of two-dimensional matter.

We describe ways to avoid blister formation during graphene growth, and also demonstrate how ion implantation can be used to intentionally create blisters under a perfect two-dimensional layer without introducing damage to it.

By varying the incident angle of ion irradiation we find that at large impact angles graphene can be eroded without noble gas trapping. This finding is relevant to avoid undesired effects in graphene and other two-dimensional sheets upon ion beam nanopatterning.

Moreover, with scanning tunneling microscopy we image through the hexagonal boron nitride blister lid and find a superstructure corresponding in lattice parameter to what we expect for a crystalline Xe layer. We conclude that due to the strong adhesion of two-dimensional layers to Ir(111) the pressure inside the blisters is in the GPa range resulting in Xe solidification.

By exposing graphene and monolayer hexagonal boron nitride to high ion doses, the two-dimensional layers are amorphized. Surprisingly, upon annealing, graphene as well as monolayer hexagonal boron nitride recover to perfection, except of vacancy islands resulting from sputtering and noble gas blisters.

Finally, we study the potential of graphene as a sputtering shield for the underlying metal substrate. It is demonstrated that efficient sputter protection relies on self-repair of the ion damage in graphene, which takes place efficiently in the temperature range of chemical vapor deposition growth.

The second part of this thesis is dedicated to carbon radical exposure of graphene on Ir(111). We comprehensively discuss the different pathways for carbon radicals deposited onto graphene on Ir(111) over a broad range of deposition temperatures. At high temperatures we observe graphene bilayer growth. To go beyond, we provide evidence for a hitherto unknown mechanism of carbon incorporation into the preexisting graphene layer resulting in in-plane compression and eventually in wrinkle formation upon cool down. The discovery of this phenomenon is of greatest importance for Gr bilayer growth via radical carbon deposition as wrinkle formation will deteriorate the graphene quality. At low deposition temperature we reveal that upon carbon deposition onto the moiré formed by graphene and Ir(111) a periodic carbon cluster lattice emerges.

Frequently used Symbols and Abbreviations

2D	-	Two-Dimensional
BE	-	Binding Energy
CVD	-	Chemical Vapor Deposition
DFT	-	Density Functional Theory
(L)DOS	-	(Local) Density of States
E_{F}	-	Fermi Energy
fcc	-	Face Centered Cubic
GFWHM	-	Gaussian Full Width at Half Maximum
Gr	-	Graphene
hBN	-	Hexagonal Boron Nitride
L	-	Langmuir, $1\,\mathrm{L} = 1 \times 10^{-6}\,\mathrm{Torr \cdot s} \approx 1.33 \times 10^{-6}\,\mathrm{mbar \cdot s}$
LEED	-	Low-Energy Electron Diffraction
LFWHM	-	Lorentzian Full Width at Half Maximum
MD	-	Molecular Dynamics
ML	-	Monolayer
MLE	-	Monolayer Equivalents
PKA	-	Primary Knock-On Atom
QMS	-	Quadropole Mass Spectrometer
STS/STS	-	Scanning Tunneling Microscopy/Spectroscopy
(HR)TEM	-	(High-Resolution) Transmission Electron Microscopy
TPD	-	Temperature Programmed Desorption
UHV	-	Ultra-High Vacuum
XPS	-	X-Ray Photoelectron Spectroscopy

Contents

I Introduction **1**

II Fundamentals **5**

1 Graphene and Hexagonal Boron Nitride **7**

1.1 Graphene on Ir(111) 7

1.2 Hexagonal Boron Nitride on Ir(111) 10

1.3 Strain and Wrinkle Formation 12

1.4 Intercalation 14

1.5 Supported 2D Layers as Template for Self-Assembly 15

2 Ion Surface Interactions and Defect Production **17**

3 Defects in Graphene and Hexagonal Boron Nitride **25**

3.1 Structural Defects 25

3.2 Generation of Defects 28

III Experimental **31**

4 Experimental Techniques **33**

4.1 Scanning Tunneling Microscopy 33

4.2 Low-Energy Electron Diffraction 34

4.3 X-Ray Photoelectron Spectroscopy 35

4.4 Temperature Programmed Desorption 36

5 Setup and Procedures **39**

5.1 The Ultra-High Vacuum System Athene 39

5.2 The Beamline I311 at MAX-Lab 41

5.3 Sample Preparation and Analysis 41

5.4 Density Functional Theory Calculations 44

5.5 Molecular Dynamics Simulations 45

IV Ion Irradiation **47**

6 From Noble Gas Trapping to Blister Formation in Graphene on Ir(111) **49**

6.1 Xenon Trapping 51

6.2 Energetics of Xenon Trapping 55

6.3 Morphology of Trapped Xenon 59

6.4 Energy and Mass Dependence 65

6.5 Blister Formation by Preimplantation . . . 75
6.6 Conclusions . . . 77
7 Blister-Free Ion Beam Patterning of Supported Graphene 79
8 Graphene as the Ultimately Thin Sputtering Shield 93
9 Xenon Trapping and Nano-Crystals underneath Hexagonal Boron Nitride on Ir(111) 101
9.1 Xenon Trapping . . . 102
9.2 Edge Termination . . . 109
9.3 Nano-Crystals . . . 111
9.4 Nano-Crystal Formation by Preimplantation . . . 112
9.5 Conclusions . . . 113
10 Amorphization and Recrystallization 115
11 Comparison of Graphene and Hexagonal Boron Nitride on Ir(111) 133
12 Noble Gas Trapping – A Review 137
V Carbon Radical Exposure 141
13 Graphene Bilayer Growth and Wrinkle Formation 143
13.1 Morphology after Radical Carbon Deposition . . . 144
13.2 Energetics of Carbon Penetration and Graphene Bilayer Nucleation . . . 148
13.3 Discussion . . . 151
13.4 Conclusions . . . 153
14 A Carbon Cluster Superlattice on Graphene on Ir(111) 155
14.1 Structure and Binding . . . 156
14.2 Temperature Dependent Growth . . . 160
14.3 Coverage Dependent Growth . . . 162
14.4 Thermal Stability . . . 166
14.5 Conclusions . . . 171
VI Summary and Outlook 173
VII Appendix 179
A A Hexagonal Boron Nitride/Graphene Heterostructure 181
B Carbon Clusters on Hexagonal Boron Nitride on Ir(111) 183
C Oxygen Etching of Carbon Clusters on Graphene on Ir(111) 187
D Deutsche Kurzzusammenfassung *(German Abstract)* 189

E Liste der Teilpublikationen *(List of Publications)* **193**

F Danksagung *(Acknowledgements)* **197**

G Bibliography **201**

H Offizielle Erklärung **227**

PART I

Introduction

In recent years, two-dimensional (2D) atomic crystals were put into the limelight of fundamental as well as application oriented research. The growing interest stems from their unique physical properties which differ from those of their three-dimensional (3D) counterparts [1–4]. The most prominent example of the family of 2D materials is Graphene (Gr) – a one-atom thick layer of carbon perfectly arranged in a honeycomb lattice. With its outstanding mechanical and electronic properties it is a promising building block for replacing silicon when crossing the boarder to future nanoelectronic devices [5–8]. However, one of the main obstacles towards achieving this goal is the absence of a band gap, which basically means that Gr's electronic conductivity cannot be switched off completely. So in order to meet application-oriented demands, one should be able to tailor Gr's characteristics.

It was demonstrated that when two Gr layers are stacked as in graphite, applying a perpendicular electric field creates a controllable band gap [9]. The challenge is now to produce uniform large-scale bilayers of Gr to harvest this potential. Epitaxial growth on transition metal surfaces by chemical vapor deposition (CVD) methods, *i.e.*, the deposition of carbon containing precursors, and elemental carbon exposure present the most effective routes to grow Gr bilayers [10, 11]. For the latter approach, a thorough understanding of the growth mechanism is still unavailable.

Another member of the family of 2D materials is hexagonal boron nitride (hBN) which in this work always refers to a monolayer of hBN. It is also known as *white Gr* since it is Gr's isostructural and isoelectronic analogue with the honeycomb lattice formed by two different sublattices - one made of N atoms and one made of B atoms. Its properties are certainly no less exciting than those of Gr. Since the hBN lattice is built of two different sublattices, a band gap of about 5 eV emerges [12, 13]. The material is frequently used as a non-interacting and insulating substrate in hBN/Gr stacked heterostructures [2, 14].

Apart from their use in electronic applications more fundamental issues may be solved by 2D materials. In water desalination, nanostructured Gr and hBN layers with perforations are envisioned to fix the acute problem of clean water supply [15–19]. In order to create such perforations the tools of surface science may be used. To this end, low-energy ion exposure combined with controlled thermal annealing is a versatile method to create such defects and subsequently new morphologies in systems with reduced dimensionality [20]. Thus, obtaining quantitative information on ion-induced defects and their stability in 2D systems is worthwhile.

Irradiation of solids has been intensively studied in light of its deteriorating effects. For example the bubble and blister formation in consequence of light element implantation in

nuclear and fusion reactors limits the lifetime of their components [21]. However, the same phenomena may also be used beneficially to achieve mircoslicing of Si wafers [22]. In case of graphite – Gr's 3D counterpart – He^+ irradiation was found to result in bubble formation, blistering, and eventually exfoliation [23, 24]. With respect to Gr, blister formation has received considerable research interest since it evokes huge pseudomagnetic fields [25–27]. Further, Gr blisters can be used as adaptive-focus lenses [28] or as nanoreactors to perform confined reactions [29]. In this thesis a new route towards blister formation in supported 2D layers is presented. By means of ion irradiation and annealing we show that Gr and hBN act as one-way valves that trap the implanted species at the interface resulting in highly pressurized gas filled cavities.

Further, 2D materials supported by lattice-mismatched substrates present an appealing testing ground for the investigation of molecular and cluster self-assembly [30–34]. This is due to the emergence of a moiré superstructure, which arises from the lattice mismatch between the 2D sheet and its substrate. The phenomenon of self-assembly opens up a new avenue towards the realization of nanoscale architectures with tailored properties [30]. In this work we show that carbon radical exposure of Gr/Ir(111) results in a highly ordered and extremely stable cluster superlattice that may provide a starting point for functionalization.

This thesis has two main objectives: First, to study the response of epitaxial Gr and hBN grown on an Ir(111) substrate to ion irradiation and damage annealing. Second, carbon radical exposure is studied leading to bilayer growth and C cluster self-assembly. In the following the content of this work is outlined. In Part II the fundamental properties of Gr and hBN are introduced and the basic concepts of ion surface interactions as well as defect structure and generation in Gr and hBN are characterized. Part III describes the experimental techniques used in this thesis. Further the corresponding setups and procedures are reviewed. In Part IV we investigate the phenomena that occur when energetic atoms impinge on 2D materials resting on a metal substrate. In Part V we provide the first comprehensive picture of the fate of C radicals deposited on Gr/Ir(111) over a wide temperature range. Finally, in Part VI the results are summarized and an outlook to future research is given.

PART II

Fundamentals

CHAPTER 1

Graphene and Hexagonal Boron Nitride

Graphene and hexagonal boron nitride are two prominent members of the family of 2D materials. Gr is a two-dimensional crystal consisting of hexagonally arranged carbon atoms. Since its successful isolation and characterization in 2004 [1] the material has focused intense experimental and theoretical efforts. For this achievement A. K. Geim and K. S. Novoselov were awarded the Nobel Prize in Physics in 2011 [35]. In the following years Gr research has evolved into a rapidly growing field of research and concomitantly fostered the endeavor to explore other two-dimensional materials. One of the 2D materials scientists dedicated their research to is Gr's isostructural binary complement hexagonal boron nitride, which is also referred to as white graphene. Compared to the zero-gap semiconductor graphene, hBN - its insulating counterpart - consists of B and N atoms occupying the A and B sublattice of the honeycomb lattice, respectively. In this chapter these two materials are briefly introduced and since most relevant to this work their preparation and structural properties on Ir(111) are summarized.

1.1 Graphene on Ir(111)

The most peculiar property of Gr is its electronic structure that arises from its monoatomic thickness and lattice symmetry [36]. The C atoms in Gr are sp^2 hybridized and the in-plane sp^2 orbitals form a σ band. The out-of-plane p_z orbitals form a delocalized π-system. The dispersion relation displayed in Figure 1.1 is almost linear for low energies. In this regime the carriers in Gr are massless Dirac fermions and can be described by the relativistic Dirac equation. The conduction and valence band touch at the six corners (K-points) of the first Brillouin zone with the Fermi energy E_F situated right in between them making

Gr a semiconductor without band gap. This evokes phenomena like room-temperature ballistic transport [37], a half-integer quantum Hall effect [38], and Klein tunneling [39]. Properties like low dimensionality, flexibility, optical transparency [40], and high charge carrier mobility [1] make Gr a promising candidate in a variety of applications, including transparent electrodes in touch-screens and solar cells, radio-frequency electronics, or post-CMOS nanoelectronics [7, 8, 38, 41–45].

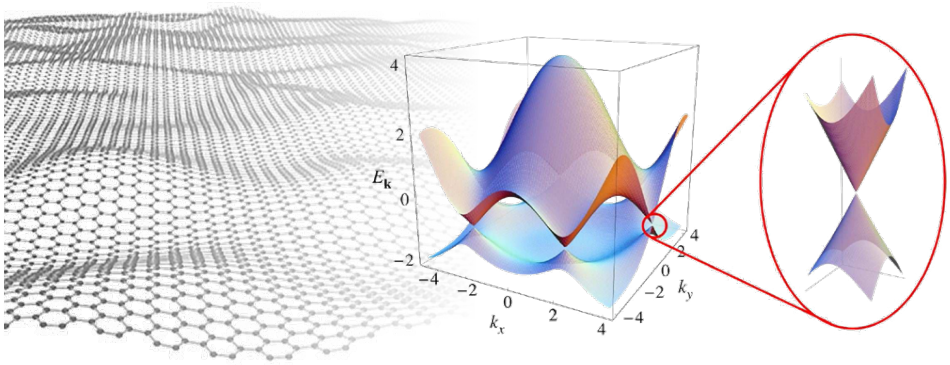

Figure 1.1: Graphene. Real space artistic representation (left) and band structure of the π-system of Gr (right). The magnification shows the linear dispersion in the vicinity of the K-point. Sketch by J. C. Meyer. Bandstructure reprinted with permission from [6]. Copyright 2009 by the American Physical Society.

The chemical decomposition of hydrocarbons on a catalytically active metal surface is up to now the only pathway to large-scale Gr production. In this work Gr is epitaxially grown on Ir(111) which yields high-quality Gr films self-limited to a monolayer. Details on the growth procedure are given in Chapter 5.

Due to a small deviation in the lattice constants of Gr $a_{\mathrm{Gr}} = 2.46\,\text{Å}$ and Ir(111) $a_{\mathrm{Ir(111)}} = 2.72\,\text{Å}$ a moiré superstructure consisting of (10.32 × 10.32) Gr unit cells resting on (9.32 × 9.32) Ir atoms arises resulting in a periodicity of 25.3 Å [46]. This is illustrated in Figure 1.2(a), showing an atomically resolved scanning tunneling microscopy (STM) topograph with the moiré as well as the schematic representation in (b). The unit cell is indicated by a white rhombus. The morphology observed in STM depends strongly on tunneling parameters and tip state [46]: The top-regions either appear as bright dots in a dark sea (called topographic contrast as this is equivalent to the real height distribution [47]) or as dark dots in a bright sea (reversed contrast). In Figure 1.2, the reversed contrast that is most frequently imaged is presented.

Figure 1.3 shows the moiré unit cell obtained by density functional theory (DFT) calculations. Due to varying lateral positions of the C atoms with respect to the Ir lattice three high symmetry regions, marked by circles, emerge. In the top region, the carbon

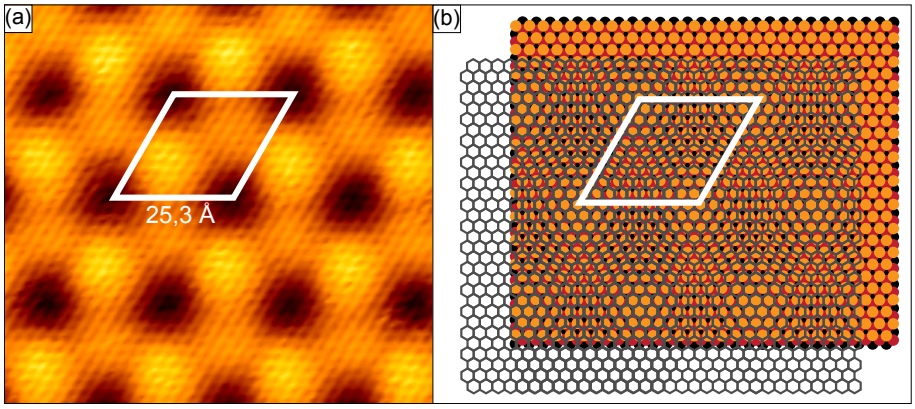

Figure 1.2: The moiré of graphene/Ir(111). (a) Atomically resolved STM topograph of Gr on Ir(111) in the reversed contrast. The white rhombus indicates the moiré unit cell. (b) Schematic visualization of the moiré superstructure. Gr (gray) on top of the Ir(111) surface (orange, red, black).

ring is centered above an atom of the metal surface, whereas in the fcc (hcp) region, the center of the C ring is situated above an fcc (hcp) adsorption site. As a consequence the binding between the carbon layer and the metal substrate varies across the moiré cell (weaker in the top regions, stronger in the fcc/hcp regions) causing a corrugation of 0.8 Å. On average the binding energy of Gr to Ir(111) is 69 meV per C atom [48] making the Gr/Ir(111) system a 'weakly' interacting system. The average height of the Gr above the iridium surface is (3.38 ± 0.04) Å [47].

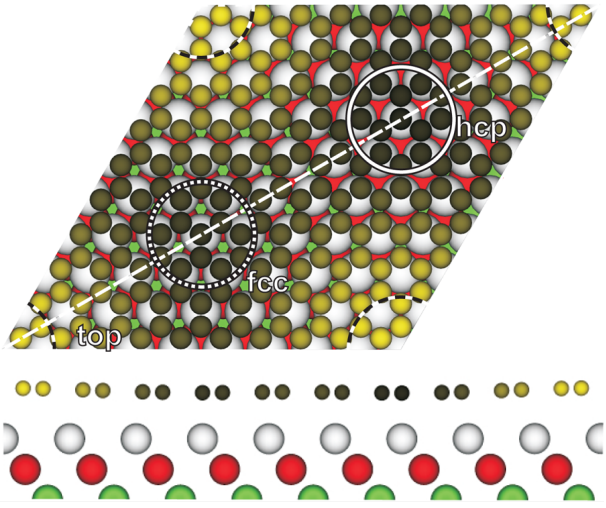

Figure 1.3: Structure of graphene on Ir(111). Top view (top) and side view (bottom) [cut along the dashed line in top view] of a moiré unit cell of Gr on Ir(111) calculated by DFT including van der Waals interactions. Regions of high symmetry stacking are encircled. Adapted with permission from Ref. [47]. Copyrighted by the American Physical Society.

1.2 Hexagonal Boron Nitride on Ir(111)

Although hexagonal boron nitride has a similar honeycomb structure compared to its carbidic analog Gr, it contains distinct chemical species – one sublattice is made by N atoms and the other one by B atoms. Its mechanical properties are quite similar but it exhibits completely different electronic properties. hBN is an insulator with a wide band gap of approximately 5 eV [12, 13]. The covalent in-plane B-N bonds are partially ionic. Due to the electronegativity differences between the B and N atoms the π electrons tend to localize around the N atomic centers. In the electronic bandstructure of hBN the maximum of the valence band is located at the K-point of the first Brillouin zone whereas the minimum of the conduction band is situated at the Γ-point creating an indirect band gap. hBN is frequently used as a non-interacting, flat, and insulating substrate for Gr in vertical van der Waals heterostructures like field effect transistors [49, 50] or light emitting diodes [51].

Just like Gr, hBN is often grown by CVD on a variety of metal substrates such as Rh(111), Ru(0001), and Ir(111) [12, 48, 49, 52–56]. The standard precursor molecule is borazine ($B_3H_6N_3$). On a substrate with significant interaction, like Ir(111), hBN aligns with the dense-packed direction of the metal and consequently only two rotational domains differing by an angle of 180° are found [48].

Based on their moiré analysis by STM, Farwick zum Hagen *et al.* determined the lattice constant of hBN to $a_{\mathrm{hBN}} = 2.49\,\text{Å}$ with a moiré periodicity of 29.1 Å [48]. This is illustrated in Figure 1.4(a) displaying an atomically resolved STM topograph of hBN/Ir(111) with its moiré (indicated by a white rhombus). Within the hole at the right margin of the topograph one can identify the parallel atomic rows of Ir(111). As in Gr, hBN shows a contrast inversion in STM strongly depending on tunneling parameters [48, 56]. In the inset of Figure 1.4(a) the actual geometry of the system is shown, *i.e.*, the topographic contrast. Again a white rhombus represents the moiré unit cell.

The incommensurate (11.7×11.7) on (10.7×10.7) moiré unit cell is in DFT calculations approximated by an (12×12) on (11×11) commensurate supercell depicted in Figure 1.5. This configuration constitutes the energetically more favorable of the two possible orientations. Similar to Gr three different regions of high local symmetry can be distinguished according to the adsorption sites of the B and N atoms with respect to the underlying substrate. For example $\mathrm{B_{top}N_{fcc}}$ declares a position with a B atom on top of an Ir atom and an N atom in a threefold hollow site of the fcc type. It is apparent from the side view of the DFT calculation that this area together with the $\mathrm{B_{fcc}N_{hcp}}$ area represent a flat,

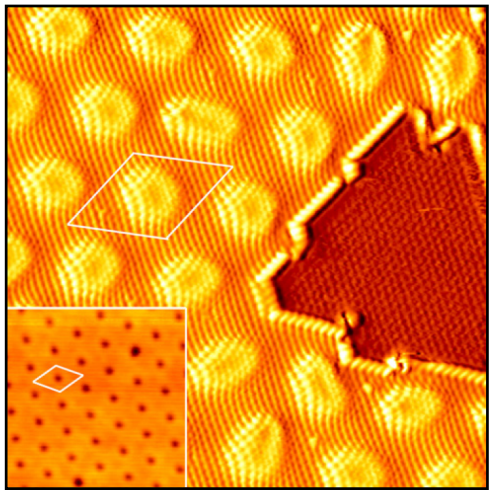

Figure 1.4: Hexagonal boron nitride. Atomically resolved hBN layer with a triangular shaped hole exposing bare Ir(111). Image size is 14.4 nm × 14.4 nm. Inset: STM topograph of hBN/Ir(111) in the topographic contrast. Image size is 18 nm × 18 nm. The moiré unit cell is indicated by white rhombuses. Reprinted with permission from [48]. Copyright 2016 American Chemical Society.

physisorbed region, referred to as hill region. However, the $B_{hcp}N_{top}$ area is chemisorbed forming the valley area within the moiré. The energetically less favorable 180 ° rotated domain is characterized by $B_{top}N_{hcp}$, $B_{fcc}N_{top}$, and $B_{fcc}N_{top}$. Again, strongest binding is found where an N atom is situated on top of an Ir atom.
With a corrugation larger than 1.5 Å hBN/Ir(111) is a strongly corrugated hill-and-valley system ($h_{max} = 3.6$ Å, $h_{min} = 2.1$ Å) [48]. The average binding of hBN/Ir(111) is approximately 86 meV per atom [48].

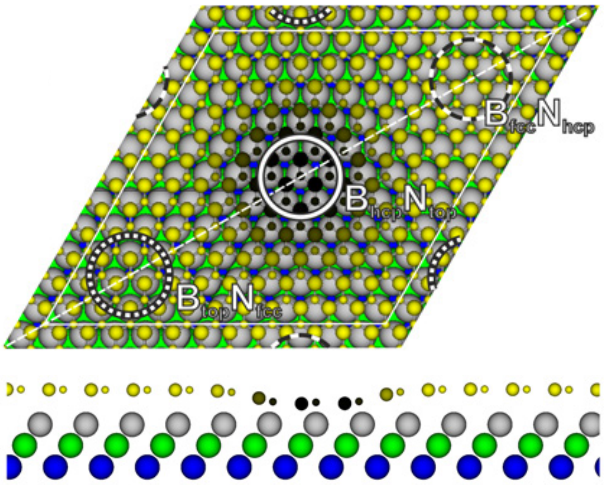

Figure 1.5: Structure of hexagonal boron nitride on Ir(111). DFT-results for the energetically favorable orientation of hBN/Ir(111) in top (top) and side view (bottom) (cut along the dashed white line). B atoms (large spheres) and N atoms (small spheres) are colored according to their height above the Ir(111) substrate. The unit cell and areas of high symmetry are indicated. Adapted with permission from [48]. Copyright 2016 American Chemical Society.

1.3 Strain and Wrinkle Formation

The epitaxial growth of Gr and hexagonal boron nitride is conducted at high temperatures. As a result of the different thermal expansion coefficients of the 2D layer and Ir, the 2D sheet is set under compressive stress upon cool down to room temperature. In case of Gr/Ir(111), this compressive strain eventually leads to a delamination of Gr from the substrate and the formation of one-dimensional defects in the form of wrinkles [57]. At a larger scale a network of such wrinkles is observed. However, a residual compressive strain remains within the Gr layer. The stress relaxation process in Gr/Ir(111) during cooling can be explained by an interplay between compressive strain in the film and wrinkle formation with a characteristic hysteresis as visible in Figure 1.6. This hysteresis suggests an activated relief mechanism.

After Gr growth at elevated temperature compressive strain is built up within the Gr layer upon cool down from markers A to B. At B, the strain energy has become large enough to overcome the activation energy for wrinkle formation and the Gr relaxes by forming wrinkles. The activation energy consists of two contributions: (i) The energy needed to bend the Gr layer and (ii) the energy to delaminate the Gr sheet from the substrate [57]. It is found that, independent of the growth temperature, this activation energy is

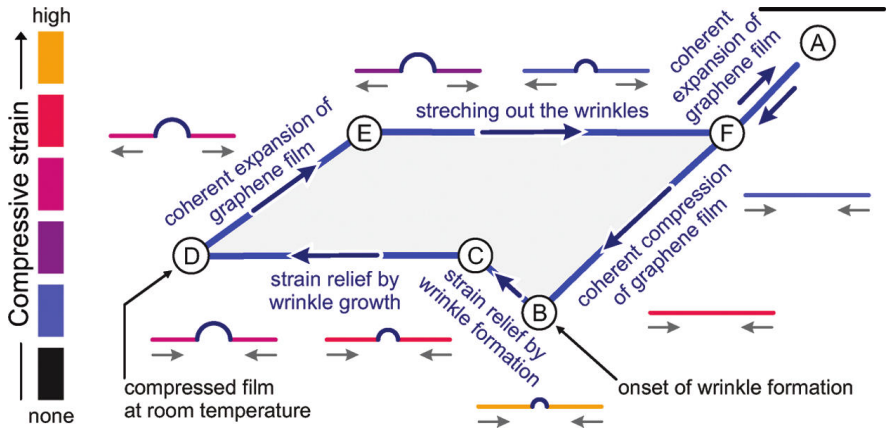

Figure 1.6: Hysteresis of wrinkle formation and smoothing. Sketch of the interplay of strain and wrinkle formation for Gr/Ir(111) during a cycle of cooling and reheating. The gray arrows indicate the compression/expansion in Gr induced by thermal compression/expansion of the substrate. Reprinted with permission from [58]. Copyright 2012 American Chemical Society.

overcome after cool down by approximately 450 K [57, 58]. Between markers B and C further wrinkles nucleate and eventually grow from C to D while the Gr lattice remains slightly compressed. The wrinkles accommodate approximately 2/3 of the compressive strain while 1/3 of the compressive strain remains in the Gr layer [59]. In general, for a thermal misfit of approximately 0.3% the Gr layer remains flat [57].

Following the reverse process of heating the sample, leads first to an expansion of the Gr lattice (D to E), while the wrinkles are only smoothed out between markers E and F. Further increasing the temperature above the Gr growth temperature leads to tensile strain within the Gr layer.

The reappearance of wrinkles at identical positions after cycles of heating and cooling suggests that wrinkles are anchored to defects within the Gr layer [60]. It was proposed that wrinkle formation itself and their relief is possible without leaving stress-induced morphological defects behind [58], but recent STM studies suggest crack formation at wrinkle crossings [61]. As will be discussed in the following section, these defects at wrinkles are suspected to enable transport of atoms across Gr layers resulting in intercalation [61].

In the case of hBN/Ir(111) there are no hints for wrinkle formation upon cool down. However, a compressive strain of about 0.6 % was observed and traced back to the mismatch in expansion coefficients [48]. The stronger binding of the hBN layer towards the Ir(111) surface compared to Gr/Ir(111) ($E_{\mathrm{b,hBN/Ir}} \approx 86\,\mathrm{meV/atom}$, $E_{\mathrm{b,Gr/Ir}} \approx 69\,\mathrm{meV/atom}$ [48]) most probably inhibits the delamination and stress relaxation via wrinkle formation.

1.4 Intercalation

In chemical terms, intercalation describes the inclusion of molecules or atoms into a layered material without essentially changing its structure. Prominent examples are intercalation compounds on the basis of graphite - the 3D counterpart of graphene. Here, intercalation expands the van der Waals gap between adjacent sheets, which requires energy usually supplied by charge transfer between the intercalant and graphite. Albeit less prominent, due to its structural similarity to graphite, hBN is also used as a host material for intercalation compounds [62]. In general, intercalation involves complex diffusion processes along and across the layers and is strongly affected by the presence of defects [63]. Depending on the participating species a certain threshold vapor pressure is needed to initiate intercalation which also depends on temperature and morphology [63].

In the case of 2D materials, intercalation means the insertion of atomic or molecular species between the 2D sheet and its substrate which in this work is Ir(111). The process is driven by the reduction of the chemical potential, *i.e.*, the adsorption underneath the 2D sheet is energetically more favorable for the applied experimental conditions. Some chemical species like alkali metals easily diffuse to the interface upon room temperature adsorption whereas the intercalation of, *e.g.*, transition metals requires elevated temperatures [64, 65]. For even other species, *e.g.*, CO, high pressures are needed to achieve intercalation at all [66]. The detailed intercalation mechanism depends on the specific intercalant and is in many cases still under debate. Most probable pathways are via edges and defects of the 2D layer [61, 65, 67].

Intercalation of epitaxially grown 2D materials has attracted enormous attention due to its multifaceted application potential. One effect of intercalation is the decoupling from the substrate. The modified interaction can be harnessed to electronically decouple the 2D sheet [14, 68–70] or to chemically decouple and thereby exfoliate it [71]. Further, intercalation is a feasible method to chemically dope the 2D material [72, 73], a similar effect as electric field doping in field effect transistors [1]. Thereby, in the case of Gr, the chemical potential of the Dirac electrons can be altered and even shifts of the Fermi level up to the van Hove singularity of Gr is possible [73]. Finally, confined reactions were performed at the Gr/substrate interface [74–76].

Within this work a novel approach to facilitate intercalation of rare gas atoms below metal-supported 2D-materials is exploited. We use ion irradiation to inject and trap atoms under Gr and hBN on Ir(111) [77]. This approach opens up new avenues for confined reactions or 2D layer growth at the interface.

1.5 Supported 2D Layers as Template for Self-Assembly

Owing to their moiré pattern, Gr and hBN on Ir(111) serve as perfect templates for ordered cluster growth. The varying interaction of the Gr sheet with the metal substrate within the moiré unit cell results in preferential binding of vapor-deposited metal atoms. The formation and stability of metal clusters depend on several parameters, such as lattice constant, cohesive energy, and interaction of the metal and the 2D layer [78]. The high stability of a range of metal clusters on Gr/Ir(111) can be explained by rehybridization of the C atoms. DFT calculations and X-ray photoelectron spectroscopy (XPS) measurements show that the carbon atoms in the vicinity of a cluster adsorption site rehybridize from sp^2 to sp^3 upon cluster deposition [79, 80]. By this rehybridization the carbon atoms form alternating bonds to the underlying iridium atoms and the metal atoms above. This is only efficiently done in the fcc and hcp regions of the moiré cell where an iridium atom is located beneath the carbon atom. Thus, clusters are preferentially located at hcp and for low temperatures also at fcc sites, resulting in a periodic cluster superlattice as shown in Figure 1.7.

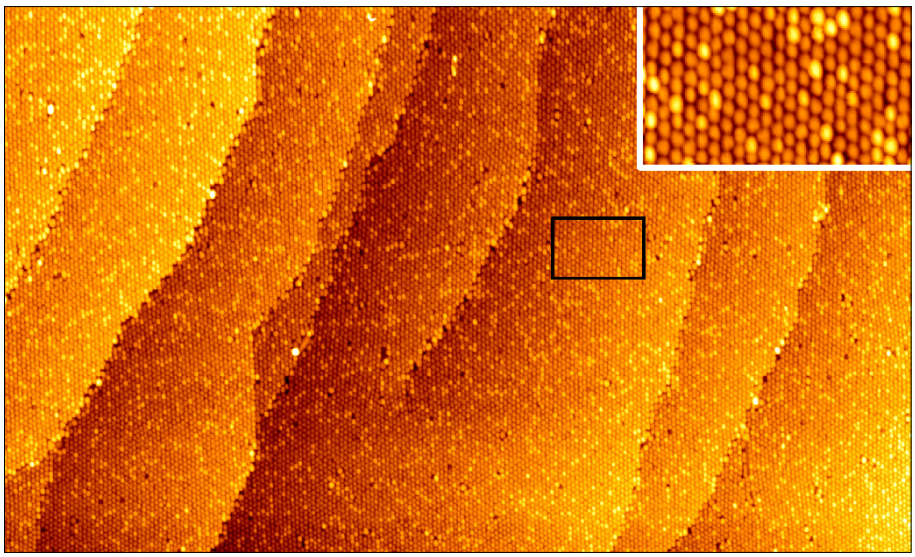

Figure 1.7: Cluster superlattice. Ir cluster superlattice on Gr/Ir(111). Image size is 500 nm × 300 nm, inset 50 nm × 30 nm. Reprinted with permission from Ref. [81]. © IOP Publishing & Deutsche Physikalische Gesellschaft. Published under a CC BY-NC-SA license.

CHAPTER 2

Ion Surface Interactions and Defect Production

Ion bombardment is a versatile tool for surface modifications. In order to understand the mechanisms of ion induced surface modifications it is of utmost importance to understand damage formation mechanisms at the level of the interaction of a single ion with the target material, in particular the surface.
In this chapter the focus is on the interaction of charged particles in the keV range with a solid target. First, the energetics of the interaction of one ion with the target material is discussed, followed by a brief description of bombardment induced defect production and thermally activated diffusion processes.

Stopping Power

When a highly energetic particle such as an ion impinges on a substrate it experiences an energy loss and decelerates due to a transfer of its kinetic energy to the target material. This energy loss can be described by three mechanisms: the ion is elastically scattered by the target nucleus (nuclear stopping) as well as inelastically by the target electrons (electronic stopping); above a particle and isotope dependent threshold energy the ion is also inelastically scattered by the target nucleus inducing nuclear reactions.
The stopping power $S(E)$ of a material can be written as

$$N \cdot S(E) = -\frac{\mathrm{d}E}{\mathrm{d}x} = -\left(\frac{\mathrm{d}E}{\mathrm{d}x}\right)_{\mathrm{d}} - \left(\frac{\mathrm{d}E}{\mathrm{d}x}\right)_{\mathrm{e}} - \left(\frac{\mathrm{d}E}{\mathrm{d}x}\right)_{\mathrm{n}}, \tag{2.1}$$

where N is the atomic density of the target material and $\mathrm{d}E/\mathrm{d}x$ describes the energy loss per unit path length. The index d is denoted for displacement, as nuclear stopping explains permanent displacement of target atoms, e is assigned to the electronic stopping and n to nuclear reactions. Nuclear reactions become important only at very high projectile

energies ($\gg 1\,\mathrm{MeV}$) and will therefore not be discussed further. For intermediate energies (MeV) electronic stopping gains importance, whereas in the energy range considered in this work (keV range) electronic losses play a tangential role and scattering with the target nucleus is the dominant process. Hence, the interaction can be treated by using the Coulomb potential:

$$V(r) = \frac{Z_1 Z_2 e^2}{r}\chi(r), \tag{2.2}$$

where $\chi(r)$ is the screening function that screens the repulsive forces of the nuclei because of the partial shielding by the surrounding electrons. The screening function $\chi(r)$ can be approximated by unity in case of swift (MeV) particles and then the term describes classical Rutherford scattering.
In crystalline materials the impinging ion may also undergo channeling. This means that the ion gets focused in between crystal planes and atomic rows. Consequently, a decrease of the relative importance of $\left(\frac{\mathrm{d}E}{\mathrm{d}x}\right)_\mathrm{d}$ with respect to $\left(\frac{\mathrm{d}E}{\mathrm{d}x}\right)_\mathrm{e}$ can be observed. Moreover, defect production and sputtering are strongly hampered. Thus, the nuclear and electronic stopping and with this defect production is not only influenced by the target density but also by the crystal structure.

Ion Ranges in Solids

Directly related to the energy loss is the average ion penetration depth $R(E)$. It is described by

$$R(E) = \int_E^0 \frac{\mathrm{d}E}{\mathrm{d}E/\mathrm{d}x}, \tag{2.3}$$

assuming a continuous deceleration of the particle. The average projected range R_p is given by

$$R_\mathrm{p} = C_l M_2 \left(\frac{Z_1^{2/3} + Z_2^{2/3}}{Z_1 Z_2} E\right)^{2/3}, \tag{2.4}$$

and is defined as the projection of $R(E)$ onto the primary ion direction (compare Figure 2.1).

Kinematics of Binary Collisions

A point defect is created in a binary collision if the primary ion transfers sufficient energy to the target atom to displace it permanently from its lattice site. The energy transfer of

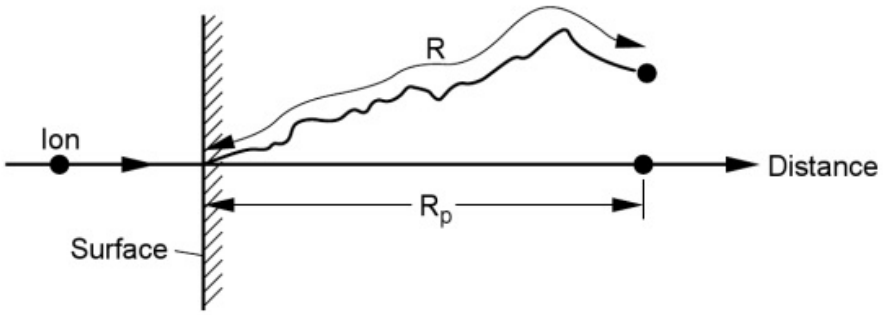

Figure 2.1: Ion range in solids. Illustration of the total path length R, which gives a projected range R_p, along the direction parallel to the incident ion. From [82]. With permission of Springer.

a keV ion onto a target atom can be calculated from a simple two body scattering event as displayed in Figure 2.2. The maximum energy $E_{\max}$ is transferred in a head-on collision and is given by

$$E_{\max} = \frac{4mM}{(m+M)^2}E. \tag{2.5}$$

Here m is the mass of the primary particle with kinetic energy E and M is the mass of the target atom, which is assumed to be at rest.

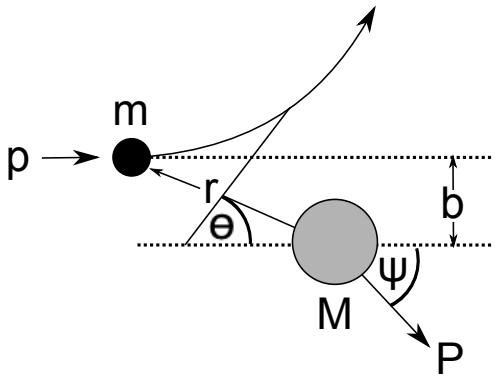

Figure 2.2: Binary collision. Explanation see text. Redrawn from [83].

The corresponding fraction of transferred energy is small for large mass differences and reaches unity when the masses are identical. However, most collisions will occur with non-zero impact parameters resulting in a reduced energy transfer of

$$E = E_{\max}\cos^2\Psi, \tag{2.6}$$

with Ψ the scattering angle of the recoiling target atom. This recoil angle depends on the scattering potential and increases with the impact parameter b (compare Figure 2.2). Hence, the probability for collisions with low energy transfer increases with increasing

scattering angle of the recoiling target atom. Many subsequent large angle scattering events can therefore result in sub-threshold energy transfer without defect creation.

Defect Production and Diffusion Processes

If a lattice atom is struck by a particle possessing enough energy to enable its displacement, a primary knock-on atom (PKA) is produced by the transfer of recoil energy. In the case of light (H^+, He^+) or low energetic (eV range) heavy ions the PKA may be able to further displace lattice atoms from their regular lattice sites, but only isolated defects arise. The trajectories of the involved atoms in a single displacement event are depicted in Figure 2.3.

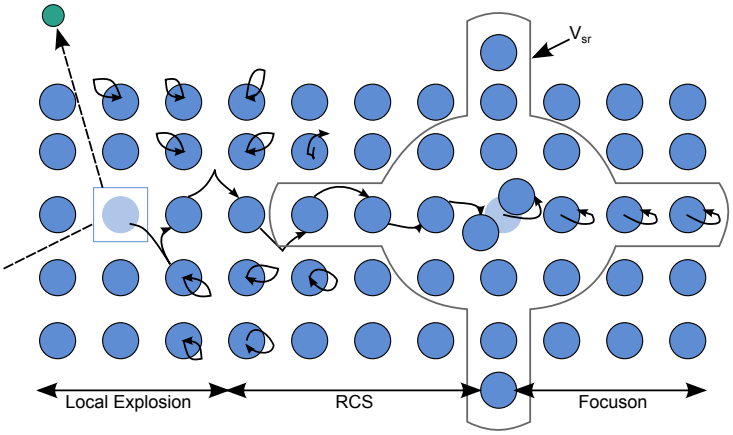

Figure 2.3: Single displacement event. Sketch of a single displacement event. Explanation see text. Redrawn from [84].

Initially, the primary ion hits a target atom and causes a local explosion in its vicinity. Thereby, the recoil energy is randomized among the atoms closest to the PKA. From here, a replacement collision sequence (RCS) evolves. In this sequence the PKA transfers some of its energy onto its neighboring atom and, thus, replaces it. This RCS continues until there is not enough energy to replace any further atom from its regular lattice site. Since the last replaced atom cannot return to its regular lattice site, because this is occupied by the preceding atom, an interstitial is formed. The residual energy is transferred to the atoms lying behind the RCS forming a focuson, which describes a collective motion without displacement. A focuson will also be present for projectile energies that do not exceed the displacement threshold.

To produce a stable vacancy-interstitial pair, also known as Frenkel pair, the vacancy and interstitial have to be well separated. This is most effective along close-packed rows.

Only if in the spontaneous recombination volume V_{sr} no vacancy is found, the interstitial is prevented from recombination.

For heavy, high energy ($1 - 10^3$ keV) ions the transferred energy is large enough to enable the displaced atom to displace further lattice atoms initiating a collision cascade, shown in Figure 2.4. As a result, temporary or permanent displacements occur, where the latter form bulk (vacancies, interstitials) and surface (surface vacancies, adatoms) defects.

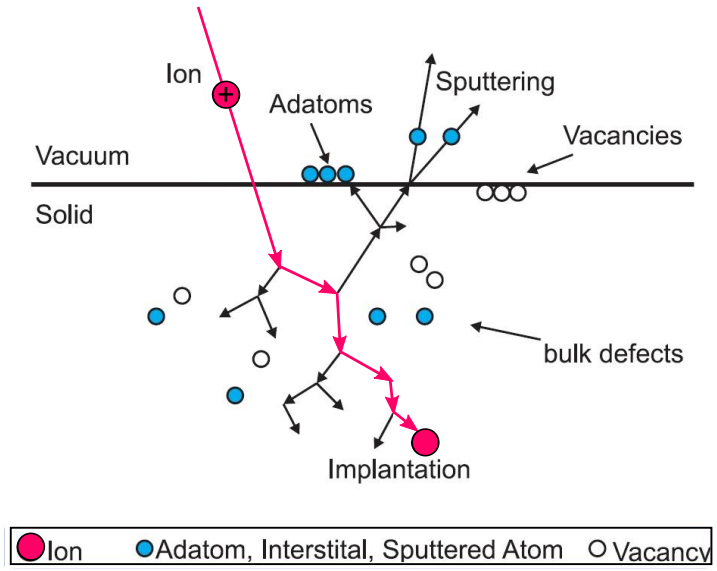

Figure 2.4: Ion induced defects by a collision cascade. Sketch of the ion induced defects in a solid in course of a collision cascade. Redrawn from [85].

The cascade evolution can be divided into several stages. First, a collision cascade develops that, second, terminates into a liquid like zone, the thermal spike, followed by, third, a recovery phase. This whole process occurs in a time interval of picoseconds and is called displacement cascade. In the first 0.1 - 0.3 ps the PKA is decelerated by sequent recoils producing several branches of collision cascades until the energy of all moving atoms has dropped below E_d. During this sequence the distance between each collision decreases. In the end (within 0.25 ps), the energy of the PKA is distributed relatively fast between many atoms in such a small volume that a collective motion of the atoms leads to a thermal spike. Simulations predict that the temperature in the spike region reaches multiples of the melting temperature confirming the existence of a molten core. At the same time, the local atomic density reduces by up to 20 % within this zone and compressed material is found in the surrounding [82]. This is the effect of a shock front initiated by the spike formation. In the following cooling phase ($\sim$ 3 ps) stable interstitials and clusters of interstitials are produced outside the molten zone. The core itself cools down via phonons,

solidifies, and recrystallizes after about 10 ps. Here, interstitials annihilate with nearby vacancies in the quenching zone leaving only as much vacancies in the core as stable interstitials are produced and forming a depletion zone [86].
Whenever the impinging ion transfers enough energy close to the surface or a collision cascade intersects it, sputtering occurs, which will be discussed below. Moreover, electronic excitations of the target material will appear.
Since all experiments are carried out at finite temperature, diffusion processes have to be considered and will, therefore, be briefly addressed in the following. The defect evolution is subject to temperature activated processes that are mainly governed by mobilities of interstitials and vacancies. The jump rate ν depends on the migration activation energy E_m and is given by

$$\nu = \nu_0 \exp(-E_\mathrm{m}/kT), \tag{2.7}$$

where $\nu_0 \approx 10^{13}\, s^{-1}$ and is approximated by the Debye frequency. In general, interstitial mobilities set in at lower temperatures than vacancy mobilities with typical energies on the order of 1.3 eV for vacancies and 0.15 eV for interstitials in metals [83]. Thus interstitials in metals are mobile at relatively low temperatures. To reduce their free energy interstitials and vacancies will agglomerate into defect clusters. At high temperatures, both types of defects are mobile resulting in their recombination before agglomeration. Hence, at high irradiation temperatures only surface vacancy islands due to the sputtered material occur. At even higher temperatures, these vacancy islands will diffuse further and attach to step edges.

Gas Implantation and Bubble Formation

Depending on fluence, energy, and irradiation temperature, a considerable amount of the incoming ions will be trapped within the sample. The consecutive capture of implanted gas atoms by a vacancy, leading to a defect-impurity complex, initiates bubble formation. When a critical number of gas atoms is reached, the induced stress can be reduced by the emission of interstitial atoms or clusters thereof, which in turn allows capture of further gas atoms. For clusters larger than approximately ten atoms the favored geometry is a platelet, *i.e.*, a dislocation-loop. This stress relief mechanisms is also referred to as loop punching. At high temperatures bubble formation can also occur in course of the agglomeration of several defect-impurity complexes. Above temperatures of approximately half the melting temperature T_m vacancy mobility is high and the bubbles are in thermal equilibrium with the surrounding lattice. The gas pressure can be approximated by

$$P = \frac{2\gamma}{r}, \tag{2.8}$$

where r is the radius and γ the surface tension (or surface free energy) of the cavity. With a typical value for the surface tension of 1 N/m a cavity of radius 10 Å will have an equilibrium pressure of 2 GPa leading to atomic densities far above that of the liquid phase [83, 87]. Even higher pressures can be found at low implantation temperatures ($\approx 0.15\,T_\mathrm{m}$), where self-interstitials and gas atoms are sufficiently mobile but vacancies are not [88].

Sputtering Yield

Once a surface atom undergoes a knock-on collision with an energetic particle or a collision cascade breaks the surface, it can gain enough kinetic energy to exceed the surface binding energy and become ejected from the surface. The characteristic parameter is the sputtering yield

$$Y = \frac{\text{number of sputtered atoms}}{\text{number of incident ions}}. \tag{2.9}$$

The sputtering yield is proportional to the energy loss and inversely proportional to the surface binding energy E_b. It is strongly dependent on the angle of incidence as for an increasing angle with respect to the surface normal the amount of energy deposited in the near-surface region is increased. Only for glancing incidence this tendency is reversed and the sputtering yield drops sharply [see Figure 2.5 (a)]. This effect is due to a significant increase of the reflection coefficient due to overlapping shadow cones, *i.e.*, the areas behind the atoms that are forbidden for the impinging ion due to Coulomb repulsion, along the ions trajectory. This can be seen in Figures 2.5 (b) to (d) showing trajectories of 1 keV Ar ions impacting at $\theta = 60°$, $\theta = 70°$, and $\theta = 80°$ on Al. While the ion is able to penetrate the crystal in a broad angular range, at an angle of $\theta = 70°$, the ions are reflected off the surface. Sputtering still occurs since the ions deposit a decent amount of energy to the surface in large-angle scattering events. In case of $\theta = 80°$, the ions are specularly reflected and channeled by the surface. Almost no energy is transferred to the surface minimizing erosion.

Formation of Surface Vacancies and Adatoms

The discussion up to know concentrated on the ion irradiation effects within the bulk or on sputtering of particles off the surface. At the surface, ion irradiation can cause substantial morphological changes. At low fluences, isolated defects such as surface vacancies

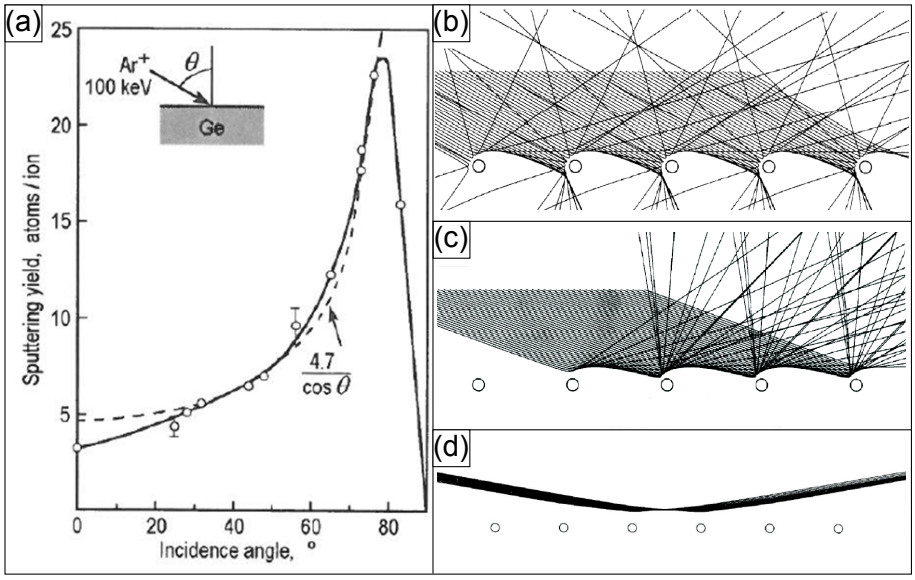

Figure 2.5: Sputtering yield. (a) Variation of the sputtering yield with ion incidence angle θ for 100 keV Ar bombardment of Ge. Reprinted from [89]. With permission of Springer. (b) - (d) Sketches of trajectories of 1 keV Ar ions in Al for (b) $\theta = 60°$, (c) $\theta = 70°$, and (d) $\theta = 80°$. Reprinted from [90], Copyright 2002, with permission from Elsevier.

and adatoms are created. At slightly elevated temperatures these defects are mobile and may annihilate or accumulate to form adatom and vacancy clusters and at increasing temperatures extended adatom and vacancy islands. Eventually, at high annealing temperatures all adatoms and surface vacancies annihilate and bulk vacancies migrate to the surface so that exclusively vacancy islands are present. At this stage determination of sputtering yields by STM analysis is possible [86].

For ion irradiation of crystalline materials at glancing incidence angles ($> 75°$) the ion can undergo subsurface channeling, *i.e.*, the ion may enter between crystal planes and perform an oscillatory motion just below the surface [91, 92]. As a result, vacancies and adatoms are produced along the channel where the ion hits the topmost layer from below. This effect is enhanced at ascending step edges since an impact can be considered as perpendicular here. The ion energy loss per unit length is substantially reduced and, therefore, ion trails are elongated.

CHAPTER 3

Defects in Graphene and Hexagonal Boron Nitride

As outlined above, graphene and hexagonal boron nitride have attracted considerable interest in the past decade due to their outstanding electronic and structural properties, making these materials promising candidates for nanotechnological applications. Defects may deteriorate their intrinsic properties and performance. However, many applications even require the controlled introduction of defects into the 2D material.
In this chapter, defects which may appear during growth or which are intentionally introduced by particle irradiation are reviewed.

3.1 Structural Defects

Due to the ability of the sp^2-hybridized atoms in Gr and hBN to arrange themselves into a variety of polygons, the number of structural defects is essentially infinite. Here, the focus is on a few defect structures which are of interest to this work. Specifically, defects in Gr are of interest since most experiments in this work are on Gr and furthermore studies on defects in hBN are still scarce.

Stone-Wales Defects

The simplest example of an intrinsic defect in the Gr lattice is the Stone-Wales defect which is formed by a carbon bond rotation of 90°. The four adjacent hexagons are then transformed into two pairs of pentagons and heptagons. Since its formation energy is approximately 5 eV, with a kinetic barrier of roughly 10 eV, its equilibrium concentration

is negligible. However, it can be formed in non-equilibrium conditions. Once formed the reverse process has a kinetic barrier of roughly 5 eV making the defect stable at typical experimental temperatures. Stone-Wales defects in hBN change the local curvature at the defect site and are highly reactive due to the formation of B-B and N-N bonds [93–95]. They are energetically less favorable than other topological defects in the form of squares and octagons, where alternating bonds (N-B) are present [94, 95].

Vacancy Defects

When the threshold of displacement is overcome, *e.g.*, in course of energy transfer in a ballistic collision with an ion, vacancies are formed. In freestanding or quasi freestanding Gr the three dangling bonds that are formed after the removal of one C atom reconstruct into a pentagon-nonagon pair as illustrated in Figure 3.1(a) and (b). The remaining undercoordinated C atom appears as a bright protrusion in STM due to a higher density of states at the Fermi energy [96] [see Figure 3.1(c)]. However, on a substrate interacting stronger with the Gr, *e.g.*, Ir(111), the dangling C bonds surrounding the vacancy can be saturated at the substrate giving rise to a funnel-like shape of the defect and resulting in fewer states at the Fermi energy [20].

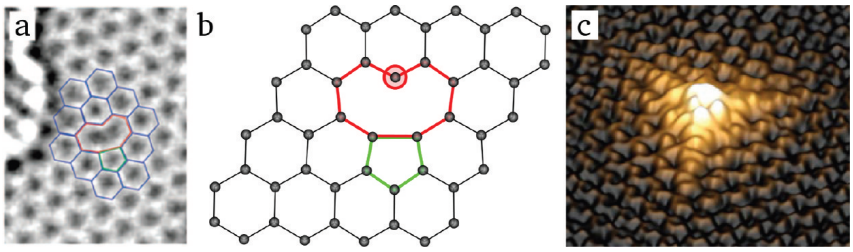

Figure 3.1: Single vacancy in graphene. (a, b) Atomic scale transmission electron microscopy image of single vacancy in Gr and corresponding atomic structure as obtained by DFT calculations. Reprinted with permissions from [97] and [98]. Copyright 2008, 2011 American Chemical Society. (c) STM image of single vacancies in graphite. The vacancies appear as bright protrusions in STM due to an increased local density of state at the Fermi energy. Reprinted figure with permission from [96]. Copyright 2010 by the American Physical Society.

Point defects have also been observed for hBN, however, due to the binary nature of hBN, their appearance differs. Figure 3.2(a) shows an high-resolution transmission electron microscopy (HRTEM) image of defects in hBN exhibiting triangular shapes of various sizes, all pointing is the same direction. Models for these defect structures are presented in Figure 3.2(b). The smallest triangles represent single vacancies whereas the larger ones

consist of several vacancies [99]. For free-standing hBN it was found that the edges are of zig-zag type and N terminated [99]. This is attributed to the theoretical prediction that the displacement threshold for B atoms is smaller compared to N atoms [100]. However, again crucial differences occur when the hBN sheet is placed on a substrate. Farwick zum Hagen and coworkers [48] showed that in case of hBN/Ir(111) the edges of vacancy type defects are B terminated due to stronger binding of B atoms to the substrate .

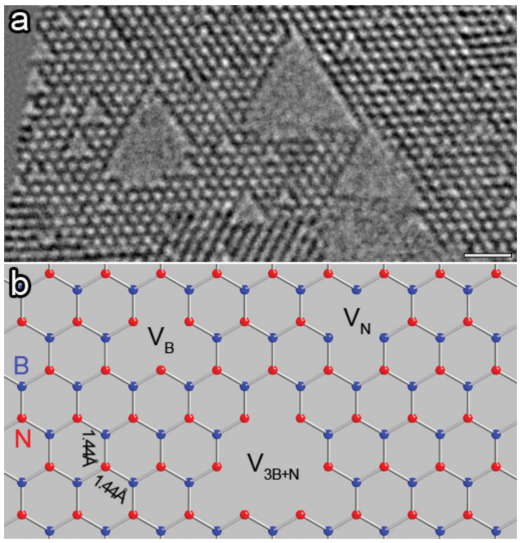

Figure 3.2: Atomic defects in hexagonal boron nitride monolayers. (a) A typical HRTEM image showing several triangular shaped vacancy defects with the same orientation in hBN. (b) Models for the atomic defects in hBN. V_B, V_N, and V_{3B+N} stand for a single B or N vacancy, and a tetravacancy (3B + 1N), respectively. Reprinted figure with permission from [99]. Copyright 2009 by the American Physical Society.

Adatoms and Impurities

Interstitial atoms, as they appear in 3D crystals, do not exist in 2D materials due to the extreme energies needed to place an additional atom to any in-plane position. Therefore, additional atoms use the third dimension and form adatoms. For a C adatom placed on top of freestanding Gr the energetically favored position is the bridge site, *i.e.*, on top of a C-C bond. The adatom can form covalent bonds to the 2D layer with a binding energy of the C adatom on the order of 1.5 - 2 eV for freestanding Gr [101, 102]. Similar to the case of C on Gr, a C adatom on hBN prefers the bridge-like site of the B-N bond with an adsorption energy of 0.95 eV [103]. Metal adatoms on the other hand can be trapped by imperfections of the 2D layer by forming covalent bonds to the defect site [104].

Further point defects that occur in Gr and hBN are the incorporation of foreign atoms as substitutional impurities. One prominent example of this is the replacement of C atoms by B or N atoms which leads to doping of Gr [105, 106].

One-Dimensional Defects

As will be discussed below grain boundaries which are composed of aligned dislocations form one-dimensional defects. In Gr the core of the dislocation is a pentagon-heptagon pair. In hBN the merging of two domains is more difficult. However, in both cases the defects along the grain boundary display sites of higher reactivity.

3.2 Generation of Defects

The high formation energy of single vacancies in Gr and hBN reduces their appearance well below the melting temperature of graphite to an undetectable concentration in thermal equilibrium. However, non-equilibrium defects can be introduced during crystal growth, by irradiation with energetic particles, or by chemical treatment. Since not relevant to this work the latter will not be addressed here.
As outlined in Chapter 1 large-scale growth of Gr and hBN is achieved by chemical vapor deposition. In this process the 2D sheet usually grows from several nuclei forming different domains that may be rotated to each other depending of the 2D-substrate systems and their interaction. When two rotated domains merge a line defect, *i.e.*, a grain boundary which is composed of aligned dislocations, is formed. In case of Gr/Ir(111), due to the moderate interaction, different rotational domains may occur after CVD growth. However, for properly chosen grows conditions all domains are aligned with only small-angle misorientations that lead to the observation of small-angle in-plane tilt boundaries terminating in heptagon-pentagon pairs (5-7 defects) [107]. In case of hBN/Ir(111) as discussed above, only two domains rotated by 180° with respect to each other occur. The merging of two rotated domains of hBN is not straight forward. 5-7 defects inevitable introduce homo-elemental bonding which is weaker than hetero-elemental bonding. Alternatively, the domains can merge via the formation of 4-8 rings which are free of homo-elemental binding but have a higher strain energy. The nature of the boundary is thus determined by the balance of strain and chemical bonding. Nevertheless, for hBN/Ir(111) the exact determination of the structure remains ambiguous since it could also incorporate binding to substrate atoms.

Under electron irradiation, *e.g.*, in a transmission electron microscope (TEM) setup, the energetic electrons interact with the target nucleus and electronic system. Thereby, two defect creation mechanisms are activated: bond rotation and atom ejection. Atom ejection is only facilitated when the threshold energy for displacement T_d is overcome ($E_{d,Gr} = 18 - 22\,eV$ [108, 109], $E_{d,B} = 19\,eV$, $E_{d,N} = 23\,eV$ [109]). Due to the electrons small mass, this needs rather high electron energies exceeding 100 keV, while bond rotation is already activated at lower electron energies.

During TEM imaging irradiation induced bond rotation and C atom ejection is frequently observed [110]. This leads to the migration of dislocations which is usually accomplished via Stone-Wales bond rotations (glide) or the loss of a C dimer (climb) at a certain position (green ellipse) as visualized in Figure 3.3. Theoretically, the dislocation can climb in the opposite direction by the insertion of a C dimer. However, this is not observed in TEM studies.

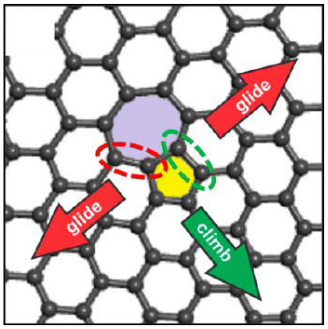

Figure 3.3: Dislocation migration. Schematic diagram showing possible migration directions for dislocations in Gr. A dislocation can move along the glide plane via bond rotation or climb perpendicular to the glide plane via the removal of two C atoms. Reprinted with permission from [110]. Copyright 2015 American Chemical Society.

In case of ion irradiation atom ejection in a ballistic knock-on displacement event occurs already at energies in the keV range as discussed in Chapter 2. Thorough MD simulation studies on the defect generation in Gr and hBN have been carried out by Lehtinen *et al.* [111–113].

In terms of defect generation by particle irradiation distinct differences arise in supported 2D materials. A prominent example is Gr on $SrTO_3$, a dielectric material [114]. Swift heavy ion irradiation induces hill-hock formation by electron excitation in the substrate and combined with defect creation in Gr causes it to split-up and fold along the ions trail [114]. Another example is the effect of interface channeling which describes the oscillatory motion of the ion at the Gr/Ir(111) interface due to consecutive reflections at the substrate and Gr inducing chains of holes within the Gr layer.

PART III

Experimental

CHAPTER 4

Experimental Techniques

In this chapter the basic concepts of the experimental techniques applied in this thesis are briefly summarized.

4.1 Scanning Tunneling Microscopy

A scanning tunneling microscope works based on the quantum mechanical tunneling effect and enables the imaging of surfaces at the atomic scale and in real space. Its invention by G. Binning and W. Rohrer in 1981 was honored by the Noble Prize in Physics in 1986 [115]. In scanning tunneling microscopy, a sharp - in the ideal case atomically sharp - conductive tip is laterally scanned over the sample surface by piezo actuators at a distance of only a few Å. At such close proximity the electronic wavefunctions of the last tip atom and the sample overlap. When a bias voltage U_s is applied between them a tunneling current I is enabled to flow. During the scanning process a feedback loop regulates the vertical distance z. The value of I depends on the local density of states (LDOS) of the tip and the sample (ρ_t,ρ_s), their distance z, and the tunneling matrix element $M(E)$. In the approximation of two planar electrodes the tunneling current results to

$$I \propto \int_{-\infty}^{+\infty} |M(E)|^2 \rho_\mathrm{t}(E - eU_\mathrm{s}) \rho_\mathrm{s}(E) \left[f(E - eU_\mathrm{s}) - f(E) \right] \mathrm{d}E, \tag{4.1}$$

where $f(E)$ is the Fermi function, U_s the applied sample bias voltage, and E is the energy of the respective state [116].

In a simplified theory by J. Tersoff and D. Hamann [116] the tunneling current is approximated by

$$I \propto U_s \rho_t(E_F)\rho_s(\mathbf{R}_s,E_F), \tag{4.2}$$

where $\rho_s(\mathbf{R}_s,E_F)$ is the density of states of the sample surface at the center $\mathbf{R}_s$ of a metallic s-orbital of the STM tip. The theory assumes eU_s to be small compared to the workfunction of the sample Φ_s ($eU_s \ll \Phi_s$).
For semiconducting surfaces $eU_s \ll \Phi_s$ does not hold anymore, therefore 4.1 needs to be modified. In the Wentzel-Kramers-Brillouin approximation a transmission probability $T(U_s,\Phi_s)$ depending on U_s and Φ_s is introduced. This gives

$$I \propto \int_{E_F}^{E_F+eU_s} |T(U_s,\Phi_s)|\rho_t(E)\rho_s(\mathbf{R}_s,E)dE, \tag{4.3}$$

Within this approximation the distance dependence of the tunneling current I can be approximated [115] by

$$I(z) \propto exp(-k\sqrt{\Phi}z), \tag{4.4}$$

with a constant $k = 2\frac{\sqrt{2m}}{\hbar} \approx 1.025\, eV^{-\frac{1}{2}}\text{Å}^{-1}$ and the electron mass m. The potential barrier Φ is given by

$$\Phi = \frac{\Phi_s + \Phi_t - eU_s}{2}, \tag{4.5}$$

where $\Phi_{s,t}$ are the work functions of the sample and tip, respectively. The exponential dependence of the tunneling current on the tip to sample distance results in a high vertical resolution. The resulting STM topograph is a superposition of the topography and the LDOS. A more comprehensive overview of STM theory can be found in [117].
In addition to scanning over the sample, information on the electronic structure at a given sample position can be obtained by scanning tunneling spectroscopy (STS). In STS the density of states is measured by using the lock-in technique, where the differential conductivity is recorded. According to J. Tersoff and D. Harmann the density of states is proportional to the differential conductivity

$$\frac{dI}{dU}(U) \approx |T|^2\rho_t(E_F)\rho_s(E_F). \tag{4.6}$$

4.2 Low-Energy Electron Diffraction

Low-energy electron diffraction (LEED) is opposed to STM an averaging technique to obtain structural information of a surface in the reciprocal space. For LEED measurements

the sample is illuminated by an electron beam with energies of about 20 - 300 eV and a typical spot size on the order of 1 mm. The elastically scattered electrons are then accelerated towards a fluorescent screen. This experimental setup allows direct observation of the diffraction pattern. It is ideally suited for surface analysis due to two reasons: (i) The de Broglie wavelength of the electrons $\lambda = \frac{h}{\sqrt{2mE}}$ is of the order of the interatomic distances satisfying the diffraction conditions. (ii) The mean free path of the electrons is a few atomic layers making LEED very surface sensitive.
Besides the information obtained from the spot geometry the sharpness and intensity of the LEED pattern give qualitative information on the structural perfection of the sample. A highly-ordered surface gives rise to bright sharp spots with a low background intensity. Structural defects, crystallographic imperfections, and thermal fluctuations cause a broadening and weakening of the spots concomitant with an increase in background intensity. The absence of a LEED pattern is a strong indicator for a disordered or amorphous surface.
A more detailed analysis of the spot profile can give insight into the domain size of the sample under investigation, since the spot width is inversely proportional to the number of regular scattering units. In LEED I-V curves the spot intensity is analyzed as a function of the primary electron energy. This technique allows detailed determination of the atomic positions within the unit cell [89].
For a comprehensive description of LEED the reader is referred to [89].

4.3 X-Ray Photoelectron Spectroscopy

X-ray photoelectron spectroscopy is a surface-sensitive averaging technique to investigate the elemental composition of a sample and the chemical state of the constituting atoms. The technique is based on the photoelectric effect, *i.e.*, the emission of electrons due to photon absorption. In XPS the sample is irradiated with a focused beam of monochromatic X-rays with a photon energy $h\nu$ and the kinetic energy E_{kin} of the emitted electrons is measured. According to energy conservation and in the single particle picture the binding energy (BE) of the electron is then given by

$$E_{\mathrm{B}} = h\nu - E_{\mathrm{kin}} - \Phi, \tag{4.7}$$

where Φ is the workfunction of the sample. Thus to obtain the BE of the core electron besides its kinetic energy the workfunction needs to be known. To circumvent this, the cut-off of electron emission at the Fermi energy can be measured and thus energies can

be referenced to the Fermi level. In a typical XP spectrum the intensity of the detected electrons is then plotted as a function of the BE. Since BEs are element specific the composition of the sample can be derived by analyzing the intensities in the XP spectrum. As is the case of LEED, due to the strong interaction of electrons with matter the electrons that escape from the sample without inelastic scattering stem from the surface-near region (a few nm). Moreover, compared to other photoemission techniques XPS is perfectly suited to probe the discrete core levels since the photoionisation cross-section is greatest for photon energies close to the binding energy of the photoelectron.

The core level BE of a specific element varies depending on its chemical environment. Thus the difference in the BE of a core level of an atom of the same species in a different environment yields a so called core level shift (CLS) detectable with XPS. A typically observed CLS is the surface core level shift which is due to the different chemical environment of the surface atoms of a solid compared to the atoms in the bulk.

In an XPS setup monochromatic light is generated either by a lab source or synchrotron radiation from an electron storage ring. The kinetic energy of the photoelectrons is typically measured by a hemispherical analyzer with a fixed transmission mode, which means that the photoelectrons are decelerated by a retarding voltage and pass the analyzer with a constant pass energy. To obtain a full XP spectrum the retarding voltage is varied.

4.4 Temperature Programmed Desorption

In temperature programmed desorption (TPD) the temperature of a sample is monotonically increased and the increase in pressure due to the desorbing species is simultaneously recorded with a mass spectrometer as a function of the sample temperature. The resulting desorption traces yield information about, *e.g.*, the desorption energy, kinetics, and initial coverage of adsorbate layers. Moreover, TPD is frequently used to study noble gas implantation. Here, the sample is exposed to an ion beam with a well defined energy and fluence and subsequently the release rate of the gas upon heating is monitored by TPD. By varying the irradiation parameters such as ion energy, fluence, and temperature one can deduce the release kinetics from and the binding energies to various trapping sites from the desorption traces.

Although the resulting spectra are complex and a detailed interpretation of the resulting data in terms of atomistic processes is ambiguous, the observed desorption peaks after noble gas irradiation of Ni could consistently be divided into the following processes [118, 119]:

- **A-band release (300 K - 650 K):**
  Gas release in this regime is attributed to surface diffusion processes which enables gas atoms trapped in near-surface regions to escape from their trapping site.

- **B-band release (650 K - 1000 K):**
  In this regime two distinct desorption peaks are observed that are traced back to noble gas trapped in vacancies in the bulk or close to the surface.

- **C-band release (1000 K - melting point):**
  The C band consists of several peaks and is due to migration or dissociation of agglomerates (clusters of vacancies and gas atoms) initially situated deeper in the bulk. The C band has an energy and fluence threshold and only appears for fluences of $\approx 10^{-18}$ ions/m^2 for Ar and He and when the gas is implanted beyond a threshold distance, which is on the order of a few atomic layers, within the bulk. The deduced binding energy increases with the size of the agglomerate.

CHAPTER 5

Setup and Procedures

Parts of Chapter 5.3, 5.4, and 5.5 are literally taken from my publications [77, 120–122].

All experiments described in this thesis were conducted in ultra-high vacuum (UHV) setups in Cologne (STM, TPD, and LEED) and at the I311 beamline of Max IV Laboratory in Lund (XPS). In this chapter both setups are introduced and the methods for sample preparation, DFT calculations, as well as MD simulations are presented.

5.1 The Ultra-High Vacuum System Athene

Most experiments in this thesis were performed in the UHV system Athene in Cologne, which is schematically depicted in Figure 5.1 in front and side view. To achieve UHV conditions, different pumps are in use. The main pump capacity is attained by a turbomolecular pump (1) and an ion getter pump (2) attached to the main chamber. Additional pumping is performed by a titanium sublimation pump (3) embedded into a cooling trap (4) filled with liquid nitrogen during measurements. A small turbomolecular pump (5) is used to evacuate the load lock (6) and to differentially pump the ion source (7).
The Ir(111) sample is installed on a sample holder (8) which is hosted on a base plate mounted on a translatable and rotatable manipulator (9). Besides the sample holder inserted into the base plate the system can host up to two more sample holders stored in a sample garage. The sample holders can be extracted via the load lock system (6) without breaking vacuum conditions. The sample in the base plate can be heated up to 1600 K via electron beam heating and cooled down to 50 K by a liquid helium flow cryostat, which

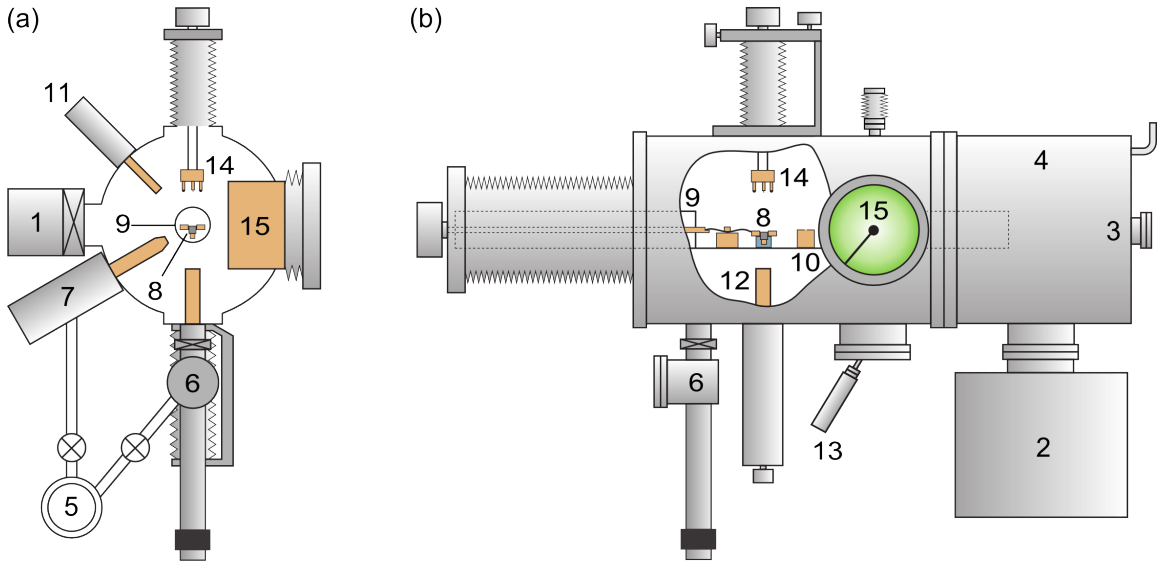

Figure 5.1: Ultra-high vacuum system Athene. Sketch of the system in (a) front and (b) side view. For the numerations within the schematic see the description in the text.

is connected to the base plate through copper braids. Precise temperature measurement is accomplished by a type K thermocouple attached to the sample.

For sample cleaning and ion irradiation experiments the system is equipped with a differentially pumped scanning fine focus ion gun (7). Through a gas inlet system noble gas can be brought into the ion gun where it is ionized and accelerated towards the sample. Uniform erosion is provided by a deflection unit. The ion current in accurately measured in a Faraday cup (10) mounted next to the sample on the manipulator.

The chamber incorporates three leak valves to supply gases into the system (not shown in the schematics). Inside the chamber the gases are guided through dosing tubes increasing the local pressure at the sample position by a factor of approximately 50 compared to the chamber pressure. The residual gas can be analyzed by a quadrupole mass spectrometer (QMS) (11).

For carbon or metal deposition a four pocket e-beam evaporator (12) is attached to the chamber. The fluxes can be measured via the integrated ion monitor of the electronics or via the Faraday cup. Carbon can also be supplied through a current heated water-cooled carbon evaporator (13).

For sample analysis a home-built, magnetically stabilized, variable temperature STM (14) in the inverted beetle design was used [123]. Further LEED measurements were performed using a three grid rear view analyzer (15). The data is recorded by a video camera directly mounted onto the LEED flange.

A more detailed description of the chamber and the STM can be found in [124].

TPD experiments were performed in the similar UHV system TuMA III using a QMS equipped with a Feulner cup [125] to obtain a better signal to noise ratio. For a detailed description of the TuMA III system the reader is referred to [126].

5.2 The Beamline I311 at MAX-Lab

All XPS measurements were conducted at the I311 beamline of the MAX II storage ring of the MAX IV Laboratory in Lund, Sweden, which is operated at 1.5 GeV with a maximum beam current of 300 mA. I311 is an undulator based X-ray beamline. The undulator consists of a periodic array of magnets that forces the electron on a sinusodial path where they emit synchrotron radiation at every period. The interference of these contributions yield radiation of high brilliance. The spectrum of an undulator is not continuous but can be tuned by changing the gap between the two magnetic arrays. Within the beamline itself the radiation is monochromized and focused by gratings, mirrors, and X-ray optics. The experimental endstation consists of a separate analyzer and preparation chamber with base pressures in the 10^{-10} mbar range. The analyzer chamber is equipped with a hemispherical electron analyzer and a CCD camera. The preparation chamber includes usual equipment needed for sample preparation such as ion gun, LEED, gas inlet system, and evaporators.

5.3 Sample Preparation and Analysis

Preparation of Ir(111)

Cleaning of Ir(111) was conducted by cycles of Xe^+ (Cologne) or Ar^+ (Lund) irradiation at room temperature, and annealing to 1520 K (Cologne) or 1300 K (Lund). If necessary the sample was additionally cleaned by O_2 treatment at 1120 K to reduce C impurities or high temperature ion irradiation at 970 K.

Growth of Graphene and Hexagonal Boron Nitride

A well-oriented and closed Gr layer was grown by one cycle of room temperature adsorption of ethylene (C_2H_4) until saturation, thermal decomposition at 1470 K (Lund: 1300 K) followed by Gr growth using 100 L ethylene at 1270 K (Lund: 1170 K) [127]. A partially Gr-covered Ir(111) sample (approximately half monolayer (ML) coverage) was achieved by three cycles of room temperature ethylene adsorption and subsequent thermal decomposition at 1470 K (temperature programmed growth) [128]. Deviations from these

growth procedures are indicated in the respective sections. A high quality, fully closed hBN layer is grown by chemical vapor deposition of 100 L borazine ($B_3H_6N_3$) at 1250 K.

Ion Irradiation

For the ion irradiation experiments in Part IV the ion flux was measured by a Faraday cup prior to and after each experiment (Cologne) or was controlled through adjusting the sample current that itself was calibrated for each ion energy by a Faraday cup in the Cologne setup (Lund). Except for Chapter 7 and 8 the ion incidence was $\approx 30°$ with respect to the surface normal for all XPS experiments (Lund) and at normal incidence for all other experiments (Cologne). Sputtering yields and ion ranges deviate by less than 10% for these two angles of incidence. Ion irradiation was performed with He^+, Ne^+, Ar^+, or Xe^+ ions in the energy range from 100 eV to 5 keV. The lowest ion energy of 100 eV was achieved by accellerating the ions to 200 eV and applying a counter-voltage of 100 V to the sample. If not stated otherwise the exposure was conducted at room temperature. In Chapter 7 3 keV Xe^+ room temperature ion irradiation was performed at angles ϑ ranging from 0° to 85° with respect to the surface normal. For the experiments in Chapter 8 the irradiation of bare and Gr-covered Ir(111) samples was conducted by using 500 eV Xe^+ as well as 200 eV Ar^+ and Xe^+ ions at normal incidence, with the sample temperature kept at 1000 K during exposure.

As damage accumulation can affect defect production in Gr [129], for the STM results in Figures 6.8, 6.14, 6.15, 7.1 we established experimental conditions such that the probability of an ion to impinge on a damaged Gr area remains small. This was accomplished by ion irradiation in consecutive cycles of low fluence irradiation and annealing. If not stated otherwise, we implemented for each parameter set (ion energy, mass, angle) three cycles with an ion fluence of $F = 0.01$ monolayer equivalents (MLE) and an annealing temperature of 1000 K for 300 s. Here 1 MLE corresponds to the surface atomic density of Ir(111), *i.e.*, 1.57×10^{19} particles per m^2. For all other annealing experiments durations and temperatures are indicated.

Carbon Radical Exposure

High purity C was sublimated from a commercial e-beam evaporator with a typical deposition rate of 0.15 ML/min. In the STM chamber in Cologne the evaporator was calibrated by determination of the area fraction of Gr on a clean Ir(111) surface after room temperature C exposure and subsequent annealing to 1470 K. In the Lund setup the obtained rate

was checked prior to XPS measurements by comparing the C 1s peak after normalization to the Ir 4d peak.

To grow bilayer Gr the monolayer of Gr/Ir(111) was exposed to C at 1170 - 1200 K. For C cluster formation C was deposited at room or slightly elevated temperature of 400 K if not stated otherwise.

Scanning Tunneling Microscopy and Spectroscopy

STM imaging was conducted at room temperature with a typical sample bias of $U_s \approx -1\,\mathrm{V}$ and a tunneling current of $I_t \approx 1\,\mathrm{nA}$. For C cluster imaging the typical tunneling parameters were slightly different ($U_s \approx$-5 to -2 V and $I_t \approx 0.5\,\mathrm{nA}$).

STM topographs were post-processed using the SPIP software.

To quantify the amount of trapped Xe in blisters STM image analysis was conducted by determining the area fraction above a threshold height of 180 pm higher than the average Gr level. To quantify the amount of sputtered C atoms, the area fraction below a threshold height of -100 pm with respect to the average Gr level was determined. While this method took into account all vacancy islands (larger aggregates of at least nm lateral size), the missing material of small funnel shaped vacancy clusters had to be added assuming a typical tetravacancy size [20].

STS measurements were performed at $T = 5\,\mathrm{K}$ with a W tip. The LDOS was measured by stabilizing the the tip above a chosen sample position and recording the $\mathrm{d}I/\mathrm{d}U$ signal with a lock-in amplifier [$U_{\mathrm{mod}} = 4\,\mathrm{mV}$, $f = (480 - 610)\,\mathrm{Hz}$] as a function of the energy E =eV with open feedback loop.

X-Ray Photoelectron Spectroscopy

All XP spectra were collected at room temperature in normal emission geometry. In Chapters 6 and 9, for Xe 3d and Ir 4s a photon energy of 1000 eV was used with a total energy resolution of light and analyzer better than 400 meV. After subtraction of a polynomial background the spectra were normalized to the the Ir 4s peak. For determination of the trapped Xe the spectra were integrated to yield the peak area. All C1 s core levels were measured with a photon energy of 390 eV and a total energy resolution better than 60 meV. Ir 4f spectra were measured with a photon energy of 120 eV and a total energy resolution better than 45 meV. In Chapter 10 the B 1s and N 1s core levels were measured with a photon energy of 284 eV and 400 eV and total energy resolutions of 72 eV and 155 eV, respectively. All BE are calibrated to the Fermi edge.

In Chapter 14 the spectra were fitted with Doniach-Šunjić functions [130] convoluted with Gaussian functions after linear background subtraction. The Doniach-Šunjić function includes an asymmetry parameter accounting for electron-hole pair creation and a Lorentzian full width at half maximum (LFWHM) taking the broadening due to the limited lifetime of the core hole into account. The experimental broadening caused by the resolution of the beamline is taken into account by the convolution with the Gaussian function having a Gaussian full width at half maximum (GFWHM). Thus the total width of the peak is given by the convolution of the Lorentzian and Gaussian width. Ir 4f spectra were always normalized to the Ir $4f_{7/2}$ bulk peak. Throughout this work only the Ir $4f_{7/2}$ region is shown and is referred to as Ir 4f. In Chapter 10, after subtracting a polynomial background, the C 1s integrated intensities were normalized to unity whereas in Chapter 14 the absolute intensities were normalized to unity.
BE are given as the positive values referenced to the Fermi edge, thus a positive CLS corresponds to a BE increase. For curve fitting the spectra are often deconvoluted into several components corresponding to different species of atoms on the surface.

Temperature Programmed Desorption

All TPD measurements were conducted with a heating rate of 5 K/s. The resulting desorption traces are plotted without background subtraction.

Low-Energy Electron Diffraction

For global structural characterization, low-energy electron diffraction patterns were recorded at room temperature and are presented with inverted contrast for better visibility. The electron energy is $E = 68\,\text{eV}$ for all presented LEED pattern.

5.4 Density Functional Theory Calculations

All density functional theory calculations in this thesis were performed by Arkady V. Krasheninnikov.
The first-principles DFT calculations were performed using the plane-wave-basis-set Vienna *ab initio* simulation package [131, 132]. The projector augmented wave approach [133] was used to describe the core electrons and a non-local van der Waals functional [134] to describe exchange and correlation. A plane wave kinetic energy cutoff of 400 eV was found to converge energy differences between different configurations within 0.1 eV. The same accuracy was achieved with regard to the number of k-points ($3 \times 3 \times 1$) in

the two-dimensional Brillouin zone. All structures were relaxed until atomic forces were below 0.002 eV/Å. The calculations were carried out for a 200-atom 10×10 Gr supercell on top of a 9×9 three-atomic-layer-thick Ir(111) slab containing 243 atoms, as in our previous work [20, 135], or for the same Ir slab without Gr. 20 Å of vacuum was added in the transverse direction to separate the periodic images of the slab. The simulation supercell used for the calculations of the migration path/energy of Xe from under graphene is shown in Figure 6.5. In practice, the Xe atom was placed in several positions along the path, and the atom was allowed to move only perpendicular to Ir(111) during geometry optimization. All other atoms were allowed to move without any constraints. To assess the role of Ir substrate steps in Gr flake nucleation, we also carried out simulations for a rectangular 272 atom Ir slab with a step on the (111) surface. 20 Å of vacuum was added in the transverse direction to separate the periodic images of the slab.

5.5 Molecular Dynamics Simulations

All molecular dynamics (MD) simulations in this thesis were performed by Harriet E. Åhlgren and Jani Kotakoski.

The classical MD simulations were run with the PARCAS code [136] including only the atomic interactions, as for low ion energies electronic stopping can be neglected to good approximation. For each energy and system, 96 to 300 ion impacts at randomly chosen impact points were simulated, each towards a pristine target. To model the substrate, we used Pt ($Z = 78$, mass 195 u) instead of an Ir substrate ($Z = 77$, mass 192 u) because a well-established interaction model exists for Pt-Pt and Pt-C [137], unlike for Ir-Ir and Ir-C. Due to the similarity in atomic masses, structure, and chemistry of these two species, only minor differences are expected in the MD simulation results. Possible differences introduced by replacing Ir with Pt in the simulations are discussed in Chapter 7. The simulation cell size and time were adapted to allow sufficient relaxation of the system prior to analysis. Heat dissipation at the system edges was modeled with the Berendsen thermostat [138]. The distance between the Gr sheet and the substrate was set to 3.31 Å in agreement with the experimentally determined height of 3.31 Å [139]. Before the final relaxation the substrate lattice constant was stretched by 1 % in order to coincide the two subsystems. The Pt-Pt and Pt-C interactions were modeled by the potentials of Albe *et al.* [137], those of C-C by the bond-order potential of Brenner *et al.* [140] with a repulsive part [141] for small atom separations, and the ion interactions by the universal repulsive potential [141]. The cutoff radii for the interactions were 4.0 Å for Xe-C and Xe-

Pt (symmetry is used, *e.g.*, Xe-C equals C-Xe), 2.0 Å for C-C, 2.8 Å for C-Pt, and 3.3 Å for Pt-Pt. As the Xe-C and Xe-Pt interactions are of van der Waals type, the neglect of the attractive Xe interactions does not introduce a significant error to our simulations. To be quantitative, the binding energies of Xe to graphite (and thus to good approximation to Gr) or Pt(111) are 0.25 eV [142] or 0.27 eV [143], while the binding energy of a C atom to Pt(111) is much larger, 9.2 eV, in our MD simulations. In Chapter 6 the cell consisted of 18360 to 45900 Pt atoms to which 2584 C atoms were added for Gr/Pt(111). The ions were shot in perpendicular direction with respect to the sample. In Chapter 7 the system included a graphene sheet (6380 C atoms) placed on top of a (111)-oriented Pt crystallite (38700 Pt atoms). For each angle 100 impacts of 3 keV Xe ions at randomly chosen impact points were simulated.

PART IV

Ion Irradiation

CHAPTER 6

From Noble Gas Trapping to Blister Formation in Graphene on Ir(111)

*This chapter is based on three manuscripts published in PRB **92**, 085429 (2015) [77], ACS Nano **9**, 4664 (2015) [121], and ACS Nano **8**, 12208 (2014) [120]. It contains contributions from E. H. Åhlgren, U. A. Schröder, A. J. Martînez-Galera, W. Jolie, M. A. Arman, C. Busse, J. Kotakoski, J. Knudsen, A. V. Krasheninnikov, and T. Michely. I was responsible for the design of the experiments, carried out all STM and TPD measurements and analyses (except for the experiment presented in Figure 6.18), was involved in all XPS and STS measurements, analyzed the XPS data, and wrote the drafts of the manuscripts. MD simulations and according histograms as well as figures were done by E. H. Åhlgren and J. Kotakoski, whereas the DFT calculations and images were provided by A. V. Krasheninnikov. Our first manuscript in ACS Nano **8**, 12208 (2014) [120] contains a false interpretation of the phenomena discussed in this chapter. Based on further experiments we shortly after published another manuscript in ACS Nano **9**, 4664 (2015) [121] correcting the interpretation. Nevertheless the experimental and theoretical work remains valid and a thorough presentation of the final results can be found in this chapter.*

When Gr adheres to a substrate, Gr blisters or bubbles can be formed by intentionally pressurizing a cavity in the substrate [29, 144–147], by agglomeration of atoms or molecules residing or being created in the space between Gr and the substrate [28, 148, 149], or even as a result of thermal processing [150]. Such bubbles and blisters in Gr are of considerable interest in view of potential applications ranging from microscopic adaptive-focus lenses [28] via fluid cells for transmission electron microscopy imaging [151] or high

pressure/ high temperature chemistry [149] to surfaces with properties switchable by pressure [29]. Blister and bubble formation have also received considerable interest from a more fundamental point of view, since the strain associated with them gives rise to huge pseudomagnetic fields in Gr [25–27] and thus to a quantization of the electronic structure into Landau levels.

Bubble formation, blistering, and exfoliation in consequence of implantation of light elements like He, D, or H are phenomena that have been thoroughly investigated in the context of nuclear and fusion materials [21]. These phenomena were turned into useful technology by Bruel when applied to achieve microslicing of Si-wafers in silicon on insulator technology [22]. Similarly, He^+ irradiation of graphite in the basal plane orientation with a few ten keV ion energy has been found to result in gas bubble formation, blistering, and exfoliation [23, 24]. Using low energy B and N ion implantation, substitutional doping of freestanding Gr was pioneered by Bangert *et al.* [152]. With similar low ion energies substitutional N implantation of Gr on SiC was accomplished by Telychko *et al.* [153]. For low energies and fluences (negligible damage), Cun *et al.* [53, 154–156] demonstrated that implanted Ar^+ ions may come to rest under a 2D-layer strongly adhering to a metal surface and remain there upon annealing.

In this chapter we demonstrate that Xe^+ irradiation of Gr on Ir(111) is accompanied by Xe trapping at the interface and that even a defective Gr layer on Ir(111) effectively traps Xe supplied by ion irradiation up to very high temperatures. Upon annealing the trapped Xe aggregates cause flat bulges in Gr that transform eventually into highly pressurized blisters. Using a combined experimental and theoretical approach, we uncover that efficient Xe trapping is favored by collisional (reduced ion reflection due to Gr cover) and chemical (strong Gr edge bonds with Ir) effects. By proper noble gas pre-implantation and thermal processing, we grow noble gas filled Gr blisters with tunable size, areal density, and without introducing ion irradiation damage. The observed phenomena are expected to take place for a variety of substrates, ion species, energies, and 2D-layers as will be discussed in the next chapters.

We envision that implantation of atoms with low solubility into a substrate covered with Gr (or another 2D-layer) followed by annealing could be used for stimulating confined reactions in the space between Gr and the substrate, and as 2D-layers are transparent to light, for confined photo-chemical reactions. Such an approach could also be used for reactive growth of interfacial layers in between the substrate and a 2D-layer.

6.1 Xenon Trapping

In the first set of XPS experiments we exposed a bare Ir(111) sample to 0.5 keV Xe^+ at 300 K and conducted successive annealing to 1000 K and 1300 K. The ion fluence was 0.1 MLE, where 1 MLE is 1.57×10^{19} ions/m^2, *i.e.*, numerically identical to the surface atomic density of Ir(111). The bottom XP spectrum in Fig. 6.1(a) displays the Ir 4s core level peak together with the Xe $3d_{3/2}$/Xe $3d_{5/2}$ doublet after irradiation at 300 K. The Xe $3d_{5/2}$ BE of 669.7 eV is consistent with values measured for implanted or adsorbed Xe at other metals [157, 158] [1]. Since Xe does not adsorb on Ir(111) at 300 K (see our calculations below and Ref. [143]), the Xe 3d signal must be attributed to Xe implanted into the Ir sample. Upon annealing to 1000 K the Xe 3d signal diminishes and has vanished after annealing to 1300 K [middle and top spectra in Figure 6.1(a)]. Consistent with similar studies for noble gas irradiation of other metals [118, 159], we explain these changes as follows: due to thermal excitation Xe is released from its capture sites inside the crystal, diffuses to the surface, and finally desorbs to the vacuum, such that only little (1000 K) or no (1300 K) Xe is left in the crystal.

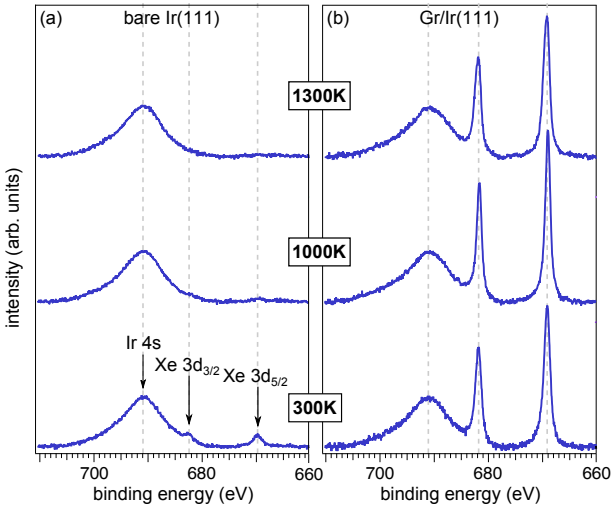

Figure 6.1: XPS of Xe trapping after 0.5 keV Xe^+ irradiation. XP-spectra of the Ir 4s, Xe $3d_{3/2}$, and Xe $3d_{5/2}$ core levels for (a) bare Ir(111) and (b) Gr covered Ir(111) after exposure to 0.1 MLE of 0.5 keV Xe^+ at 300 K and annealed to stepwise increasing temperatures, as indicated.

[1] For Gr/Ir(111) the Xe $3d_{5/2}$ peak energy is between 669.0 eV and 669.2 eV at all temperatures, while for bare Ir(111) at 300 K it is 669.7 eV. This variation is presumably due to a better extra-atomic screening of the implanted Xe as opposed to the trapped one [157], but its explanation is beyond the scope of the present investigation.

Conducting precisely the same irradiation experiment, but for Ir(111) fully covered by Gr, yields dramatically different XP spectra as shown in Figure 6.1(b). Already after irradiation at 300 K [bottom spectrum of Figure 6.1(b)] the integrated Xe $3d_{5/2}$ intensity is an order of magnitude higher (compare Table 6.1). All the additional intensity (and thus nearly all intensity) must be due to Xe trapped in between the Gr cover and the Ir substrate. Annealing to 1000 K and 1300 K hardly changes the integrated Xe 3d peak intensity. The interpretation is straightforward: trapped Xe did not escape to any significant extent from under Gr to the vacuum, despite the fact that the Gr cover was heavily damaged by the Xe^+ irradiation.

Table 6.1 compiles the integrated Xe $3d_{5/2}$ intensities after ion exposure and annealing for bare Ir(111) and Gr/Ir(111). The intensities are given in % of the Xe $3d_{5/2}$ intensity of an adsorbed, saturated Xe layer on bare Ir(111). Assuming a Xe saturation coverage of 0.33 ML on Ir(111) [160] and neglecting attenuation effects, division of the tabulated intensities by a factor of three yields the amounts of trapped Xe in ML with respect to Ir(111). Thus, after annealing to 1000 K, 4.1 %ML Xe is estimated to be trapped, *i.e.*, more than 40 % of the incident ions. This value is a lower bound, since the Ir 4s photoelectron attenuation through the adsorbed Xe layer for Xe/Ir(111) and the attenuation of the Xe 3d signal from deeper layers in Ir are neglected. Both factors tend to increase our estimate. Irrespective of these uncertainties, it is obvious that a substantial fraction of the incident Xe remains underneath Gr up to the highest annealing temperature of 1300 K.

Table 6.1: Integrated Xe intensities after 0.5 keV Xe^+ irradiation. Integrated Xe $3d_{5/2}$ intensities I_{bare} and I_{Gr} of bare and Gr covered Ir(111), respectively, after exposure to 0.1 MLE 0.5 keV at 300 K as well as annealing to 1000 K and 1300 K. Also, the intensity ratio $I_{\mathrm{Gr}}/I_{\mathrm{bare}}$ is specified for the ion energies and temperatures used. Intensities are given as % of the integrated Xe $3d_{5/2}$ intensity of a saturated Xe layer on Ir(111) and are calibrated to the Ir 4s peak height measured simultaneously.

	I_{bare}	I_{Gr}	$I_{\mathrm{Gr}}/I_{\mathrm{bare}}$
300 K	1.3	11.5	9
1000 K	0.4	12.2	34
1300 K	< 0.2	11.6	> 60

While XPS tells about the Xe remaining at the sample after irradiation, a complementary view is provided by TPD, which yields information about the Xe leaving the sample after

irradiation through thermal activation. The solid gray line in Figure 6.2 is the thermal desorption trace of Xe after 0.5 keV irradiation of bare Ir(111) with similar parameters as used for the XPS experiment. It exhibits a double peak structure with peak desorption temperatures of 745 K and 880 K. Beyond 1000 K the desorption rate gradually increases up to the end of the heating ramp at 1330 K. The dashed gray line in Figure 6.2 is the thermal desorption trace of Xe after irradiation of Gr/Ir(111). It is a flat featureless curve with its slope increasing slightly for temperatures beyond 1000 K. Despite an order of magnitude more Xe in the Gr/Ir(111) sample, the integrated amount of Xe desorbing is lower by about a factor of two. Therefore, our TPD data elucidate that only a small fraction of the total amount of Xe in the Gr/Ir(111) sample desorbs up to 1300 K.

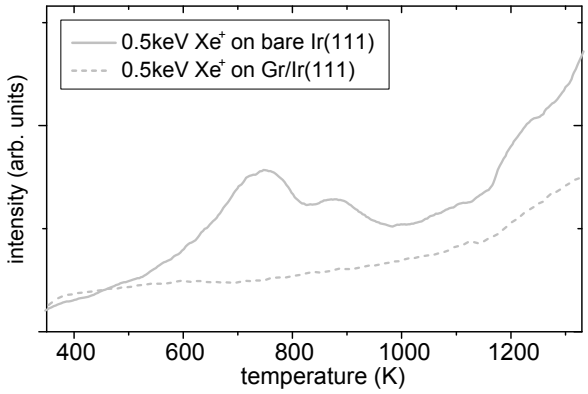

Figure 6.2: TPD after 0.5 keV Xe^+ irradiation. TPD of Xe (131 amu) after exposure of bare Ir(111) and Gr/Ir(111) to 0.1 MLE 0.5 keV Xe^+ at 300 K. Solid gray line: bare Ir(111); dashed gray line: Gr/Ir(111). Heating rate 5 K/s.

The experimental data are substantiated by our MD simulations (compare Table 6.2), for which we used a Pt instead of an Ir substrate (see Part III). For 0.5 keV Xe hitting bare Pt(111) at normal incidence, when the energetic phase of the collision has ended (0.5 ns after the impact), 98 % of the impinging Xe has been reflected (*i.e.*, returned to vacuum) and only 2 % of the primary ions have been implanted into the Pt crystal (into a depth of less than three atomic layers). The same simulations with Xe hitting Gr/Pt(111) yield a strikingly different picture. Then, only 2 % of the projectiles are reflected and 5 % are implanted into Pt, but 93 % of the Xe ions are stuck in between Gr and the Pt(111) surface (see Figure 6.3 for depth distributions). Apparently, the primary Xe ions penetrate the Gr sheet easily; much more easily than a Pt layer. The reason for this is twofold: (i) due to the much smaller nuclear charge of C ($Z = 12$) compared to Pt ($Z = 78$) the scattering cross section of Xe with C is much smaller than that with Pt (and Ir); (ii) even in a head-on collision with a C atom the Xe atom loses less than a third of its energy and

continues to move towards the metallic substrate. There, the Xe projectiles effectively transfer energy to the substrate Pt atoms (mass ratio 131 u to 195 u), such that in case of momentum reversal they no longer possess enough energy to pass through the Gr sheet and are instead trapped. Note also that when impinging the Gr sheet from below, the Xe projectiles have not only much less energy and thus a larger scattering cross section with C, but under nearly all circumstances off-normal or grazing direction, such that the transparency of the Gr sheet for ion passage is strongly reduced. The results of the MD simulations are fully consistent with the XPS observation that an order of magnitude more Xe remains within the sample if there is a Gr cover present (compare Figure 6.1 and Table 6.1). Still, they do not explain why the trapped Xe does not escape to the vacuum by diffusion through irradiation induced vacancies and vacancy islands in the Gr sheet. Note also that the MD simulations are conducted for a perfect Gr sheet, while in the experiment ion induced damage of successive impacts accumulates.

Table 6.2: Results of MD simulations for 0.5 keV Xe^+ irradiation. Fraction of reflected, trapped, or implanted primary 0.5 keV Xe ions given in % as obtained by MD simulations > 95 events per case. Also specified is the average depth of implantation $\overline{r}_{im}$ measured from the topmost Pt layer.

	Pt(111)	Gr/Pt(111)
reflected	98	2
trapped	-	93
implanted	2	5
$\overline{r}_{im}$ (nm)	0.4	0.2

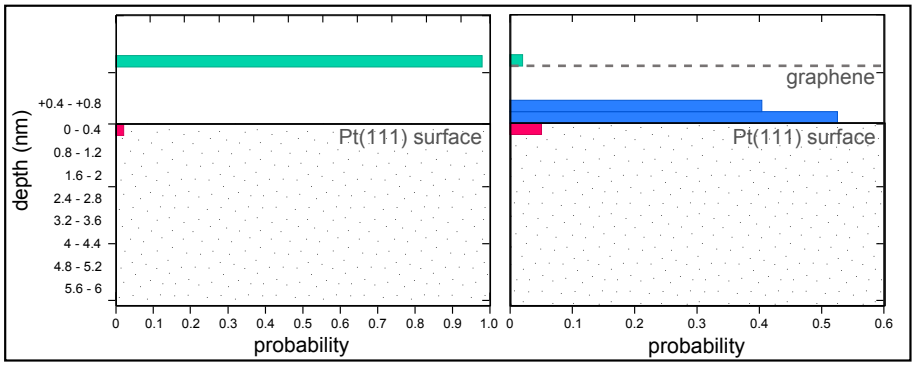

Figure 6.3: Depth distributions for 0.5 keV Xe^+ on graphene/Ir(111) by molecular dynamics simulations. Xe depth distributions after irradiation of bare Pt(111) (left) and Gr/Pt(111) (right) with 0.5 keV Xe^+, as obtained by MD simulations. Prior to analysis the system was allowed to relax. The dotted area marks the bulk Pt substrate, the solid black line indicates the Pt(111) surface and the dashed gray line separates trapped atoms under Gr and reflected Xe atoms above. The histogram bar for reflected Xe is shaded green, those for Xe trapped between Gr and the Pt(111) surface are shaded blue, and those representing implanted Xe within the Pt bulk are shaded red. Note that due to the large amplitude waves in Gr initiated by the Xe impacts, also Xe atoms up to 1.2 nm above the Pt(111) are still under the Gr sheet.

6.2 Energetics of Xenon Trapping

To understand why trapped Xe remains under a defective Gr layer, we carried out DFT calculations, as described in Part 4. We first evaluated the adsorption energy of Xe atoms on bare Ir(111) and Gr/Ir(111) to be −0.21 eV and −0.17 eV, respectively. These numbers are consistent with previous experimental results for Xe adsorption on Pt(111) (−0.27 eV) [143] and Xe adsorption on graphite (−0.25 eV). The adsorption energies also agree up to a factor of about two with more accurate calculation schemes using many-body perturbation theory for Xe adsorbed to graphite, to Gr, or to Ni(111), see *e.g.* [161–163]. In any case, the DFT numbers calculated here indicate the absence of chemical bonding and are in magnitude more than a factor of 30 smaller than the barriers for the penetration of Xe atoms through the graphene edge, as shown below. Next we inserted a single Xe atom between the Gr sheet and Ir(111). After full geometry optimization, taking the energies of isolated Gr/Ir(111) and the Xe atom as the reference, we found that it costs 2.9 eV to place a Xe atom between Gr and Ir [see Figure 6.5(a) for geometry]. This energy penalty results from the deformation caused by the Xe atom in the Gr sheet (elastic energy) and the local delamination of the Gr sheet from its substrate (delamination energy). Note

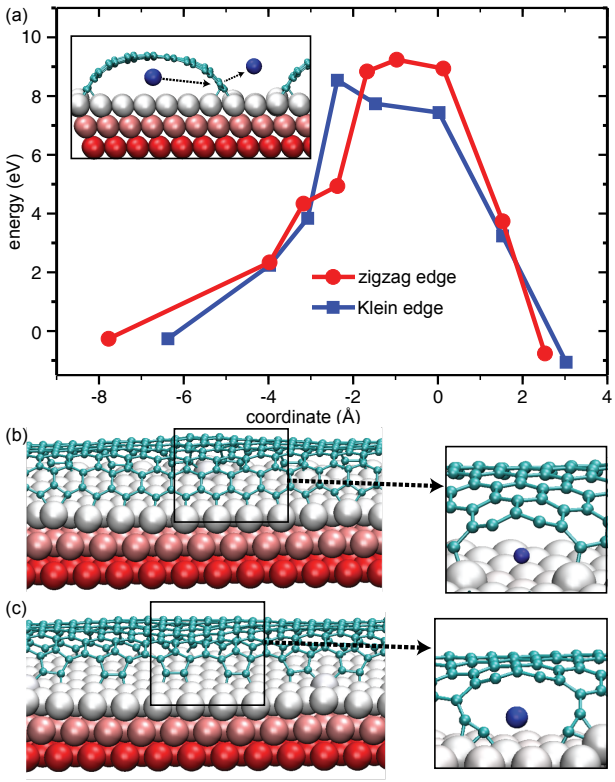

Figure 6.4: Density functional theory calculations on Xe^+ escape from underneath graphene/Ir(111). (a) System energy as a function of the reaction coordinate (0 corresponds to the Xe atom at the Gr edge position) for two different edge structures and the path of a Xe atom schematically depicted in the inset. (b) Structure of zig-zag edge (left) and zoomed structure with the Xe atom in the transition state (right). (c) Structure of the reconstructed Klein edge (left) and zoomed structure with the Xe atom in the transition state (right).

that escape of a trapped Xe into the Ir bulk is impossible due to the very high interstitial formation energy exceeding 10 eV. The most likely escape path for Xe is thus to go via Gr edges onto the free Ir terrace, where the Xe atom would desorb rapidly under all temperatures of concern, as schematically depicted in the inset of Figure 6.4(a). Due to Gr sputtering, such edges are formed in large number during irradiation and annealing, but Gr dangling bonds are saturated due to the strong interaction of Gr with the metal giving rise to bending of the sheet towards the metal surface already at room temperature [20, 120]. The energy of the system as a function of the coordinate of the Xe atom along the path is presented in Figure 6.4(a) for two particular edge structures. First, the zig-zag edge that terminates vacancy islands in the Gr sheet [compare 6.5(c), left edge]. Additionally, the reconstructed Klein edge is considered here [compare 6.5(c), right edge], as such edge structures develop for freestanding Gr under sputtering conditions [164]. For both structures an activation energy of more than 8 eV is obtained. Figure 6.4(b) and (c) show the atomic structure of Gr edges binding to Ir(111), and the close-ups present the Gr edge structure and the Xe atom in the transition state. For passage through the zig-zag edge [Figure 6.4(b)] 2 C-Ir bonds must be broken temporarily, while for passing through the reconstructed Klein edge [Figure 6.4(c)] two C-C bonds need to be broken in the C pentagons bound to the substrate. We also calculated the barrier for escape through an open corner in a Gr vacancy island edge and obtain a similar energy barrier as visible from Figure 6.6. For an efficient release of Xe at 1300 K a much lower barrier, below 4 eV, would be necessary. Although computational cost prevents us from exploring the entire space of possible edge structures that may arise during irradiation and annealing, it is clear from our calculations that the passage of a Xe atom from under Gr involves breaking of strong Gr-Ir or Gr-Gr bonds. Hence, very little Xe is released even through a highly defective Gr sheet with a large number of smaller and larger vacancy islands as well as for temperatures up to 1300 K. As the escape of Xe from under Gr is impaired by Gr edge binding, the fraction of trapped Xe calculated in the MD simulations is indeed a good first estimate for the experimentally observed trapping efficiency.

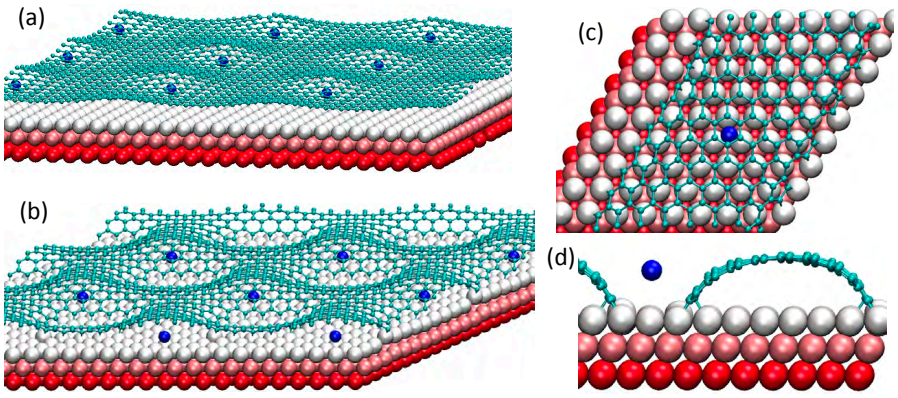

Figure 6.5: Super cell geometries used for density functional theory calculations. (a) Periodic images of the supercell used in the calculations of a Xe atom under perfect Gr. The Xe atom is located in the TOP area, where an Ir top site is in the center of the carbon ring (compare also ref. [20]). (b) The same for perforated Gr with triangular vacancy islands. (c) The supercell used for the calculation of the Xe atom passage through the zigzag edge (left) and the reconstructed Klein edge (right). The Xe atom is under Gr. (d) The same atomic structure viewed along the edges, after escape of Xe atom.

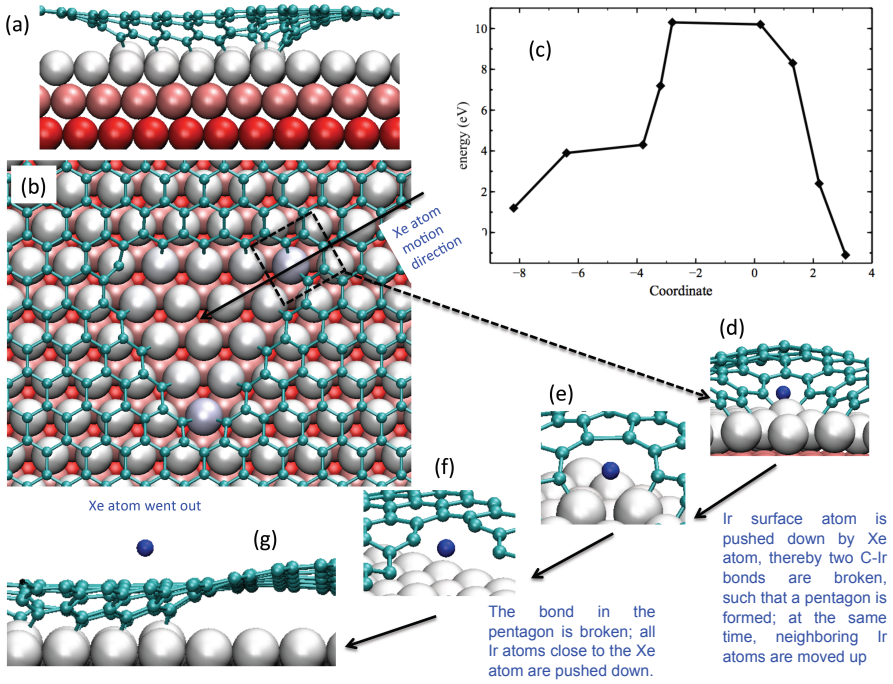

Figure 6.6: Results of density functional theory calculations for Xe atom diffusion through the edge of a graphene vacancy island. (a) The atomic structure at the Gr-Ir interface near the vacancy island. C and Ir atoms are represented as small and large balls, respectively, Ir atoms colored according to the elevation. (b) Top view. (c) System energy along the path. (d-g) Atomic configurations along the migration path.

6.3 Morphology of Trapped Xenon

The real space view of the noble gas trapping under the Gr sheet is presented in the STM topographs of Figure 6.7. After room temperature irradiation the sample displays a rather dense distribution of small scale protrusions of 0.3 nm - 0.5 nm height [compare Figure 6.7(a)]. Experiments with lower fluence show unambiguously that the protrusions are deformations in the Gr sheet, which itself is defective but globally intact [120]. Based on our XPS and TPD experiments, as well as the MD simulations and DFT computations discussed above, we must interpret these protrusions to result to a large extent from Xe atoms, which give rise to Gr's local deformation. Additionally, Ir adatoms pushed onto the Ir(111) surface by collisions [165] contribute to the formation of protrusions in the Gr sheet. This statement is backed-up by the inset of Figure 6.7(a), where Ir adatom clusters are visible after irradiation of bare Ir(111) using the same ion beam parameters.

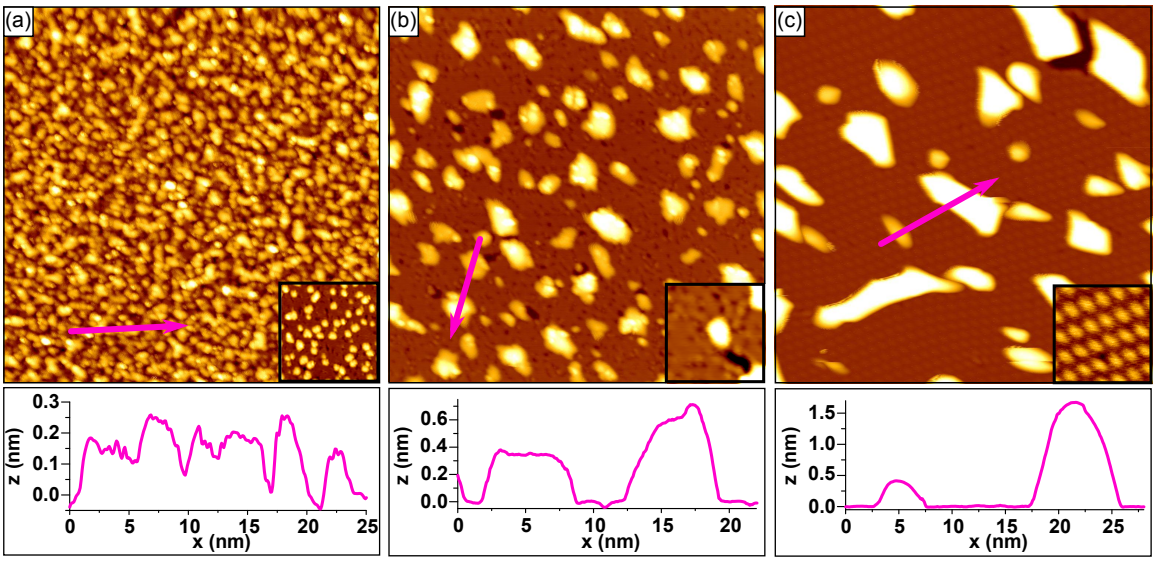

Figure 6.7: Sample morphology after 0.5 keV Xe^+ irradiation and annealing. STM topographs of Gr/Ir(111) and associated height profiles after exposure to 0.1 MLE of 0.5 keV Xe^+ (a) at 300 K, (b) annealed to 1000 K, and (c) annealed to 1300 K. The height profiles below the topographs are taken along the arrows indicated. Insets: (a) bare Ir(111) after exposure to ion irradiation with the same parameters, (b), (c) are zooms of the corresponding topograph. Image sizes are 90 nm × 90 nm, inset sizes are (a) 24 nm × 24 nm and (b), (c) 15 nm × 15 nm.

After annealing the sample to 1000 K the morphology is dramatically changed [compare Figure 6.7(b)]. The number of protrusions is strongly reduced and two types of elevations are visible: first, flat bulges with a well defined height around 0.35 nm, and second,

larger, smoothly curved blisters with a maximum height up to 0.8 nm [height profile in Figure 6.7(b)]. Also visible are dark areas of few nm size and point-like dark spots with typical separations of 2-3 nm, as highlighted by the inset. These features are vacancy islands within the Gr sheet, either extended nm-sized areas or small point-like spots pinned to preferential binding sites within the moiré formed of Gr with the Ir(111) substrate (compare to reference [20]). The vacancy islands result from aggregation of vacancies created in Gr due to sputtering.

Upon annealing to 1300 K the morphology coarsened and is now dominated by few, large blisters with lateral dimensions of the order of 10 nm and heights around 1.5 nm, as shown in Figure 6.7(c). Also some shallower blisters are present. The point-like vacancy clusters have nearly vanished. Large vacancy islands are present in quite low density. One of those is visible in the upper right corner of Figure 6.7(c), between two large blisters. Apparently the small vacancy clusters detached during annealing from their preferential binding sites and aggregated to large vacancy islands, consistent with the findings of Standop *et al.* [20]. It is striking that the vacancy island visible in Figure 6.7(c) is bound by large blisters. This observation underlines the strong binding of Gr to the Ir(111) substrate and the impermeability of the Gr edge for Xe, as found in our DFT calculations. A rather regular moiré corrugation with a 2.5 nm pitch indicates that the Gr lattice has restored itself completely [compare inset of Figure 6.7(c)].

We tentatively interpret the evolution from atomic scale protrusions to large blisters as follows. After room temperature irradiation, a mixture of Xe atoms, Ir adatoms, and detached C atoms is present under the defective Gr cover. Upon annealing to 1000 K the Ir adatoms and adatom clusters recombine with Ir surface vacancies restoring a flat surface [20], while the detached C atoms are largely reincorporated into the Gr sheet. The agglomeration of the remaining Xe atoms (and of the implanted atoms diffusing from the Ir bulk to the surface) gives rise to monolayer Xe platelets that cause flat bulges. Their formation is driven by minimization of deformation and delamination energy within Gr: disperse single Xe atoms cause a much larger deformation of Gr and much more delamination of Gr from the substrate than one flat aggregate containing all Xe atoms. The assumption of a monolayer thick Xe aggregate is consistent with the uniform apparent STM bulge height of about 0.35 nm, similar to the Xe van der Waals diameter of 0.43 nm. Since the Gr sheet presses the Xe together, we tentatively assume that also the lateral spacing of the Xe atoms is close to that of solid Xe. This could be realized, *e.g.*, by a $(\sqrt{3}\times\sqrt{3})$-Xe structure with a coverage of 0.33 ML [160]. When the flat bulges grow larger, a shape transformation to smoothly curved blisters takes place. While the delamination

energy grows with the square of the linear dimension of the flat bulge, its strain and bending energy - primarily localized along the rim of the bulge - grows only proportional to it. Therefore, at some point a transition to a more three-dimensional shape of the Xe cavity takes place, lowering the delamination energy for a given amount of Xe. After annealing to 1300K the measured blister height and radius (approximating the blister as spherically symmetric) with the calculated adhesion energy of Gr to Ir(111) (50meV per C atom [47]) allows one to estimate [145, 148] pressures of the order of 1GPa for the Xe in the blister. It should be noted that a similar coarsening of gas cavities during annealing, as described here, is also observed for bubbles and blisters after noble gas implantation into bulk materials [21].

A summary of the different shapes occurring during this evolution and additional interesting features are depicted in Figure 6.8 showing the residual damage after 0.03 MLE of 1 keV Xe^+ irradiation and annealing to 1000 K. Figure 6.8(a) presents an atomic resolution STM topograph. Vacancy clusters remain visible as well as two flat Xe filled bulges. By detailed inspection [inset of Figure 6.8(a)] it becomes obvious that the Gr lattice rows are continuous over the edge of the bulges. The height profile displayed in Figure 6.8(d) along the red line in (a) reveals the typical height of approximately 0.35 nm. The proposed geometry is sketched in Figure 6.8(g).

Often, we observe 3-fold scattering patterns on the bulges as visible in Figure 6.8(b) (magnified in the inset) that we interpret to be caused by residual ion induced point defect structures (*e.g.*, a monovacancy or a small cluster thereof). These scattering pattern are only observed when Gr is well decoupled from the substrate [96, 166]. They are never observed for defects in Gr resting directly on Ir(111).

The height profile in Figure 6.8(e) of the bulge in the lower part of Figure 6.8(b) makes plain that its height exceeds the typical height of 3.5 nm, indicating a transition from monolayer Xe platelets at the interface giving rise to flat bulges to the more curved blister as discussed above. Presumably, more than one monolayer of Xe is found at the interface. However, the Xe inside the blister might be less ordered due to the increased height caused by the flexibility of Gr and the resulting decreased pressure inside the blister. The corresponding schematic is sketched in Figure 6.8(h). Finally, a fully curved blister which is most frequently found after higher annealing temperatures is displayed in the atomic resolution STM topograph in Figure 6.8(f) with the corresponding profile and schematics in (f) and (i), respectively. A typical height of the curved blisters is 0.8 nm.

We performed spectroscopic measurements at $T = 5$ K with a W tip on a flat bulge similar to the structures displayed in Figure 6.8(a) shown in the inset of Figure 6.9(a).

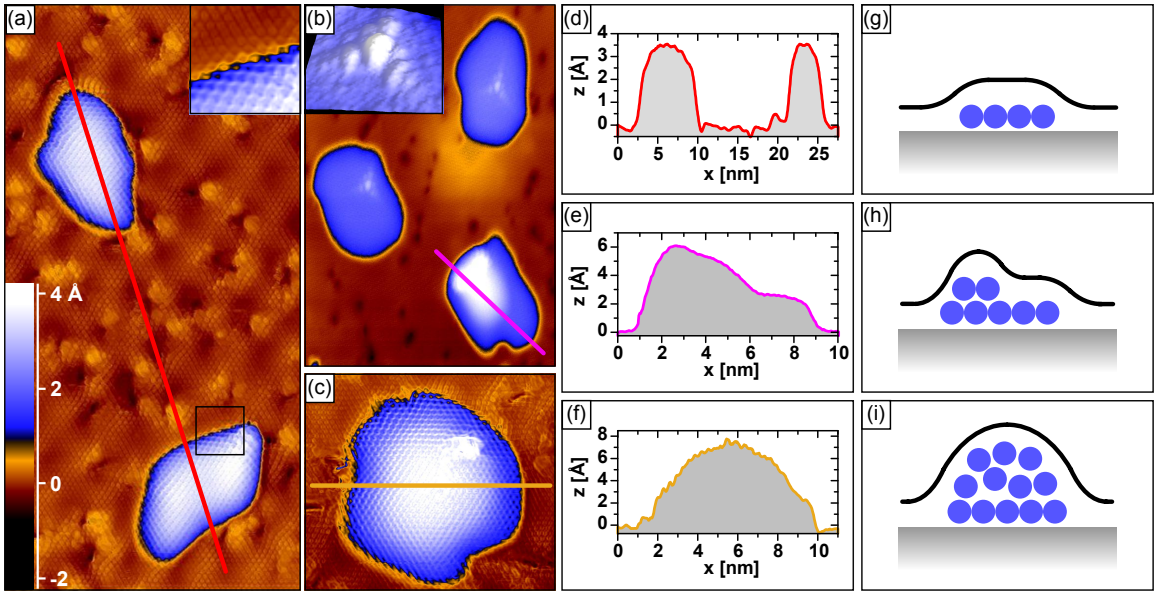

Figure 6.8: Xe filled bulges and blister. (a) Atomic resolution STM topograph of Gr/Ir(111) after 3 cycles of 0.01 MLE 1 keV Xe^+ normal incidence irradiation followed by annealing at 1000 K. Image size is 16.5 nm × 29.7 nm. Inset in upper right corner: Magnified view of the area indicated by the black square displaying a continuous Gr layer over the edge of a bulge. Color scale indicated in the lower left corner was chosen to make atomic resolution on the base level and on the bulges visible. Image size is 2.6 nm × 2.5 nm. (b) In the upper image part, two Gr bulges covering Xe platelets display a threefold symmetric $(\sqrt{3} \times \sqrt{3})$ scattering pattern. In the lower part, a bulge starting to transform into a more curved blister is visible. Image size is 19.1 nm × 25.5 nm. Inset in upper left corner: Magnified 3D-view of a scattering pattern presented in (b). Image size is 6 nm × 6 nm. (c) Xe filled curved blister. Image size is 11.7 nm × 10.1 nm. (d), (e), and (f) display height profiles along the lines indicated in (a), (b), and (c), respectively. (g), (h), and (i) are schematic cross sections corresponding to the height profiles in (d), (e), and (f), respectively.

The LDOS on and next to the bulge is measured by stabilizing the tip and recording the $\mathrm{d}I/\mathrm{d}U$ signal with a lock-in amplifier [$U_{\mathrm{mod}} = 4\,\mathrm{mV}$, $f = (480 - 610)\,\mathrm{Hz}$] as a function of energy $E =$ eV with open feedback loop. Figure 6.9(a) compares a spectrum measured on Gr/Ir(111) with a spectrum measured on a Xe filled bulge. The blue spectrum measured on Gr/Ir(111) shows a shoulder around -0.1 eV which we attribute to the hole-like surface state of Ir(111), which is known to persist under a monolayer Gr [167, 168]. The green spectrum on the bulge does not show any surface state feature. Instead, a pronounced dip is found, with a width of 0.15 eV. We attribute this feature to electron tunneling mediated by Gr's phonons [169]. The absence of the Ir(111) surface state feature in the spectrum on the bulge directly proves that no islands of Ir adatoms are located under the bulge and the Gr on top of the Xe platelet is decoupled from the substrate, consistent with our interpretation.

In STS measurements on the three-fold scattering pattern as observed in Figure 6.8(b), we find a strong peak in the local density of states close to the Fermi level at 0.25 eV as visible in Figure 6.9(b) consistent with observations for monovacancies in decoupled Gr in literature [96]. Measuring the LDOS next to the defect reveals a very smooth dependence on energy (a possible Dirac dip at approximately 0.175 eV is visible).

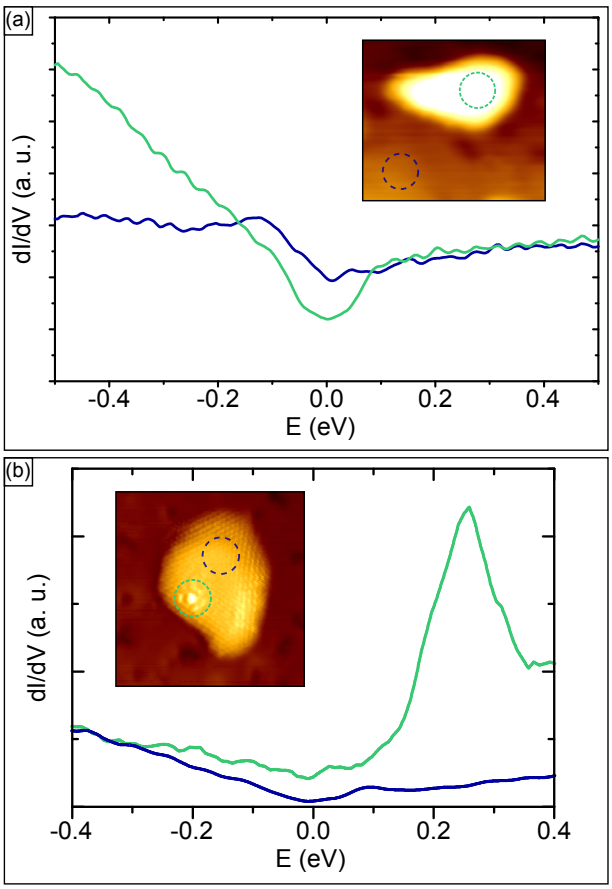

Figure 6.9: Scanning tunneling spectroscopy on bulges and defects. (a) Point spectra recorded on and next to a Xe filled blister (I_{stab} = 0.08 nA, V_{stab} = 0.5 V). The positions of data acquisition are visualized by thin colored circles in the STM topograph shown in the inset. Image size is 8 nm × 7 nm. (b) Point spectra recorded on a Xe filled blister with three-fold symmetric LDOS modulations (I_{stab} = 0.1 nA, V_{stab} = 0.5 V). The positions of data acquisition are visualized by thin colored circles in the STM topograph shown in the inset. Image size is 10 nm × 10 nm.

6.4 Energy and Mass Dependence

To explore how trapping depends on ion energy, we conducted the same set of experiments with an ion energy of 3 keV. Despite the increased Gr sputtering and damaging (the yield for C atom detachment from the Gr sheet increases from 1.0 to 1.8 according to our MD simulations) the general picture is unchanged: the Gr sheet strongly reduces ion reflection and enables efficient Xe trapping upon irradiation at 300 K.

To analyze differences to the 0.5 keV situation, we first consider changes for the irradiation of bare Ir(111). Compared to 0.5 keV, for 3 keV Xe^+ into bare metal substantially more Xe is implanted (more than 40 % of the impinging Xe atoms) into a larger average depth of 1 nm, as apparent from the MD results shown in Table 6.3 and the depth distribution in Figure 6.10. This is consistent with the corresponding XPS data in Figure 6.11(a) as well as with the integrated Xe intensities in Table 6.4. Consequently, substantially more Xe is released from bare Ir during heating as visible in the Xe desorption trace in Figure 6.12 (solid black line). Note that the maximum Xe intensitiy in Figure 6.12 is increased by a factor of three compared to the thermal desorption trace for 0.5 keV in Figure 6.2. However, even after heating to 1300 K some Xe is left in the Ir crystal, presumably due to incorporation of Xe in stable bulk vacancy clusters formed in consequence of the more violent Xe impacts.

Table 6.3: Results of molecular dynamics simulations for 3 keV Xe^+ irradiation. Fraction of reflected, trapped, or implanted primary 3 keV Xe ions given in % as obtained by MD simulations > 95 events per case. Also specified is the average depth of implantation $\overline{r}_{im}$ measured from the topmost Pt layer.

	Pt(111)	Gr/Pt(111)
reflected	57	6
trapped	-	41
implanted	43	53
$\overline{r}_{im}$ (nm)	1	0.9

With the Gr cover the implantation into Ir does not change much, but trapping under the Gr sheet becomes frequent (> 40 % of the impinging Xe), thereby strongly suppressing reflection. As for the 0.5 keV case, the presence of the Gr cover gives rise to a substantial enhancement of the Xe 3d XPS intensity after 300 K irradiation, which must be attributed to Xe trapping (compare Figure 6.11 and Table 6.4). Xe release is largely prevented by the

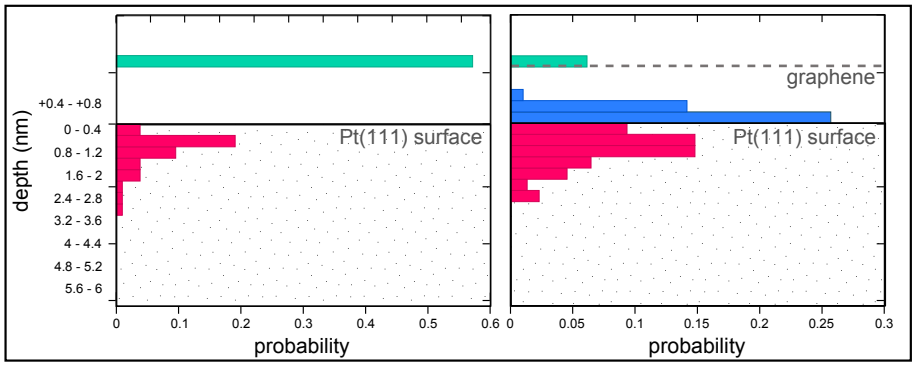

Figure 6.10: Depth distributions for 3keV Xe on graphene/Ir(111) by molecular dynamics simulations. Xe depth distributions after irradiation of bare Pt(111) (left) and Gr/Pt(111) (right) with 3 keV Xe^+, as obtained by MD simulations. Prior to analysis the system was allowed to relax. The dotted area marks the bulk Pt substrate, the solid black line indicates the Pt(111) surface and the dashed gray line separates trapped atoms under Gr and reflected Xe atoms above. The histogram bar for reflected Xe is shaded green, those for Xe trapped between Gr and the Pt(111) surface are shaded blue, and those representing implanted Xe within the Pt bulk are shaded red. Note that due to the large amplitude waves in Gr initiated by the Xe impacts, also Xe atoms up to 1.2 nm above the Pt(111) are still under the Gr sheet.

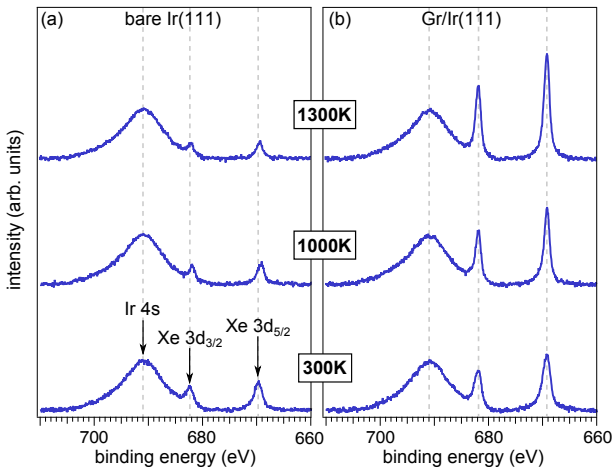

Figure 6.11: XPS of Xe trapping after 3 keV Xe^+ irradiation. XP-spectra of the Ir 4s, Xe $3d_{3/2}$, and Xe $3d_{5/2}$ core levels for (a) bare Ir(111) and (b) Gr/Ir(111) after exposure to 0.1 MLE of 3 keV Xe^+ at 300 K and annealed stepwise to increasing temperatures, as indicated.

Table 6.4: Integrated Xe intensities after 3 keV Xe irradiation. Integrated Xe $3d_{5/2}$ intensities I_{bare} and I_{Gr} of bare and Gr covered Ir(111), respectively, after exposure to 0.1 MLE 3 keV Xe^+ at 300 K as well as annealing to 1000 K and 1300 K. Also, the intensity ratio $I_{\mathrm{Gr}}/I_{\mathrm{bare}}$ is specified for the ion energies and temperatures used. Intensities are given as % of the integrated Xe $3d_{5/2}$ intensity of a saturated Xe layer on Ir(111) and are calibrated to the Ir 4s peak height measured simultaneously.

	I_{bare}	I_{Gr}	$I_{\mathrm{Gr}}/I_{\mathrm{bare}}$
300 K	2.9	5.9	2
1000 K	1.9	6.0	3
1300 K	1.5	8.0	6

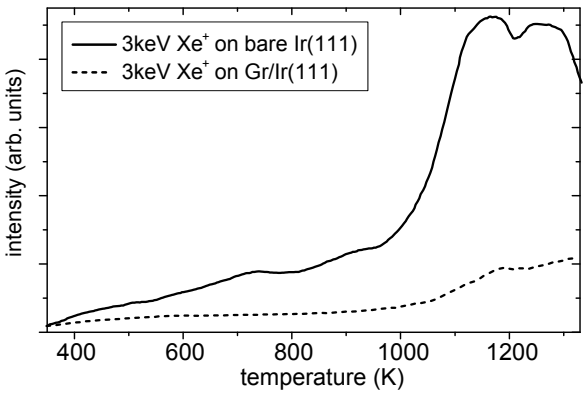

Figure 6.12: Temperature programmed desorption after 3 keV Xe^+ irradiation. TPD of Xe (131 amu) after exposure of bare Ir(111) and Gr/Ir(111) to 0.1 MLE 3 keV Xe^+ at 300 K. Solid black line: bare Ir(111); dashed black line: Gr/Ir(111). Heating rate 5 K/s.

Gr cover, as obvious from the comparison of bare Ir(111) and Gr/Ir(111) Xe desorption traces after 3 keV ion irradiation shown in Figure 6.12. In consequence, by annealing, the amount of trapped Xe continuously increases by Xe streaming to the interface from its implantation sites in the Ir bulk. The STM images in Figure 6.13 display a markedly larger Gr removal resulting from the higher sputtering yield of 3 keV Xe ions, but otherwise a similar morphological evolution from atomic scale protrusions to large blisters.

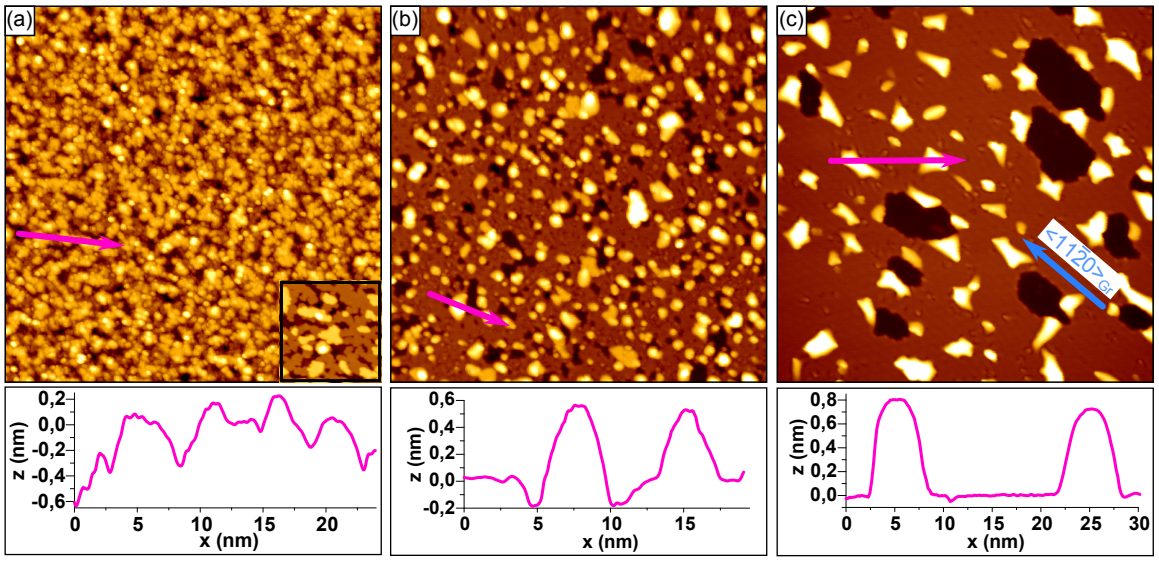

Figure 6.13: Sample morphology after 3 keV Xe^+ irradiation and annealing. STM topographs of Gr/Ir(111) and associated height profiles after (a) exposure to 0.1 MLE of 3 keV Xe^+ at 300 K. Additionally annealed to (b) 1000 K and to (c) 1300 K. Inset in (a) displays the topography of bare Ir(111) after identical ion beam treatment as used for Gr/Ir(111). Adatom and vacancy clusters are visible. The blue arrow in (c) marks the $\langle 11\bar{2}0 \rangle_{Gr}$ direction of the Gr lattice, indicating a predominant zig-zag termination of the vacancy islands [128, 170]. The height profiles below the topographs are taken along the pink lines indicated. Image sizes are 90 nm × 90 nm, inset size is 24 nm × 24 nm.

To investigate the trapping efficiency in a broader parameter space we further analyzed the ion energy dependence of the irradiated and annealed morphology, using Xe^+ as ion species, a fixed fluence of $F = 0.03$ MLE, and 1000 K as annealing temperature. Figures 6.14(a)-(e) display equally sized STM topographs after exposure and annealing in the energy range from 0.1 to 5 keV. All topographs exhibit Xe filled bulges and blisters. The size tends to shrink with increasing ion energy, while the number density of the bulges and blisters increases. Exact numbers on mean bulge size and number density with respect to ion energy are provided in Table 6.5.

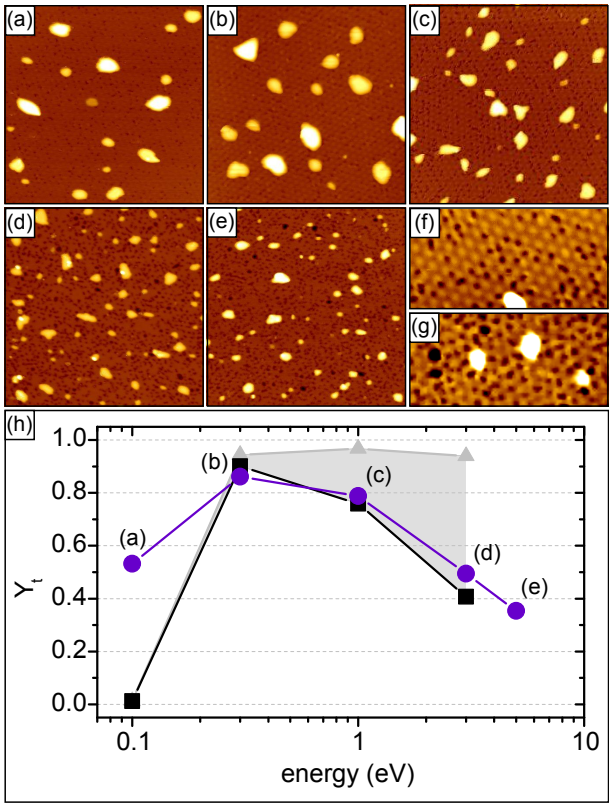

Figure 6.14: Dependence of Xe trapping yield on ion energy. STM topographs of Gr/Ir(111) after Xe^+ ion irradiation under normal incidence with increasing energies of (a) 0.1 keV, (b) 0.3 keV, (c) 1 keV, (d) 3 keV, and (e) 5 keV, fluence $F = 0.03$ MLE, $T_{\mathrm{anneal}} = 1000$ K. All image sizes are 80 nm × 80 nm. (f), (g) Close up of (a) and (e), respectively. Image sizes are 40 nm × 40 nm. (h) Xe trapping yield Y_t as a function of ion energy: experimental data (purple dots) and MD data for Xe trapped at the interface (black squares) as well as the sum of trapped Xe at the interface and within the bulk (gray triangles). Gray shaded area represents the Xe trapped within the bulk.

Table 6.5: Mean blister size and number density in dependence of ion energy. Mean size of the Xe bulges and blisters and the their number density as a function of the energy of the incident Xe^+ ion for a fluence of $F = 0.03$ MLE and after annealing to 1000 K.

Ion Energy (keV)	Mean Blister Size (nm^2)	Blister Number Density ($\frac{1}{nm^2}$)
0.1	18.47	0.0028
0.3	28.45	0.0027
1.0	13.11	0.0056
3.0	6.16	0.0074
5.0	4.70	0.0070

As visible in the magnified view of Figure 6.14(f), small vacancy clusters located within the fcc and hcp areas of the moiré are already visible for the lowest ion energy. They reflect the limited mobility of vacancies in Gr on Ir(111) and the energetically strongly preferred rebonding of Gr dangling bonds to the substrate in these areas, as discussed by Standop *et al.* [20]. For energies $\geqslant 3$ keV more such pinned vacancy clusters are produced and also larger vacancy clusters are apparent, as exemplified by the magnified view in Figure 6.14 (g) after 5 keV Xe^+ irradiation. The increased carbon sputtering may be traced back to a more violent cascade in the Ir substrate, causing a higher probability of recoil Ir-atoms hitting the Gr layer from below, resulting in sputtering of C atoms from the Gr. The higher C sputtering yield in combination with the pinning of the Gr to the substrate at higher ion energies results in a smaller mobility of the noble gas atoms at the interface explaining the trend of forming more but smaller blisters as reported above and in Table 6.5.

The trapping yield Y_t estimated by STM image analysis is plotted in Figure 6.14 (h) as a function of Xe^+ ion energy. While the trend of Y_t with ion energy does not depend on the details of our analysis procedure described in Part 4, considerable uncertainty is introduced by the delaminated bulges, for which only a single layer of Xe underneath is assumed probably underestimating the actual amount of Xe. As obvious from Figure 6.14 (h), Y_t increases from 0.1 keV to 0.3 keV, reaches a maximum in the range of 0.3 keV to 1.0 keV, and then drops again.

Determination of Y_t from MD simulations is facilitated since we can directly obtain the final positions of the ions within the simulation cell. In contrast to our experiments in the simulation a distinction between those Xe ions being trapped at the Gr/metal interface

and those coming to rest within the substrate can be made. The black data points in Figure 6.14(h) represent the ions trapped at the interface whereas the gray data points stand for the sum of the ions at the interface and within the bulk. So the gray shaded area represents the ions within the substrate.

The accordance between experiment and simulations is remarkably good when comparing the experimental data (purple dots) only to those ions coming to rest at the interface in the simulation (black squares). For ion energies up to 0.3 keV this represents almost all ions that remain in the sample. For higher ion energies this assumption is still justifiable since we know from the thermal desorption traces of 3 keV Xe^+ that up to 1000 K only a marginal amount of Xe will leave its trapping sites within the bulk and with this not contribute to blister formation. However, at the lowest ion energy of 0.1 keV the discrepancy can not be ignored. Finally, the MD simulation show that beyond 0.3 keV ion reflection towards the vacuum is almost constant and negligible.

At low ion energies the scattering cross section of the ion with the C lattice is comparably large making a transit without damaging the Gr impossible. However, even the maximal possible energy transfer of the 0.1 keV Xe^+ ion to a C atom in a head-on collision is only slightly above the displacement threshold for C in Gr. In most cases the ion will encounter in non-zero impact parameters thus the energy transfer to the C atoms is insufficient to detach it from Gr and hence the ion will be reflected to vacuum. Since at such low ion energies the ion gun is at its experimental limits only minor deviations in the ion's energy towards higher energies might cause major differences to the simulated data possibly explaining the extreme deviation. At high energies, the displacement threshold is easily overcome and the scattering cross section for the collision of the primary ion with the C and Ir atoms decreases. Therefore, the ion can easily transit deep into the substrate instead of coming to rest at the interface as visible from the MD data. Consequently, the trade-off between momentum transfer (favored by increasing the ion energy) and scattering cross section (shrinking with increasing ion energy) implies a maximum Xe trapping at intermediate energies, where the ion can pass the low Z carbon lattice but cannot penetrate into the high Z metal substrate.

Since the scattering cross section and with it the trapping yield should also scale with the atomic number of the projectile, we next turn to the investigation of the dependence of Y_t on the ion species at normal ion incidence. We exposed a complete Gr layer to the noble gas species with atomic numbers $Z = 2$, 10, 18, and 54 and conducted three cycles of ion exposure and annealing with total fluences of $F = 0.3$ MLE, 0.1 MLE, 0.03 MLE, and 0.03 MLE, respectively. The dataset is shown in Figure 6.15(a) - (d) with the corre-

sponding plot in Figure 6.15(e) representing Y_t in dependence of the atomic number Z (purple dots).

Comparing the STM topographs in Figure 6.15(a) - (d), it can indeed be recognized that trapping strongly increases with atomic number. This increase is even stronger than visually represented by the topographs, since the fluences for He^+ [Figure 6.15(a)] and Ne^+ [Figure 6.15(b)] are ten and three times higher, than the fluence for Ar^+ [Figure 6.15(c)] and Xe^+ [Figure 6.15(d)] irradiation. The quantitative analysis of the experiments shown in Figure 6.15(e) (purple dots) is qualitatively well reproduced by the results of the corresponding MD simulations (black squares) even though the absolute numbers for intermediate atomic numbers are somewhat lower in experiment. Again the gray triangles represent the sum of atoms coming to rest at the interface and in the bulk.

Interestingly, as visible from the inset in Figure 6.15(a), for He^+ irradiation flat bulges and blisters are almost absent, even after an ion fluence of 0.3 MLE, indicating that trapping at the interface does not take place. However, a substantial amount of vacancies in the covering Gr layer, *i.e.*, indicate significant C atom sputtering. Even though in MD simulations a considerable amount of He is stuck in the substrate and might diffuse to the interface upon annealing, presumably, due to the small van der Waals diameter (0.28 nm for He compared to 0.43 nm for Xe), He may escape from under Gr without the need to break Gr edge bonds. Indeed, our DFT calculations of He diffusion from under the Gr sheet with the same path as for Xe showed that the barrier for He escape is considerably smaller, on the order of 3-4 eV. Sputtering with He^+, preferably even at elevated temperature, may therefore be a method to avoid noble gas trapping during ion irradiation of Gr on a substrate. In view of practical application, this behavior opens a route towards the realization of a Gr nanomesh [20] fabricated on a metal substrate without trapping.

Additional insight is obtained by an analysis of individual MD simulation events. We start with the discussion of a characteristic 0.3 keV He^+ event displayed in Figure 6.16(a) 0.6 ps after the impact. The impinging ion penetrates the Gr layer without damage and is then reflected at the metal substrate. Upon further reflection at the Gr sheet it sputters one C atom towards the vacuum. After backscattering at the Gr sheet, the ion is again reflected at the substrate, moves through the Gr, and escapes into the vacuum. In other simulation events, sputtering is caused by a displaced carbon atom instead of the ion itself. The combination of normal incidence transparency of Gr for He, the high backscattering probability of He at Ir with little energy loss due to the mass ratio 4:192, and the lower Gr transparency for backscattered He or carbon atoms arriving from the backside at off-

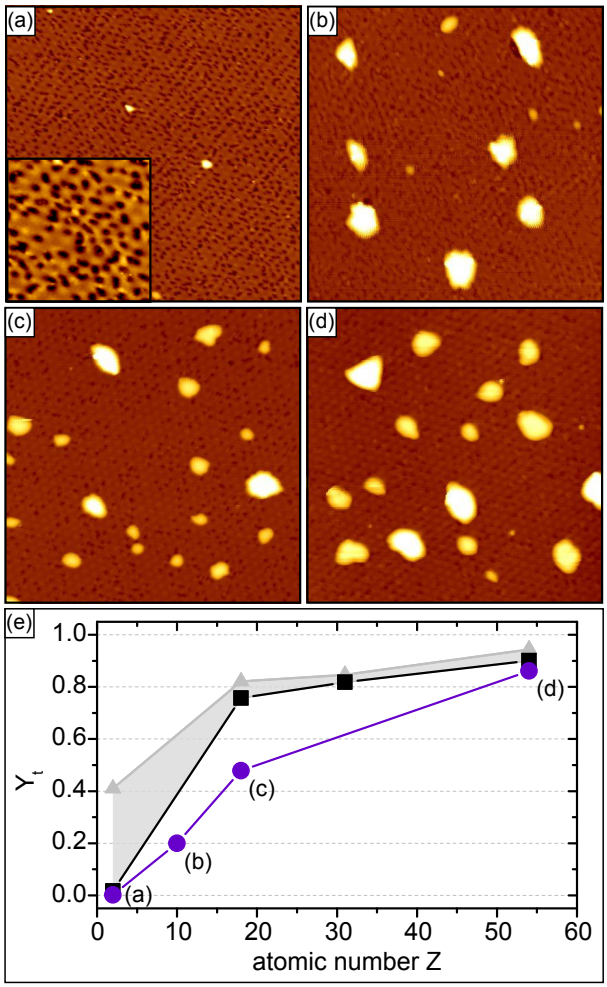

Figure 6.15: Dependence of trapping yield on ion's atomic number. STM topographs of Gr/Ir(111) after three cycles of 0.3 keV normal incidence ion irradiation and annealing to 1000 K. Projectile atomic number and total ion fluence are (a) 2 (He^+), F = 0.3 MLE, (b) 10 (Ne^+), F = 0.1 MLE, (c) 18 (Ar^+), F = 0.03 MLE and (d) 54 (Xe^+), F = 0.03 MLE. Image sizes are 80 nm × 80 nm. Inset in (a) is 20 nm × 20 nm. (e) Trapping yield Y_t plotted against atomic number Z: experimental data (purple dots) and MD data for ions trapped at the interface (black squares) as well as the sum of trapped ions at the interface and within the bulk (gray triangles). Gray shaded area represents the ions trapped within the bulk.

normal, often grazing, incidence give rise to the comparatively high sputtering yield of He, combined with low trapping. Those ions traveling into the substrate neither contribute to trapping since they can easily escape the system due to their small size.

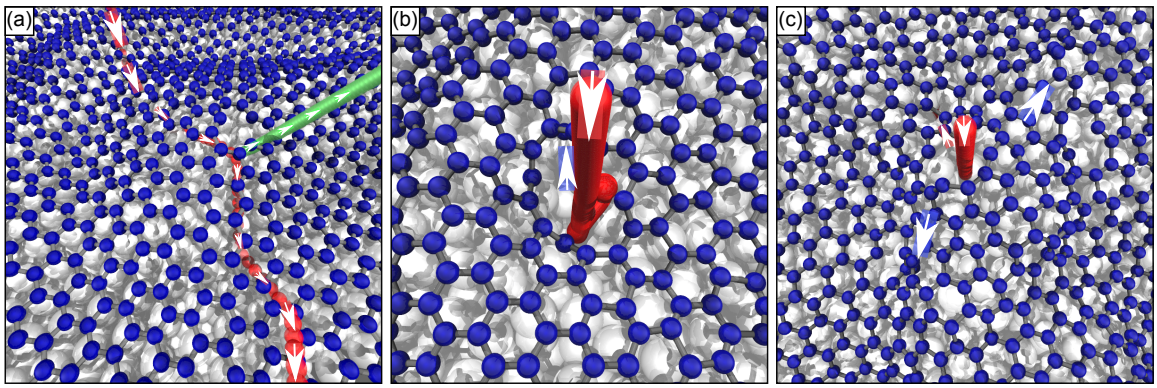

Figure 6.16: Molecular dynamics simulation events. Top view representations of MD snapshots after single ion impacts at normal incidence. (a) A frame of a 0.3 keV He irradiation event at 598 fs with overlayed intermediate positions of the ion (red) and a sputtered C atom (green). The ion first penetrates Gr without damage, is then reflected at the Ir substrate and sputters upon further reflection at the Gr sheet one carbon towards the vacuum. The ion undergoes a second reflection at the substrate before it moves through the Gr sheet and escapes to the vacuum. (b) A frame of a 0.3 keV Xe irradiation event at 579 fs. The ion impacts the Gr sheet pushing it towards the substrate and detaching one C atom (marked with the arrow on a blue background). At the end of the simulation the ion comes to rest at the Gr/substrate interface. (c) A frame for a Xe irradiation event at 5 keV after 398 fs with intermediate ion positions overlayed (red). The ion impacts the Gr sheet detaching two C atoms (marked with arrows on blue background) and travels further into the substrate.

It is instructive to oppose the 0.3 keV He^+ event with a typical 0.3 keV Xe^+ event, as displayed in Figure 6.16(b) 0.6 ps after the ion impact. On its way forward, the Xe ion disrupts the Gr layer, detaches a C atom entirely from Gr and comes to rest at the interface almost instantaneously upon encounter with the Ir substrate, due to efficient energy transfer (mass ratio 131:192). No sputtering takes place and besides a detached C atom [marked with an white arrow on blue background in Figure 6.16(b)] several additional under-coordinated C atoms adhere to the substrate. Thus, the substantial trapping for Xe opposed to the one for He is consistent with the average displayed in Figure 6.15(e). Comparing the 0.3 keV Xe^+ event of Figure 6.16(b) to a 5 keV Xe^+ event as shown in Figure 6.16(c) illuminates the effect of ion energy on the trapping mechanism. Even

though the Xe encounters a C atom it penetrates the Gr sheet by displacing the C atom. Thereafter, the ion hits a substrate atom and hence is scattered into the bulk.
Finally, we note that changing the angle of incidence of the primary ion changes the balance of sputtering and trapping as will be discussed in Chapter 7.
In our view, the phenomenon of trapping after irradiation of 2D materials is of general relevance. It does not depend sensitively on ion beam parameters (energy, species, charge state), as long as the ions are able to penetrate the 2D layer. It should also take place for other combinations of substrate and 2D layer materials, as long as (i) the implanted species does not react with substrate and 2D layer, (ii) the solubility of the implanted species in the substrate is low, and (iii) the 2D layer interacts strongly with its defects and edges to the substrate [171].

6.5 Blister Formation by Preimplantation

In the experiments described up to now, blister formation is a by-product of ion irradiation and always involves damaging of the Gr sheet. However, it is also possible to separate ion irradiation and blister formation, enabling us to create blisters under a perfect Gr sheet with number density and size controllable by thermal processing. To reach this goal we first implanted Xe at 300 K into bare Ir(111), using sufficiently high and varied ion energies to ensure high gas release temperatures and gas incorporation with a broad depth distribution. To remove surface damage, the sample was flash annealed to 1200 K and subsequently a Gr sheet was grown at 1200 K. Figure 6.17(a) displays the resulting morphology characterized by smooth circular bulges of subatomic height due to gas bubbles in Ir [165], as well as irregularly shaped (often triangular) blisters that formed due to gas release from the Ir crystal *during* Gr growth at 1200 K. The Xe still present in the subsurface bubbles can be released and trapped underneath the perfect Gr sheet by additional annealing to 1500 K, as shown in Figure 6.17(b). The bubbles within the Ir crystal vanished, while the volume of the blisters increased by a factor of five.
We envision that similar procedures of pre-implantation and annealing could be used to create pressurized nanoreactors with one reagent supplied through release of implanted species from the substrate. Also the growth of interfacial layers, *e.g.*, insulators, could be accomplished by providing a reagent from the bulk after 2D-layer growth or transfer and optional intercalation.
A further technologically relevant detail indicated by our investigations is that high temperature 2D-layer growth on an improperly degassed substrate with a higher than equilib-

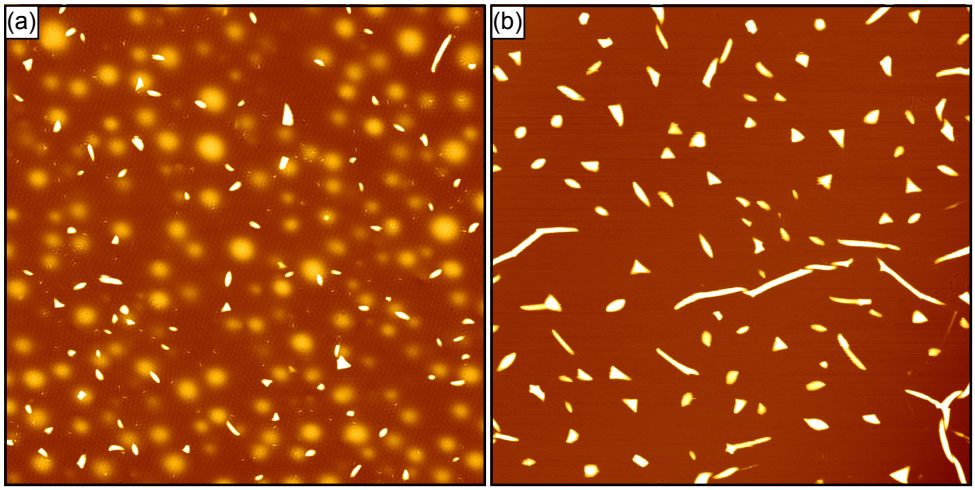

Figure 6.17: Implantation of Xe prior to graphene growth. (a) STM topograph of Gr/Ir(111) after successive exposure to 0.2 MLE of 5 keV, 4 keV, 3 keV, and 2 keV Xe^+ (accumulated exposure 0.8 MLE) at 300 K, subsequent annealing to 1200 K, and eventually growth of a complete layer of Gr at 1200 K. (b) sample after additional flash annealing to 1500 K. Image sizes are 250 nm × 250 nm.

rium gas concentration may result in inferior quality of the 2D-layer through the formation of gas cavities (blisters, bubbles, wrinkles) at the interface. For example, Gr grown on a metal substrate that was sputter-cleaned with keV noble gas ions and not annealed sufficiently long well *above* the Gr growth temperature, is likely to display gas filled blisters after growth. An example for blister formation during Gr growth on a sputter-cleaned and insufficiently annealed Ir(111) substrate is shown in Figure 6.18.

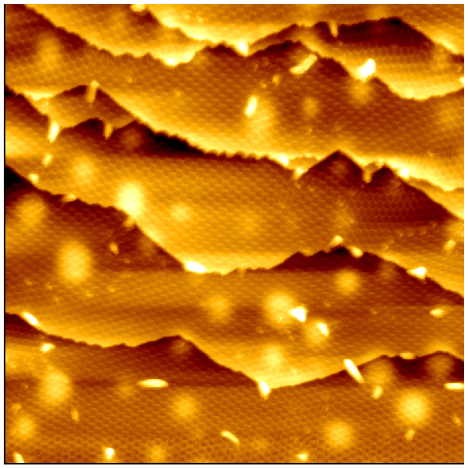

Figure 6.18: Sample morphology after sputter cleaning with 4 keV Xe^+ and insufficient annealing prior to graphene growth. STM topograph of Gr/Ir(111). Sample preparation prior to growth was accomplished by sputter cleaning with 4 keV Xe^+ and subsequent annealing to 1200 K. Room temperature ethylene adsorption to saturation and thermal decomposition at 1200 K followed by ethylene exposure at 1200 K was used for growth of the Gr sheet. Residual subsurface bubbles within the Ir crystal as well as small blisters in the Gr sheet are visible. Image size is 180 nm × 180 nm.

6.6 Conclusions

In conclusion, we have determined the mechanisms of atom trapping underneath Gr on Ir(111) during Xe^+ ion irradiation. It relies on the combination of two effects. First, for an ion energy up to a few keV a Gr layer on Ir(111) effectively decreases ion reflection in favor of ion trapping in between Gr and its substrate. The efficient trapping results from the easy penetration of Xe through Gr (small scattering cross section) and efficient energy loss to the metallic substrate, making escape after momentum-reversal unlikely. Second, the irradiation induced Gr edges bind strongly to the Ir(111) substrate making escape of Xe through out-diffusion at the Gr edge an unlikely process, even at annealing temperatures of 1300 K. Driven by the reduction of elastic and delamination energy of Gr, upon annealing the trapped Xe first forms monolayer thick Xe islands under flat bulges in Gr and, when growing larger at higher temperatures, three-dimensional pressurized blisters in the Gr sheet.

The bulge and blister formation upon ion irradiation must be assumed to take place for a broad range of different ion beam parameters (energy, species, and charge) as well as 2D-materials which adhere to the substrate. We demonstrated that ion beam implantation methods in combination with proper thermal processing may be a pathway to enable

reactions in pressurized nanocavities or to grow homogeneous interfacial layers between a perfect 2D material and its substrate.

CHAPTER 7

Blister-Free Ion Beam Patterning of Supported Graphene

This chapter is based on a manuscript published in Nanotechnology **28**, *055304 (2017) [172]. It contains contributions from E. H. Åhlgren and Thomas Michely. I was responsible for the design of the experiments, carried out all STM measurements and analysis, and wrote the draft of the manuscript. MD simulations and resulting images were done by E. H. Åhlgren.*

As discussed in the previous chapter structuring Gr and modifying its unique properties by ion beam patterning is a long time envisioned goal to enable an implementation of Gr in novel nanotechnologies. In order to materialize this approach a microscopic understanding of the defect production mechanisms is mandatory. Several theoretical and experimental investigations have provided information on the interaction of freestanding Gr with ions, on ion induced damage, and its effect on Gr's properties [111, 112, 173–179]. However, for nearly all applications Gr rests on a substrate. This circumstance strikingly alters the defect production in the Gr layer and will be of relevance for applications as diverse as ion beam cutting [180–182], patterning [20, 114], and doping [152, 153, 183]. Not only the resulting defect patterns in the Gr sheet and the underlying substrate are diversified, but the ion itself faces a larger variety of final destinations. Not only substitution or adsorption, but also implantation into the bulk material or trapping at the substrate-Gr interface becomes possible.

In Chapter 6 it was found that upon exposure with energetic noble gas ions a large fraction of these species penetrates the Gr adlayer and is irreversibly trapped at the interface between Gr and its substrate.

While such pressurized blisters display interesting properties (*e.g.* giving rise to pseudo-magnetic fields in Gr [26]) and open the pathway to high pressure – high temperature chemical reactions in confined spaces [77], it is an important question whether trapping of the primary ion species can be avoided at all during ion beam erosion of Gr. It is obvious that in the context of ion beam cutting and nanopatterning such blister formation is an undesired side effect. In Chapter 6 we demonstrated already that a variation of the noble gas species has a profound effect on trapping and blistering: At otherwise identical conditions (fluence, flux, temperature, and substrate material) He trapping is least efficient, presumably due to its smaller atomic size and therefore higher escape probability at edges and defects. However, since the sputtering yield of He is quite small, this finding is of limited practical relevance when considering efficient erosion and patterning of Gr.

In this chapter we build on the previous investigations in Chapter 6 and investigate whether the balance of erosion versus trapping/blistering can be shifted in a favorable direction by changing the ion beam angle of incidence on the Gr layer. This issue is investigated by combining well-defined STM experiments with MD simulations.

Figures 7.1(a)-(f) display the STM topographs of Gr/Ir(111) after a total of 0.03 MLE 3 keV Xe^+ ion exposure in three portions of 0.01 MLE, each followed by annealing to 1000 K. Four features can be distinguished in the topographs: (i) The moiré periodicity of Gr with a pitch of 2.5 nm [32] is visible, most pronounced in Figure 7.1(f). (ii) Small dark vacancy clusters in the Gr layer pinned to the moiré periodicity are most obvious in the inset of Figures 7.1(a) and (e). Such an arrangement of vacancy clusters with the moiré periodicity was found by Standop *et al* [20] for the same system and coined nano-mesh. (iii) Vacancy islands, *i.e.*, dark islands in the Gr layer of several nm-size are present most frequent in Figure 7.1(c). (iv) Bright protrusions with lateral extension of up to 10 nm and typical height of 0.3 nm are visible most pronounced in Figure 7.1(a). Based on the results in Chapter 6 we identify these protrusions as Xe filled blisters. With the estimated pressure in the blisters of the order of GPa, the measured blister height of 0.3 nm, and quantitative XPS determining the amount of trapped Xe [77], we assume Xe to form a monolayer in the blisters with a separation between neighboring Xe atoms close to the nearest neighbor bulk separation, as has been found for Xe adsorbed at low temperature on other dense packed metal surfaces [160].

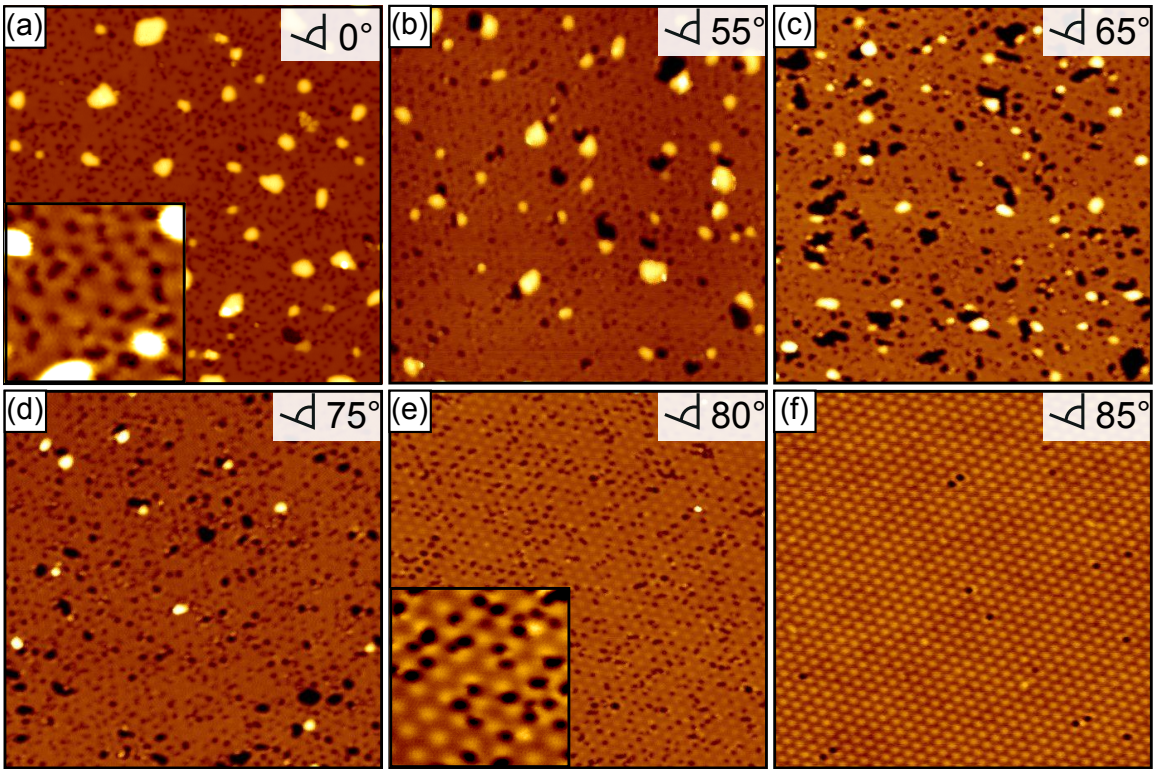

Figure 7.1: Angular dependent Xe trapping and graphene erosion. STM topographs of Gr on Ir(111) after three steps of 0.01 MLE 3 keV Xe^+ irradiation at room temperature, each followed by annealing to 1000 K. The angles are indicated in the topographs. Image size is always 80 nm × 80 nm. Trapped noble gas gives rise to bright blisters, sputtered graphene to dark vacancy islands. The insets highlights the additional presence of vacancy clusters pinned in the Gr moiré superlattice. Inset sizes are 15 nm × 15 nm.

By increasing the angle of incidence, the amount of trapped noble gas gradually decreases until at 80° in Figure 7.1(e) no more blisters are present [feature (iv)]. The amount of sputtered carbon, represented by vacancy clusters and vacancy islands [features (ii) and (iii)], increases with ϑ up to 65° [Figure 7.1(c)] and then rapidly decreases until it vanishes for $\vartheta = 85°$ [Figure 7.1(f)]. Quantitative image analysis results in the data displayed in Figure 7.2(a) and (b). Under the assumptions spelled out above and for the experimental conditions used, the area covered by blisters can be transformed into an experimental trapping yield $Y_{\mathrm{t,exp}}$, *i.e.*, the fraction of incident Xe ions trapped underneath Gr. It decreases gently from 0.5 to 0.4 by increasing ϑ from 0° to 55°, but then rapidly falls to zero at 80° [dark blue dots in Figure 7.2(a)]. The experimental sputtering yield $Y_{\mathrm{s,exp}}$ increases from about 2 at 0° to a maximum of 7.5 at 65°, from whereon it rapidly decreases until it almost completely vanishes at 85° as shown in Figure 7.2(b) as dark red dots. Noteworthy, at 80° it is distinctly different from zero, namely 1.1. This finding implies that at 80° erosion of Gr without trapping should be possible, since $Y_{\mathrm{t,exp}}(80°) < 10^{-2}$.

For comparison with the experimental results and in order to gain additional insight into the processes involved, we conducted 0 K MD simulations, where each ion was hitting a perfect Gr layer. This is in contrast to the experimental situation, where a fluence of 0.01 MLE is accumulated at room temperature before the layer is repaired through an annealing step. The fraction of ions trapped at the interface between Gr and the metal substrate $Y_{\mathrm{t,MD\ interface}}$ – at the location where in experiment blister formation is observed – is plotted as blue squares in Figure 7.2(a). In magnitude and overall trend the data compares reasonably well with experiment, but the peak in $Y_{\mathrm{t,MD\ interface}}$ at 70° is not found in experiment. For completeness, also the total amount of ions not reflected from the substrate, *i.e.*, the sum of $Y_{\mathrm{t,MD\ interface}}$ and the fraction of ions implanted into the bulk metal substrate $Y_{\mathrm{t,MD\ substrate}}$ is plotted in Figure 7.2(a) as light blue triangles.

The carbon sputtering yield obtained in the MD simulations $Y_{\mathrm{s,MD\ backward}}$ is plotted in Figure 7.2(b) as orange squares. In magnitude and overall trend it agrees remarkably well with the experimental yield $Y_{\mathrm{s,exp}}$. Specifically, both yields are peaked between 65° (experiment) and 70° (theory), though the calculated peak value is substantially larger than in experiment. Exploiting the power of MD simulations, we add to this quantity $Y_{\mathrm{s,MD\ forward}}$, the yield of carbon atoms that were found to be detached in forward direction at the end of the simulation time, and plot the sum $Y_{\mathrm{s,MD\ backward}} + Y_{\mathrm{s,MD\ forward}}$. This quantity can not be obtained in experiment, as C atoms detached in forward direction readily reintegrate into the Gr sheet during annealing. For comparison, the same two

quantities $Y_{\text{s,MD backward}}$ and $Y_{\text{s,MD backward}} + Y_{\text{s,MD forward}}$ are plotted in Figure 7.2(c) for *freestanding* Gr using the same color code.

Finally, to understand better the unique features in sputtering of supported Gr, we conducted additional MD simulations for freestanding Gr that are presented in Figure 7.2(c). As in Figure 7.2(b) for supported Gr, we distinguish between carbon atoms detached from the Gr sheet in forward direction ($Y_{\text{s,MD forward}}$) and carbon atoms detached from the Gr sheet in backward direction ($Y_{\text{s,MD backward}}$). Note that for freestanding Gr the sum of the two yields is the sputtering yield, while for supported Gr the sputtering yield is given only by $Y_{\text{s,MD backward}}$.

In Figure 7.3 ion trajectories and Gr damage patterns of typical events at the four different angles 0°, 60°, 70°, and 80° are represented. This data will be analyzed in more detail in the discussion.

First, we need to discuss the reliability of the experimentally obtained yields $Y_{\text{s,exp}}$ and $Y_{\text{t,exp}}$. In brief, we are convinced that they represent experimental trends in a proper way, as all data are affected by systematic errors similarly. However, quantitatively they may be off considerably. For $Y_{\text{s,exp}}$ mostly the usual image analysis errors apply. They may be substantial in the present case due to the smallness of the vacancy islands and the difficulty to take into account properly the size of the small vacancy clusters, which which appear as point-like dark spots in the STM topographs. Based on their funnel-shape in higher resolution topographs they were assumed and approximated here to be tetravacancies, consistent with their calculated appearance and low energy of formation [20]. Due to their high potential energy and mobility [20], the presence of single vacancies can be ruled out after annealing to 1000 K.

In comparison to the MD data one also has to consider that in MD the ion always hits a virgin surface, while in experiment a fluence of 0.01 MLE accumulates before the damage is partly healed by an annealing step. Though the fluence step of 0.01 MLE is small, specifically when the damage created by each ion is large, as for grazing incidence, the experimental deviation from the virgin surface may affect $Y_{\text{s,exp}}$.

From these remarks it is clear, that the sputtering yield we are talking about is an *initial* yield. While in sputtering of a bulk material the $Y_{\text{s,exp}}$ is often rather insensitive to the surface morphology and a steady state situation is quickly reached, for fundamental reasons this is not the case for a 2D material: (i) as the 2D material becomes consumed, its area shrinks and thus the fraction of ions hitting it; (ii) the structure of a 2D material changes during erosion without reaching a steady state (amorphization, step formation).

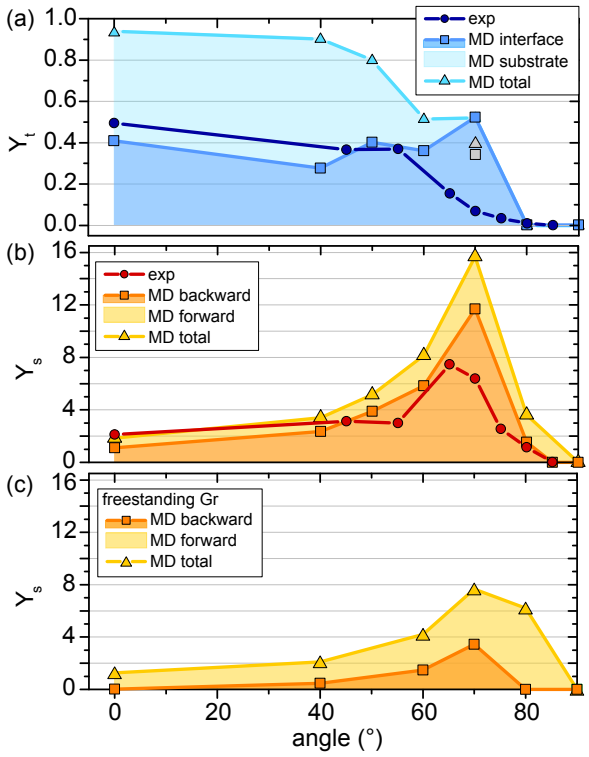

Figure 7.2: Angular dependence of Xe trapping and C sputtering.(a) Angular dependence of the experimental Xe trapping yield $Y_{\mathrm{t,exp}}$ (blue dots) for 3 keV Xe^+, the corresponding interface trapping yield $Y_{\mathrm{t,MD\ interface}}$ (blue squares) and the summed yield of trapped and bulk implanted Xe atoms $Y_{\mathrm{t,MD\ interface}} + Y_{\mathrm{t,MD\ substrate}}$ (blue triangles), as obtained by MD simulations. Gray data points for 70° were calculated with the projection of the ion direction onto the surface 10° off the high symmetry $[\bar{1}\bar{1}2]$ direction (see text). (b) Angular dependence of the experimental carbon sputtering yield $Y_{\mathrm{s,exp}}$ (red dots) for 3 keV Xe^+ and the corresponding carbon sputtering yield obtained in the MD simulations $Y_{\mathrm{s,MD\ backward}}$ (orange squares), which is made up of carbon atoms leaving the Gr sheet in backward direction. The yellow area represents the carbon detached from the Gr sheet in forward direction, *i.e.*, implanted into the bulk. In addition, the simulated summed yield of sputtered C atoms and of C atoms detached from the Gr sheet in forward direction $Y_{\mathrm{s,MD\ backward}} + Y_{\mathrm{s,MD\ forward}}$ is plotted as yellow triangles. (c) Simulated MD data as in (b) and represented with same symbols, but for *freestanding* Gr. The yellow area represents again the carbon detached from the Gr sheet in forward direction, which is sputtered. Lines to guide the eye. The full data set can be found in the Supplementary Information in tabular form.

Table 7.1: Angular dependence of Xe trapping and C sputtering from experiment and simulation. Data plotted in Figure 7.2 on the angular dependence of the experimental Xe trapping yield $Y_{\mathrm{t,exp}}$ for 3 keV Xe^+, the corresponding interface trapping yield $Y_{\mathrm{t,MD\ interface}}$, the substrate trapping yield $Y_{\mathrm{t,MD\ substrate}}$, and the summed yield of trapped and bulk implanted Xe atoms $Y_{\mathrm{t,MD\ substrate}} + Y_{\mathrm{t,MD\ interface}}$, as obtained by MD simulations. Further, the angular dependence of the experimental carbon sputtering $Y_{\mathrm{s,exp}}$ for 3 keV Xe^+ and the corresponding carbon sputtering yield obtained in the MD simulations $Y_{\mathrm{s,MD\ backward}}$, which is made up of carbon atoms leaving the Gr sheet in backward direction. In addition the simulated yield of C atoms detached from the Gr sheet in forward direction $Y_{\mathrm{s,MD\ forward}}$ is given as well as the summed yield $Y_{\mathrm{s,MD\ backward}} + Y_{\mathrm{s,MD\ forward}}$. Finally, the same sputtering yield as for Gr/Ir(111) are given for freestanding Gr.

	Gr/Ir(111)								freestanding Gr		
Θ [°]	$Y_{\mathrm{t,exp}}$	$Y_{\mathrm{t,MD\ interface}}$	$Y_{\mathrm{t,MD\ substrate}}$	$Y_{\mathrm{t,MD\ interface}} + Y_{\mathrm{t,MD\ substrate}}$	$Y_{\mathrm{s,exp}}$	$Y_{\mathrm{s,MD\ forward}}$	$Y_{\mathrm{s,MD\ backward}}$	$Y_{\mathrm{s,MD\ backward}} + Y_{\mathrm{s,MD\ forward}}$	$Y_{\mathrm{s,MD\ forward}}$	$Y_{\mathrm{s,MD\ backward}}$	$Y_{\mathrm{s,MD\ backward}} + Y_{\mathrm{s,MD\ forward}}$
0	0.50	0.41	0.52	0.94	2.13	0.73	1.11	1.85	1.24	0.02	1.26
40	–	0.28	0.63	0.90	–	1.05	2.35	3.41	1.63	0.47	2.1
45	0.37	–	–	–	3.13	–	–	–	–	–	–
50	–	0.4	0.4	0.8	–	1.27	3.89	5.16	–	–	–
55	0.37	–	–	–	2.99	–	–	–	–	–	–
60	–	0.36	0.16	0.51	–	2.31	5.85	8.16	2.73	1.47	4.2
65	0.15	–	–	–	7.48	–	–	–	–	–	–
70	0.07	0.52	0	0.52	6.38	3.99	11.69	15.67	4.21	3.45	7.66
75	0.04	–	–	–	2.54	–	–	–	–	–	–
80	0.01	0	0	0	1.14	2.08	1.54	3.61	6.2	0	6.2
85	0.00	–	–	–	0.01	–	0	–	–	–	–
90	0	0	0	0		0	0	0	0	0	0

Additional systematic errors are relevant for $Y_{\mathrm{t,exp}}$, when comparing it to the MD data. Experimentally, $Y_{\mathrm{t,exp}}$ can only be determined by an annealing step, allowing the trapped Xe to form well defined and laterally extended aggregates. During the annealing step (i) some Xe may be lost to the vacuum by escape through the holes (vacancy islands) and (ii) some Xe implanted into the Ir may be released and stream to the interface. By comparing density functional theory calculations, MD simulations and experimental data, it was shown in ref. [77] that release of trapped Xe during heating is small, if not negligible. Using thermal desorption spectroscopy, we demonstrated that by annealing to 1000 K after room temperature 3keV Xe^+ irradiation only minor fraction of the Xe implanted into the Ir selvage is released, at least at normal incidence. As both errors tend to cancel each other, we do not expect that they affect the trends in our experimental data in a substantial way.

As a last step in our error discussion, we need to assess the accuracy of our MD simulations. In the past, it has been found that sputtering yields derived from dedicated MD simulations may deviate by up to a factor of two from the results of corresponding experiments, specifically also for Pt(111) [184–188]. Redinger *et al.* [184] pointed out that part of this discrepancy may be due to the fact that interatomic potentials are usually fitted to the bulk properties of the material; therefore they describe surface properties relevant for ion induced surface damage and sputtering less reliably. Nevertheless, the qualitative experimental trends were always reproduced rather well by the MD simulations, providing thereby insight into the atomistics of the irradiation processes. In view such quantitative deviations in previous work, the annoying replacement of the Ir(111) substrate through Pt(111) - born out of a lack of adequate potentials - appears not to be a crucial problem. Taking into account that atomic masses, nuclear charge, density, structure, and chemistry of Ir and Pt are similar as well as that for the present simulations an adequate description of C-C and C-metal interactions is most relevant, we do not expect gross errors through our replacement. This expectations is backed up by the fact that SRIM [189] sputtering yields for 3 keV Xe^+ incident on Pt and Ir at various angles deviate only by about 5 %.

Given the sources of error in experiment, the differences in the impact situation in simulation (virgin surface, 0 K) and experiment (damage accumulation up to 0.01 MLE at 300 K, annealing to 1000 K), and the inherent difficulties of MD simulations to adequately reproduce surface processes at metals, the agreement of the experiment (dots) and simulation (squares) in Figure 7.2(a) and (b) is remarkable. To obtain deeper insight into the mechanisms involved, we now take a look to the damage patterns and ion trajectories of characteristic events as shown in Figure 7.3.

Figure 7.3(a) and (b) illustrate a typical defect pattern in the Gr sheet and the corresponding ion trajectory for $\vartheta = 0°$, respectively (see Supplementary Information for a movie of the event). The ion penetrates the Gr layer readily and due to the small scattering cross section for the fast Xe ion with the low Z C atoms, it causes only little damage to Gr. In the high Z substrate the ion's scattering cross section is much larger and it is efficiently stopped within the first few layers. Either it remains in the metal bulk or it scatters back. When hitting the Gr sheet on its way back, in most cases the ion has not enough energy to penetrate it and becomes trapped. Only 6% of all impinging ions are neither implanted nor trapped [compare Figure 7.2(a)]. This picture does not change substantially up to $\vartheta = 50°$.

A characteristic event for 60° is represented in Figures 7.3(c) and (d). Due to the grazing incidence geometry, Gr has become more opaque to the ion and more damage is created upon first passage. Moreover, also the substrate has become more opaque, the kinetic energy normal to the surface is reduced by a factor of 2, and, depending on the impact parameter, the ion may already be scattered back in the top metal layer, as shown in Figure 7.3(c). On its way out, the same ion passes again the Gr sheet and adds to the damage created upon first passage as highlighted by Figure 7.3(d). Consistent with this example, the MD carbon sputtering yield $Y_{\mathrm{s,MD\ backward}}$ increases from 1.1 at 0° to 5.8 at 60° [compare Figure 7.2(b)], and the Xe implantation into bulk has largely ceased [light blue area in Figure 7.2(a) represents bulk implantation].

In addition to the backscattering events as visualized in Figures 7.3(c) and (d), at 70° a new type of damage event is observed, for which a characteristic example is shown in Figures 7.3(e) and (f). The ion penetrates the Gr, is reflected from the substrate surface, but does not penetrate the Gr from below. Instead, it conducts an oscillatory motion at the interface of Gr and its substrate, as displayed in Figure 7.3(e). This phenomena is called interface channeling and was already observed for similar irradiation conditions [20]. As a result, Gr has multiple holes in a line-like formation accompanied by ample C sputtering as visible in Figure 7.3(f). In consequence, Xe implantation to the bulk reduces to zero. The Xe ion is still trapped with 50 % chance and due to channeling the carbon sputtering yield is sharply peaked [compare Figures 7.2(a) and (b)].

At 70° the MD simulations do not agree too well with the experimental data as visible in Figures 7.3(a) and (b). First, the experimental sputtering yield $Y_{\mathrm{s,exp}}$ is not as sharply peaked and as high as the MD yield $Y_{\mathrm{s,MD\ backward}}$, which reaches a value of 11.7 compared to 6.4 in experiment. Channeling events are especially extended and rely on the perfection of the channel. Figure 7.1(c) and (d) ($\vartheta = 65°$ and $\vartheta = 75°$) show at a first

glance that the amount of damage present even after annealing will affect the ability of the material to channel ions. Specifically, the vacancy clusters present with the moiré pitch of 2.5 nm with their edge C atoms bent down to the substrate will impede channeling and may thus reduce the resulting yield. Second, the experimental trapping yield $Y_{\mathrm{t,exp}}$ is with 0.07 much smaller than the simulated one with $Y_{\mathrm{t,MD\ interface}} = 0.51$. Suppression of channeling in experiment is certainly one factor leading to the lower trapping yield, and a second one might be the large damage in the Gr sheet that could foster escape of Xe during annealing. We also conducted dedicated MD simulations to find out, whether the difference in temperature during irradiation (0 K in MD and 300 K in experiment) or differences in the direction of the ion beam with respect to the substrate ($[\bar{1}\bar{1}2]$ direction in MD and 10° off $[\bar{1}\bar{1}2]$ in experiment) might contribute to this deviation. While MD simulation conducted at 300 K yield within the limits of error the same results as the 0 K simulations, for ion impacts 10° off the $[\bar{1}\bar{1}2]$ direction, comparable to the experimental direction of incidence, MD yields substantially lower trapping efficiencies in better agreement with the experiment [gray square and triangle in Figure 7.2(a)]. Apparently, when channeling takes place, not only slight differences between the experimental and the MD simulation situation lead to quantitative differences, but consistent with this, also changes in the MD parameters affect the ion trajectories and the related damage sensitively.

At $\vartheta = 80°$, due to the reflection of the impinging Xe ions already at the Gr sheet, trapping is absent in the simulation in perfect agreement with the experiment. Already at $\vartheta = 70°$ the metal substrate was impenetrable and caused to 100 % ion reflection upon first encounter. The same holds at $\vartheta = 80°$ for the low Z, but dense, Gr sheet, as visible for the ion trajectory shown in Figure 7.3(g). Nevertheless, upon ion reflection the Gr sheet becomes damaged at the impact location as shown in Figure 7.3(h). The carbon atoms are detached in forward direction, but some of them are backreflected by the heavy substrate atoms with enough kinetic energy to become sputtered. Both, experiment and MD simulation, agree that the sputtering yield is still substantial, where $Y_{\mathrm{s,exp}} = 1.1$ compares well with $Y_{\mathrm{s,MD\ backward}} = 1.5$.

Finally, comparing the two MD data sets for sputtering yields of supported [Figure 7.2(b)] and freestanding Gr [Figure 7.2(c)] we find characteristic differences. (i) $Y_{\mathrm{s,MD\ backward}}$ is dramatically enhanced through the presence of a substrate: by a factor of 50 at $\vartheta = 0°$ and still by a factor of 4 at $\vartheta = 70°$. The reason is simple: The heavy substrate enables momentum reversal, either for carbon atoms detached in forward direction that are subsequently backscattered and sputtered, or for the primary ion. In the latter case, the effect is most pronounced at grazing angles where the ion is enabled to hit the Gr sheet

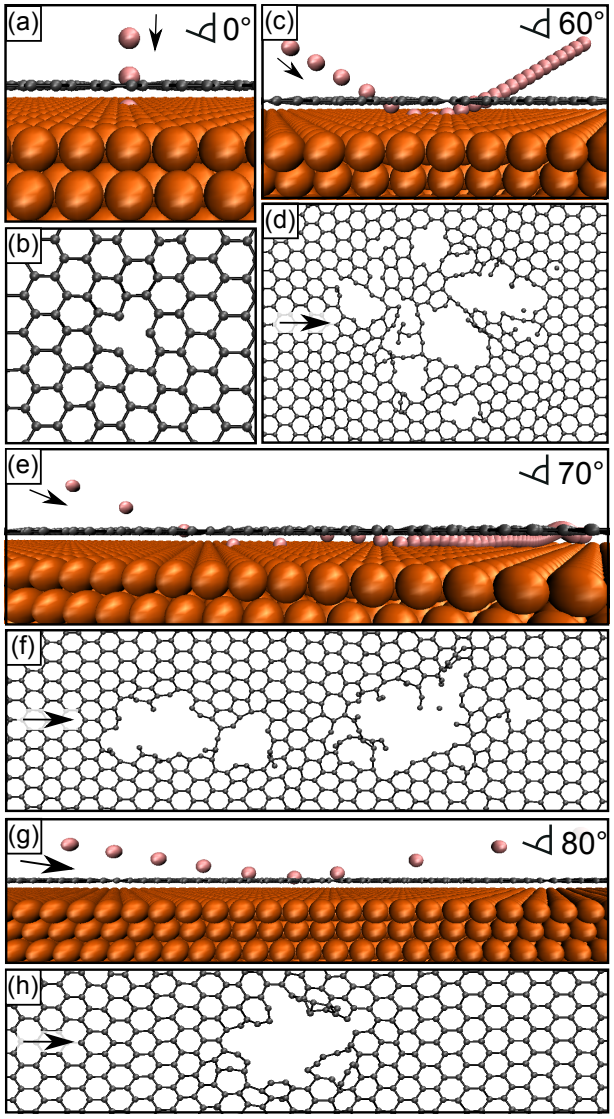

Figure 7.3: Molecular dynamics simulations events at different impact angles. Visualization of single, simulated 3 keV Xe impacts on Gr/Pt(111) at an angle of (a), (b) 0°, (c), (d) 60°, (e), (f) 70°, and (g), (h) 80°. (a),(c),(e), and (g) are side view images of the ion trajectory (red spheres), with the ion shown every 8 fs in (a) and (c), every 21 fs in (e), and every 14 fs in (g). The direction of the impinging ion is marked by a black arrow. (b), (d), (f), and (h) are top view representations of the Gr sheet at the end of the simulation time of 0.5 ns. In (d), (f), and (h) the projection of the ion direction on the surface is indicated by a black arrow along the $[\bar{1}\bar{1}2]$ direction. Movies of the events are provided as Supplementary Information of [122] (3keV-0deg.avi, 3keV-60deg.avi, 3keV-70deg.avi, and 3keV-80deg.avi, respectively).

one or several times from below (channeling), thereby causing sputtering. Certainly, also energized substrate atoms may contribute to carbon sputtering, although in view of the small substrate sputtering yields (0.4-0.7) and the low energy of the energized Ir atoms, this channel appears less relevant. (ii) $Y_{\mathrm{s,MD\ forward}}$ is only slightly larger for freestanding Gr up to $\vartheta = 70°$, but then takes off with 6.2 for freestanding Gr compared to 2.1 for supported Gr at $\vartheta = 80°$ [yellow area in Figures 7.2(b) and (c)]. The reason is that for metal supported Gr the C atoms will be hold back by the restoring force exerted by the substrate and only occasionally detach from the Gr sheet. (iii) The sputtering yield of the supported Gr is generally as high or higher than the one of freestanding Gr, except for the highest simulated angle of $\vartheta = 80°$. Here one has to compare $Y_{\mathrm{s,MD\ backward}}$ [orange squares in Figure 7.2(b)] for supported Gr with $Y_{\mathrm{s,MD\ backward}} + Y_{\mathrm{s,MD\ forward}}$ [yellow triangles in Figure 7.2(c)] for freestanding Gr. The behavior can be understood on the basis of what has already been outlined above. Momentum reversal at the substrate enhances sputtering in the supported case, especially in the channeling regime around $\vartheta = 70°$, while at extremely grazing angles the detachment of C atoms hit by the ion is suppressed for supported Gr by the substrate.

Based on our analysis, normal incidence irradiation maximizes trapping of the primary noble gas ion, while for grazing incidence at $\vartheta = 80°$ erosion without trapping should be possible. To substantiate our finding we conducted continuous grazing incidence 3 keV Xe^+ ion exposure for a larger fluence of 0.3 MLE while the sample was kept at the elevated temperature of 1200 K, where no more pinning of vacancy clusters to the moiré should take place and only large vacancy islands should result. In fact, the representative STM topograph in Figure 7.4 after such an experiment displays no blisters and thus no indication of noble gas trapping. Large Gr vacancy islands nucleated at the upper edges of preexisting substrate steps, ascending with respect to the projected ion beam direction. This is well understandable, as for Gr bending over ascending, illuminated substrate steps the local Xe flux is much higher as on the terrace [184]. Therefore the nucleation probability is highest at these locations. Due to the high temperature, the vacancy islands maintain a compact shape by edge diffusion, thereby minimizing their edge energy. Through lateral diffusion the vacancies created at other locations on the substrate anneal to these islands. Remarkably, except of large vacancy islands, virtually no other irradiation induced damage is present in the Gr sheet. For nanopattering applications certainly lower irradiation temperatures, keeping the erosion locally better confined *and* the absence of trapping would be desirable. Future work in this direction would be important and is currently planned.

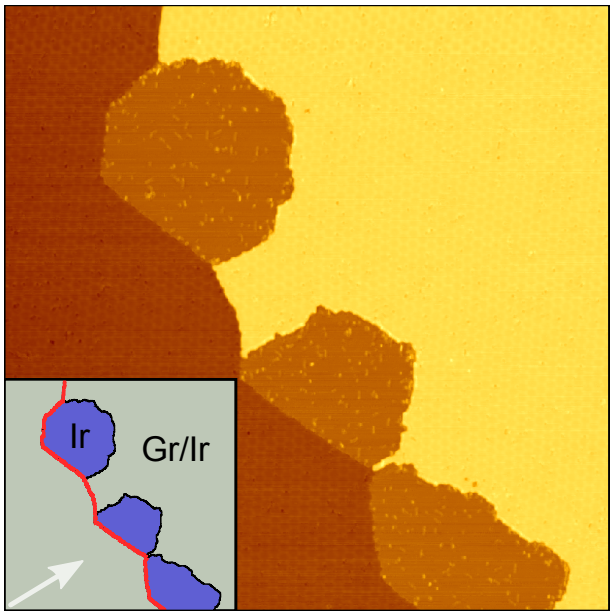

Figure 7.4: Graphene erosion without noble gas trapping. STM topograph of Gr on Ir(111) after 0.3 MLE 3 keV Xe^+ irradiation 80° off normal at 1200 K. Surface erosion is present in form of large vacancy islands (blue in inset) in absence of noble gas trapping, *i.e.*, blister formation. Within the vacancy islands adsorbates are visible on the bare metal (bright dots). Image size is 150 nm × 150 nm. Inset: Schematic of the different surface areas. The red line indicates the position of an Ir substrate step. Arrow indicates approximate projected direction of ion beam incidence.

In conclusion our data for metal supported graphene suggest a selectivity between surface erosion and noble gas trapping by choosing the angle of incidence. At angles close to normal incidence noble gas trapping dominates. This results in blister formation in the Gr after thermal treatment. By increasing the angle of incidence close to 70 ° off normal surface erosion is most efficient. Erosion and patterning without blister formation is demonstrated for an incidence angle of 80 ° at elevated temperature. With this insight it is possible to selectively use the advantages of both phenomena. To erode Gr in a controlled manner without noble gas trapping grazing incidence ion irradiation should be applied. On the other hand, in order to deform the Gr sheet by gas filled blisters, *e.g.*, to strain the Gr, a normal or close to normal incidence is favorable. In addition, we shed light on the global differences in irradiation of freestanding versus supported Gr and provide a first MD data set comparing the two cases. Our simulations document that for off-normal incidence, except for very grazing angles, momentum reversal through the substrate enhances the Gr sputtering yield.

In future we plan to use angle dependent MD simulations of trapping and sputtering also for lighter noble gases and different ion energies as a guideline to experiments that maximize sputtering and minimize trapping. Experiments with continuous ion exposure at elevated temperature will be used to explore the relevance of thermally activated processes for noble gas escape form underneath the Gr sheet. Lastly, reactive ion beams (*e.g.* of oxygen) could be an alternative means to pattern Gr at relatively low temperature without trapping.

CHAPTER 8

Graphene as the Ultimately Thin Sputtering Shield

The results of this chapter are published in 2D Materials **3**, *025032 (2016) [122]. All experiments were planned and interpreted with the help of Thomas Michely. I carried out all experiments, performed the data analysis, and prepared the draft of the manuscript.*

The reduction of particle radiation induced degradation is an inherent and common task to material science. For example, in the design of fusion reactors it is still a prevalent challenge to prevent the erosion of reactor walls by energetic particles from the plasma [190]. In electron and He ion beam microscopy it is for many cases of utmost importance to limit irradiation induced changes in the sample. Recent transmission electron microscopy studies demonstrated that electron irradiation induced damage in 2D materials can be prevented by embedding them into single sheets of graphene (Gr) [177, 191, 192]. An early example for a self-sustained protection effect against ion irradiation was described by Morita *et al* [193]. They found that, for an elevated temperature of 650°C, Ni sputtering by keV noble gas ions is suppressed for extended times by a thin - approximately two-atomic layer thick - carbon film. The sputtering losses are replenished by carbon segregation from the bulk. Under the conditions applied by Morita *et al*, most likely the carbon was present at the surface in the form of Gr [194]. Based on MD simulations Åhlgren *et al* as well as Standop *et al* proposed a strong reduction of Pt substrate sputtering in the presence of a monoatomic Gr cover-layer [20, 195].

In this light we experimentally analyze in this chapter the potential of Gr as the ultimately thin sputter protection for metal surfaces. In a comparative STM study we oppose the responses of a bare Ir(111) sample and a Gr-covered sample to noble gas ion irradiation in the energy range below 1 keV. At high temperatures, where damage in the Gr cover largely anneals between successive ion impacts, we find a reduction in the Ir sputtering yield by about two orders of magnitude. Eventually, we analyze the conditions for efficient sputter protection, speculate how it could be maintained for large ion fluences, and discuss the applicability of our concepts to other materials.

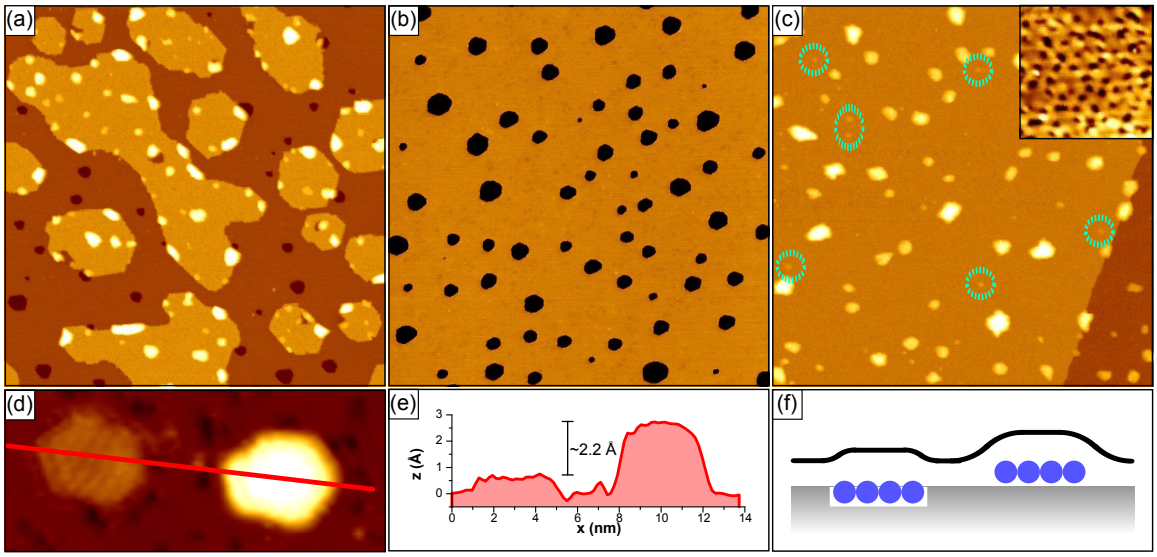

Figure 8.1: Graphene as the ultimately thin sputtering shield. STM topograph of (a) 0.5 ML Gr on Ir(111), (b) bare Ir(111), and (c) 1 ML Gr on Ir(111), after exposure to 0.05 MLE 500 eV Xe^+ at 1000 K. Image sizes are 225 nm × 225 nm. In (c) some noble gas platelets embedded into the first substrate layer are highlighted by green dashed circles. Inset in (c) with higher magnification and enhanced contrast shows vacancy clusters in the Gr layer. Image size of inset is 20 nm × 20 nm. (d) STM topograph with an embedded and an on-top interfacial noble gas platelet after 0.1 MLE 1 keV Xe^+ exposure and subsequent post-annealing to 1100 K. Image size is 14 nm × 6 nm. The profile along the red line in (d) and the corresponding schematic sketch are shown in (e) and (f), respectively.

Figure 8.1(a) directly visualizes the protective effect of Gr during ion exposure. Prior to irradiation half a monolayer of Gr was grown on Ir(111). Subsequently, the sample was exposed to 0.05 MLE 500 eV Xe^+ at 1000 K. The STM topograph in Figure 8.1(a) taken after irradiation displays two predominant height levels that still reflect the initial situation: the lower level is bare Ir(111), whereas the higher is formed by the Gr-covered areas. Within the area of bare Ir, hexagonally shaped monolayer deep depressions are

visible, while within the Gr-covered area, bright protrusions are present, but almost no depressions. The hexagonal depressions are monolayer deep surface vacancy islands. In consequence of Ir sputtering, they form by thermal diffusion and aggregation of vacancies left behind by the sputtered atoms [185, 196, 197]. Their area directly reflects the amount of Ir sputtered. The bright protrusions within the Gr covered area are noble gas filled blisters and bulges. They result from the aggregation of noble gas at the Gr/Ir(111) interface as outlined in Chapter 6. The origin of their formation is the dramatically reduced primary ion reflection in the presence of the Gr cover, *i.e.*, efficient trapping, in combination with strong Gr-Ir bonds at the Gr edges that prevent escape of Xe by diffusion, even at elevated temperatures. The virtual absence of surface vacancy islands underneath the Gr area indicates a strong suppression of Ir sputtering. Similar to the primary ion, energetic Ir atoms with energies which would be sufficient to leave the sample in uncovered areas, are held back and trapped by the Gr cover. In the presence of surface diffusion, trapped but displaced Ir atoms recombine with surface vacancies such that a perfect Ir surface is maintained. In the following we will substantiate our reasoning with dedicated experiments and derive quantitative estimates for the suppression of Ir sputtering by the Gr cover.

To quantify the sputter protection of Ir through the Gr cover, for reference we need the sputtering yield of bare Ir(111) determined as precise as possible. To this end, bare Ir(111) (without any Gr coverage) was exposed to 0.05 MLE of 500 eV Xe^+ ions at 1000 K [compare Figure 8.1(b)]. Image analysis of the surface vacancy island area due to sputtering for many topographs results in an estimate for the yield $Y_{\mathrm{s,bare}}$ of (1.56 ± 0.05) atoms/ion. We conducted two additional experiments, one for a higher ion fluence (0.1 MLE) and one with additional post-annealing to 1200 K. The measured yields all agree within the limits of error and as best estimate $Y_{\mathrm{s,bare}} = (1.53 \pm 0.03)$ is obtained. Therefore, we conclude that at 1000 K and for 500 eV Xe^+, annealing of the radiation damage to the surface is complete, making the surface vacancy island area representative for the removed material. We limit our experiments to primary ion energies well below 1 keV, because at higher energies indeed stable vacancy clusters must be expected to survive annealing to 1000 K, whereby our approach would be invalidated [197]. We note that for image analysis areas next to preexisting steps were excluded, as steps are sinks for vacancies and thus cause surface vacancy island depleted zones. Moreover, from the independence of the derived yield on ion fluence we conclude that imaging artifacts of the STM tip have no, or only a negligible, effect on the results.

Our value is in reasonable agreement with binary collision calculations (SRIM [189]), which give 1.76 atoms per ion. Using the semi-empirical equation by Seah *et al* [198, 199] for our case results in 1.59 atoms per ion [200]. In view of the crudeness of the two approaches, the agreement with our experimental value is surprising. Earlier, Petersen *et al.* [197] obtained ≈ 1.3 atoms/ion for 0.5 keV Xe^+ on Ir(111). However, in that study lower ion fluences and lower irradiation temperatures were used, potentially resulting in larger imaging errors and incomplete damage annealing to the surface, respectively.

Two additional reference values were determined using the same methodology: For 200 eV Xe^+ we have $Y_{\mathrm{s,bare}} = (0.69 \pm 0.10)$ atoms/ion and for 200 eV Ar^+ we have $Y_{\mathrm{s,bare}} = (0.68 \pm 0.03)$ atoms/ion (compare Table 8.1).

After having established the reference value $Y_{\mathrm{s,bare}}$, the Ir sputtering yield of the Gr covered Ir(111) is analyzed by conducting experiments like that visualized in Figure 8.1(c). A closed Gr layer is grown on a clean Ir(111) surface and irradiated with 0.05 MLE of 500 eV Xe^+ at 1000 K. For proper image interpretation of Figure 8.1(c) it is important to note that the step visible in the topograph at the right-hand margin, running from top to bottom, is a preexisting step in the Ir substrate that was overgrown by the Gr sheet (Gr covers the substrate in a carpet-like fashion [107]). In the entire image only Xe filled bulges and blisters are visible. Surprisingly, no holes in the Gr sheet are apparent at the magnification shown, which seems to contradict our expectations of Gr sputtering. However, the better resolved inset of Figure 8.1(c) displays a regular array of small vacancy clusters. These vacancy clusters represent the sputtered carbon. Based on this and similar experiments as rough estimate, a carbon sputtering yield of 0.9 atoms/ion for Gr on Ir(111) under 500 eV Xe^+ irradiation is obtained (compare also [20]). The peculiar arrangement of the vacancy clusters is due to the fact that, at these temperatures, vacancies in the Gr layer on Ir(111) are still confined to the superlattice unit cell with a pitch of 2.53 nm formed by the moiré of Gr with the substrate [20]. The reason for the confinement is the strong binding of the vacancy cluster dangling bonds to the Ir substrate at specific locations of the moiré.

In the entire topograph of Figure 8.1(c) not a single hexagonal surface vacancy island in the Ir layer is visible, although Gr conforms to steps of the underlying Ir substrate. This seems to imply that no Ir was sputtered to the vacuum from under the Gr cover. Indeed the more careful analysis below confirms that only a tiny amount of Ir was sputtered, if at all. For a sample exposed to the larger ion fluence of 0.1 MLE and energy of 1 keV at room temperature, with subsequent post-annealing to 1100 K, occasionally we find a situation as shown in Figure 8.1(d). Besides small holes in the Gr layer due to C-atom

sputtering, a hexagonal elevation with a height below 1 Å is visible on the left-hand of the topograph [compare line profile in Figure 8.1(e)]. We interpret this elevation to result from a surface vacancy island filled by a monolayer of Xe atoms, as depicted in Figure 8.1(f). Consistent with this interpretation is the fact that its height is about 2.2 Å lower than that of a bulge resulting from a Xe platelet on the Ir(111) top layer, *e.g.* the bulge on the right-hand side in Figure 8.1(d). The height difference of 2.2 Å corresponds to the step height of Ir(111). Moreover, the faint internal structure of the flat hexagonal protrusion in Figure 8.1(d) may indicate a $(\sqrt{3} \times \sqrt{3})$ structure of Xe underneath Gr, the structure one expects for a dense Xe adsorption layer on Ir(111) [160]. To obtain an upper bound for the Ir sputtering yield, we therefore determine the area of all the ≈ 1 Å high protrusions, irrespective of their size and shape. Such protrusions are encircled by green dashed lines in Figure 8.1(c). Using this approach one obtains an upper bound estimate of $Y_{\mathrm{s,covered}} < 0.027\,\mathrm{atoms/ion}$ for 500 eV Xe^+. Due to filling of surfaces vacancies with Xe, one cannot foreclose annealing of excess Ir adatoms at preexisting substrate steps, which is an additional reason that the value for $Y_{\mathrm{s,covered}}$ must be considered as an upper bound value.

Table 8.1 summarizes the analysis for the 500 eV Xe^+ as well as the 200 eV Xe^+ and Ar^+ cases. The protection ratio $\frac{Y_{\mathrm{s,bare}}}{Y_{\mathrm{s,covered}}}$ is in all three cases larger than 50, with a tendency for an increase towards lower ion energies. This terminates our experimental proof of efficient protection of Ir(111) against low energy noble gas ion sputtering through a monolayer thick Gr cover.

Table 8.1: Sputtering yields. Sputtering yield for bare Ir(111) $Y_{\mathrm{s,bare}}$, sputtering yield for Gr covered Ir(111) $Y_{\mathrm{s,covered}}$, and the protection ratio $\frac{Y_{\mathrm{s,bare}}}{Y_{\mathrm{s,covered}}}$ for ion irradiation at normal incidence with different ion species and energies.

ion	E (eV)	$Y_{\mathrm{s,bare}}$	$10^{-2} \times Y_{\mathrm{s,covered}}$	$\frac{Y_{\mathrm{s,bare}}}{Y_{\mathrm{s,covered}}}$
Xe	500	1.53 ± 0.03	$< 2.7 \pm 2.3$	> 57
Xe	200	0.69 ± 0.10	$< 0.8 \pm 0.3$	> 85
Ar	200	0.68 ± 0.03	$< 1.0 \pm 1.1$	> 66

Our results appear nothing but expected in the light of previous MD simulations of single ion impacts on a perfect substrate. From such simulations it is well known that the vast majority of the sputtered atoms of a metal surface stem from the surface layer [186]. As the additional Gr sheet makes the Ir surface layer the second layer of the system, it is plausible that the Ir sputtering reduces drastically. In addition, the extraordinary strength of Gr

implies a displacement energy of around $\approx 23\,\mathrm{eV}$ [201–203], which is large compared to the low energy distribution of the Ir impinging from underneath against the Gr cover [86, 204]. Together with the high atomic areal density of Gr, this large displacement energy makes the penetration of energized Ir atoms through the sheet extremely improbable. Thus, the only channel for the escape of an Ir atom is to find the entrance hole of the primary ion (sputtering yield of 500 eV Xe^+ is around 0.9), where a C atom may be missing and some damage in the Gr sheet can be present.

Åhlgren *et al.* simulated normal incidence single ion impacts of Ar^+ on Pt(111) (Pt is a neighbor element of Ir in the periodic table) with and without a protecting Gr shield [195]. Consistent with our experimental results, according to the simulations at 300 eV the Gr shield seems to prevent Pt sputtering entirely. At ion energies of 1 keV and above the calculated protection ratios reduce somewhat and range between 5 and 25. Similar, Standop *et al.* found in MD simulations of 5 keV Xe^+ at grazing incidence on Pt(111) a protection ratio of 13 [20].

When comparing MD simulations with our experimental results, one has to bear in mind that the two situations under concern are very different. In MD simulations single ions impact on a surface that is reset to perfection after each impact. In our experiments, ions impinge on a surface, that accumulates the changes induced by previous impacts. The effect of the damage accumulation becomes obvious, when we irradiate at a lower temperature of 300 K, closer to the 0 K temperature in the MD simulations, where damage repair is largely absent. For 300 K irradiation with a fluence of 0.05 MLE 500 eV Xe^+ and subsequent annealing to 1000 K for analysis, the Ir sputtering yield of the Gr covered sample increases to $Y_{s,covered} = 0.23 \pm 0.09$ atoms/ion. The protection ratio is reduced from > 57 for irradiation at 1000 K to ≈ 9 for irradiation at 300 K.

Our experiments are therefore not a mere confirmation of theoretical predictions, but document the existence of a temperature regime, in which ion induced damage in Gr heals efficiently such that the integrity of the Gr lattice is restored prior to subsequent impacts. The relevant temperature regime coincides with the temperature range, where Gr can be grown by CVD from precursor molecules. For Ir this temperature range is roughly between 1000 K and 1500 K [128].

Certainly, for large ion fluences the sputter protection effect must eventually break down, as more and more Ir surface becomes uncovered from Gr, because Gr is sputtered. Sustained sputter protection will need regrowth of the removed Gr during irradiation. At elevated temperatures, which are needed anyway to ensure damage repair, a small vapor

pressure of hydrocarbon molecules is sufficient to maintain the full Gr coverage on Ir(111), since Gr grows by catalytic decomposition of such hydrocarbons [128].

Eventually, we need to address the question how general our finding of a Gr sputter protection effect is. First, the formation and maintenance of a high quality Gr layer on the metal substrate is a necessary condition. For Ir we established that under the same CVD conditions, where a Gr layer forms on the (111) face, a continuous Gr layer is also formed on a polycrystalline Ir sheet. Gr layers grow by CVD on a large number of mono- or polycrystalline, technologically relevant (even on carbide forming) metal surfaces like Fe, W, Co, Cu, Ni, Ru, Re, Rh, Pd, Pt, [205–214] and it seems reasonable to speculate that also on alloys of the mentioned metals Gr sheets may be formed by CVD growth. Due to the similarity of the Gr layer formation mechanism by CVD growth on all these substrates, it is plausible that in a large temperature window around typical CVD growth temperatures, efficient self-repair of the Gr layer after ion impacts will take place and that regrowth of sputtered Gr in a low hydrocarbon partial pressure is possible.

Next, from the similarity of the sputtering yields of the materials mentioned above, of the energy distributions of sputtered metal atoms, and of the ion reflection probabilities we conclude that similar protection ratios as for Ir(111) can be achieved with a Gr layer for a given ion species and energy.

Finally, as indicated by the MD simulations of Åhlgren *et al.* [195] and consistent with our results, Gr sputter protection will be most efficient for ion energies well below 1 keV, where Gr sputtering itself is still ineffective.

While at elevated temperatures, where Gr self-repair and CVD growth work well, efficient sputter protection is expected, there is no hope that sputter protection of similar efficiency can be operative at room temperature. Gr will be rapidly destroyed by the successive ion impacts and can neither be repaired nor regrown by CVD.

In conclusion, for noble gas ions with energies of ≈ 0.5 keV or below, a Gr cover on Ir(111) suppresses sputtering of the underlying metal by about two orders of magnitude for irradiation temperatures at or above 1000 K. For room temperature irradiation, suppression of sputtering diminishes and amounts to only one order of magnitude. Efficient sputter protection is thus based on self-repair of radiation damage in Gr on Ir(111), which is possible in the temperature regime where CVD growth is conducted. It is likely, that in this temperature regime progressive removal of the Gr shield can be suppressed and sputter protection can be maintained for large ion fluences by continued regrowth of the shield in a hydrocarbon partial pressure. We speculate that the mechanism of Gr sputter protection uncovered by us for Ir(111) is operative for a large number of technologically

relevant materials in a temperature window at or above the corresponding CVD growth temperature, where efficient self-repair of Gr irradiation damage takes place.

CHAPTER 9

Xenon Trapping and Nano-Crystals underneath Hexagonal Boron Nitride on Ir(111)

This chapter contains contributions from P. Valerius, M. A. Arman, J. Knudsen, and T. Michely. I was strongly involved in the planning of all experiments and the conduction of the XPS measurements, performed all TPD measurements and analyzed them. The STM measurements within this chapter were conducted and together with the XPS data analyzed by P. Valerius under the joint supervision of T. Michely and me [215]. Some of the results within this chapter are prepared for publication in [216].

In the previous chapters we presented sound evidence that even a highly defective Gr layer on Ir(111) not only efficiently traps noble gas after ion irradiation and annealing but also holds back otherwise sputtered material which we assume to hold for other 2D materials as well. Further we showed that the trapped noble gas forms highly pressurized blisters. Similar results were recently reported after low-energy ion irradiation of Gr/Ir(100) [217]. However, direct experimental proof for high pressures within the noble gas blisters is still lacking. For hBN/Rh(111) Cun *et al.* [53] showed for low ion doses that similarly to the Gr case Ar^+ ions can be immobilized at the hBN/Rh(111) interface when choosing the right irradiation parameters. These isolated Ar atoms at the interface form so called nanotents. Furthermore, in another publication on the same system they speculate on a process entitled as the *can opener effect* [155]. In this process ion induced single vacancies are assumed to migrate to the rim of the pore region of the moiré formed by hBN on

Rh(111) and thereby cut out hBN flakes, similar to the way the lid is peeled off a tin can, which then flips over, giving rise to protrusions and leaving behind 2 nm voids in their vicinity [155]. Note that this effects was by now also proposed for Gr/Ru(0001) [156]. Based on our previous results for Gr on Ir(111) it is questionable whether this process occurs for hBN/Ir(111) exposed to higher ion doses or if the proposed process does reflect reality at all.

To this end, up to now, a thorough study on the effect of high irradiation doses on the noble gas trapping and annealing behavior of supported hBN is still lacking. Several questions remain unclear: Is a highly damaged hBN film able to reconstruct and thereby retain noble gas under its lid? And is vacancy migration possible at all, since their mobility must be expected to be limited due to the obliged formation of hetero-elemental bonds.

In this chapter we therefore investigate ion irradiation of hexagonal boron nitride on Ir(111) by means of XPS, TPD, and STM measurements. Selected irradiation and annealing experiments with varying ion energies are presented in order to gain insight into the defect production, their thermal stability, as well as the noble gas trapping potential and thermal stability of trapped species for hBN/Ir(111).

9.1 Xenon Trapping

For reference, initially we irradiated a bare Ir(111) sample with 0.1 MLE 0.5 keV Xe^+ ions at room temperature and normal incidence. Subsequently the sample was annealed to 1000 K and 1300 K. In a second set of experiments we covered the Ir(111) surface by a full monolayer of hBN and exposed the sample to Xe^+ ions using the same parameters and perform the same annealing steps. For each parameter set and after each annealing step we recorded XP spectra of the Xe 3d/ Ir 4s region as shown in Figures 9.1(a) and (b).

As in Chapter IV, all spectra were normalized to the Ir 4s peak height. Besides the Ir 4s peak at room temperature the spectra for bare Ir in Figure 9.1(a) exhibits the known Xe $3d_{3/2}$ and Xe $3d_{5/2}$ doublet that vanishes with increasing annealing temperature. This is consistent with prior experiments and proves Xe implantation into the Ir bulk at room temperature followed by out-diffusion and eventually desorption upon annealing. Surprisingly, in the case of room temperature irradiation of hBN covered Ir(111) the Xe intensities are substantially higher than for the uncovered case. Thus, hBN shows a similar remarkable trapping behavior as Gr. By annealing the sample the Xe signal reduces.

To gain insight into the energy dependence of the damage within hBN upon ion irradiation, the impact of it on the trapping behavior, and the damage annealing, we conducted a

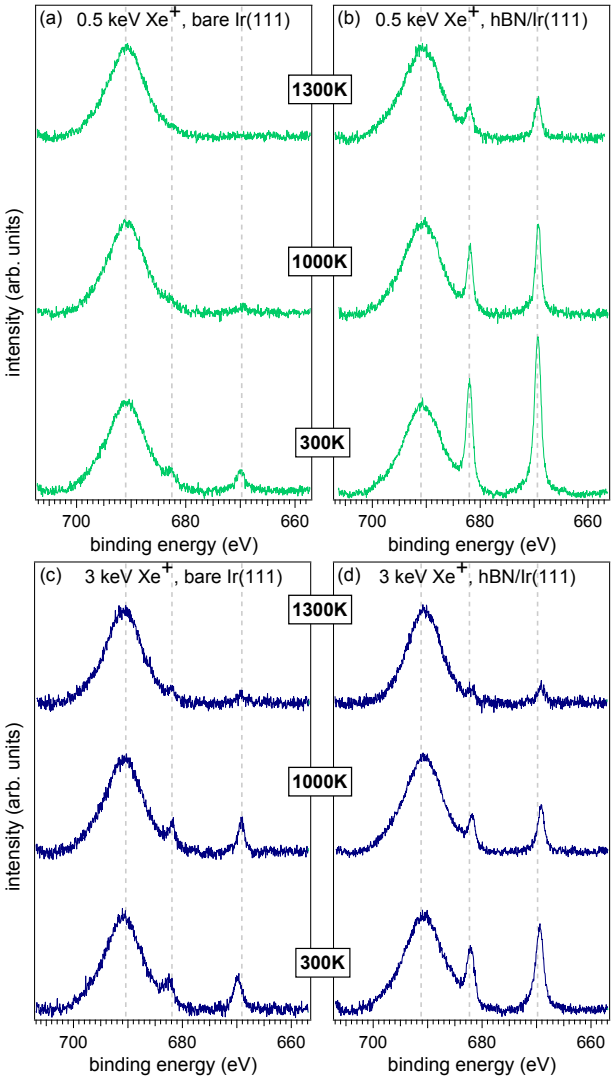

Figure 9.1: X-ray photoelectron spectroscopy of Xe trapping. XP spectra of the Ir 4s, Xe $3d_{3/2}$, and Xe $3d_{5/2}$ core levels for 0.5 keV Xe^+ irradiation of (a) bare and (b) hBN covered Ir(111) as well as 3 keV Xe^+ irradiation of (c) bare and (d) hBN covered Ir(111) at 300 K and annealed to stepwise increasing temperatures, as indicated.

similar experimental series using 3 keV Xe^+ ions. Here, the initially created damage within hBN and the loss of B and N atoms in course of sputtering is expected to be increased and might impede lattice reconstruction which probably decreases the trapping efficiency. The XP spectra after 3 keV Xe^+ irradiation are shown in Figure 9.1 for bare (c) and hBN covered Ir(111) (d). The XP spectra of the bare sample resemble the reference spectra in Chapter IV and will therefore not be further discussed, except that the Xe present in the crystal at 300 K almost entirely desorbs after annealing to 1300 K. Irradiation of hBN/Ir(111) results in an increased Xe signal compared to the bare case, but it is significantly smaller than for 0.5 keV irradiation of hBN/Ir(111). Upon annealing the signal gradually decreases with only little Xe left in the sample after annealing to 1300 K. Table 9.1 summarizes the obtained integrated intensities for 0.5 keV and 3 keV Xe^+ irradiation of bare and hBN covered Ir(111) given in % of a saturated Xe layer on Ir(111), assuming a $\sqrt{3} \times \sqrt{3}$ structure. Further, the intensity ratio $I_{\mathrm{hBN}}/I_{\mathrm{bare}}$ is specified.

Table 9.1: Integrated Xe intensities after 3 keV Xe^+ irradiation. Integrated Xe $3d_{5/2}$ intensities I_{bare} and I_{hBN} of bare and hBN covered Ir(111), respectively, after exposure to 0.1 MLE 0.5 keV and 3 keV Xe^+ at 300 K as well as annealing to 1000 K and 1300 K, respectively. Also, the intensity ratio $I_{\mathrm{hBN}}/I_{\mathrm{bare}}$ is specified for the ion energies and temperatures used. Intensities are given as % of the integrated Xe $3d_{5/2}$ intensity of a saturated Xe layer on Ir(111) and are calibrated to the Ir 4s peak height measured simultaneously.

	0.5 keV			**3 keV**		
	I_{bare}	I_{hBN}	$I_{\mathrm{hBN}}/I_{\mathrm{bare}}$	I_{bare}	I_{hBN}	$I_{\mathrm{hBN}}/I_{\mathrm{bare}}$
300 K	1.1	7.9	7	1.7	4.6	2.7
1000 K	0.3	4.0	12	1.2	2.1	1.7
1300 K	≈ 0.01	1.7	> 60	0.5	0.8	1.6

Next, we want to have a complementary look at the annealing behavior by following the Xe desorption from the sample by TPD measurements. We performed exactly the same set of experiments and recorded the thermal desorption traces as visible in Figure 9.2. The solid green line represents the desorption after irradiation and annealing of bare Ir(111) with 0.5 keV Xe^+ ions. The established double peak structure with desorption temperatures of 745 K and 880 K as well as the gradual increase above 1000 K is apparent. Surprisingly, after room temperature irradiation of hBN covered Ir(111) substantial Xe desorbs below 745 K (dashed green line). The desorption peak is comparably broad with a maximum desorption temperature of about 550 K. The previous double peak structure cannot be

resolved since the overall intensity has increased at this temperature. Above 1000 K a new double peak appears at 1080 K and 1200 K.
The TPD data for 3 keV Xe^+ ion irradiation for bare and hBN covered Ir(111) is represented by the solid and dashed dark blue lines, respectively. Again consistent with previous results in Chapter 6 several desorption peaks are observed for 3 keV Xe^+ irradiation of Ir(111). Two peaks at 745 K and 880 K as well as two additional peaks at 1150 K and 1250 K. After covering the Ir with hBN the desorption trace post 3 keV Xe^+ irradiation is almost unchanged for temperatures below 1000 K. Only a slight smearing out of the peaks is observed. However, the desorption peak at 1150 K is strongly reduced and more intensity is shifted to higher desorption temperatures.

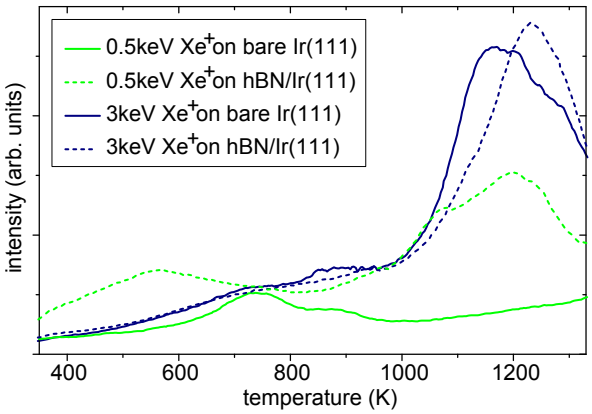

Figure 9.2: Temperature programmed desorption after Xe^+ irradiation. TPD of Xe (131 amu) after exposure of bare Ir(111) (solid lines) and hBN/Ir(111) (dashed lines) to 0.1 MLE 0.5 keV (green) and 3 keV (dark blue) Xe^+ at 300 K, respectively. The heating rate is 5 K/s.

From the XPS experiments above we can learn that for 0.5 keV Xe^+ room temperature irradiation more noble gas is trapped at the interface compared to the higher energetic 3 keV ions. This effect can be traced back to the deeper penetration of higher energetic ions and the surface sensitivity of XPS which makes Xe deep in the crystal undetectable. Having a look at the TPD traces it becomes apparent, that in fact more Xe is in the sample after 3 keV irradiation, actually independent of the presence of a hBN layer. The desorption peak below 750 K for 0.5 keV Xe tells us that Xe in a different chemical environment is present in the sample. We assume that it represents the Xe trapped at the hBN/Ir(111) interface as revealed by XPS. It is able to escape to vacuum from underneath hBN before the diffusion of the Xe trapped in the substrate is activated at temperatures of 750 K and 880 K. Desorption above 1000 K (not present for the bare sample) shows that some Xe is trapped in a more stable environment underneath the hBN cover.

Considering the significant amount of Xe streaming to the hBN/Ir(111) interface from its trapping sites within the Ir bulk after 3 keV Xe^+ irradiation and annealing the simultaneous decrease in Xe intensity in XPS in conjunction with the thermal desorption trace that is almost similar to the case of bare Ir(111), Xe retention seems less efficient compared to 0.5 keV. However, the strong Xe intensities in XPS at room temperature prove significant trapping of Xe upon impact for both energies, but also significant loss at elevated temperatures. Yet in both cases Xe remains underneath hBN after annealing to 1300 K.

Finally, we want to have a look at the damage patterns and their annealing by means of STM. First, an overview of the damage and its annealing after 0.5 keV Xe^+ irradiation is provided in Figure 9.3 including two additional annealing steps, one at an intermediate temperature of 800 K and one at a higher temperature of 1500 K. For reference, the inset in Figure 9.3(a) displays the morphology of the pristine hBN/Ir(111) after growth. The moiré superstructure arising from the (11.7×11.7) hBN unit cells on (10.7×10.7) Ir(111) unit cells with a periodicity of 2.91 nm [48] can be recognized by the hill-and-valley structure imaged in the inverted contrast with the chemisorbed valleys displayed as bright dots in the dark sea of physisorbed hills. After exposure to 0.1 MLE 0.5 keV Xe^+ ions at normal incidence the surface imaged by STM exhibits a rough morphology with an average corrugation of approximately 0.4 nm. Based on previous results for the irradiation of Gr/Ir(111) we can attribute the protrusions to Ir adatoms formed by the violent ion impact and trapped noble gas. The latter we already confirmed by XPS. The dark depressions are vacancies within the hBN sheet due to the loss of B and N atoms in course of sputtering. In view of the high ion fluence the structural integrity of the hBN layer must be assumed to be destroyed in large parts. After annealing the sample to 800 K the hBN forms again a well defined base level with vacancy clusters pinned to the moiré cells, best visible in the lower part of the STM topograph and in the inset. Since unambiguous identification of vacancies in hBN is facile, stronger evidence will be presented below. Following our results on Gr/Ir(111) irradiation the approximately (0.1 - 0.2) nm high flat protrusions are interpreted as Xe filled blisters at the interface of hBN and Ir(111). The surface damage of Ir(111) is restored by annihilation of adatoms and surface vacancies [218]. Further annealing to 1000 K and to 1300 K leads to a ripening of the Xe filled flat blisters and a reappearance of the moiré superstructure. The vacancy cluster begin to form extended vacancy island at 1300 K. Finally, after annealing to 1500 K most vacancy clusters are agglomerated into vacancy islands. However, the number density of Xe blisters seems to decrease without a significant increase in size, which is in accordance with a decrease of Xe signal in XPS and desorption in TPD.

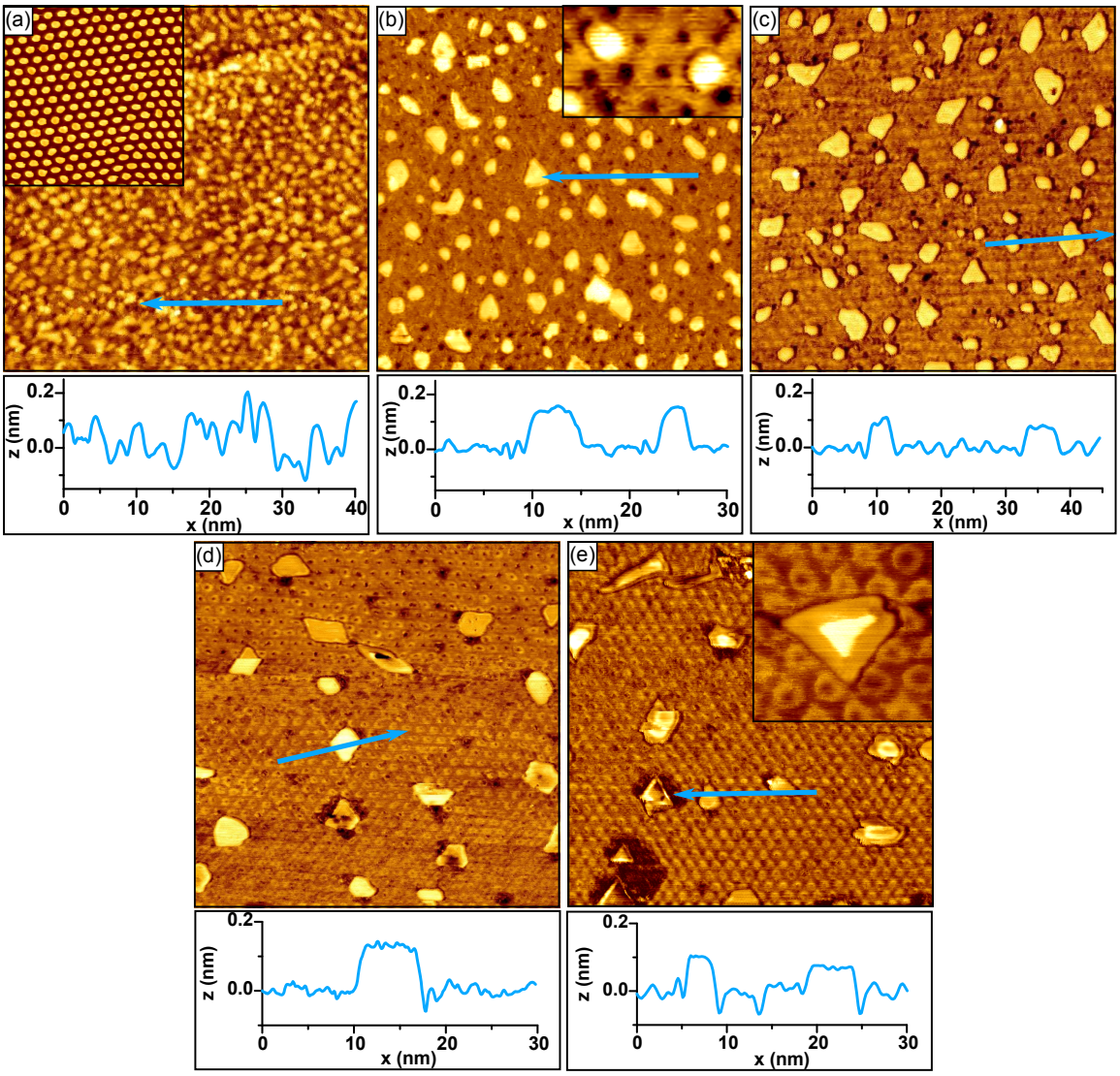

Figure 9.3: Sample morphology after 0.5 keV Xe^+ irradiation and annealing. STM topographs of hBN/Ir(111) and associated height profiles after exposure to 0.1 MLE of 0.5 keV Xe^+ (a) at 300 K, (b) annealed to 800 K, (c) 1000 K, (d) 1300 K, and (e) 1500 K. The height profiles below the topographs are taken along the indicated lines. Insets: (a) Pristine hBN/Ir(111). (b) Zoom of hexagonally arranged vacancy clusters. (e) Flat Xe filled blister exhibiting two height levels. Image sizes are 90 nm × 90 nm, inset sizes are (a) 45 nm × 45 nm, (b) 14.5 nm × 9.0 nm, and (e) 13.5 nm × 13.5 nm.

An interesting feature is observed after annealing to 1500 K: Some of the blisters display a second level while remaining flat on both levels as highlighted in the inset of 9.3(e). This is presumably due to a second layer of stacked Xe [216].

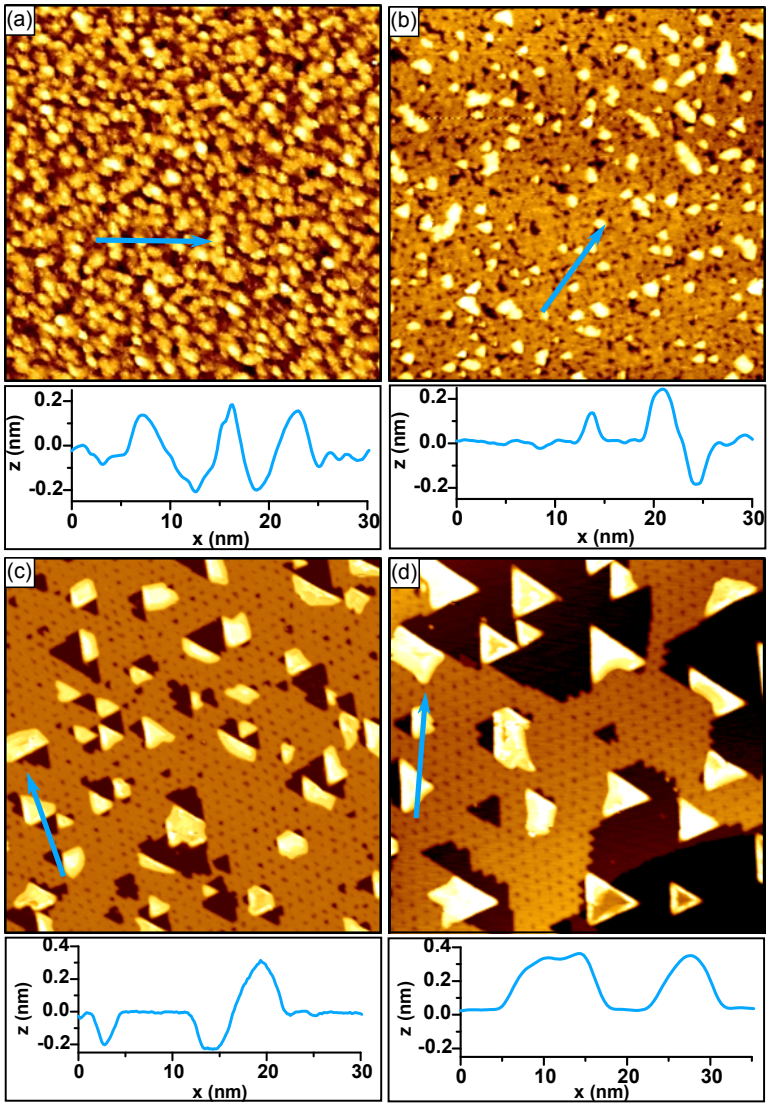

Figure 9.4: Sample morphology after 3 keV Xe^+ irradiation and annealing. STM topographs of hBN/Ir(111) and associated height profiles after exposure to 0.1 MLE of 3 keV Xe^+ (a) at 300 K, (b) annealed to 1000 K, (c) 1300 K, and (d) 1500 K. The height profiles below the topographs are taken along the lines indicated. Image sizes are 90 nm × 90 nm.

Turning to the 3 keV Xe^+ irradiation experiment the overall assessment is unchanged as visible in Figure 9.4. At room temperature the even more violent impact of the higher energetic ions causes a stronger destruction of the hBN layer and increased Ir adatom production underneath hBN. Upon annealing to 1000 K Xe filled blisters form that grow in size due to ripening at 1300 K and finally at 1500 K. The blisters at 1300 K and 1500 K

tend to from triangular shapes and also exhibit a second level as discussed above. The apparent height are comparable to the 0.5 keV case. The vacancies first display a bimodal distribution of vacancy clusters and islands at 1300 K and eventually agglomerate into extended vacancy islands at 1500 K. A detailed discussion on the triangular shape of the blisters and vacancy islands can be found in Section 9.2.

We interpret the evolution as follows: Upon annealing the surface damage of the Ir(111) anneals already at the lowest annealing temperature leaving Xe behind at the interface as the only species. Upon further annealing the smaller Xe filled blisters agglomerate and are under extreme pressure due to the strong adhesion of the hBN layer to the Ir(111) substrate. This causes in some cases the formation of a second Xe layer. The vacancy clusters on the other hand are pinned to the moiré unit cell at the location of the valleys. Even tough identification of vacancy clusters is ambiguous, due to the strong variation of valley depth depending on tip condition, the situation is clear, *e.g.*, in Figure 9.4(c) (compare profile). The pinning of the vacancy clusters to the moiré up to temperatures of 1300 K is remarkable. It reveals that the agglomeration of vacancies in the valley region exhibits an deep energetic minimum that cannot be overcome at 1300 K. This feature can be attributed to the fact that within the valley the hBN layer is chemisorbed and therefore in close proximity to the Ir surface whereas in the hill areas the hBN is physisorbed and thus further away (compare 2.1Å to 3.6Å above the Ir suface, respectively) [48]. In consequence bond formation from the hBN towards the substrate is facilitated within the valley region. A similar vacancy cluster at a hill position would remain with unsaturated bonds due to the great distance. Similar pinning of vacancy clusters to certain moiré sites was already observed for *e.g.* He^+ irradiation of Gr/Ir(111) in Chapter IV and for Xe^+ irradiation of Gr/Ir(111) in [20]. Nevertheless, these configurations were only stable up to approximately 1000 K and showed a preferential binding in two moiré sites.

9.2 Edge Termination

In the previous section a tendency of the Xe filled blisters as well as of the vacancy islands to form triangular shapes was observed. In this section we will link this observation to the edge termination of boron nitride. To this end, Figure 9.5(a) displays a large scale STM topograph of hBN/Ir(111) after 3 keV room temperature irradiation and subsequent annealing to 1300 K.

It is apparent that most blisters and vacancy islands are of triangular shape. For better visibility in Figure 9.5(b) blisters are colored red and vacancy islands green, respectively.

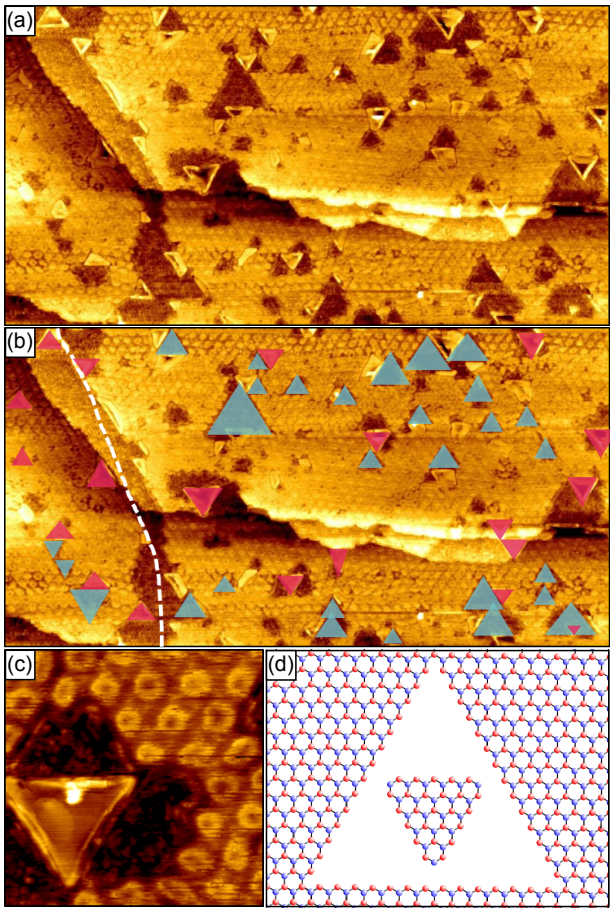

Figure 9.5: Edge termination of hexagonal boron nitride. (a) Large scale STM topograph of h-BN/Ir(111) after 3 keV Xe^+ irradiation and subsequent annealing to 1300 K. Vancancy islands and Xe filled blisters exhibit triangular shapes which are rotated by 180° with respect to each other as highlighted in (b). At the left margin of the image a former grain boundary separates two different domains of hBN/Ir(111) that are rotated by 180° [white dashed line in (b)]. Image sizes are 160 nm × 85 nm. (c) Higher resolution STM topograph of a down-pointing triangular blister within an up-pointing hBN hole. Image size is 15 nm × 15 nm. (d) Atomic model highlighting the identical edge termination of blisters and vacancy islands.

At the left margin of the topograph a dark band running from top to bottom is present [white dashed line in 9.5(b)]. It can be identified as a vacancy island band separating two hBN domains rotated by 180° with respect to each other. It is interpreted as a former rotational domain boundary. Although its atomistic structure is not known it certainly represents a high energy defect [52]. Therefore it acts as a sink for migrating vacancies. Revisiting the colored triangles it becomes apparent that after crossing the vacancy band the blisters and vacancy islands reverse directions and within one domain blisters and vacancy islands exhibit opposite orientation. Together with the observation that the sides of the triangles follow the dense packed direction if compared to the moiré superstructure one can conclude that all edges are of zig-zag type and of common chemical species [48]. Further, the close proximity of blisters and vacancy islands suggests a correlation. The zoom in Figure 9.5(b) highlights this phenomenon. A blister in perfect triangular shape is situated in the middle of a vacancy islands completely detached from the hBN sheet. Following the above observation and the DFT calculations by Farwick zum Hagen *et al.* [48], who identified that zig-zag type hBN edges on Ir(111) are boron terminated with N termination at the corners, we can draw the atomic model visible in Figure 9.5(d). It visualizes the requirement of triangle rotation for vacancy islands and blisters, respectively. Since the triangular shapes are driven by step edge energy minimization the most perfect triangular shapes are found for blisters completely decoupled from the hBN.

9.3 Nano-Crystals

With a suitable tip, a superstructure on top of the flat Xe filled blisters can be identified. Figure 9.6(a) displays an STM topograph after 0.5 keV Xe^+ irradiation followed by annealing to 1000 K. The same area is shown in Figure 9.6(b) with the contrast adjusted to highlight the periodic structure on top of the Xe filled blisters. The periodicity of the superstructure was determined by measuring along the three high symmetry directions and amounts to (4.17 ± 0.08) Å. This compares nicely to the nearest neighbor distance of solid Xe in the fcc crystal structure which is 4.38 Å [219]. Since Xe can only be found in the solid state for GPa pressures [220] or very low temperatures (162 K) [221] we can assume that the Xe in the here observed blisters is at extremely high pressures in the GPa range since it is imaged at room temperature. The slightly smaller value for the nearest neighbor distance even implies gentle compression.

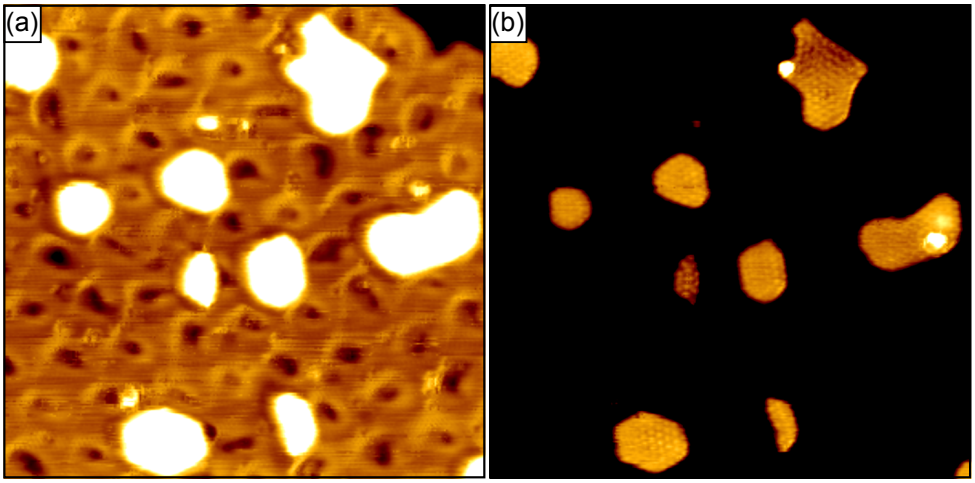

Figure 9.6: Xe nano-crystals. (a) STM topograph of h-BN/Ir(111) after 0.5 keV Xe^+ irradiation and subsequent annealing to 1000 K. (b) Same area as in (a) but with the contrast adjusted to highlight the superstructure on top of the Xe filled blisters. Image sizes are 27 nm × 27 nm.

9.4 Nano-Crystal Formation by Preimplantation

Similar to the case of Gr/Ir(111) we envision to from Xe nano-crystals at the interface of a perfect hBN sheet on Ir(111), *i.e.*, without damage due to the penetrating ions. To achieve this we use the technique introduced in Chapter IV.5 which is based on the preimplantation of noble gas into the substrate. This is achieved by successive ion exposure of the bare Ir(111) with 0.2 MLE Xe^+ ions at energies varying from 5 keV to 2 keV at room temperature to ensure a broad Xe depth distribution prior to hBN growth. Subsequently the surface damage is annealed by heating the Ir crystal to the hBN growth temperature. The sample after hBN growth at 1200 K is displayed in Figure 9.7(a). Besides the moiré superstructure proving a closed hBN layer circular submonoatomic high bulges that can be assigned to subsurface Xe blisters within the Ir bulk material are visible [165]. At this stage no Xe filled blisters are detected. The STM topograph in Figure 9.7(b) shows the same sample after additional annealing to 1500 K. The circular submonoatomic bulges disappear and instead Xe nanocrystals at the interface form due to the release of Xe from its capture sites within the crystal streaming to the Ir surface and eventually becoming trapped at the hBN/Ir(111) interface. This results proves that the concept of preimplantation and gas release underneath a perfect 2D layer also holds for hBN/Ir(111), so nano-crystal formation separated from 2D layer damage is possible.

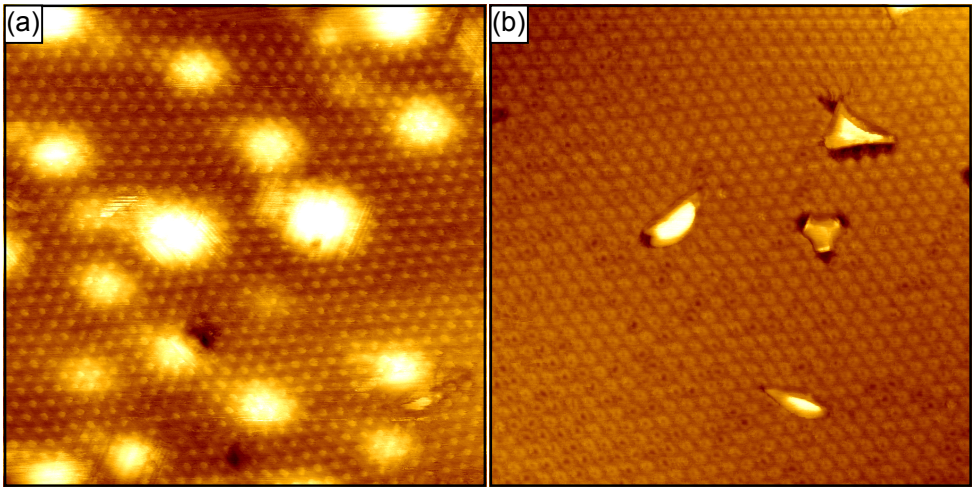

Figure 9.7: Xenon nano-crystals by preimplantation. (a) STM topograph of h-BN/Ir(111) exhibiting circular bulges arising from subsurface Xe implanted into the Ir bulk by 0.2 MLE 5 keV, 4 keV, 3 keV, and 2 keV Xe^+ irradiation at room temperature prior to hBN growth at 1200 K. (b) Same as (a) with subsequent annealing to 1500 K. Image sizes are 90 nm × 90 nm.

9.5 Conclusions

In conclusion, the experiments in this chapter show that Xe trapping and blister formation is also relevant for hBN on Ir(111) making a general validity of these phenomena for irradiation of supported 2D materials likely. The vacancy clusters created by B and N atom sputtering preferentially accumulate in the valley area of the moiré superstructure up to temperatures of 1300 K. This finding is in stark contradiction with the proposed *can opener effect* [155] which necessitates the agglomeration of vacancies at the rim of the valley region. The explanation within this theory that bright protrusions represent *cut-outs* of the valley area flipped over to lie on top of the hBN sheet can rather be explained by noble gas blisters within the hBN layer and the *cut-outs* as agglomerates of vacancies. The hBN layer which is in a quasi amorphous state after irradiation restores itself upon annealing. This is a rather surprising finding due to the hetero-atomic character of hBN and will be further discusses in Chapter 10.

The samples annealed to 1300 K or 1500 K display triangular shaped vacancy islands and blisters. From their shape and orientation we can conclude that the edges are of zig-zag type and by comparison with literature [48] determined to be B-terminated. By imaging the Xe through the hBN lid we found the first experimental evidence for extremely high pressures in the GPa range within the blisters. Finally, we showed that Xe nano-crystals

can be formed at the hBN/Ir(111) interface via the established preimplantation method introduced in Chapter 6.5.

CHAPTER 10

Amorphization and Recrystallization

This chapter contains contributions from P. Valerius, U. A. Schröder, A. J. Martìnez-Galera, M. A. Arman, J. Knudsen, and T. Michely. I was responsible for the design of the experiments, was involved in all XPS measurements, and analyzed the XPS data. The STM and LEED experiments as well as analysis on Gr/Ir(111) were carried out by myself whereas the STM and LEED measurements and analyses concerning hBN/Ir(111) were done by P. Valerius under the joint supervision of T. Michely and me. Some of the results within this chapter are prepared for publication in [216].

Gr's mechanical and electronic properties strongly rely on the perfection of it's honeycomb lattice. Already small deviations from perfection introduced during the CVD growth process represent obstacles to some envisioned applications [98]. On the other side, the intentional introduction of defects, *e.g.*, by particle irradiation, can be used beneficially to modify Gr's properties [17, 20, 222–224]. By now, most detailed knowledge on defect structures in 2D materials is obtained from TEM studies. Kotakoski *et al.* demonstrate the formation of a 2D coherent amorphous membrane composed of sp^2-hybridized C atoms using a Ga^+ focused ion beam [224]. They suggest the creation of an all-carbon heterostructure by patterning of Gr into amorphous areas within the otherwise pristine hexagonal lattice exhibiting different chemical and electrical properties [224]. Other studies demonstrate that freestanding Gr can be amorphized by electron irradiation with energies just above the threshold for atom displacement [225, 226]. An interesting application of ion irradiation of freestanding Gr is the ironing-out of wrinkles in the Gr sheet. Pan *et al.* show by a combined STEM and Raman spectroscopy study the He^+

irradiation induced flattening and in-plane contraction of a Gr sheet without complete loss of crystallinity [227]. Only for very high fluences the long range order is lost.

Surprisingly, only few microscopic studies exist about the reverse evolution from an amorphous 2D carbon membrane towards a perfect 2D Gr sheet, *i.e.*, the recrystallization of Gr. In a recent study combining TEM measurements and atomistic simulations Yoon *et al.* investigate the irradiation of freestanding Gr with noble gas ions and the subsequent annealing [228]. Zan *et al.* also used TEM to study the reknitting of etch holes in Gr [229]. In both studies the reconstruction of the generated defects into more stable structures, forming nanopores and amorphized regions is observed. Further, Chen *et al.* studied defects induced by an argon plasma and their annealing due to Gr's self-healing ability [230].

However, all electron microscopy studies introduce damage to Gr by bond rotation and atom ejection in course of electron impacts as well as C contamination by beam-aided decomposition of hydrocarbons in the TEM column. Further, all the above mentioned studies explored the amorphization and healing of a freestanding Gr sheets. But for most applications Gr will rest on a substrate. Nevertheless, only little is known about the amorphization and recrystallization of supported Gr. In the 1980's the graphitization of thin carbon films was extensively studied and observed to take place in a temperature range of 2000-3000 °C [231]. Zhou *et al.* studied the structural and electronic evolution of Gr on Silicon during Ga irradiation and found a transition from pristine Gr to amorphous carbon accompanied by changes in electrical properties [232]. However, the recrystallization was not explored.

To this end several experimental as well as theoretical works addressed the reconstruction of defects introduced by irradiation or during Gr growth through heat treatment [20, 156, 233, 234].

The amorphization and recrystallization of hBN on the other side is even less studied. Kotakoski *et al.* studied the electron knock-on damage theoretically and by TEM experiments [109]. However, amorphization of the 2D sheet is not observed. In case of supported hBN Cun *et al.* report on a self-healing mechanism of hBN/Rh(111) upon annealing after irradiation induced damaging [155].

Still, a thorough analysis on the evolution of amorphization and self-healing of supported Gr and hBN, taking a look also at the 2D-substrate interaction, is not available. In this chapter we present a comprehensive study on the ion induced amorphization and subsequent recrystallization by heat treatment of Gr on Ir(111) as well as hBN on Ir(111) studied by LEED, STM, and XPS. Especially, the interaction with the substrate is high-

lighted. Further, we show how this effect can be used to iron-out wrinkles in the Gr sheet introduced during CVD growth.

Figure 10.1(a) shows a LEED pattern (top) and the corresponding real space STM topograph (bottom) of pristine Gr/Ir(111). The diffraction pattern displays the reciprocal space and hence reflects the six-fold symmetry of Gr/Ir(111). The inner spot (yellow in inset) stems from the periodicity of the Ir lattice whereas the outer spot (orange in inset) represents the periodicity of the Gr lattice. The spots are surrounded by additional satellite reflexes originating from the moiré superstructure and higher orders thereof. The STM topograph shows the typical moiré superstructure with a pitch of 2.53 nm. The sharp LEED spots combined with the STM topograph demonstrate the high perfection of the as grown Gr film.

The LEED and STM results after 0.1 MLE 0.5 keV Xe^+ irradiation at room temperature are depicted in Figure 10.1(b). Virtually no reflexes are observed at an electron energy of $E = 68$ eV. Only at slightly higher or lower electron energies the Ir spots become faintly visible (data not shown). The STM topograph reveals a rough surface structure consisting of small scale protrusions and dark spots corresponding to noble gas and Ir adatoms at the interface as well as vacancies within Gr, respectively, according to the discussion in Chapter 6. No trace of a moiré superstructure is found. This indicates that after irradiation the Gr layer is in a disordered or amorphous state. Due to the high defect density in the Gr layer and the random height distribution of the C atoms at the surface the LEED pattern gives rise to a diffuse background.

By annealing the sample to 800 K the Ir and C reflexes reappear accompanied by very weak moiré spots as visible in Figure 10.1(c). By further stepwise annealing to 1000 K and 1300 K the spot intensity increases until finally at 1500 K the initial LEED pattern is restored [compare Figures 10.1(d)-(f)]. The corresponding STM annealing series was already discussed in Chapter 6 and is only briefly revisited here. After the first annealing step to 800 K the small scale protrusions disappear and larger bulges that can be attributed to Xe filled protrusions within the Gr appear. The Gr lattice exhibits a dense distribution of topological as well as vacancy-type defects. Upon further annealing the bulges coarsen and the vacancy defects accumulate and eventually form extended vacancy islands at 1300 K. At the same temperature the Gr lattice itself exhibits a pronounced moiré superstructure in accordance with the LEED pattern. Thus from LEED and STM analysis it becomes apparent that a completely amorphized Gr film can be restored by annealing just above its growth temperature. This is in line with similar studies on the Gr/Ru(0001) system [156].

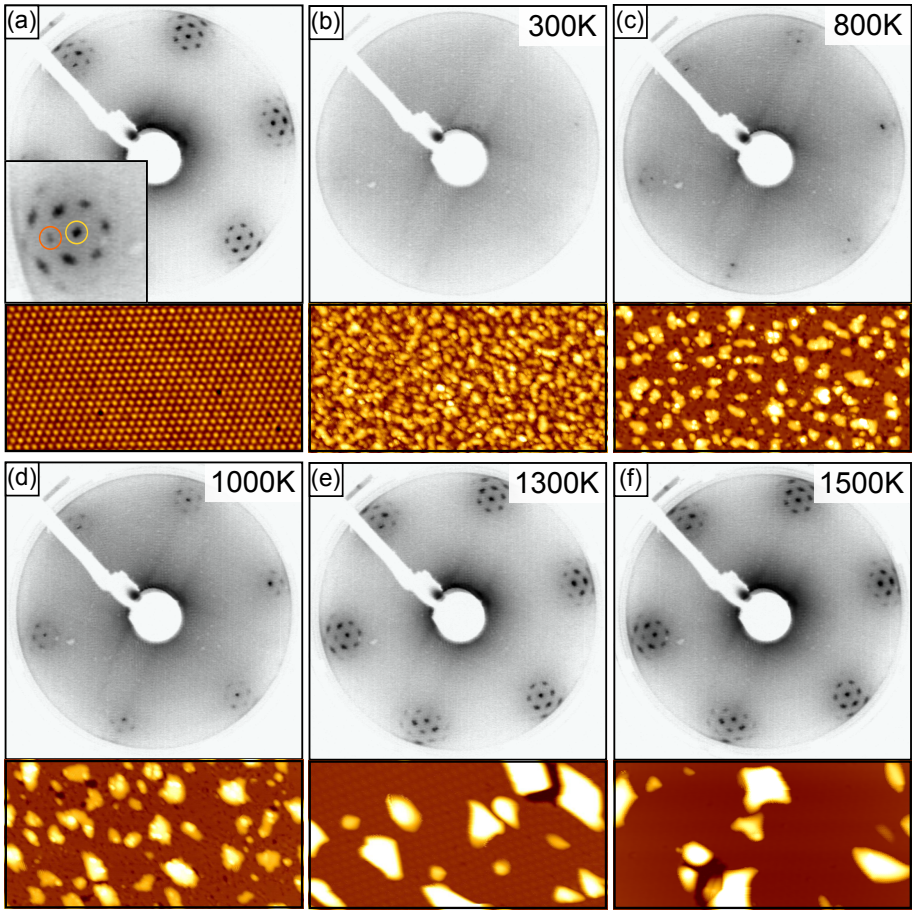

Figure 10.1: Recrystallization of graphene on Ir(111) after 0.5 keV Xe^+ irradiation followed by LEED and STM. LEED images (top) and STM topographs (bottom) of (a) pristine Gr/Ir(111), (b) after 0.1 MLE 0.5 keV Xe^+ ion irradiation at room temperature, (c) subsequently annealed to 800 K (300 s), (d) 1000 K (300 s), (e) 1300 K (120 s), and (f) flash annealed to 1500 K. All LEED images are taken at an electron energy of $E = 68$ eV. STM image size is always 90 nm × 45 nm.

To get further insight into the chemical nature of the amorphous carbon film and to learn about its interaction with the Ir(111) substrate we conducted XPS measurements. Figure 10.2 displays from bottom to top the C 1s as well as the Ir 4f region of pristine Gr/Ir(111), the same sample after 0.1 MLE 0.5 keV Xe^+ irradiation at room temperature, and subsequently annealed to increasing temperatures as indicated.

Prior to irradiation the pristine C 1s spectrum shows a sharp peak at a BE of 281.1 eV consistent with literature [80]. After irradiation the spectrum has broadened and the main peak position has shifted to lower BEs. Upon annealing the sample to 800 K the C 1s spectrum remains almost unchanged. Further annealing results in a narrowing of the spectrum until it almost restores its initial shape at 1300 K. The main peak position shows first a slightly negative and then a slightly positive CLS.

The broadening of the C 1s spectrum after irradiation reflects the presence of many inequivalent C species. Intensity to higher BEs can be associated with the formation of sp^3 hybrid C forms [235–238] whereas intensity to lower BE with the formation of a carbidic species where the C forms chemical bonds or completely adsorbs to the metal [235, 239]. The latter indicates a strong C-Ir interaction as will be proven below. However, the diversity of C species is vast and a categorization ambiguous. The narrowing of the C 1s spectrum upon annealing is indicative for Gr formation and is in line with the reappearance of the moiré spots in the LEED diffraction pattern which implies long range ordering and smoothening of the surface. The remaining broadening and slight shift to higher binding energies can be explained by two effects: First, as visible from the STM topograph vacancy islands due to C sputtering emerge. At the edges the Gr will chemically bind towards the Ir as shown by DFT in Chapter 6 inducing charge transfer to Gr, *i.e.*, a CLS explaining some of the broadening. On the other hand, the areas intercalated by Xe will be decoupled from the substrate and their BE moves closer to the position of freestanding Gr or graphite, respectively, which is located towards higher BE with respect to Gr/Ir(111) which is slightly doped [72, 240].

To further analyze the interaction of the Gr with the substrate we now turn to the discussion of the Ir 4f spectra. The pristine Ir 4f spectrum exhibits two peaks, the bulk peak (Ir_b) at a BE of 60.83 eV and the surface peak (Ir_s) shifted by -0.52 eV to 60.31 eV due to the lower coordination of the surface atoms with respect to the bulk atoms. After irradiation the surface peak has virtually vanished concomitant with a broadening of the bulk peak including additional spectral weight towards lower binding energies. Upon annealing the surface peak recovers until at 1300 K it has restored itself except for some remaining intensity in between the surface and bulk peak. Comparing the evolution of

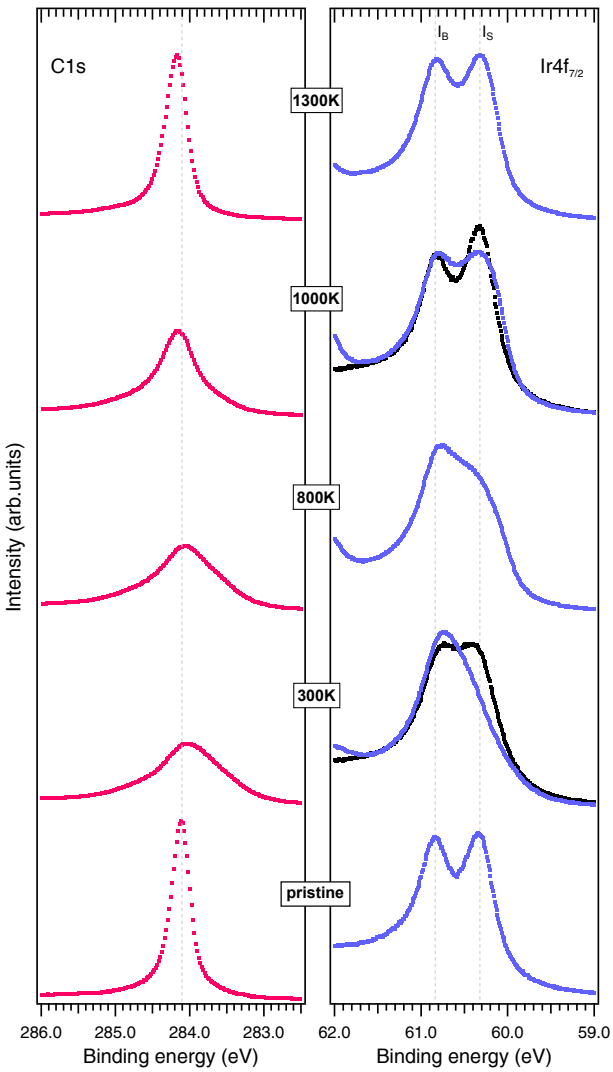

Figure 10.2: Recrystallization of graphene on Ir(111) after 0.5 keV Xe^+ irradiation followed by XPS. XP spectra of the C 1s (left) and Ir 4f (right) region of Gr/Ir(111) exposed to 0.1 MLE Xe ion irradiation at 300 K and subsequently annealed to 800 K (300 s), 1000 K (300 s), and 1300 K (120 s), respectively. The spectrum of pristine Gr/Ir(111) prior to ion irradiation is shown at the bottom of each graph. The black data in the Ir 4f region at 300 K and 1000 K correspond to ion irradiation and annealing of bare Ir(111) with the same parameters for comparison.

the Ir 4f spectrum to a bare Ir(111) sample without Gr irradiated with the same ion parameters at room temperature and subsequently annealed to 1000 K (black spectra in Figure 10.6) it becomes apparent that after irradiation the surface peak decreases, but to a lesser extent than with a Gr cover. Further, the surface component completely restores itself after annealing to 1000 K. Note that in the case of bare Ir the surface peak is slightly higher than for Gr covered Ir(111). This is explained by a reduction of the surface peak in presence of Gr, due to slight interaction.

From the comparison with the irradiated bare Ir(111) surface it is apparent that the disorder at the surface cannot account for the reduced intensity of the Ir 4f surface component. Hence, the assumption of a strong interaction of Gr with Ir is corroborated by the strong reduction of the Ir surface peak at room temperature. According to literature the increased intensity in between the position of the bulk and surface peak is due to Ir surface atoms strongly interacting with Gr [241]. Annealing the sample to 800 K results in a slight recovery of the If 4f surface peak, however, we saw that the C 1s spectra is almost unchanged. So the recovery of the Ir surface peak at this stage might be traced back to the healing of Ir surface damage which is also reflected by the reappearance of the Ir diffraction peaks in LEED. After further annealing the Ir surface peak continues to recover which is in perfect agreement with the reappearance of the sharp C 1s peak and the reduction of the sp^3 and carbidic component.

Summarizing these findings, we found that upon high dose 0.5 keV Xe^+ irradiation the Gr lattice is highly defective and corrugated. The amorphous film consists of many different C species ranging from sp^3-like over sp^2 to carbidic C that strongly interacts with its substrate. From the data it is quite clear that in the amorphous state chemical binding between C atoms and nearly all Ir surface atoms takes place. Upon annealing the Gr film recovers itself to perfection until only vacancy holes due to sputtering and blisters due to Xe intercalation remain. The strong interaction with the substrate might be the key for the complete recovery of the layer as it might catalyze the lattice reconstruction as suggested by Jacobson *et al.* as well as Karoui *et al.* for Gr/Ni(111) [233, 234].

The room temperature amorphization by higher energetic 3 keV Xe^+ ion irradiation with the same fluence of 0.1 MLE and subsequent recrystallization of Gr/Ir(111) followed by LEED, STM, and XPS is presented in Figures 10.3 and 10.4. The overall appearance after irradiation and the thermal evolution strongly resembles the case of 0.5 keV Xe^+ irradiation so that here the discussion will be brief, focusing on the differences.

After irradiation the LEED image shows no reflexes and the STM topograph shows a rough surface [see Figure 10.3(a)]. After annealing to 1000 K in contrast to the low energy

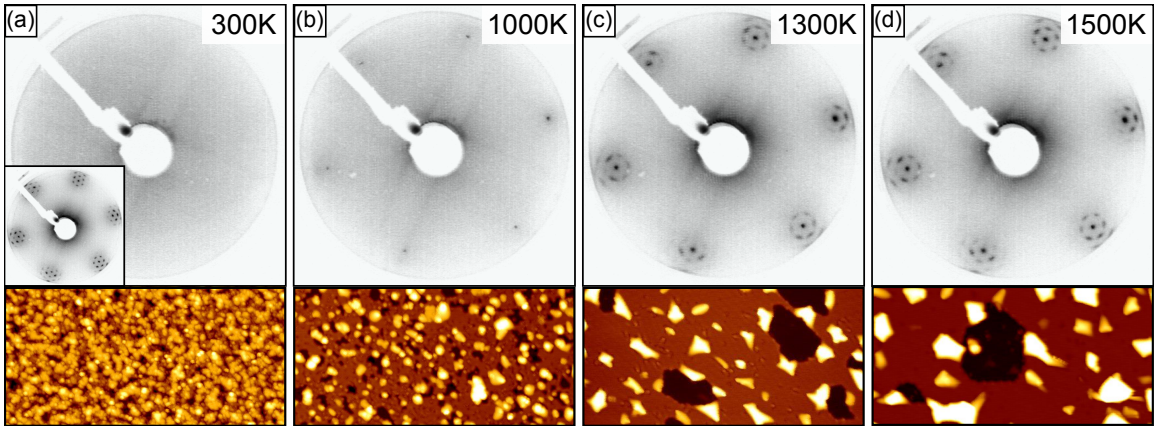

Figure 10.3: Recrystallization of graphene on Ir(111) after 3 keV Xe^+ irradiation followed by LEED and STM. LEED images (top) and STM topographs (bottom) of Gr/Ir(111) (a) after 0.1 MLE 3 keV Xe^+ ion irradiation at room temperature, (b) subsequently annealed to 1000 K (300 s), (c) 1300 K (120 s), and (d) flash annealed to 1500 K. All LEED images are taken at an electron energy of $E = 68$ eV. STM image size is always 90 nm × 45 nm. After irradiation no LEED reflexes are visible and the STM topograph shows a rough surface. Subsequent annealing results in reappearance and sharpening of the LEED reflexes and ripening of Xe filled blisters as well as recrystallization of the Gr layer as visible in STM.

irradiation the LEED pattern does not exhibit any moiré reflexes and even the C reflexes are faint [see Figure 10.3(b)]. This can be explained by comparing the corresponding STM topographs. For 0.5 keV in between the Xe filled blisters the Gr appeared rather homogeneous. Nevertheless, the corresponding topograph after the high energy irradiation shows a much denser distribution of small scale blisters as well as smaller vacancy islands and clusters. Only after annealing to 1300 K the C and moiré reflexes become visible even though the latter are slightly elongated indicating remaining defects [see Figure 10.3(c)]. Further annealing to 1500 K [Figure 10.3(d)] shows sharpened reflexes and a similar real space image of perfect Gr as for 0.5 keV irradiation. However, large vacancy islands have formed that might account for the weakening of the higher order moiré reflexes.

The increased damage and corrugation of the Gr at room temperature by the high energy impacts is also reflected by an even broader otherwise equivalent C 1s spectrum. As expected from the LEED and STM analysis the evolution of the C 1s and Ir 4f spectra is similar to the spectra discussed above. Though the Ir surface peak after the highest annealing temperature exhibits an increased intensity which we attribute to the reduced Gr coverage due to C sputtering as visible in the STM. For reference on the right side of

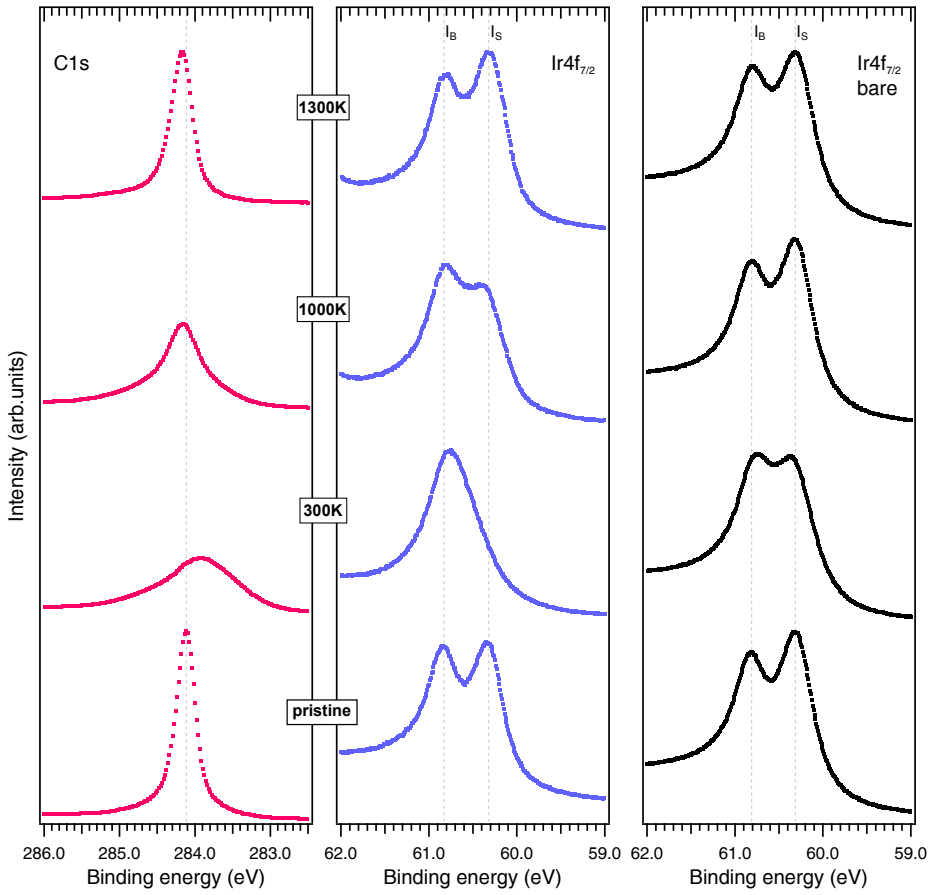

Figure 10.4: Recrystallization of graphene on Ir(111) after 3 keV Xe^+ irradiation followed by XPS. XP spectra of the C 1s (left) and Ir 4f (middle) region of Gr/Ir(111) and Ir 4f region of bare Ir(111) (right) exposed to 0.1 MLE 3 keV Xe^+ ion irradiation at 300 K and subsequently annealed to 1000 K (300 s) and 1300 K (120 s), respectively. The spectrum of pristine Gr/Ir(111) prior to ion irradiation is shown at the bottom of each graph.

Figure 10.4 the annealing series of irradiation of bare Ir(111) with 0.1 MLE 3 keV Xe^+ is shown. Its room temperature appearance and annealing is similar to the 0.5 keV case.

The latter experiments of 3 keV Xe^+ irradiation of Gr/Ir(111) shows that the annealing behavior of destructed Gr does not strongly depend on the degree of damage since after annealing both samples showed that the remaining Gr can be restored to perfection. The self-repair, even after large ion doses, can be explained by the low activation energy needed for vacancy migration in Gr/Ir(111) [20]. The integrity of Gr is rather limited by the fact that an increased ion energy or dose will result in higher sputtering and with this erosion of the 2D material. However, this problem could be overcome by supplying additional C during annealing.

Next, we want to turn to a 2D material rather unexplored with respect to its destruction and self-repair. Therefore, we repeat our irradiation experiments with hBN on Ir(111). The self-repair is expected to be suppressed due to the hetero-atomic character of hBN. DFT calculations have shown that vacancy migration in hBN is in need of homo-elemental N-N or B-B bonds which are energetically costly compared to C-C bonds. For freestanding hBN the calculated single vacancy migration barriers amount to 4.5 eV and 6 eV for N and B vacancies, respectively [100], whereas in freestanding Gr vacancy only face a migration barrier of 1.3 eV [242].

Figure 10.5(a) shows the LEED pattern as well as the STM image of the pristine hBN/Ir(111). The LEED pattern can be explained in a similar fashion as the LEED pattern for Gr/Ir(111). The brightest spot corresponds to the Ir lattice periodicity. Due to its smaller lattice constant the hBN reflex is further apart from the center. The surrounding spots can be attributed to the moiré formed by hBN with Ir(111) which is also visible in the STM topograph.

After exposing the sample to 0.5 keV Xe^+ irradiation the moiré reflexes almost completely vanish and the hBN and Ir reflexes are diminished in accordance with the vanishing of the moiré superstructure and the high defect density as well as roughening of the surface observed in the STM topograph. Upon annealing the LEED reflexes recover and finally after annealing to 1500 K are indistinguishable to the reflexes of pristine hBN/Ir(111). Nevertheless, as discussed in Chapter 9 the morphology shows Xe filled blisters that ripen upon annealing as well as vacancy type defects that accumulate in vacancy islands at 1500 K. A closer look to the remaining hBN shows that the long range order is restored and the moiré of hBN with Ir(111) reappears.

Surprisingly, the recovery is very similar to the Gr case. To see if here again the substrate plays a decisive role as a catalyst to reduce vacancy migration barriers we move to the investigation of XP spectra of the same sample after irradiation and annealing.

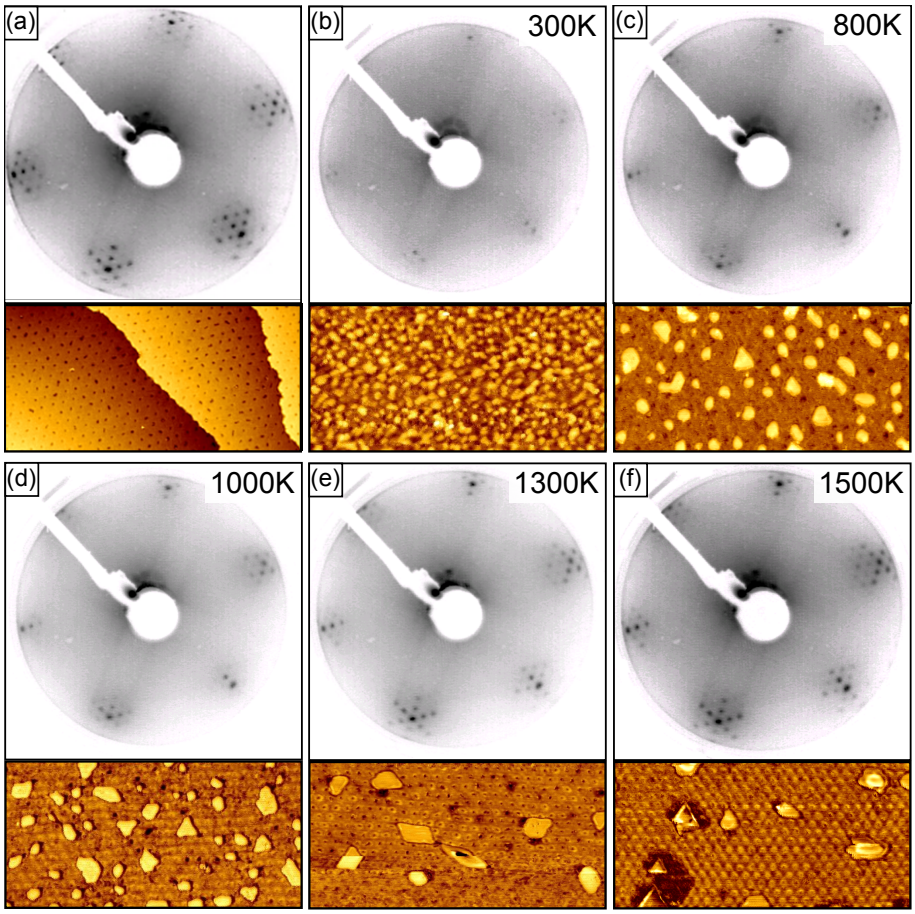

Figure 10.5: Recrystallization of hexagonal boron nitride on Ir(111) after 0.5 keV Xe^+ irradiation followed by LEED and STM. LEED images (top) and STM topographs (bottom) of (a) pristine hBN/Ir(111), (b) after 0.1 MLE 0.5 keV Xe^+ ion irradiation at room temperature, (c) subsequently annealed to 800 K (300 s), (d) 1000 K (300 s), (e) 1300 K (120 s), and (f) flash annealed to 1500 K. All LEED images are taken at an electron energy of $E = 68$ eV. STM image size is always 90 nm × 45 nm.

Figure 10.6 displays the XP spectra in the B 1s, N 1s, and Ir 4f region for pristine hBN/Ir(111) (bottom), the sample after irradiation with 0.1 MLE 0.5 keV Xe^+ ions at room temperature, and subsequently annealed to increasing temperatures as indicated. The pristine B 1s as well as the N 1s display a quite similar double peak structure. The spectra are dominated by a main component at approximately 190.0 eV (B_0) for the boron and at approximately 397.6 eV (N_0) for the nitrogen signal accompanied by a second weaker contribution shifted to higher BEs by 0.8 eV (B_1) and 1.0 eV (N_1), respectively,

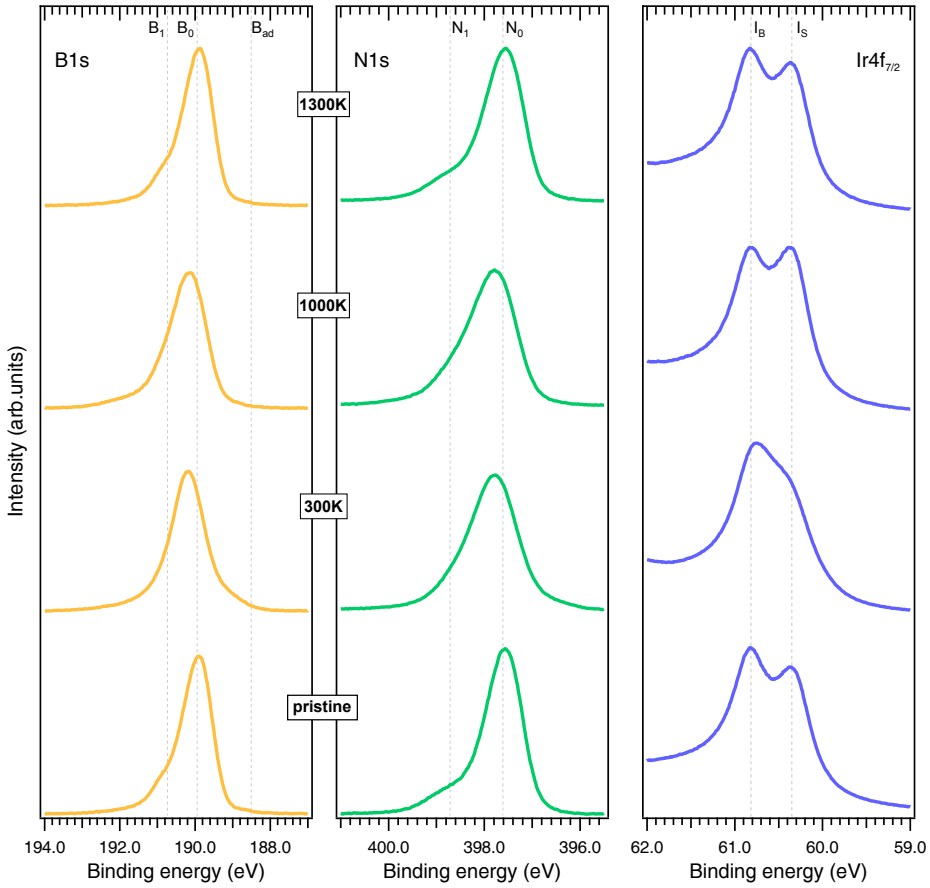

Figure 10.6: Recrystallization of hexagonal boron nitride on Ir(111) after 0.5 keV Xe^+ irradiation followed by XPS. XP spectra of the B 1s (left), N 1s (middle), and Ir 4f (right) region of hBN/Ir(111) exposed to 0.1 MLE Xe^+ ion irradiation at 300 K and subsequently annealed to 800 K (300 s), 1000 K (300 s), and 1300 K (120 s), respectively. The spectrum of pristine hBN/Ir(111) prior to ion irradiation is shown at the bottom of each graph.

consistent with data from Farwick zum Hagen *et al.* [48] and Orlando *et al.* [54]. This double peak structure is explained by a weakly bound, physisorbed (B_0, N_0) and a strongly, chemisorbed (B_1, N_1) species, respectively. Note that the very small intensity at a BE of approximately 188.6 eV in the B 1s spectrum can be attributed to atomic B adsorbed on the Ir(111) surface (B_{ad}) [54]. Further note that, due to the stronger binding of the hBN to Ir(111) the surface peak in the Ir 4f double peak is stronger reduced than for the case of Gr/Ir(111).

The B 1s as well as the N 1s spectra broaden upon ion irradiation. The B 1s spectra shows intensity to lower BE but slightly higher compared to the B adatom BE (B_{ad}). This contribution can be traced back to B species strongly interacting with the substrate but still bound in hBN consistent with the high vacancy defect density obtained from STM and the predicted B edge termination from DFT [48]. The peak shapes are almost unchanged upon annealing to 1000 K and obtain their initial shapes after further annealing to 1300 K. Since almost no hBN edges are present due to the small erosion of the layer the B_{ad} component vanishes. The reduction of the surface peak in the Ir 4f signal reveals again a quite strong interaction of the B and N species with the underlying substrate at room temperature. However, the surface peak recovers already at 1000 K. This implies less binding of B and N to Ir as compared to C. Interestingly, the Ir 4f surface peak first increases beyond its initial intensity at 1000 K and then reduces again. This can be explained by the Xe atoms intercalated at the interface decoupling the hBN layer from the Ir(111) surface. Upon annealing to higher temperatures the Xe partially escapes from underneath hBN or forms 3D structures at the expense of extended 2D platelets reducing the decoupled area.

Using higher energetic 3 keV Xe^+ ions with the same fluence of 0.1 MLE to amorphize the hBN/Ir(111) the LEED reflexes are completely gone and will not recover to perfection as visible from the annealing series presented in Figure 10.7. However, the evolution visible from the STM topographs is quite similar. But again, much more B and N atoms are sputtered by the energetic particle resulting in erosion of the 2D layer accounting for the weakening of the LEED reflexes. Otherwise, even the destruction with 3 keV Xe^+ does not inhibit the hBN to reconstruct to perfection with long range ordering as visible from the reappearance of the moiré. Only extended vacancy islands remain.

The stronger erosion of hBN by 3 keV ions also becomes apparent in the XP spectra. After irradiation the B 1s spectrum shows a strong shoulder towards lower BE close to B_{ad} that survives to a small extent even annealing to 1300 K. This finding is in line with the STM analysis revealing a higher sputtering yield for 3 keV Xe^+ ions accompanied by

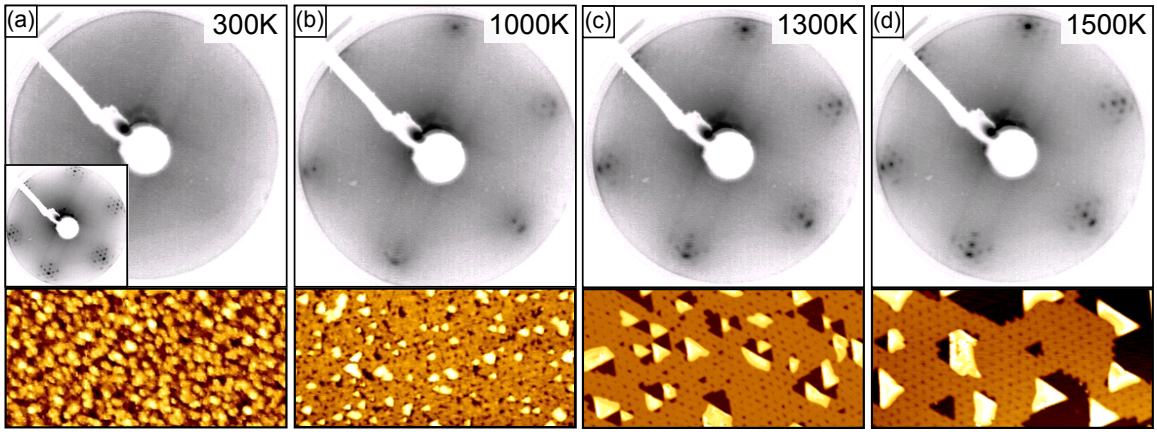

Figure 10.7: Recrystallization of hexagonal boron nitride on Ir(111) after 3 keV Xe^+ irradiation followed by LEED and STM. LEED images (top) and STM topographs (bottom) of hBN/Ir(111) (a) after 0.1 MLE 3 keV Xe^+ ion irradiation at room temperature, (b) subsequently annealed to 1000 K (300 s), (c) 1300 K (120 s), and (d) flash annealed to 1500 K. All LEED images are taken at an electron energy of $E = 68$ eV. STM image size is always 90 nm × 45 nm.

more vacancy defects that form more abundant and larger vacancy islands upon annealing. So the shoulder towards B_{ad} is a good indicator for the amount hBN edges.
Another new feature in the B 1s spectrum is the intensity towards higher BE. We speculate that this constitutes some boronoxide contamination that forms with adsorbing oxygen from the background pressure [243].
Altogether, our observations reveal an unexpectedly similar self-healing mechanism for hBN on Ir(111) which we attribute to the catalytic behavior of the substrate. Thereby, B and N atoms can saturate their dangling bonds created upon atom ejection. The substrate can also catalyze defect diffusion by enabling transition states involving substrate binding.

One way to make use of the recrystallization ability of Gr/Ir(111) after destruction via ion irradiation is the ironing-out of wrinkles introduced during the CVD growth process. As outlined in Part II, wrinkle release partly the compressive strain generated during cool down from the growth temperature [57]. Such wrinkles are frozen into the morphology and do not even disappear during transfer. A typical wrinkle structure in CVD Gr/Ir(111) is shown in the inset of Figure 10.9. To reduce the strain state of Gr we irradiated the sample with 0.03 MLE 0.3 keV He^+ ions and subsequently annealed it to 1100 K. After annealing in many locations wrinkles are consumed. In Figure 10.9 the location of such a consumed wrinkle is shown. The previous center of the starlike structure is marked by a blue dot. Along the 120° arms of the wrinkle configuration, mostly a perfect laminated

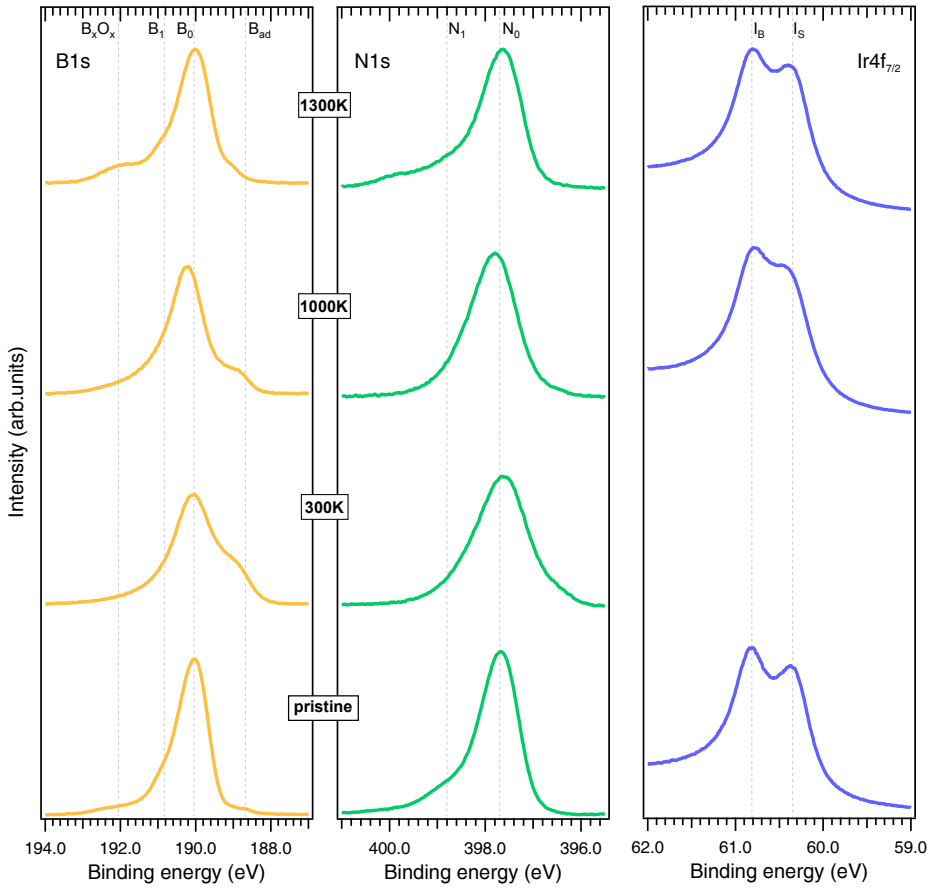

Figure 10.8: Recrystallization of hexagonal boron nitride on Ir(111) after 3 keV Xe^+ irradiation followed by XPS. XP spectra of the B 1s (left), N 1s (middle), and Ir 4f (right) region of hBN/Ir(111) exposed to 0.1 MLE Xe ion irradiation at 300 K and subsequently annealed to 1000 K (300 s) and 1300 K (120 s), respectively. The spectrum of pristine Gr/Ir(111) prior to ion irradiation is shown at the bottom of each graph.

Gr sheet is observed. Some Gr vacancy islands nucleated and also some delamination is left. However, this results documents that wrinkles can be removed by ion beam methods without destruction of the Gr lattice which relies on the recrystallization process catalyzed by the Ir substrate.

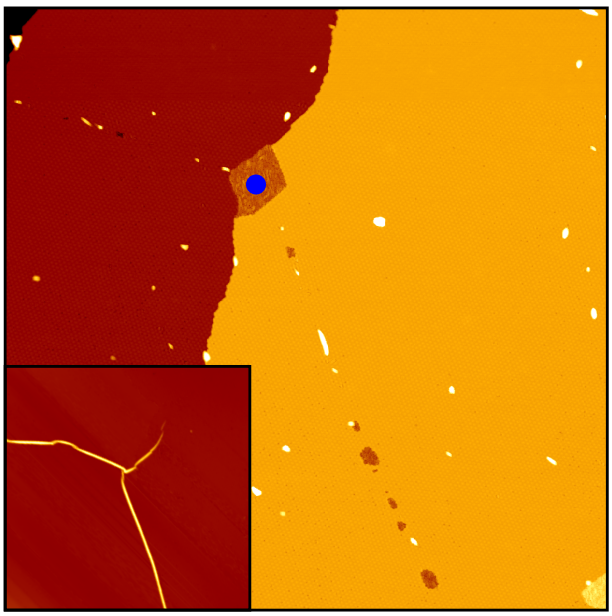

Figure 10.9: Ironing-out wrinkles in graphene on Ir(111) by ion irradiation. STM topographs of Gr/Ir(111) after 0.03 MLE 0.3 keV He^+ ion irradiation at room temperature and subsequently annealing to 1100 K. A three-armed wrinkle structure has been removed by irradiation and annealing. Compare inset for such wrinkle structure before irradiation and annealing. STM image sizes are 360 nm × 360 nm.

To summarize, in this chapter we have monitored the amorphization of Gr/Ir(111) and hBN/Ir(111) upon exposure to 0.1 MLE 0.5 keV and 3 keV Xe^+ ion irradiation, respectively, and followed their self-healing by means of LEED, STM, and XPS. We could show that amorphization after high doses results in a complete loss of long-range ordering of the 2D materials. However, perfect crystallinity can be achieved by thermal treatment. For Gr the self-repair can easily be explained by the low activation energy for vacancy diffusion [20] whereas for hBN the recrystallization is surprising due to the high migration barriers for B and N vacancies as obtained for freestanding hBN due to homo-elemental binding [242]. With respect to our XPS data revealing strong hBN-Ir interaction it can be assumed that the underlying Ir substrate acts as a catalyst and lowers the activation barrier for vacancy migration enabling large diffusion lengths. This can be traced back to the fact that dangling bonds created by the knock-on damage can be partly compensated by the substrate avoiding homo-elemental bonds as calculated for Rh(111) [244].

Finally, we showed that the self-repair ability of Gr can be used beneficially and opens up a pathway for ironing-out wrinkles that are inevitable introduced during epitaxial growth by means of irradiation and damage annealing.

CHAPTER 11

Comparison of Graphene and Hexagonal Boron Nitride on Ir(111)

In Chapters 6 to 10 we studied the response of graphene and hexagonal boron nitride resting on Ir(111) to ion irradiation and presented evidence for the intercalation of rare gas atoms underneath the two-dimensional layers resulting in the formation of highly pressurized blisters. Further, the amorphization and recrystallization behavior was studied. First, in Chapter 6 we elucidated the mechanisms of noble gas trapping and the root of stabilization by means of MD simulations and DFT calculations by taking the example of Gr/Ir(111). Thereby, we found that for ion energies of up to a few keV the Gr layer inhibits ion reflection in favor of ion trapping. This phenomenon can be traced back to an easy penetration of the noble gas through the Gr layer and an efficient energy loss to the substrate. Upon momentum reversal the decelerated noble gas atoms are captured by the Gr mesh. Since Gr edges bind strongly to the substrate the noble gas is unable to escape even at elevated temperatures. Due to the generality of these mechanisms and the similarities of Gr and hBN with respect to their atomic mass (compared to the atomic mass of the other collision partners) and their interlayer bonding a transfer to the hBN/Ir(111) system seems applicable.

In this chapter the findings for the two systems, namely Gr/Ir(111) and hBN/Ir(111), with respect to noble gas trapping and blister formation are compared. The common characteristic will be discussed and the differences will be pointed out. Finally, their amorphization and recrystallization behavior is compared.

Table 11.1 summarized the Xe trapping efficiencies of Gr and hBN on Ir(111). Apparently, both systems show efficient trapping of noble gas at the 2D material/metal interface. At room temperature the efficiencies for both materials and energies are comparable.

However, upon annealing differences are found, if revisiting the XP spectra. In general, for the case of Gr/Ir(111), an increase of Xe intensity is found which can be attributed to noble gas streaming from the bulk to the interface combined with virtually no out diffusion, as apparent from the desorption traces in Figure 11.1(a). As opposed to this, upon annealing the hBN/Ir(111) sample shows a reduction of the Xe intensity in XPS that is reducible to strong out diffusion from underneath hBN [compare to Figure 11.1(b)]. These findings indicate similar kinetics during the ballistic phase of the impact (comparable trapping probability at room temperature) but different thermally activated barriers for the out diffusion at the 2D layer edges [stronger decrease in Xe intensity and high TPD signal for hBN/Ir(111)].

Table 11.1: Comparison of the integrated Xe intensities after irradiation and annealing for graphene and hexagonal boron nitride on Ir(111). The integrated Xe $3d_{5/2}$ intensities for 0.5 keV and 3 keV Xe^+ irradiation of Gr/Ir(111) (I_{Gr}) and hBN/Ir(111) (I_{hBN}), respectively, are presented.

	0.5 keV		**3 keV**	
	I_{Gr}	I_{hBN}	I_{Gr}	I_{hBN}
300 K	11.5	7.9	5.9	4.6
1000 K	12.2	4.0	6.0	2.1
1300 K	11.6	1.7	8.0	0.8

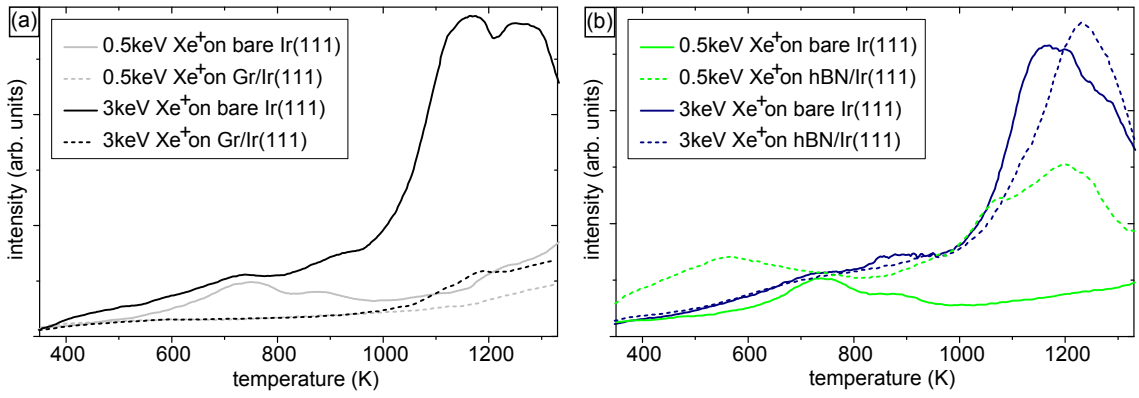

Figure 11.1: Comparison of temperature programmed desorption data for graphene on Ir(111) and hexagonal boron nitride on Ir(111) after Xe^+ irradiation. TPD of Xe (131 amu) after exposure of bare Ir(111) and (a) Gr or (b) hBN covered Ir(111) to 0.1 MLE 0.5 keV and 3 keV Xe^+ at 300 K, respectively. Color code is specified in the images. Heating rate is 5 K/s.

Furthermore, the morphological similarities and discrepancies are worth reviewing. In Gr/Ir(111) we observed a transformation of flat bulges to rather curved blisters upon annealing as visualized in Figure 11.2(a) and the corresponding profile in (c). The blister shapes are rather random. Contrary, for hBN the flat blister structure mostly withstands annealing. Instead of forming curved structures a second flat level emerges as apparent from the STM topograph in Figure 11.2(b) and its profile in (d). This phenomenon can be explained by the stronger adhesion of the hBN layer to the substrate compared to Gr. Where Gr starts to delaminate the hBN further compresses the Xe resulting in nano-crystals with distinct step heights. The atomic structure of the Xe nano-crystal was images by means of STM through the covering hBN layer. The blisters in hBN tend to detach from the hBN layer by accumulating vacancies in its vicinity and form triangular shapes. This shape is traced back to the preferred B terminated zig-zag edges, a phenomenon not observed for Gr since the Gr is way more flexible due to its homo-elemental nature.

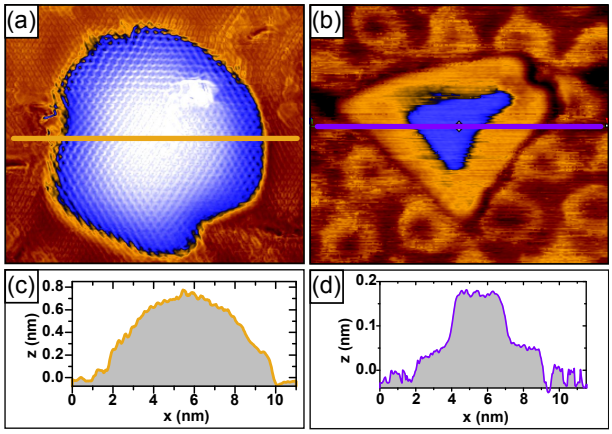

Figure 11.2: Comparison of blisters in graphene and hexagonal boron nitride on Ir(111). Comparison of typical Xe filled blister shapes in Gr (a) and hBN (b) on Ir(111). The corresponding profiles along the lines in (a) and (b) are displayed in (c) and (d), respectively, and show a smooth cured shape for Gr/Ir(111) and a two level structure for hBN/Ir(111). Images sizes are 11.5 nm × 10.0 nm.

Moreover, we showed for both systems that the implantation and blister formation process can be separated by pre-growth implantation resulting in gas filled blisters in otherwise defect-free 2D layers.

Finally, by means of LEED and XPS we showed that both 2D materials can be amorphized and recrystallized using ion irradiation and thermal treatment. Despite the large differences in the calculated activation energies for vacancy diffusion for Gr and hBN both materials show equal self-healing behavior. We attribute this to the metal support which catalyzes vacancy migration.

CHAPTER 12

Noble Gas Trapping – A Review

In the recent years the controlled intercalation of selected species below graphene or hexagonal boron nitride resting on a metal substrate by means of ion irradiation has focused intensive research efforts. The effect of immobilization of the ions directly at the 2D-substrate interface or implantation into the bulk and consecutive annealing has now been demonstrated for several Gr- and hBN-metal systems [53, 77, 120, 121, 154–156, 217, 245–248]. In this chapter the key results will be briefly reviewed and linked to this work.

Many studies focused on the immediate immobilization of noble gas ions at the interface by using low acceleration voltages which result in an energy transfers to the 2D material that just exceed the displacement threshold for the respective species in the 2D material but does not cause severe damage to the substrate [53, 154–156, 246, 248]. Thereby, the noble gas comes to rest in between the metal substrate and the covering 2D material without penetrating into the bulk. For individual atoms this phenomena has been reported by Cun *et al.* and de Lima *et al.* for the cases of Ar, Ne, and Rb trapped at the hBN/Rh(111) interface forming so called nanotents [53, 154, 155, 245]. Their STM and XPS studies are backed-up by DFT calculations [53, 248]. All studies show that the impinging ion causes minor damage to the hBN layer which can be repaired by thermal treatment. The ion itself is found at wire crossings [which are comparable to the weaker bound hill areas in hBN/Ir(111) within this work] which was also reported to be the calculated optimized configuration of Ar atoms at the hBN/Rh(111) interface. Upon annealing they claim to observe a *can-opener effect* [53, 155] which was already falsified in Chapter 9 of this work. For the system Gr/Ru(0001) they make similar observations [156]. However, for Gr/Ru(0001) the Ar atoms are stabilized in the top regions of the moiré. In general they

observe that the immobilized atoms go to the areas furthest apart from the substrate [top region for Gr/Ru(0001), wire region for hBN/Rh(111)] and tend to cluster.

Zamborlini *et al.* used higher fluences of low energy Ar^+ ions (0.1 - 0.5 keV) to create Ar filled nanobubbles in Gr/Ir(100) upon annealing and studied their appearance by means of STM, XPS, and LEEM [217]. The nanobubbles undergo a ripening process that is driven by the minimization of the energy cost due to film distortion and loss of adhesion, similar to the results in this work. By *ab inito* DFT calculations they estimate GPa pressures for the intercalated Ar. They claim to have made similar observations for Ne^+ irradiation of Gr/Ir(100) and Ar^+ irradiation of Gr/Ni(111).

The latter system was also studied by Späth *et al.* [247] who observed Ar trapping at the Gr/Ni(111) interface by irradiation of Ni(111) before Gr growth. Similar to the pre-implantation experiments presented in this work they observe the intercalation of Ar upon Gr growth by means of XPS. Interestingly, they observe the stabilization of Gr against thermal decomposition due to Ar intercalation. They attribute this effect to the inertness of Ar that passivates the catalytically active Ni substrate. They identify from the C 1s signal that in areas without intercalation the dissolution of Gr starts at approximately 1050 K whereas in the intercalated areas the Gr is stable up to 1150 K. In this work, high pressures of the intercalated species are assumed on the basis of geometrical considerations.

The XPS results by Späth *et al.* were soon corroborated by a combined XPS and STM study by Larciprete *et al.* [246]. They confirm that the intercalated Ar atoms are sealed by Gr bound chemically to the Ni(111) substrate and that the Ar filled blisters are more stable against thermal decomposition. Even though we do not observe Gr blisters completely detached from the remaining Gr sheet due to the higher stability of Gr/Ir(111) against thermal decomposition, frequently Xe filled blisters at Gr edges are observed. However, for hBN/Ir(111) we observe similar blisters bound directly to the Ir substrate sealing noble gas.

Due to the similarity of the systems our results for noble gas trapping (Xe^+, Ar^+, Ne^+) nicely compare to the work on Gr/Ir(100) done by Zamborlini *et al.* [217] for Ar^+ irradiation. The observed morphologies obtained by STM after irradiation and subsequent annealing as well as the ripening process resemble each other as well as the stability of the blisters at 1350 K. However, differences can be found in the XPS C 1s signal. Even though the morphology from STM suggests quite similar ion doses Zamborlini *et al.* observe a recovery of the C 1s peak already at 870 K whereas in our experiments more than 1000 K is needed for the recovery. The Ar 2p signal reveals a transition from a 2D to

a 3D character of the Ar at interface, which is attributed to the increased height of the blisters which are assumed to contain multilayer Ar. The calculated diffusion barrier of Ar at interface is 40 - 120 meV which explains the accumulation of Ar. Finally, from the shape obtained by STM and ab inito calculations they estimate a pressure in GPa range within the blisters.

Despite the high effort, up to now a direct experimental proof of the high pressure and with this solidification of the noble gas within the observed blisters was missing. In this work we provide direct evidence of the solid nature of Xe at the hBN/Ir(111) interface.

PART V

Carbon Radical Exposure

CHAPTER 13

Graphene Bilayer Growth and Wrinkle Formation

This chapter contains contributions from T. Knispel, S. Simon, C. Teichert, A.V. Krasheninnikov and T. Michely. I was responsible for the design of the experiments, conducted or was involved in all STM and XPS measurements, and analyzed all data. DFT calculations were provided by A. V. Krasheninnikov and are published in [120].

Since the pioneering work of Novoselov *et al.*[1] on the isolation and electronic properties of graphene it is envisioned to be used in future nanoelectronics. However, monolayers of Gr face the issue of having a peculiar zero gap electron dispersion keeping the lid on its possible application. The production of large scale Gr bilayers has resurrected the dream of implementing the 2D material in technology since applying an electric field opens up a bandgap [249–252]. Currently, there are several approaches to grow Gr multilayers by CVD methods [11, 170, 253, 254] or by C segregation from the bulk [11, 139, 255, 256]. Moreover, the sublimation of elemental C onto Gr monolayers on metals at elevated temperatures showed bi- and multilayer Gr growth [11, 253, 257]. Due to the weak C adatom binding to Gr but strong binding to the substrate the second layer nucleates and growth underneath the first layer in all cases [11, 253]. Nie *et al.* [11] present conclusive evidence for the underlayer growth mechanism during bilayer growth by C deposition, *i.e.*, the penetration of C through Gr and subsequent growth of the second Gr layer at the Gr-substrate interface. However, no atomistic insight into the condition of the initial Gr layer after C penetration is presented. For a complete picture of the fate of radical C

deposited onto Gr resting on a substrate further questions need to be addressed: What happens to the initial Gr layer? Do all C radicals stick to Gr or is there reevaporation? And how does the fate of the C radicals depend on defects in the initial Gr layer?
In this chapter we address the above raised questions and comprehensively discuss the different pathways for C radicals deposited onto Gr on Ir(111) at high temperatures. First, we investigate the formation of Gr bilayers at the interface. To go beyond we elucidate the hitherto unknown mechanism of C incorporation into the preexisting Gr layer which results in in-plane compression at high temperature and eventually in extensive wrinkle formation upon cool down. The discovery of this phenomenon is of utmost importance for Gr bilayer growth via C radical deposition as wrinkle formation will deteriorate the mechanical as well as electronic properties of Gr [258, 259].

13.1 Morphology after Radical Carbon Deposition

To start with we want to acquire a detailed picture of the morphology of the initial Gr layer grown by CVD on the hot Ir(111) surface. A large scale STM topograph of the as grown Gr monolayer on Ir(111) imaged at room temperature is depicted in Figure 13.1(a). Two arched preexisting substrate step edges are present. The Gr layer covers the Ir(111) surface in a carpet like fashion. The precursor used for Gr growth requires bare metal to become dehydrogenated and eventually incorporated at the growing edge which limits the growth strictly to one ML. Further, no Gr bilayer growth by segregation from the bulk is observed due to the low C solubility in Ir at the applied temperatures. Occasionally wrinkles are present (not shown) that form in CVD Gr/Ir(111) as a result of the different thermal expansion coefficients of Gr and its growth substrate. Upon cool down the Gr layer is set under compressive strain due to the thermal contraction of the metal that is partially released by wrinkle formation [59]. The extent to which the strain is stored within the Gr lattice or released by delamination, *i.e.*, wrinkle formation, is a result of the balance between the energy needed to delaminate and bend the Gr to form a wrinkle and the energy needed to compress the sheet [59]. But what happens if the Gr lattice is forced to accept more C by supplying C radicals?
To address this question Figure 13.1(b) shows a sample after CVD Gr growth and consecutive deposition of 0.8 ML radical C all at 1200 K. In between Gr growth and C deposition the sample was kept at the elevated temperature. Surprisingly, essentially no Gr bilayer formation is observed. Instead, besides the preexisting curved substrate step edges a dense wrinkle network emerges as visible from the bright lines in the STM topograph.

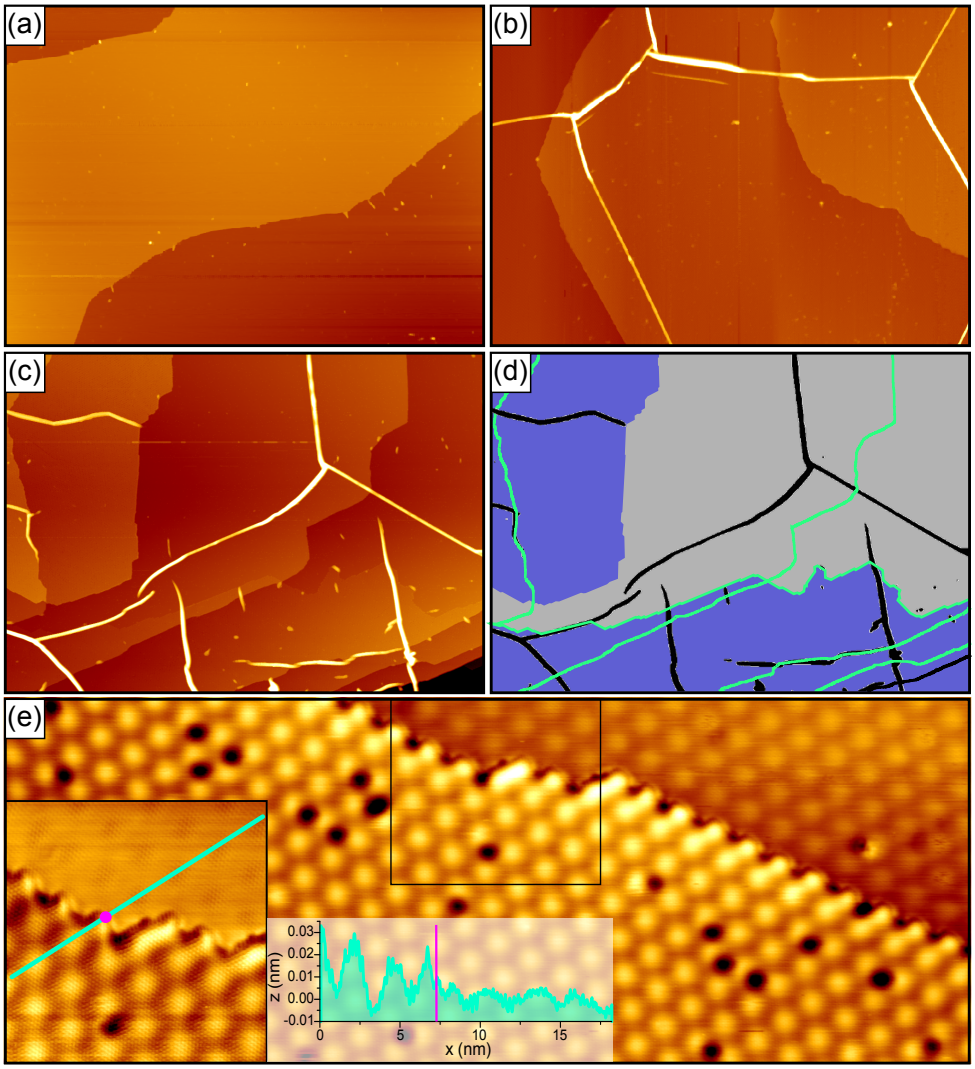

Figure 13.1: Carbon intercalation of graphene on Ir(111). (a) STM topograph of the as grown CVD Gr/Ir(111). (b) CVD Gr/Ir(111) plus 0.8 ML C deposited at 1200 K without intermittent cool down. A wrinkle network has formed. (c) CVD Gr/Ir(111) after deposition of 1.6 ML C at 1200 K without intermittent cool down. Besides a wrinkle network extended Gr bilayer islands are visible. (d) Schematic of (c): monolayer Gr is colored in gray, bilayer Gr islands are colored in blue, wrinkles in black, and the position of step edges are indicated by green lines. Image sizes are 680 nm × 480 nm. (e) STM topograph of Gr/Ir(111) after additional C deposition. In the middle of the topograph a transition from bilayer Gr (lower left) to monolayer Gr (upper right) coinciding with an Ir substrate step edge is shown. The Gr layer at the interface grows into the ascending substrate step edge by deforming the edge with the periodicity of the moiré. Several point defects are present in the lower Gr layer. Image size is 73 nm × 28 nm. Insets: STM topograph of the area in the black box with atomic resolution. Image size is 15 nm × 15 nm. The profile along the cyan line shows stronger moiré corrugation on the bilayer Gr. The pink dot and line indicate the transition from mono to bilayer Gr.

The mean height of the wrinkles is 2 nm with a maximum measured height of more than 4 nm (mean height after CVD growth is 0.6 nm and maximum height is 2.2 nm).

Performing exactly the same experiment but depositing 1.6 ML C radicals onto the full ML Gr/Ir(111) yields again a dense wrinkle network as visible in Figure 13.1(c). In addition, large extended bilayer areas have formed as visible at the left margin as well as at the bottom of the STM topograph and marked in blue in the corresponding schematic in Figure 13.1(d) for better visibility. Preexisting step edges and wrinkles are marked in green and black, respectively. Those extended second layer Gr islands at the interface terminating at an ascending Ir step edge grind into the preexisting step edge and thereby strongly reshape it as visible at the upper rim of the lower bilayer area. This results in rather straight Ir step edges that are only modulated in units of the moiré. A similar behavior but to a lesser extent was already observed for temperature programmed grown Gr islands on Ir(111) [128]. A higher magnification STM topograph of such a Gr island at the interface attached to a substrate step edge covered by the CVD monolayer Gr is shown in Figure 13.1(e) (lower left: bilayer Gr; upper right: monolayer Gr). It clearly shows the modulation of the step edge with the moiré periodicity. This interaction between the second Gr layer and the substrate step edge gives the first confirmation that the second Gr layer actually grows at the interface. However, it should be noted that even though we now find Gr bilayers the amount of bilayer area is again much smaller than the deposited amount.

By inspecting the bilayer area in more detail small dark spots becomes apparent that can be attributed to vacancy-type defects in the lower Gr sheet. They saturate their dangling C bonds to the substrate creating defect funnels [20]. Atomic resolution imaging across such a defect reveals continuous C rows in the covering Gr layer. The abundance of such defects within Gr grown by C radicals was also observed for Gr growth from C radicals on pristine Ir(111) (data not shown).

From the inspection of the moiré superstructure in Figure 13.1(e) it can be derived that the Gr that grows at the interface aligns with the covering sheet. However, comparatively rare Gr bilayers show additional moiré structures arising from Gr islands at the interface rotated with respect to the cover layer. In general, the moiré observed on top of bilayer Gr is more prominent and has a higher apparent corrugation as visible in the inset of Figure 13.1(e) and the corresponding profile. Depending on tip and tunneling conditions the usual apparent height of the bilayer with respect to the monolayer Gr is approximately 0.27 nm. All the above mentioned properties facilitate the identification of bilayer Gr.

Remarkably, it turned out that the exact experimental procedure strongly affects the resulting morphology. In a last experiment we again deposit 0.8 ML C radicals at a slightly lower temperature of 1170 K on CVD Gr/Ir(111) grown at 1270 K. This time the sample was cooled to room temperature twice in between Gr growth and C deposition. The resulting STM topograph and the corresponding schematic is displayed in Figure 13.2(a) and (b). Again a dense network of large wrinkles is visible. What is new for this low C dose is the large amount of extended Gr bilayer islands. Further, small scale wrinkles and protrusions as well as small triangular shaped bilayer islands are present.

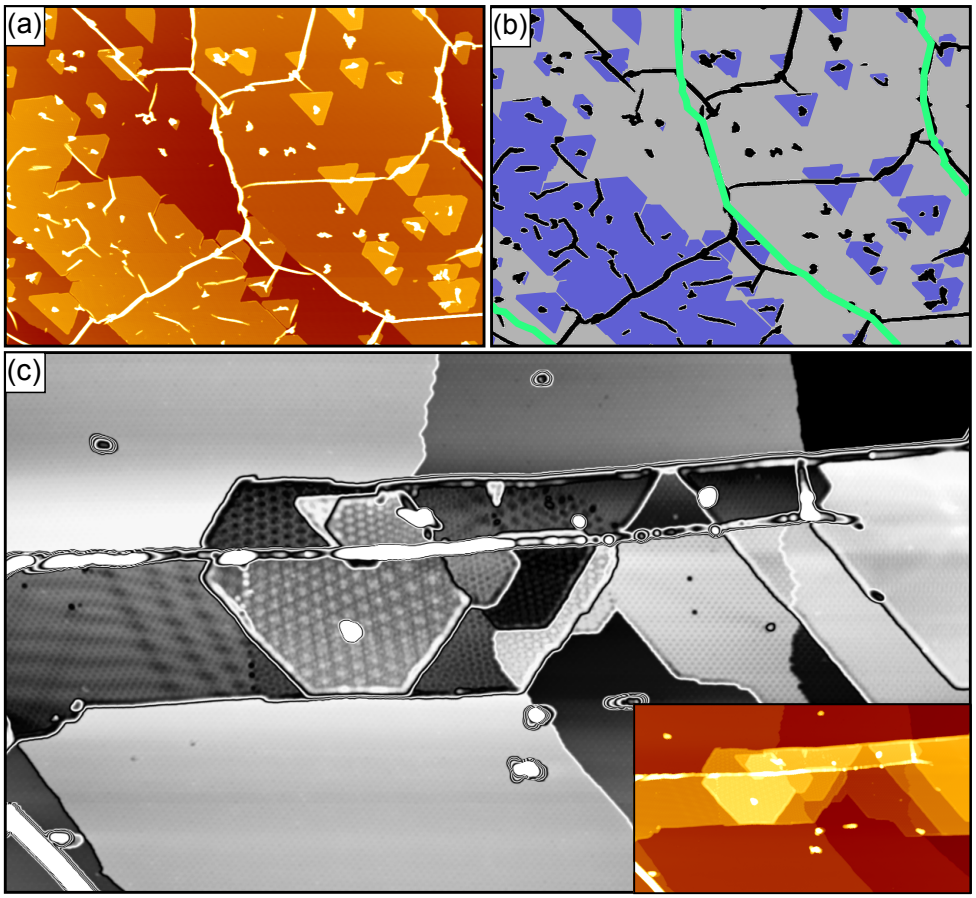

Figure 13.2: Carbon intercalation of graphene on Ir(111) through defects. (a) STM topograph of CVD Gr/Ir(111) after deposition of 0.8 ML C at 1170 K with cool down between CVD growth and C deposition. Image size is 680 nm × 480 nm. (b) Schematics of (a) with the same color code as in Figure 13.1. (c) STM topograph of Gr/Ir(111) with preexisting substrate step edges running from top till bottom. In the middle of the topograph a wrinkle is intercalated by one to several layers of Gr exhibiting manifold moiré patterns. An iterative black and white color scale is applied to visualize the moiré pattern on all levels, true color scale image in the inset. Image size is 360 nm × 200 nm.

Further, the local proximity of wrinkles and bilayers visible in Figure 13.2(a) and (b) leads one to expect a strong coherence between intercalation and wrinkle formation. In some cases bilayers and even multilayers formed along wrinkles - a phenomenon that was not observed before. Figure 13.2(c) shows a wrinkle running from left to right that is intercalated by C forming several layers of Gr at the interface. The color scale is adjusted in such a way that the different moiré superstructures become visible. These develop due to the different rotations of the stacked multilayers. On the left hand side a bilayer area attached to the wrinkle is visible. The gradual emergence of a larger scale moiré pattern indicates strain within the Gr sheet progressively altering the lattice constant.

13.2 Energetics of Carbon Penetration and Graphene Bilayer Nucleation

To comprehensively unravel the fate of C radicals deposited onto Gr/Ir(111) at high temperatures and eventually to understand the phenomena observed above we next consider the energetics of a C monomer penetrating a Gr sheet using ab initio calculations. Figure 13.3 represents the energy of the system as a function of the reaction coordinate. The potential energies are given with respect to a C atom bound within an infinite Gr sheet. From first sight it becomes apparent that the C radical can dramatically lower its potential energy by adsorbing on the Ir(111) surface. Only minor energy barriers are involved and once adsorbed in an hcp adsoption site on the Ir(111) surface the energy penalty is only 0.7 eV, *i.e.*, the C atom is almost bound as good as within Gr. In more detail, by adsorbing to the Gr layer the C atom lowers its potential energy by 1.55 eV. After overcoming an energy barrier of only 0.9 eV [260] it goes into the dumbbell configuration (potential energy +6.8 eV) from where it has to conquer another small energy barrier to get into a metastable state where the C atom is binding to the Gr and the metal substrate (potential energy +3.4 eV). Finally, the C atom reaches the lowest energy configuration at the Ir surface.

Even though considering only a C monomer is an oversimplification since the C is evaporated in the form of monomers, trimers, and less frequently as dimers [262, 263], we can conclude that the C radical can penetrate the Gr if all kinetic barriers are overcome. These findings are in line with similar calculations for C penetration through Gr on Cu(111) by Wu *et al.* [264] as well as for free-standing Gr by Tsetserisa *et al.* [260]. However, since lateral diffusion of C adatoms on Gr is easy [102], it remains unclear if the C will penetrate through the perfect Gr mesh or at specific defect sites, such as 5-7-defects.

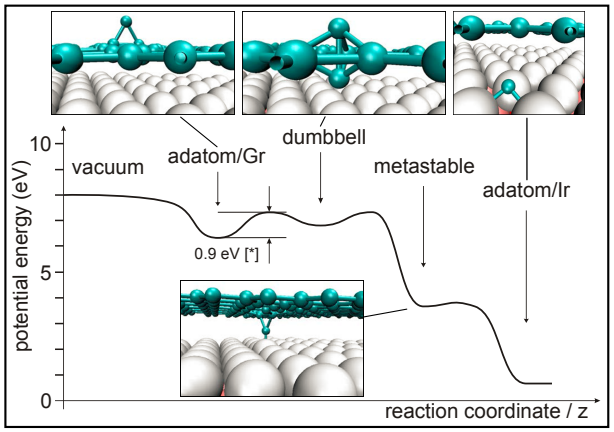

Figure 13.3: Energetics of carbon penetrating graphene on Ir(111) from density functional theory. System energy as a function of the reaction coordinate for a carbon atom coming from vacuum, adsorbing on the Gr/Ir(111), and penetrating the Gr layer to become an adatom on the It(111) surface. Zero energy corresponds to a C atom bound in an infinitely extended Gr sheet. The insets present the C atom in the adatom, dumbbell, metastable, and adatom position. (* from Ref. [261]).

To get microscopic insight into the nucleation of the second Gr layer at the Gr/Ir(111) interface, we studied the energetics of monomers, dimers, and small C flakes on Ir with and without a Gr layer on top. As we show below, the energetics of C atoms on the free Ir(111) surface and at the interface with a Gr layer is similar, so that we carried out most calculations for the free surface, which allowed us to avoid excessive computations.

The energy of formation per atom $E_c(N)$ for a Gr flake consisting of N C atoms on a surface of a metal slab is defined as

$$E_c(N) = (E_{tot}[\text{slab} + N] - E_{tot}[\text{slab}])/N - \mu_G, \tag{13.1}$$

where $E_{tot}[\text{slab} + N]$ and $E_{tot}[\text{slab}]$ are the total energies of the slab with and without the adsorbed N-atom Gr flake, respectively, and μ_G is the chemical potential of a C atom in free-standing Gr. $E_c(N)$ can be interpreted as the energy penalty per C atom to form an N-atom flake on the metal with respect to an infinite Gr sheet. Note that for $N \to \infty$, E_c gives the van der Waals Gr-metal interaction energy (per C atom), which is essentially zero as compared to typical values of E_c for small Gr flakes. $E_c(1)$ is the C-monomer formation energy. Adding the cohesive energy of Gr to $E_c(1)$ yields the C monomer binding energy to the slab.

For C monomers on Ir(111), we found that the most favorable adsorption position is the hcp threefold hollow site with $E_c(1) = 0.72\,\text{eV}$ (see Figure 13.4) as mentioned above. The

C monomer is located about 1 Å above the Ir surface. At the fcc threefold hollow site $E_c(1) = 1.08\,\text{eV}$, *i.e.*, adsorption at this site is disfavored by 0.36 eV.

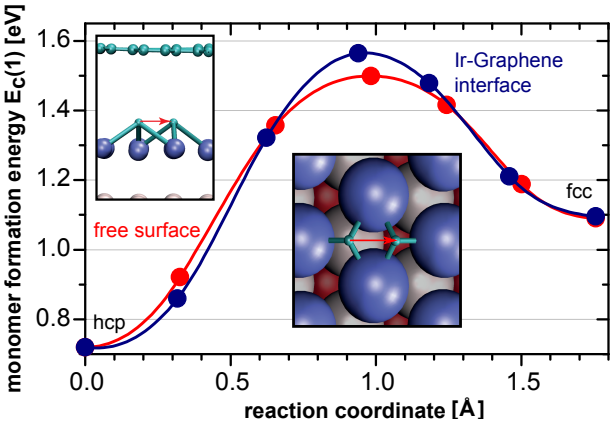

Figure 13.4: Carbon monomer formation energies. Variation of monomer formation energy $E_c(1)$ along the minimum energy path from an hcp to an fcc adsorption site during the migration of a C-monomer on Ir(111) (red) and at the interface of Gr/Ir(111) (blue). The insets show the atomic geometries of the C monomer in the hcp and the fcc threefold hollow sites as well as the migration path. The points are the results of nudged elastic band DFT calculations. Lines to guide the eye. Blue data down-shifted by 0.2 eV for direct comparison.

We also calculated the activation energy for C monomer diffusion on Ir(111) using the nudged elastic band (NEB) method [265]. With an activation energy of 0.8 eV, C monomers are highly mobile at the deposition temperature. Calculations for the monomer at the Gr/Ir(111) interface resulted in similar numbers. In the top areas of the moiré, the C-monomer formation energy at the interface of Gr/Ir(111) is almost identical to the one on bare Ir(111), while in the fcc and hcp areas it is disfavored by 0.2 eV as compared to bare Ir(111). The migration barrier at the interface of Gr/Ir(111) is only marginally increased compared to the one on bare Ir(111), as obvious from Figure 13.4 (blue data down-shifted by 0.2 eV for direct comparison).

To understand the energetics of Gr nucleation, we calculated $E_c(N)$ for small Gr flakes in sp^2-hybridized configurations on Ir(111) (red data in Figure 13.5). $E_c(N)$ first increases, that is, the formation of dimers and small C aggregates are energetically unfavorable with regard to spatially separated monomers. Such a behavior of C monomers, which is at variance with the one on copper [266], originates from the large separation between the hcp and fcc sites on Ir(111) as compared to the carbon dimer bond length (1.6 Å vs. 1.2 Å). Consequently, the dimer is 'stretched' when the two C atoms are put in the neighboring lowest energy hcp and fcc positions. The trend is reversed when the aggregate become

larger, *i.e.*, then $E_c(N)$ decreases with flake size. The critical size is 5 atoms and the nucleation barrier is about 3 eV ($\approx$ 0.6 eV per atom).
Additionally, we calculated formation energies of small flakes at an Ir step edge. As seen from the blue data in Figure 13.5, the nucleation barrier decreases by about 2 eV due to the presence of the step, while the size of the critical nucleus remains unchanged. Therefore, we conclude that the presence of Ir steps lowers the nucleation barrier.

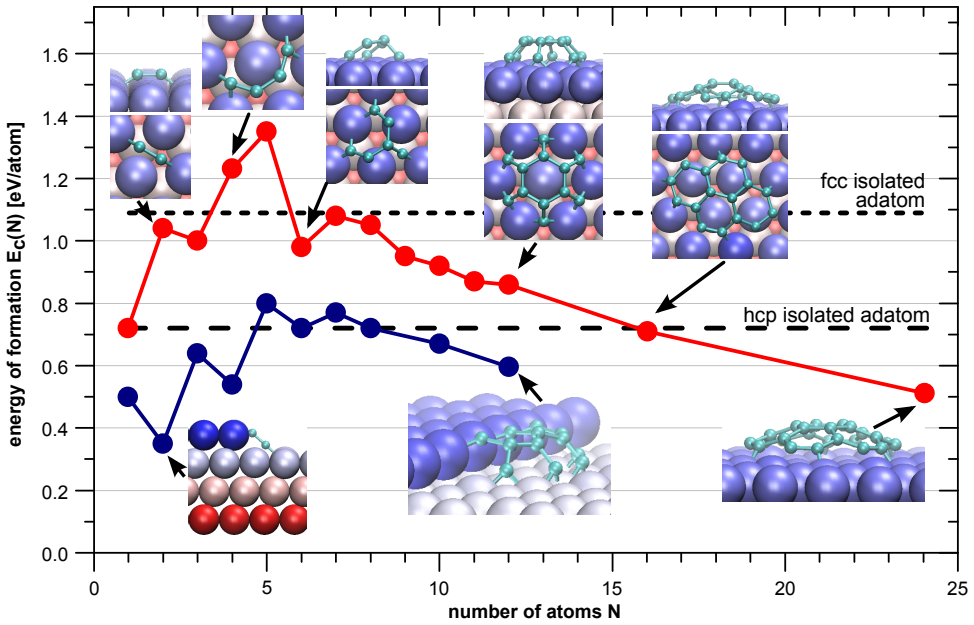

Figure 13.5: Energetics of graphene nucleation. Energy of formation $E_c(N)$ per atom (with regard to the energy of a C atom in an isolated infinite Gr sheet) in flakes consisting of N atoms on the Ir(111) terrace (red data) and at the step edge (blue data) as calculated by DFT. Lines to guide the eye. The insets show some configurations. Ir atoms represented as large balls are colored according to their z-coordinate. The nucleation barrier is smaller for platelets attached to the step edge.

13.3 Discussion

With these experimental and theoretical results at hand we can draw the following scenario for C radical deposition onto Gr/Ir(111) at high temperatures. Our first finding is that for a perfect Gr sheet re-evaporation of C radicals is substantial at 1200 K since the observed amount of bilayer Gr does not account for the deposited amout of C. This proves that the involved kinetic barriers for C transmission are still relevant at the applied temperatures. The high re-evaporation rate can be understood by considering the involved adsorption

energies and kinetic barriers. The C atom gains 1.55 eV when adsorbing in the bridge configuration. Note that adsorption energies are lower by more than 1 eV for C adatoms on top of a surface C atom [102]. Keeping in mind that the sample is at 1200 K, re-evaporation becomes highly possible.

The emergence of a dense wrinkle network points to the fact that some of the supplied C was integrated into the CVD grown Gr layer. This results in compressive stress already at high temperature that is even more increased upon cool down leading to enhanced relaxation into wrinkles. Note that the increased wrinkle formation cannot be explained by a smaller adhesion of the cover Gr layer to the second Gr layer at the interface compared to the Ir substrate, since we observe wrinkle formation without bilayer formation for small C doses.

Further, from the abundance of wrinkles in absence of bilayers at low C doses we can deduce that the C that is not re-evaporated into vacuum is *first* incorporated into the Gr sheet, where the C atom has the lowest possible chemical potential, before it is transmitted to the interface. We speculate that the integration is realized via repetitive defects in the Gr, such as 5-7-defects. Here, two C atoms can be accommodated causing a 'climb' of the 5-7-defect without local elastic distortion [110]. Globally, the addition of extra C results in a compression of the Gr lattice. However, other defects in the Gr sheet may also account for the incorporation.

Since we observe no bi- and multilayer growth anchored to wrinkles for samples kept at high temperature at all times, we claim that the compression of the Gr sheet at high temperature due to integrated C does not lead to delamination, *i.e.*, wrinkle formation before cool-down. N'Diaye *et al.* showed that a compression of 0.3 % is accomodated by the Gr lattice without delamination [57]. So this limited amount of extra C is accepted by the Gr layer at high temperature resulting in additional wrinkle formation upon cool down. However, the virtual absence of Gr bilayers in the case of 0.8 ML C deposition cannot be explained by the incorporation of the supplied C into the Gr layer since the small amount of extra C stored in the wrinkles is too small to account for the difference in deposited amount of C and observed amount of bilayer Gr, *i.e.*, re-evaporation is relevant.

The penetration of C atoms through the Gr sheet only becomes relevant when the Gr layer is sufficiently compressed and the energy cost to further incorporate C is higher than the energy barriers involved in the transmission. Even though a dilute C adatom concentration at the interface at an early stage is likely, only when the Gr sheet is saturated the C atoms go through the Gr to the Ir in high number forming a C adatom gas. Once a critical C concentration is reached nucleation of Gr bilayers starts. The calculated

nucleation barriers for small Gr flakes at the Gr/Ir(111) interface of 3 eV and 2 eV on the terrace and at an Ir substrate edge, respectively, prove that nucleation is possible without external nucleation centers.

However, the increased amount of C intercalation and the local proximity of wrinkles and Gr bilayers as well as multilayers for samples that were cooled to room temperature in between Gr growth and C deposition demonstrates that the history of the Gr sheet and defects within matter. There exists a memory effect for wrinkle formation and dissolution. The most likely scenario is the following: Upon wrinkle formation cracks are formed within wrinkles, especially at wrinkle crossings [61]. These defects anchored to Gr wrinkles deteriorate the integrity of the Gr and similar to the case of Cs intercalation facilitate C intercalation [61]. Our findings suggest that wrinkles once formed upon cool-down do not completely dissolve upon re-heating and due to the pre-existing delamination along these surviving wrinkles Gr multilayer formation is enabled. Further, our experimental observation of a high concentration of small scale wrinkles and small bilayer islands suggest that defects act as access sites for C incorporation and transmission as well as nucleation center for wrinkle and bilayer formation.

These finding show that only by changing the experimental procedure more C can penetrate the Gr layer and form bilayer islands and less C is re-evaporated into the vacuum. Thus the structure of the initial Gr layer is altered by the intermittent cool down and these changes are even memorized after reheating the sample. However, we cannot rule out that the difference of 30 K between the experiments with and without intermittent cool-down has minor impact on the intercalated amount of C, since re-evaporation will scale with the sample temperature.

13.4 Conclusions

In summary, we found that C deposition onto Gr/Ir(111) at 1200 K is accompanied by strong re-evaporation of the C towards the vacuum. However, re-evaporation is decreased when the Gr sheet exhibits wrinkles and defects from prior cool down. The wrinkles formed during cool down are not completely dissolved upon re-heating facilitating C intercalation. For a perfect Gr sheet we find that first the additional C is integrated in the existing Gr sheet leading to a compression of the layer already at elevated temperatures and eventually in ample wrinkle formation upon cool down. C transmission through the Gr layer and with this Gr bilayer formation is only efficient once the C incorporation is terminated due to the limited compressive strain.

Our findings highlight that high quality and defect-free Gr bilayer fabrication by C deposition on metals is not possible. The reason is the additional incorporation of C into the Gr cover layer at high temperatures. However, we speculate that high quality Gr bilayer growth without wrinkles is possible through post-growth ion beam treatment at high temperatures and grazing incidence.

CHAPTER 14

A Carbon Cluster Superlattice on Graphene on Ir(111)

This chapter contains contributions from T. Knispel, S. Simon, C. Teichert, M. A. Arman, J. Knudsen, A.V. Krasheninnikov and T. Michely. I was responsible for the design of the experiments, conducted or was involved in all STM and XPS measurements. I analyzed all data except the data in Figure 14.7 which was analyzed by T. Knispel under my supervision. DFT calculations were provided by A. V. Krasheninnikov.

In the previous chapter we comprehensively discussed the fate of C radicals deposited onto Gr/Ir(111) at high temperatures leading to wrinkle formation and Gr bilayer growth from below. At low temperatures, it is a matter of common knowledge that the thermal evaporation of C on any substrate results in amorphous C films . This technique is widely used for preparation of specimen for, *e.g.*, electron microscopy [267]. In an early work, Tontegode *et al.* [257] investigated the deposition of C on monolayer graphite on a metal and observe the same behavior, *i.e.*, the formation of a thick nongraphite film. However, up to now, nothing is known about the interaction of C radicals with Gr at low temperatures. The structure and chemical nature of the C films remains ambiguous.

In this chapter we investigate what happens to C radicals being deposited onto Gr/Ir(111) when kinetic barriers become relevant. We reveal that instead of Gr bilayer growth from below, at low temperatures, C radical deposition onto Gr/Ir(111) yields a periodic C cluster superlattice. Only for ample C deposition the superstructure is lost and an amorphous C film emerges. The cluster superlattice turns out to be highly stable upon

annealing. By DFT calculations and dedicated STM and XPS experiments we work out the origin of stability and unfold the degradation mechanisms.

14.1 Structure and Binding

The STM topograph in Figure 14.1 (a) shows Gr/Ir(111) after the deposition of 0.1 ML C onto Gr/Ir(111) at 400 K. As already anticipated in the introduction of this chapter no Gr bilayer formation is observed. The STM topograph shows a carbon cluster superlattice with a periodicity corresponding to the moiré formed by Gr with the Ir substrate. With approximately one C cluster within every moiré unit cell the deposited amount corresponds to an average cluster size of 21 C atoms.

The structure of the C clusters as imaged with the STM reveals a rich diversity varying from ring-like to wavy features as visible in Figure 14.1 (b). The absence of peaks in the density of states that would be imaged as a high intensity peak indicates that the C atoms form a closed structure without dangling bonds. The STM topograph resembles molecular orbitals of C_{60} molecules images by a C_{60} tip by Lakin *et al.* [268] as well as the sp^2 shell of nanodiamond monolayers as observed by Pawlak *et al.* [269].

To determine the position of the C clusters within the moiré unit cell we deposited a small amount of C onto Gr/Ir(111) to image the clusters along with the moiré superstructure. A small scale image of this sample is presented in Figure 14.1 (c) with a hexagonal lattice superimposed on the atop sites of the moiré. This shows that the C clusters preferably bind to the hcp region of the moiré as indicated by the green up pointing triangles.

To further investigate the binding character within the C clusters and towards the Gr sheet we conducted DFT calculations for many different cluster configurations. Small nanodiamond structures consisting exclusively of sp^3 hybridized C within a Gr sheet resulted in no low energy configuration. The energetically most favorable structure emerged from a fullerene endcap of sp^2 C placed above Gr/Ir(111) in the hcp area. The resulting optimized 19 extra C atoms on Gr/Ir structure is shown in Figure 14.1(d). The number of C atoms in the cluster approximately corresponds to the average cluster size after 0.1 ML C sublimation as displayed in Figure 14.1(a). The structure relaxes into an sp^2 C shell with the edges forming sp^3 bonds with the Gr sheet. The Gr sheet itself reacts to this by rehybridization, *i.e.*, by forming sp^3 bonds toward the substrate next to those C atoms binding to the C cluster above. Due to the rehybridization towards the substrate the cluster formation is limited to those areas within the Gr where a C atom is directly above an Ir atom, *i.e.*, the hcp or fcc site. In agreement with the observations in the STM

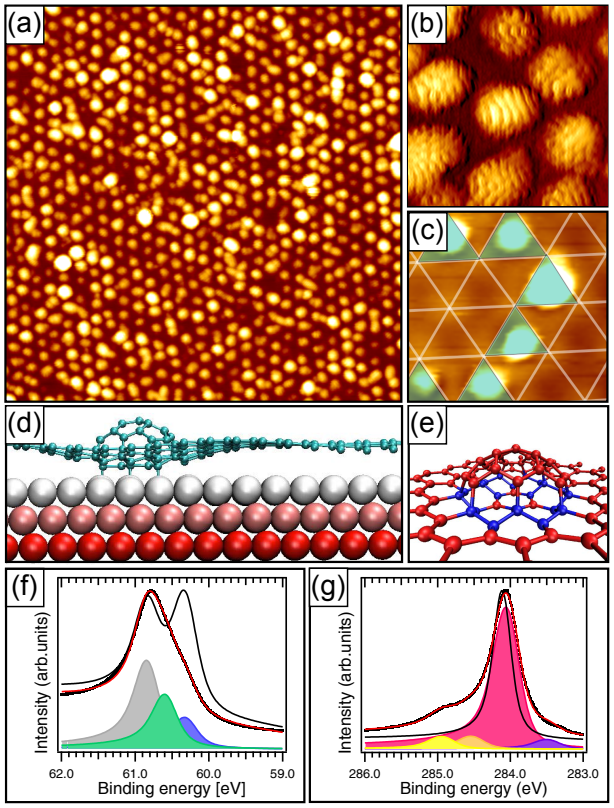

Figure 14.1: Carbon cluster superlattice. (a) C cluster superlattice on Gr/Ir(111) after deposition of 0.1 ML additional C. Image size is 60 nm × 60 nm.(b) High resolution STM topograph of 0.1 ML C clusters on Gr/Ir(111). Image size is 7.5 nm × 7.5 nm. (c) Low coverage of C clusters on Gr/Ir(111) with a hexagonal lattice superimposed on the top areas of the moiré to highlight the preferred adsorption site of the C clusters in the hcp region (green triangles). Image size is 8.5 nm × 8.5 nm. (d) DFT calculation of 19 additional C atoms positioned in the hcp area. (e) Cluster from (d) with the C atoms colored according to their coordination: red for 3 neighbors and blue for 4 neighbors. (f) Ir 4f spectrum of 0.3 ML C on Gr/Ir(111). (g) XP spectra of the C 1s peak of the same sample as in (f). The experimental spectra are shown as black dots, the fits as solid red lines, and the filled curves represent the components of the fit. For comparison the spectra of pristine Gr/Ir(111) are superimposed (black curve).

experiments we therefore find no binding of the identical structure placed above the atop region in DFT calculations. A similar rehybridization mechanism was already predicted and subsequently observed for metal clusters on Gr's moiré with its substrate [79, 80, 270]. This rehybridization and the resulting different bond characters are elucidated in Figure 14.1 (e) that shows the C cluster from Figure 14.1 (d) without the substrate and with the C clusters colored according to their coordination (red: sp^2, blue: sp^3). It becomes apparent that even though we find many different binding angles the cluster is basically comprised of an sp^2 shell as well as sp^3 diamond-like C. Although this cluster represents only one possible configuration it demonstrates the root of stability, *i.e.*, stable sp^3 diamond-like C bonds connecting the C cluster above as well as the whole slap towards the Ir substrate.

XPS is the perfect tool to experimentally identify these different bond characters as it gives insight into the chemical nature of the sample. Figures 14.1(f) and (g) show the XP spectra of the Ir 4f and the C 1s peak region of Gr/Ir(111) before and after 0.3 ML C exposure, respectively. We first have a look at the as grown Gr film on Ir(111). In each figure the pristine Gr/Ir(111) spectra are shown as black lines for comparison. The Ir 4f spectrum before C exposure can be fitted by two components. One component at a BE of 60.83 eV representing the Ir bulk component Ir_b and one component at a BE shifted by -0.52 eV to 60.31 eV originating from the undercoordinated surface atoms and is therefore called the Ir surface component Ir_s consistent with literature [271]. Both components are fitted with a GFWHM of 0.26 eV and LFWHM of 0.27 eV. The pristine C 1s peak shows only one narrow peak that can be fitted by a single component at 284.1 eV with a GFWHM of 0.21 eV and a LFWHM of 0.18 eV. For better visibility the fit components of the pristine sample are omitted in the graph.

The data after 0.3 ML C deposition is displayed as black dots. The corresponding fits are shown as solid red lines and the different fit components as filled curves. After C deposition the spectral weight of the iridium surface component, Ir_s, is strongly reduced to 69 % of its inital value and concomitant a third component at a BE of 60.58 eV has to be introduced for a reasonable fit of the data. The BEs for Ir_b and Ir_s as well as the GFWHM and the LFWHM are kept constant with respect to the pristine case. The decrease of the surface component can be explained by chemical bonds of the C atoms to the Ir surface in line with our DFT calculations and with similar data of Gerber *et al.* for Pt clusters on Gr/Ir(111) [272]. The C 1s peak shows a strong broadening compared to the pristine case. Additionally, for the formerly one component peak several new components have to be introduced for reasonable peak fitting. All components are fitted with a GFWHM of 0.63 eV to account for the broadening of the peak and a LFWHM of 0.18 eV. The choice

of the components is the consequence of an iterative fitting procedure which aimed at reproducing the data for all spectra as good as possible with simulatneously keeping as many parameter constant as possible. The two introduced components towards higher binding energies can be associated with rehybridized sp^3 C within and underneath the C cluster as well as to C atoms in the Gr sheet in direct vicinity to the cluster [80]. The small contribution towards lower BE to the formation of carbidic C as already discussed in Chapter 10 which might arise from C penetrating the Gr sheet and adsorbing on the substrate or from C still in contact with the Gr but close to the substrate. The assignment of different C species is ambiguous since we find many different C species within our clusters as demonstrated by STM. However, a grouping of these species is validated by the reasonably good fits of the XPS data. The BEs of the additional components are kept constant for all C 1s fits to come in this chapter. Since they have no straightforward meaning, we refrain from a detailed discussion of their position.

A final and straightforward experimental proof for the rehybridization of the Gr layer underneath the C clusters forming covalent bonds with the Ir surface can be found in the STM topograph in Figure 14.2. It shows 0.3 ML radical C on 0.5 ML Gr/Ir(111) intercalated with oxygen prior to C deposition. Due to the intercalated species the Gr layer is decoupled from its substrate and the moiré superstructure is virtually lost. Therefore no preferred binding site exist for the C adatoms and no rehybridization is possible, similar to the case of metal clusters on Gr/Ir(111) [273]. The C accumulates on top of the Gr in large irregular piles. In the higher magnification image in Figure 14.2(b) one can see that in some areas the large C clusters seem to deintercalate the oxygen as visible from darker trenches and islands within the Gr. This might point to a strong interaction of the C and Gr with the substrate despite the oxygen buffer layer.

On the basis of our STM and XPS results backed up by DFT calculations we established that C deposition onto the moiré formed by Gr with the Ir(111) surface at room temperature results in a C cluster superlattice. The scenario of C cluster binding is similar to the one reported for metal clusters on the same substrate [80] and relies on the rehybridization of the C atoms within the Gr sheet alternatively to the cluster above as well as to the substrate.

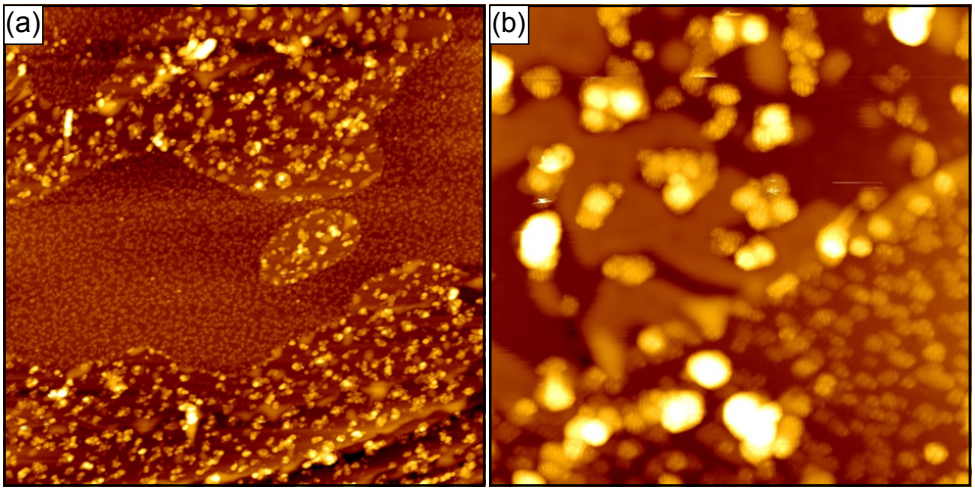

Figure 14.2: Carbon deposition on decoupled graphene. STM topographs of 0.5 ML Gr/Ir(111) intercalated with 100L oxygen at 450K prior to C deposition at 400 K. No regular C cluster superlattice is visible, only large accumulations of C. (b) High resolution image of (a). One can see that the Gr layer is partially deintercalated due to the C accumulations binding towards the substrate and with this relaminating the Gr layer. Image sizes are 180 nm × 180 nm and 45 nm × 45 nm, respectively.

14.2 Temperature Dependent Growth

Interestingly, at very low temperatures C deposition on Gr/Ir(111) does not lead to the formation of a regular C cluster superlattice. Instead approximately similar sized C clusters adsorb randomly on the surface as visible in Figure 14.3(a) which shows C clusters on half a monolayer Gr on Ir(111) deposited at 50 K. At these low temperatures there is not enough energy available for the C atoms to overcome diffusion barriers and find the lowest energy configuration therefore the clusters are formed rather randomly. Once the C clusters have assmebled slight annealing to room temperature does not increase the cluster ordering since the strong C-C bonds are hard to break once formed. Deposition of C onto Gr/Ir(111) at a sample temperature of 450 K and 550 K apparently results in lower cluster ordering, too, as visible in Figures 14.3(e) - (f). In Figure 14.3(f) one can even identify a depleted zone at the rim of the Gr islands indicative for C diffusion over distances larger than one moiré unit cell. So only intermediate temperatures lead to the formation of a regular C cluster superlattice as shown in Figures 14.3(c) and (d) for sample temperatures of 300 K and 400 K, respectively. Within this temperature range the C atoms are able to diffuse within the moiré unit cell and can find the energetically most favorable binding site. Still, their energy is low enough to be confined to the moiré cell.

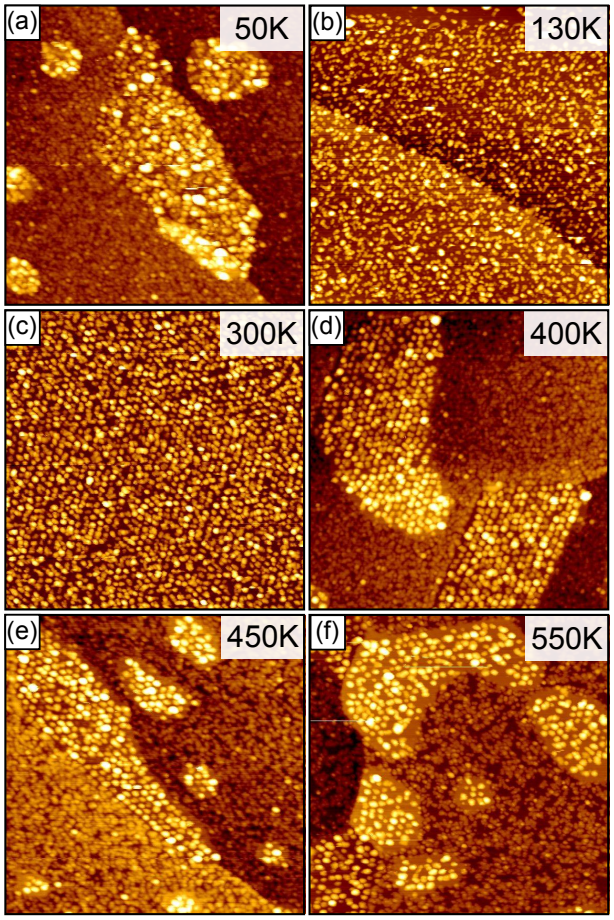

Figure 14.3: Temperature dependent carbon deposition on graphene on Ir(111). STM topograph of 0.5 ML (a, d, e, f) or 1 ML (b, c) Gr/Ir(111) after radical C deposition of 0.4 ML C (a, c, d, e, f) or 0.2 ML C (b), respectively. Deposition temperatures are indicated in the topographs. Image sizes are 100 nm × 100 nm.

14.3 Coverage Dependent Growth

In the previous sections the cluster binding to the Gr layer was examined for a specific cluster size. The aim of the present chapter is to extend the study to the growth of C clusters as a function of C coverage and investigate their structure and binding. Therefore, we first investigate STM data followed by XPS analysis.

Figure 14.4 shows a sequence of STM topographs obtained after the deposition of increasing amounts of radical C onto a full ML Gr/Ir(111). The average cluster sizes range from 6 C atoms to 645 C atoms. Note however, that at the lowest deposited amount of 0.03 ML not all moiré unit cells are occupied by a C cluster. Therefore the average cluster size will be larger than the one obtained from assuming a moiré occupation of one. After deposition of 0.1 ML C virtually all moiré unit cells are filled. Apparently, the deposition of 1 ML C or more results in a loss of the periodic arrangement of the C clusters. However, even for the highest deposited amount a cluster-like structure can be identified. The height distribution of the C clusters up to a coverage of 1 ML is depicted in Figure 14.4(f). It becomes apparent that the mean height of the clusters growth from approximately 0.2 nm, to 0.4 nm up to 0.8 nm concomitant with a broadening of the distribution.

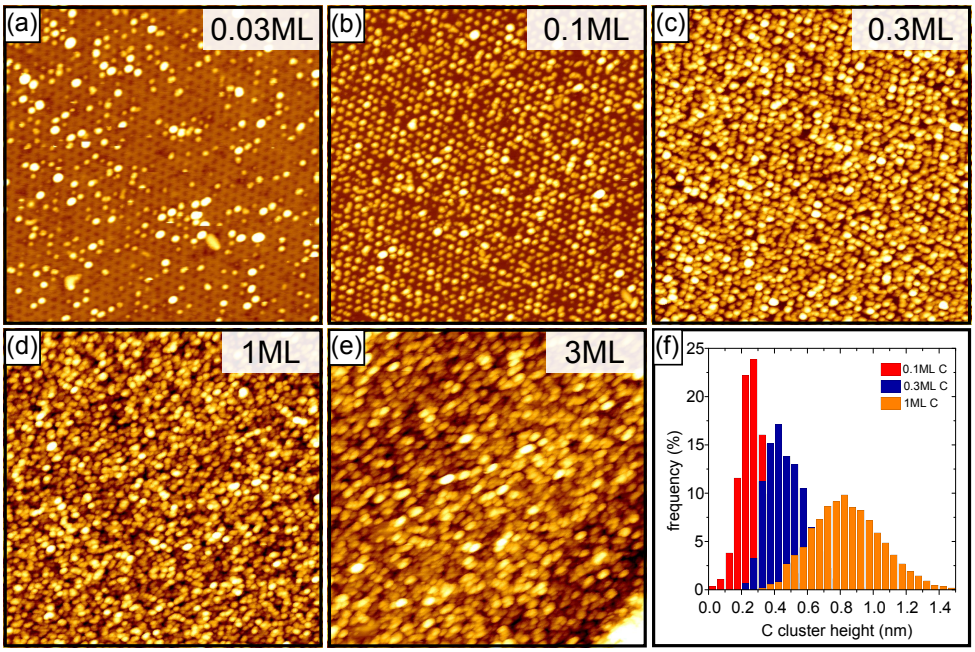

Figure 14.4: Carbon cluster deposition series. STM topograph of C clusters on Gr/Ir(111) with increasing C coverages of (a) 0.03 ML, (b) 0.1 ML, (c) 0.3 ML, (d) 1 ML, and (e) 3 ML deposited at 400 K. The distribution of the cluster height for 0.1 ML, 0.3 ML, and 1 ML C are given in (f).

The instability of small C clusters against diffusion is demonstrated in the STM topograph series in Figure 14.5. It shows STM topographs of 0.03 ML C on Gr/Ir(111) imaged one after another. It documents the instability of the C clusters by revealing their strong interaction with the STM tip. Equally colored circles in adjacent images highlight cluster manipulation by the STM tip. In Figure 14.5(a) the white arrow indicates a C cluster that was picked-up from one scan line to the other. The easy manipulation during STM imaging is in line with our DFT calculations for small C cluster with a size of six C atoms that are disfavored by approximately 1 eV per C atom with respect to the larger 19 atom clusters introduced above.

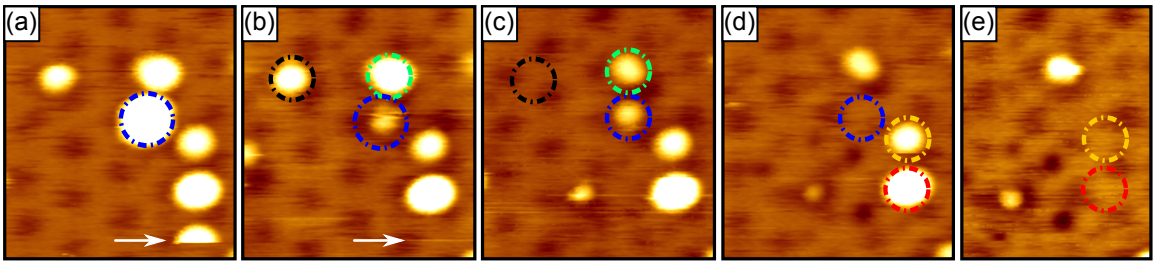

Figure 14.5: Instable carbon clusters at low coverages. STM topograph series of C clusters on Gr/Ir(111) taken at the same location one after another. Carbon clusters that disappear from one scan to the other are marked with a small circle. Same colored circles represent identical sample positions. The white arrow in (a) marks a cluster that is removed by the STM tip from one scan line to the next and is absent in (b).

Our STM data suggest three different growth regimes: a nucleation regime below 0.1 ML C coverage which is characterized by mobile C adatoms and small clusters thereof. A periodic growth regime between 0.1 ML and 1 ML where individual C clusters grow and are confined to the moiré unit cell. And finally, for coverages above 1 ML a regime where the C clusters coalesce and the periodicity is lost.
Next, we want to monitor this evolution by means of XPS measurements to find out more about the binding of the C clusters to Ir(111) in the different growth regimes. As a reminder, for a coverage of 0.3 ML we established the following XPS fingerprints:

(i) The C 1s spectrum is fitted with four components. Two components to higher BE can be assigned to sp^3 hybridized C atoms within the cluster as well as C atoms in closest vicinity of the clusters. The component to lower BE to carbidic C. Finally, a broadening of the main components indicated many different C species present in the sample.

(ii) The Ir 4f spectrum is fitted by three components, I_b, I_s, and I_{int}, where I_{int} is a

new component introduced to account for the pinning of the C towards the Ir substrate.

Figure 14.6 shows the C 1s and Ir 4f spectra for pristine Gr/Ir(111) (bottom) and increasing C coverages ranging from 0.03 ML to 1 ML, as indicated. For reasonable peak fitting the BE of the main component in the C 1s spectra was allowed to shift whereas the other three components were kept constant at BEs of 283.5 eV, 284.5 eV, and 284.9 eV. The LFWHM was 0.18 eV for all components and spectra whereas the GFWHM was increased for high C coverages to account for the broadening of the peak (0.21 eV for 0 ML; 0.20 eV for 0.03 ML; 0.24 ML for 0.1 ML; 0.37 eV for 0.3 ML; 0.63 eV for 1 ML). The Ir 4f spectra were fitted with the three components introduced above keeping all parameter except the intensities constant.
The evolution of the C 1s spectra with increasing C coverages shows at 0.03 ML C on Gr/Ir(111) only a broadening of the main peak. At a deposition of 0.1 ML the three new components have to be introduced which gain in intensity upon further deposition. The absence of additional intensity towards higher or lower BEs for the lowest C coverage indicates minor or no rehybridization from sp^2 to sp^3, in line with the observed instability. The Ir 4f spectra for successive C deposition shows an increase of the interface component I_{int} in expense of the surface component I_s, which is in line with an increased amount of C atoms binding to Ir with increasing cluster size.

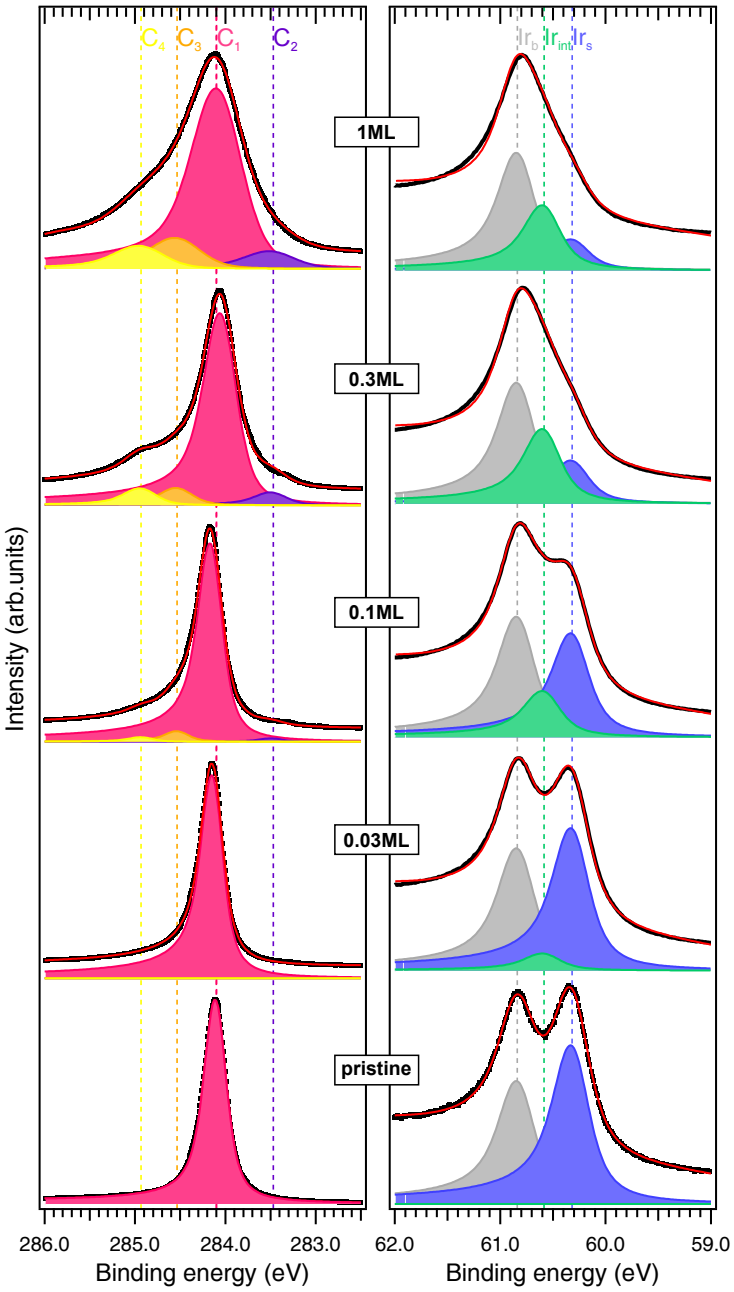

Figure 14.6: Carbon cluster deposition series monitored in C 1s and Ir 4f. C 1s (left) and Ir 4f (right) core level spectra for pristine, 0.03 ML, 0.1 ML, 0.3 ML, and 1 ML C deposition. The experimental spectra are shown as black dots, the fits as solid red lines, and the filled curves represent the components of the fits.

14.4 Thermal Stability

According to our DFT calculations the C cluster superlattice formed close to room temperature represent a metastable configuration where the C atoms are bound 1 eV worse than in a perfect Gr sheet. At these temperatures the C atoms are unable to overcome the small energy barrier involved in the penetration of Gr and therefore become trapped in the local energy minimum and arrange into clusters. To test the stability of the C cluster superlattice and to analyze if the C atoms can be released from its trapping sites we conducted an annealing series.

Figure 14.7 presents the C cluster lattice (a) after deposition of 0.3 ML C at 300 K and after annealing to (b) 870 K, (c) 1070 K, (d) 1270 K, and (e) 1470 K all for 120s. The cluster lattice is almost intact up to 870K. Annealing to higher temperatures causes a gradual decrease in the cluster density as visible from the graph in Figure 14.7(f) presenting the number of clusters per moiré cell as a function of annealing temperature. Further, it becomes apparent that more than 50% of the C clusters are stable even after annealing to 1070K. Besides the decay of the C clusters another interesting observation is made in the STM topographs. Already at 870K small flat islands are present growing in size upon annealing. They can be attributed to Gr bilayer islands. This is highlighted by the profile in Figure 14.7(g) along the green line in (e). Going across a descending step edge from the lower left corner of the image to the upper right, one crosses an area of bilayer Gr. While the height difference measured at the start and end of the profile is approximately 0.2 nm matching the height of an Ir(111) step, in the middle a protrusion is visible exceeding a height of approximately 0.3 nm measured from the lower terrace. This corresponds to the apparent height of bilayer Gr as established above. Since we do not observe ripening of the clusters our results imply no thermally activated diffusion of C clusters on Gr/Ir(111). However, at 870K the C starts to intercalate the Gr and form bilayer Gr.

To explain the transformation from C clusters on top of Gr/Ir(111) to bilayer Gr at the interface we revisit the calculated atomic structure in Figure 14.1(d). The sample cannot be considered as an sp^2 layer with C clusters on top but rather as an sp^2 C layer patterned with areas of sp^3 C including binding towards the substrate. Upon annealing once in a while a C atom is detached from the Gr layer and becomes an adatom at the Ir substrate where it is strongly bound. As in the case of high temperature intercalation the C atoms at the interface accumulate and form a second Gr layer. The cavity formed within the Gr layer by the detachment of a C atom is immediately filled by a C atom from the cluster promoting the cluster decay. This exchange mechanism is similar to the

penetration mechanism presented above and has also been predicted for C adatoms on Gr/Cu(111) by Wu *et al.* [264].

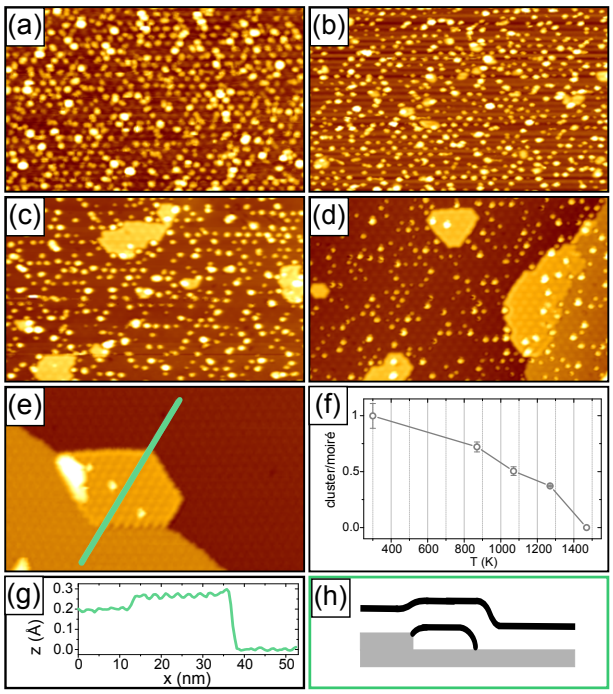

Figure 14.7: Annealing series of 0.3 ML carbon on graphene on Ir(111). (a) 0.3 ML C deposited on Gr/Ir(111) at 300 K and subsequently annealed to (b) 870 K, (c) 1070 K, (d) 1270 K, and (e) 1470 K. Image sizes are 80 nm × 50 nm. (f) Cluster density in clusters per moiré unit cell as a function of annealing temperature. (g) Profile along green line in (e). (h) Schematic illustrating the profile in (g).

Similar to the deposition series in the preceding section we follow the XPS fingerprint of the C cluster decay with increasing temperature. Figure 14.8 displays the C 1s and the Ir 4f spectra for 0.3 ML C deposited at 400 K, where the best-ordered cluster lattice was observed (bottom) and after annealing the same sample to increasing temperatures as indicated in the image. The curve fitting has been done in the same manner as above. The thermal evolution is exactly inverse compared to the formation of the C clusters. With increasing temperature the additional components in the C 1s spectrum decrease concomitant with a decrease of the Ir_{int} component in favor of the Ir_s component. These findings are in line with the STM observations. Upon annealing the C clusters decay and form bilayer Gr at the Gr/Ir(111) interface. This finally results in a recovery of the peak shape of the C 1s component as well as the Ir surface component. A small intensity at the carbide BE remains in the C 1s spectrum which is also reflected in a remaining spectral weight for I_{int} in the Ir 4f spectrum.

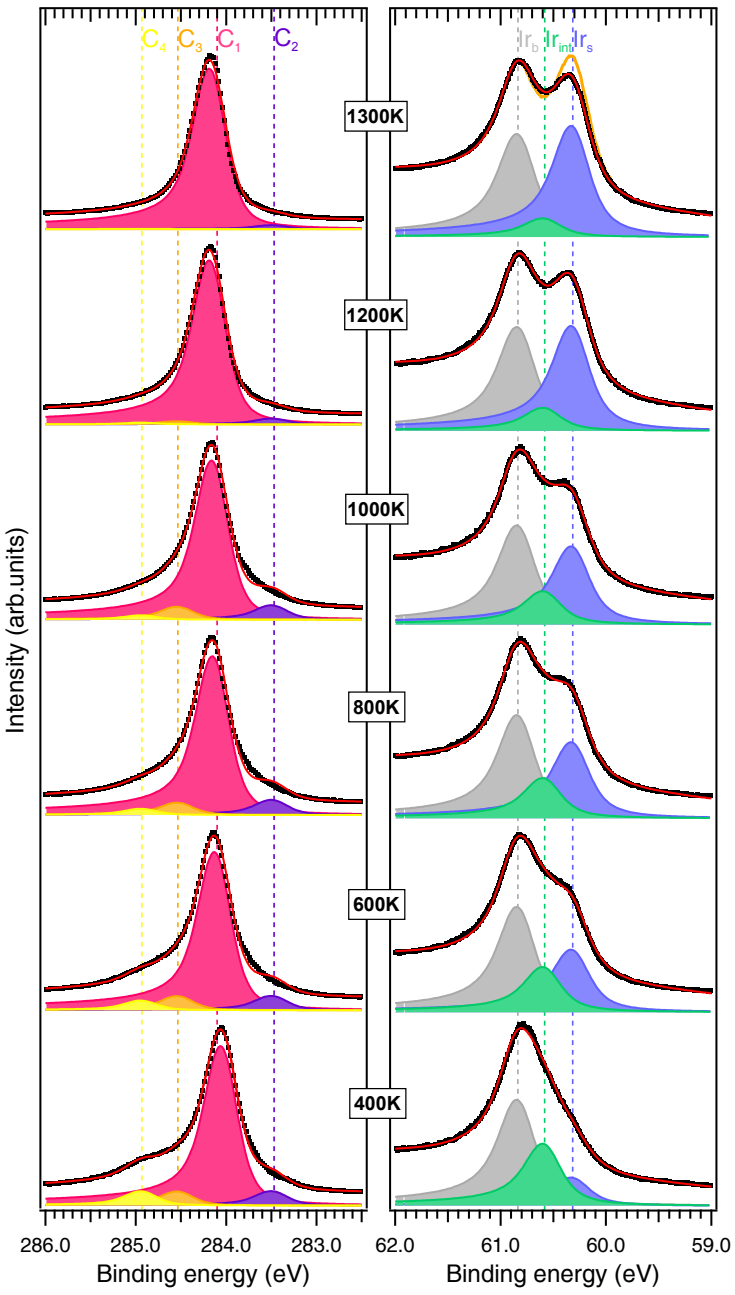

Figure 14.8: Thermal decay of carbon clusters monitored in C 1s and Ir 4f. C 1s, and Ir 4f core level spectra after the deposition of 0.3 ML C onto Gr/Ir(111) at 400 K (bottom) and subsequent annealing to increasing temperature as indicated in the figure. The experimental spectra are shown as black dots, the fits as solid red lines, and the filled curves represent the components of the fits.

Interestingly, we observe that the decay mechanism comes to hold once a second Gr layer has formed at the Gr/Ir(111) interface. To proof this hypothesis, we want to dedicate the next part of our discussion to the annealing of a closed layer of amorphous C on Gr/Ir(111). Figure 14.9(a) represents the Gr/Ir(111) after deposition of 1 ML radical C. The inset shows a close up of the amorphous C and Figure 14.9(c) presents a schematic along the red line in the inset in (a). After deposition we find C clusters on a monolayer of Gr/Ir(111). Figure 14.9(b) shows the sample after annealing to 1470 K for 60 s. The topograph exhibits several Ir steps running from the upper left to the lower right corner of the image. Further it is dominated by bright protrusions similar to the cluster-like structures in (a) but slightly grown in size and additional dark patches are visible. A zoom into the black box in (b) is displayed in (d). The profile along the purple line in (d) is shown in (e) along with the corresponding schematic in (f). The profile starts on C clusters on bilayer Gr, continues to monolayer Gr that crosses a substrate step, and eventually goes to C covered bilayer Gr. The presence of bilayer Gr underneath the amorphous C can best be seen in the dashed circle in Figure 14.9(d) where a small patch is not covered by C clusters. Here it becomes apparent that going from the upper to the lower terrace one goes from monolayer to bilayer Gr.

This experiment shows that independent of how much C is deposited on Gr/Ir(111) at low temperature only one additional layer can be formed at the interface upon annealing to 1470 K. This illustrates that binding towards the metal substrate is a necessary condition for the penetration and decay of the C clusters. The excess C on bilayer Gr is extremely stable and does not penetrate the bilayer. This finding is in line with the theoretical prediction of Wu *et al.* [264] pointing out that the penetration of a bilayer is much more difficult than a monolayer for Gr on Cu(111).

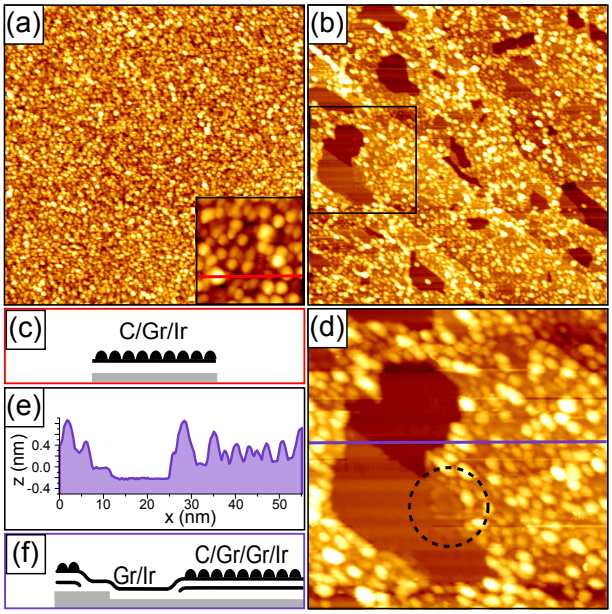

Figure 14.9: Annealing of 1 ML carbon on graphene on Ir(111). STM topograph of 1 ML C deposited on a fully closed Gr film on Ir(111) at room temperature with a zoom in the inset. (b) Sample from (a) after annealing to 1470 K for 60 s. Image sizes are 180 nm × 180 nm and inset 20 nm × 20 nm. (c) Schematic of the profile along the red line in the inset of (a). (d) Zoom of the black box in (b). Image size is 55 nm × 55 nm. (e) and (f) show the corresponding profile and schematic of the purple line in (d).

14.5 Conclusions

In conclusion, in this chapter we provide the first STM study on low temperature C sublimation on Gr/Ir(111) and thereby observe a C cluster superlattice. By STM and XPS measurements as well as DFT calculations we highlight the structure of these C clusters that are comprised of an sp^2 shell and form covalent sp^3 bonds to the Gr layer. Their stability is rooted in sp^3 C bonds from the Gr to the substrate. Once the nucleation regime for small C coverages is overcome a periodic C cluster lattice emerges with the clusters being confined to the moiré unit cell. The cluster superlattice is stable up to temperatures of approximately 800 K and thereafter decays by intercalation into Gr bilayers. Finally, we demonstrated that by room temperature adsorption of radical C and subsequent annealing the number of Gr layers formed at the interface is limited to one since the metal substrate is needed to catalyze the penetration of C atoms.

PART VI

Summary and Outlook

Ion Irradiation

In the first part of this thesis we investigated the phenomena that occur when energetic atoms impinge on a 2D sheet resting on a metal substrate. We demonstrated nearly complete trapping of the incident ions under Gr and hBN at conditions, where without the 2D cover nearly all ions are backscattered into the vacuum. Upon heating the trapped atoms cannot leave from under Gr or hBN up to very high temperatures, but accumulate under the 2D material in blisters, where the gas has pressures of the order of GPa. A unique combination providing chemical information from XPS and TPD complementing each other and microscopic insight by STM was used to identify the trapping effect and morphological consequences upon thermal processing. With the help of two levels of theoretical modeling, *i.e.*, MD simulations and DFT calculations, we reached an unambiguous interpretation of the experimental data of Xe irradiation of Gr on Ir(111). The trapping relies on the combination of two effects. First, for an ion energy of up to a few keV Gr on Ir(111) effectively decreases the probability for ion reflection in favor of ion trapping in between Gr and its substrate. The effect can be traced back to an easy penetration of the Xe ion through the Gr sheet and an efficient energy loss within the heavy substrate. Upon momentum reversal it is unlikely that the decelerated ion penetrates the Gr mesh resulting in immobilization at the interface. Upon annealing, driven by the reduction of elastic and delamination energy of Gr, the Xe accumulates into highly pressurized blisters. The stability of the blisters was explain by means of DFT calculations which revealed the strong binding of Gr edges created due to surface erosion to be the root of stability since out-diffusion is hampered.

To prove that blister formation takes place for a broad range of different ion beam parameters as well as for 2D materials which adhere to a substrate we studied the dependence of trapping and blistering for different ion energies and species. We observed that the above findings for Gr on Ir(111) are valid for the investigated parameter space (Ne^+, Ar^+, Xe^+, 0.1 keV- 5 keV) except for He^+ irradiation. This is explained by a reduced diffusion barrier of He through Gr edges. In view of practical application, this behavior opens up a route towards the realization of a Gr nanomesh [20], *i.e.*, a periodic arrangement of vacancy defects self-assembled within Gr's moiré, fabricated on a metal substrate without noble gas trapping and blister formation.

Additionally, we showed that noble gas trapping and blister formation holds for a second member out of the family of 2D materials, namely hBN. In fact, the data presented in this work constitute the first experimental proof for the extremely high noble gas pressure inside blisters formed by a 2D layer with its substrate. With STM we imaged through

the h-BN blister lid and find a superstructure corresponding in lattice parameter to a crystalline Xe layer. To this end, in order to gain detailed information on the trapping mechanism for hBN covered samples complementing MD simulations could be performed in the future once the corresponding interaction potentials are available. On the other hand, DFT calculations could give insight into the interaction of hBN edges with the substrate to learn about the reduced stability of the trapped species underneath hBN.

Further we showed how ion irradiation and noble gas trapping can be separated from each other to create highly pressurized blisters underneath a perfect Gr or hBN sheet. We envision to use this process to create pressurized nanoreactors with one reagent supplied through release of implanted species from the substrate. Also the growth of interfacial layers, *e.g.*, insulators, could be accomplished by providing a reactant from the bulk after 2D layer growth or transfer and optional intercalation.

On the example of Gr on Ir(111) we elucidated the angle dependence of ion erosion and noble gas trapping. Thereby, the possibility to control the formation of noble gas blisters is shown while it is also presented how to erode 2D layers without the effect of blister formation. It is certainly of interest to study the angular dependence of trapping and sputtering for lighter noble gases and different ion energies by means of MD simulations to find optimal parameters to maximize sputtering with minimal trapping.

Furthermore, we showed that for ion energies below 1 keV a single Gr sheet reduces the erosion rate of the underlying metal by about two orders of magnitude when the sample is kept at elevated temperatures during exposure. We found that the efficient sputtering protection is based on the self-repair of radiation damage in Gr on Ir(111). We speculate that the sputter protection that would inevitable break down during prolonged ion exposure can be maintained by continued regrowth of the shield by supplying a hydrocarbon partial pressure.

For Gr as well as for hBN on Ir(111) we found that Xe^+ irradiation in the energy range from a few 100 eV to a few 1000 eV causes amorphization of the 2D layer material to a considerable extend. Surprisingly, upon annealing, the Gr as well as the h-BN recover to perfection, except for vacancy islands resulting from sputtering and for blisters formed due to aggregation of implanted species. Finally, we showed in a first attempt that the self-repair of Gr can be used beneficially to iron-out wrinkles in the sheet. To this end, surface erosion at large impact angles without noble gas trapping combined with the self-repair of the 2D sheet may pave the way for wrinkle free epitaxial Gr and deserves further investigation.

Carbon Radical Exposure

In the second part of this thesis we provided the first comprehensive picture of the fate of C radicals deposited on Gr/Ir(111) over a wide temeprature range. We revealed that C deposition at high temperatures forces the Gr lattice to accept additional C which results in a dense wrinkle network upon cool-down. This effect is always collateral to bilayer formation. Moreover, we showed that the experimental procedure is of vital importance since the formation of intrinsic wrinkles in CVD Gr is memorized even after reheating and, thereby, enhancing C intercalation and with this bilayer formation. At temperatures of 1200 K we find strong reevaporation of the deposited species. Our findings highlight that the production of high quality bilayer Gr by elemental C deposition is impeded. However, we speculate that high quality Gr bilayer growth without wrinkles is possible through post-growth ion beam treatment at high temperatures and grazing incidence.
Our results suggest that stacked hBN/Gr heterostructures might be realized by C radical deposition onto hBN/Ir(111) at high temeprature. A first attempt to form such a heterostructure on Ir(111) is presented in Appendix A.
In a broad temperature range from 50 K to 550 K atomic carbon deposition onto Gr's moiré with Ir(111) leads to the formation of C clusters. In between 300 K - 400 K a periodic arrangement of one C cluster per moiré unit cell is found resulting in a C cluster superlattice. The size of the carbon clusters is tunable between about 20 and 150 C atoms. For deposited amounts exceeding about 200 C atoms per moiré unit cell the ordering is lost, but still individual clusters remain. The C cluster superlattice is thermally stable up to approximately 800 K. Annealing to higher temperatures results in C intercalation and eventually graphene bilayer formation. On the basis of STM and XPS measurements as well as DFT calculations a model for C cluster formation, structure, stability, and decay is developed. Based on the generality of our model, we speculate that C clusters may form on other moirés of 2D materials with their supporting substrate. A first proof of this hypothesis is shown in the Appendix B on the example of C radical exposure of hBN on Ir(111). The data show that C deposition onto hBN/Ir(111) does not only reveal a cluster superlattice, but the clusters are even more stable than C clusters on Gr/Ir(111). Future work should be devoted to uncover the formation and decay mechanism for C clusters on hBN/Ir(111).
Furthermore, since the C radical source used within the framework of this thesis yields a C vapor containing monomer, trimers, and to a lesser extent dimers it would be of interest to use a C source supplying almost exclusively C monomers. This might change the intercalation mechanism as well as the C cluster formation kinetics.

PART VII

Appendix

APPENDIX A

A Hexagonal Boron Nitride/Graphene Heterostructure

In Chapter 13 we showed that the deposition of elemental C onto Gr/Ir(111) at 1200 K results in C intercalation and eventually Gr bilayer formation. To see if a similar intercalation of hBN with C is possible, in a first attempt, we exposed 1 ML hBN on Ir(111) to 0.3 ML atomic C at 1000 K. The preliminary data is shown in Figure A.1. Intercalated islands are visible at the Ir substrate step edges. The intercalation is proven by the strong interaction of the intercalated flake with the step edge resulting in a rearrangement of the step edge, highlighted by the green circle. However, on top of such intercalated areas clusters emerge. The residual C on top of hBN/Ir(111) might be due to the slightly lower temperature applied in this experiment (compare 1000 K here to 1200 K in Chapter 13). However, it is expected that the penetration of C by the exchange mechanism during C intercalation of Gr/Ir(111) does not take place in the same way for hBN/Ir(111) due to the different chemical nature of the 2D film and the deposited species. Further experiments are needed to get a deeper insight into the nature of the intercalated islands and the formation of hBN/Gr stacked heterostructures in general.

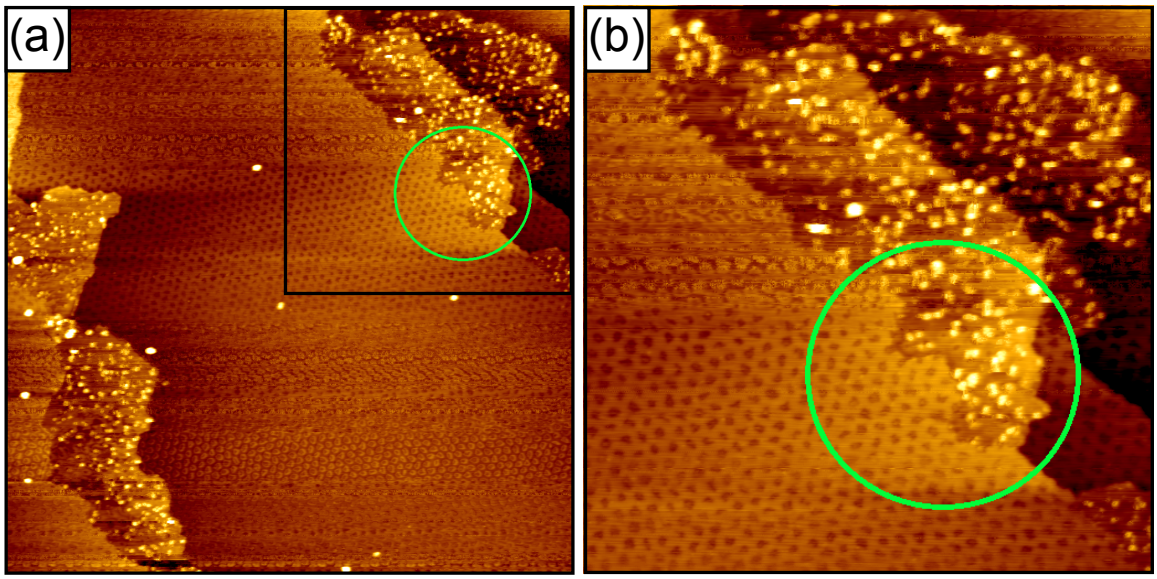

Figure A.1: Hexagonal boron nitride/graphene heterostructure. (a) STM topograph of a full layer hBN/Ir(111) after exposure to 0.3 ML atomic C at 1000 K. (b) Zoom of square in (a). The green circle highlights the interaction between the intercalated island and the Ir substrate step edge. Image sizes are (a) 180 nm × 180 nm and (b) 90 nm × 90 nm.

APPENDIX B

Carbon Clusters on Hexagonal Boron Nitride on Ir(111)

This Appendix is devoted to the investigation of the deposition of C radicals onto the moiré of hBN/Ir(111) by means of STM and XPS measurements and presents data that has not yet been analyzed in detail. Similar to C deposition onto Gr/Ir(111), as presented in Chapter 14, the deposition of C radicals onto hBN/Ir(111) results in cluster formation. Figure B.1 shows STM topographs of (a) 0.3 ML C deposited onto hBN/Ir(111) at 400 K and subsequently annealed to (b) 600 K, (c) 800 K, (d) 1000 K, (e) 1200 K, (f) 1350 K, and finally to (f) 1500 K. Figure B.1(g) presents the corresponding cluster density as a function of annealing temperature (black data). The cluster density with increasing annealing temperature for the same amount of C on Gr/Ir(111) from Chapter 14.4 is also presented in the graph (gray data). It becomes apparent that the C clusters on hBN/Ir(111) are thermally more stable than C clusters on Gr/Ir(111). In fact, the ordering of the clusters seems to improve after annealing to 600 K. Upon annealing to 1000 K areas which might stem from intercalated C emerge. However, the identification of intercalated Gr islands is ambiguous. In Figure B.1(e), (f), and (g) small patches may be attributed to C intercalation. Nevertheless, a significant amount of C clusters remains stable and some C clusters seem to coalesce and accumulate on top of hBN as visible from the bright protrusions. The higher stability as well as the reduced formation of intercalated Gr islands compared to the Gr/Ir(111) case might be traced back to the same cause as the hampered intercalation at high sample temperatures, *i.e.*, the hetero-elemental nature of the deposited species and the 2D film impeding an exchange mechanisms.

For completeness, the corresponding XP spectra of the B 1s, N 1s, C 1s, and Ir 4f regions are shown in Figure B.2. The spectra obtained on the pristine hBN/Ir(111) sample are displayed at the bottom of the graphs. The B 1s and N 1s spectra broaden upon

C deposition and at the same time the Ir 4f surface component is reduced, implying a similar stabilization mechanism of the C clusters, *i.e.*, bindidng of the 2D layer towards the substrate by partial rehybridization from sp^2 to sp^3. The C 1s spectrum presents a broad peak indicating a great variety of C species. Upon annealing not much change is observed, except that the Ir 4f surface peak recovers to some extent. This is in line with the considerable amount of residual clusters observed in STM even at 1300 K. However, for a detailed discussion of the data peak fitting has to be done.

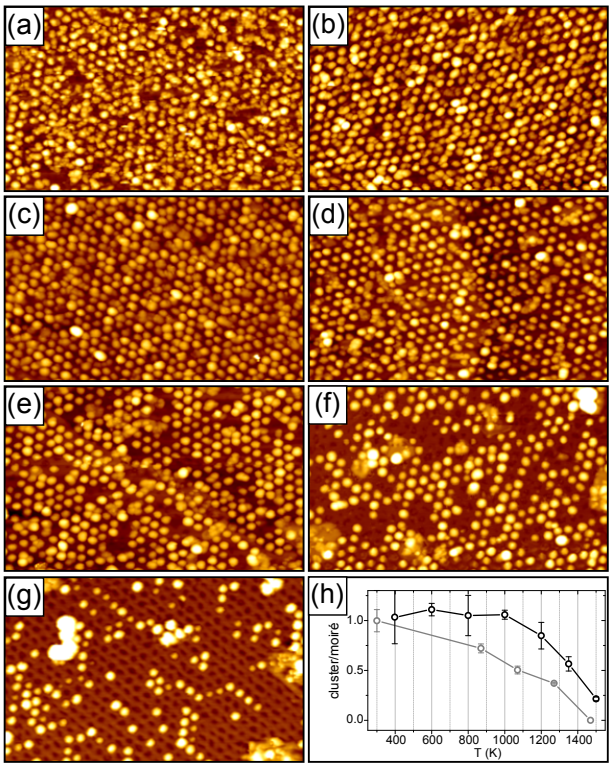

Figure B.1: Annealing series of 0.3 ML carbon on hexagonal boron nitride on Ir(111). (a) 0.3 ML C deposited on hBN/Ir(111) at 400 K and subsequently annealed to (b) 600 K, (c) 800 K, (d) 1000 K, (e) 1200 K, (f) 1350 K, and (g) 1500 K. Image sizes are 80 nm × 50 nm. (h) Cluster density in clusters per moiré unit cell as a function of annealing temperature for C cluster on hBN (black) and on Gr (gray) for comparison.

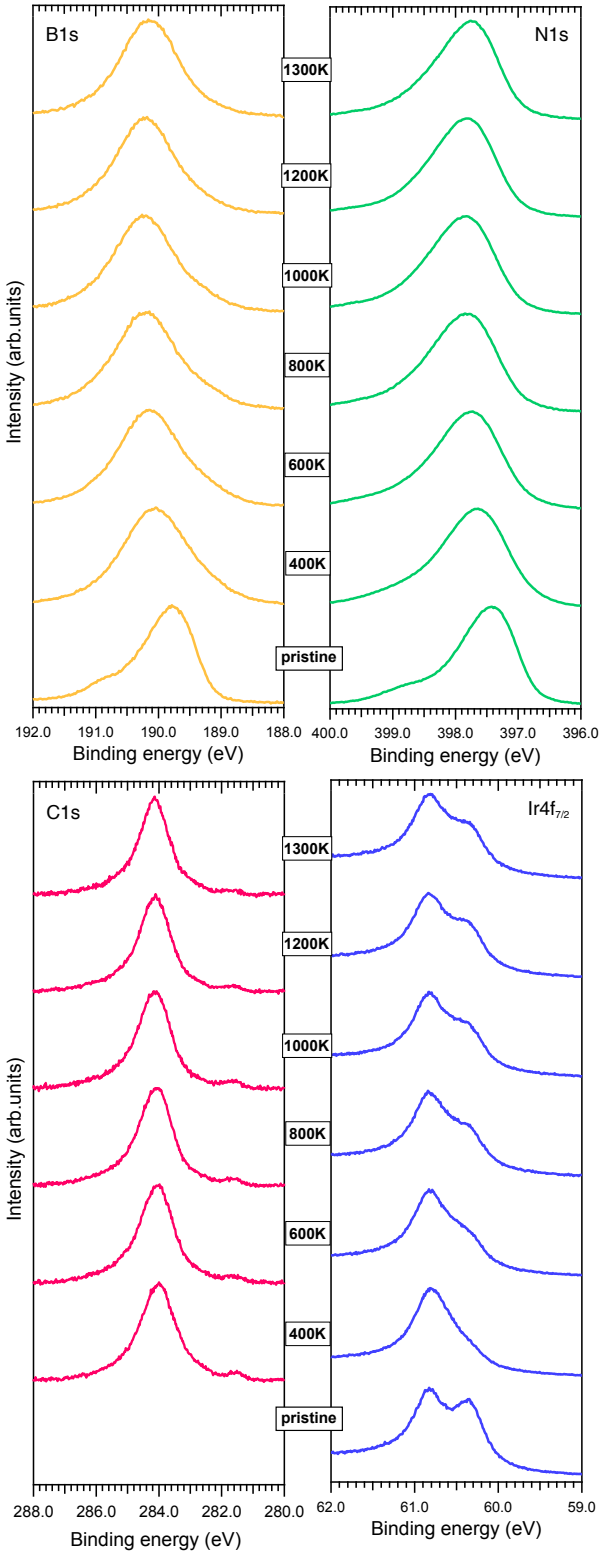

Figure B.2: Thermal decay of carbon clusters monitored by C 1s and Ir 4f. B 1s, N 1s, C 1s, and Ir $4f_{7/2}$ core level spectra of pristine hBN/Ir(111) and after the deposition of 0.3ML C onto hBN/Ir(111) at 400K and subsequent annealing to 600 K, 800 K, 1000 K, 1200 K, and 1300 K, as indicated. The pristine spectra a displayed at the bottom of each graph.

APPENDIX C

Oxygen Etching of Carbon Clusters on Graphene on Ir(111)

In Chapter 14 we studied C cluster superlattices that emerge upon C radical exposure of Gr/Ir(111) at 400 K. We showed that they have a high thermal stability. In this Appendix data that has not yet been analyzed in detail is presented that highlights their stability against oxygen etching.

Figure C.1 shows STM topographs of 0.1 ML C on Gr/Ir(111), each exposed to 750 L O_2 at (a) 400 K, (b) 500 K, and (c) 600 K. Comparing Figure C.1(a) to Figure 14.4(b) from Chapter 14.3 it becomes apparent, that the C cluster superstructure on top of the Gr islands is virtually unchanged to the as deposited superstructure after exposure to 750 L O_2 at 400 K. On the bare Ir(111) one can also identify C clusters. When exposing the same sample to the identical amount of oxygen at 500 K this leads to a reduction of the C clusters on the bare Ir(111), but still leaves the C clusters on Gr almost unchanged. Only after oxygen exposure at 600 K the rim of the Gr islands starts to be etched, as highlighted in the zoom of the red box in Figure C.1(c) displayed in (e). On the bare Ir(111) some adsorbates become visible that may be attributed to residual C and and adsorbed oxygen. The inset of Figure C.1(c) shows the sample after O_2 exposure at 700 K. A clean Ir(111) surface is visible, *i.e.*, all C is etched away.

The STM data shows that etching of C clusters on the bare Ir(111) surface starts at 500 K, whereas the onset of etching for Gr islands covered by C clusters is shifted towards 600 K. The observed trenches at the Ir steps resemble those observed for oxygen etching of Gr/Ir(111) without C clusters [274].

To compare the etching behavior of C cluster covered Gr/Ir(111) to the one of pristine Gr/Ir(111) we conducted a comprehensive XPS study. The data is summarized in Figure C.1 (d). The light and dark gray data point are taken from literature [274]. It becomes

apparent, that depositing 0.3 ML C on 1 ML Gr/Ir(111) (pink circles) shifts the onset of etching to 900 K and the deposition of 1 ML C on 1 ML Gr/Ir(111) (orange squares) even to 1000 K as opposed to 550 K for 0.5 ML pristine Gr/Ir(111) and 720 K for a full ML Gr/Ir(111). These results prove that a full ML Gr/Ir(111) covered with elemental C is more resistant against O_2 etching and even Gr islands on Ir(111) are stabilized by the C clusters. This behavior cannot be traced back to the additional amount of C since this would only slow down the etching process but not shift the onset temperature.

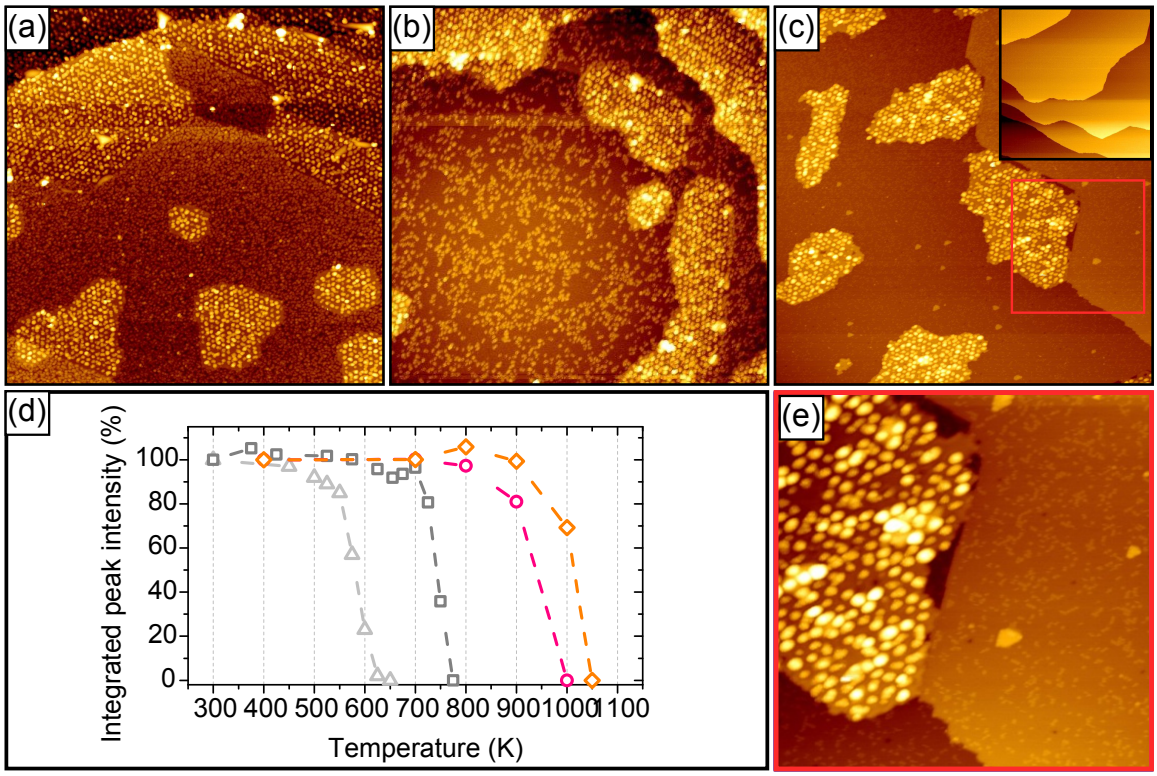

Figure C.1: Oxygen etching of C clusters on graphene on Ir(111). STM topographs of 0.1 ML C on 0.5 ML Gr/Ir(111), each exposed to 750 L O_2 at stepwise increasing temperatures of (a) 400 K, (b) 500 K, (c) 600 K, and to 700 K [inset in (c)]. (e) Zoom of red box in (c). (d) Integrated C 1s peak intensities as a function of temperature for 0.3 ML C (pink circles) and 1 ML C (orange squares) on 1 ML Gr/Ir(111) deposited at 400 K exposed to 750 L O_2 at the respective temperature. For comparison the integrated C 1s peak intensities as a function of temperature for 1ML Gr/Ir(111) (dark gray squares) and 0.5ML Gr/Ir(111) (light gray triangles) exposed to 750 L O_2 at stepwise increasing temperatures are shown (from [274]). Lines to guide the eye.

APPENDIX D

Deutsche Kurzzusammenfassung *(German Abstract)*

In den letzten Jahren sind zweidimensionale Materialien wie Graphen und Monolagen von hexagonalem Bornitrid aufgrund ihrer außergewöhnlichen Eigenschaften in den Fokus von Forschung und Wissenschaft gerückt. Die vorliegende Arbeit widmet sich der Untersuchung der Phänomene die auftauchen, wenn man Graphen und einschichtiges hexagonales Bornitrid, die beide auf einem Substrat ruhen, Ionenbeschuss und Bestrahlung mit Kohlenstoffradikalen aussetzt. Mit Hilfe von Rastertunnelmikroskopie und niederenergetischer Elektronenbeugung wird die resultierende Oberflächenmorphologie untersucht, wohingegen Röntgenphotoelektronenspektroskopie und temperatur-programmierte Desorption chemische Informationen liefern. Die experimentellen Daten werden durch molekulardynamischen Simulationen und Berechnungen im Rahmen der Dichtefunktionaltheorie untermauert, welche die mikroskopischen Mechanismen beleuchten.

Im ersten Teil wird die Reaktion von Graphen und einschichtigem hexagonales Bornitrid, die beide auf einem Substrat ruhen, auf Ionenstrahlen untersucht. Wir zeigen, dass über einen weiten Parameterraum Ionenbeschuss von Graphen und einschichtigem hexagonalem Bornitrid dazu führt, dass Edelgas in der Zwischenlage der zweidimensionalen Schicht und der Metallunterlage eingefangen wird. Die zweidimensionalen Lagen wirken wie ein Einwegventil, das beim Ausheilen die eingefangenen Atome unter hohem Druck in Blasen versiegelt. Es zeigt sich, dass der Einwegvetil-Effekt aus der Tatsache resultiert, dass die energetischen Teilchen die zweidimensionale Lage leicht passieren können, dann den größten Teil ihrer Energie an das Substrat verlieren und damit ein Entkommen durch wiederholtes Passieren der zweidimensionale Schicht nahezu unmöglich wird. Obwohl die zweidimensionale Lage stark perforiert ist, führt die starke Wechselwirkung der Kanten der durch den Ionenbeschuss entstandenen Löcher dazu, dass ein Entkommen von unter-

halb verhindert wird. Da dieses Phänomen sowohl für Graphen als auch für hexagonales Bornitrid stattfindet, kann man davon ausgehen, dass dies auch für ein breites Spektrum an Materialien aus der Familie der zweidiemnsionalen Schichten gilt.

Wir beschreiben Möglichkeiten, um das Entstehen von Blasen während des Graphenwachstums zu verhindern und demonstrieren, wie Ionenimplantation gezielt genutzt werden kann, um Blasen ohne Beschädigung der zweidimensionalen Lage zu erzeugen.

Durch das Verändern des Einfallwinkels während des Ionenbeschusses haben wir herausgefunden, dass bei einem großen Aufprallwinkel das Graphen erodiert werden kann, ohne Edelgase einzufangen. Diese Erkenntnis ist von hoher Relevanz, um ungewollte Effekte während der Nanostrukturierung von Graphen mit Hilfe von Ionenbeschuss zu verhindern.

Desweiteren bilden wir mit Hilfe von Rastertunnelmikroskopie durch den Deckel aus einlagigem hexagonalem Bornitrid eine Überstruktur ab, die den Gitterparameter einer kristallinen Xe Lage aufweist. Daraus schlussfolgern wir, dass die starke Adhäsion des einschichtigem hexagonalem Bornitrids zum Iridium extreme Drücke im GPa-Bereich verursacht und zu einer Verfestigung des Xenon führt.

Durch den Beschuss von Graphen und einschichtigem hexagonalem Bornitrid mit hohen Ionenfluenzen werden die zweidimensionalen Lagen amorphisiert. Überraschenderweise erholen sich beide Materialien nach dem Ausheilen wieder bis hin zur Perfektion. Es bleiben ausschließlich Leerstelleninseln, die durch die Ionenerosion entstehen, und edelgasgefüllte Blasen erhalten.

Schließlich untersuchen wir das Potential von Graphen als Erosionsschutz für das darunterliegende Metallsubstrat. Es wird gezeigt, dass der wirksame Zerstäubungsschutz auf der Selbstheilung des ioneninduzierten Schadens im Graphen beruht, welche bei Temperaturen im Bereich des Wachstums über die chemische Gasphasenabscheidung effizient stattfindet.

Der zweite Teil dieser Arbeit widmet sich der Deposition von Kohlenstoffradikalen auf Graphen auf Ir(111). Wir diskutieren umfangreich die verschiedenen Wege für Kohlenstoffradiakale in Wechselwirkung mit Graphen auf Ir(111) über einen weiten Temperaturbereich. Bei hohen Temperaturen beobachten wir das Wachstum von zweilagigem Graphen. Darüber hinaus liefern wir Beweise für den bisher unbekannten Mechanismus des Einbaus von Kohlenstoff in die bestehende Graphenlage. Dies führt zu einer Verdichtung innerhalb der Lage und schließlich zu Faltenbildung während des Abkühlprozesses.

Die Entdeckung dieses Phänomens ist für das Wachstum von Graphen Bilagen durch Deposition von atomaren Kohlenstoff von größter Bedeutung, da die Bildung von Falten die Qualität des Graphens vermindert. Bei tiefen Temperaturen decken wir auf, dass durch Kohlenstoffdeposition auf das moiré, das sich ausbildet wenn Graphen auf Iridium ruht, periodische Kohlenstoffcluster gebildet werden.

APPENDIX E

Liste der Teilpublikationen
(List of Publications)

Teile dieser Arbeit wurden bereits veröffentlicht in den folgenden Fachzeitschriften:
Parts of the results presented in this thesis can be found in the following publications:

[275] C. Herbig, T. Knispel, S. Simon, U. A. Schröder, A. J. Martínez-Galera, M. A. Arman, C. Teichert, J. Knudsen, A. V. Krasheninnikov, and T. Michely
From Permeation to Cluster Arrays: Graphene on Ir(111) Exposed to Carbon Vapor
under review (2017)

[216] P. Valerius, C. Herbig, M. Will, M. A. Arman, J. Knudsen, N. Atodiresei, V. Caciuc, and T. Michely
From amorphization to a triangular 2D world: annealing of ion irradiated hexagonal boron nitride on Ir(111)
in preparation (2017)

[172] C. Herbig, E. H. Åhlgren, and T. Michely
Blister-free ion beam patterning of supported graphene
Nanotechnology **28**, 055304 (2017)

[122] C. Herbig and T. Michely
Graphene: the ultimately thin sputtering shield
2D Materials **3**, 025032 (2016)

[77] C. Herbig, E. H. Åhlgren, U. A. Schröder, A. J. Martínez-Galera, M. A. Arman, J. Kotakoski, J. Knudsen, A. V. Krasheninnikov, and T. Michely
Xe irradiation of graphene on Ir(111): From trapping to blistering
Physical Review B **92**, 085429 (2015)

[121] C. Herbig, E. H. Åhlgren, U. A. Schröder, A. J. Martínez-Galera, M. A. Arman, W. Jolie, C. Busse, J. Kotakoski, J. Knudsen, A. V. Krasheninnikov, and T. Michely
Comment on "Interfacial Carbon Nanoplatelet Formation by Ion Irradiation of Graphene on Ir(111)"
ACS Nano **9**, 4664 (2015)

[120] C. Herbig, E. H. Åhlgren, W. Jolie, C. Busse, J. Kotakoski, A. V. Krasheninnikov, and T. Michely
Interfacial Carbon Nanoplatelet Formation by Ion Irradiation of Graphene on Ir(111)
ACS Nano **8**, 12208 (2014)

Weitere Publikationen:
Further publications:

[72] U. A. Schröder, M. Petrovič, T. Gerber, E. Grånäs, A. J. Martínez-Galera, M. A. Arman, C. Herbig, J. Schnadt, M. Kralj, J. Knudsen, and T. Michely
Core level shifts of doped graphene
2D Materials **4**, 015013 (2017)

[20] S. Standop, O. Lehtinen, C. Herbig, G. Lewes-Malandrakis, F. Craes, J. Kotakoski, T. Michely, A. V. Krasheninnikov, and C. Busse
Ion Impacts on Graphene/Ir(111): Interface Channeling, Vacancy Funnels, and a Nanomesh
Nano Letters **13**, 1948 (2013)

[71] C. Herbig, M. Kaiser, N. Bendiab, S. Schumacher, D. F. Förster, J. Coraux, K. Meerholz, T. Michely, and C. Busse
Mechanical exfoliation of epitaxial graphene on Ir(111) enabled by Br_2 intercalation
Journal of Physics: Condensed Matter **24**, 314208 (2012)

Konferenzbeiträge als präsentierender Autor:
Conference contributions to:

- 76th Physical Electronics Conference, Contributed talk, Fayetteville (USA), June 2016
- The European Workshop on Epitaxial Graphene and 2D Materials, Contributed talk, Bergisch Gladbach (DEU), May 2016
- APS March Meeting, Contributed talk, Baltimore (USA), March 2016
- DPG Frühjahrstagung der Sektion Kondensierte Materie, Contributed talk, Regensburg (DEU), March 2016
- 21st International Workshop on Inelastic Ion-Surface Collisions, Invited talk, Donostia-San Sebastián (ESP), October 2015
- Ion-Surface Interactions, Poster, Moscow (RUS), August 2015
- 3. SPP Workshop, Contributed talk, Kremmen (GER), May 2015
- The European Workshop on Epitaxial Graphene and 2D Materials, Contributed talk, Primosten (HRV), June 2014
- DPG Frühjahrstagung der Sektion Kondensierte Materie, Contributed talk, Berlin (DEU), April 2014
- Towards Reality in Nanoscale Materials VII, Contributed talk, Levi (FIN), February 2014
- International Symposium on Nanoscale Pattern Formation at Surfaces, Contributed talk, Copenhagen (DNK), May 2013
- DPG Spring Meeting, Poster, Berlin (DEU), March 2012

Preise und Auszeichnungen:
Awards and Honors:

- Wayne B. Nottingham Prize, Physical Electronics Conference, Fayetteville, 2016
- Ovshinsky Student Travel Grant Award, APS March Meeting, Baltimore, 2016
- Poster Prize of the 22nd International Conference: Ion-Surface Interactions, Moscow, 2015
- Member of the Honors Branch of the Bonn Cologne Graduate School of Physics and Astronomy (scholarship)

APPENDIX F

Danksagung *(Acknowledgements)*

Zum Gelingen dieser Arbeit haben viele Personen auf unterschiedliche Art und Weise beigetragen. Bei diesen möchte ich mich abschließend herzlich bedanken.

Many people have in different ways contributed to the success of this work. To those I would finally like to express my gratitude.

- An erster Stelle danke ich **Prof. Dr. Thomas Michely**. Mit seiner Vorlesung hat er mein Interesse für die Festkörperphysik geweckt. Im Rahmen meiner Bachelor- und Masterarbeit und schließlich während meiner Promotion hat er mir die Möglichkeit gegeben, an interessanten Forschungsthemen, in Kooperation mit anderen Forschungseinrichtungen und Partnern, zu arbeiten. Unsere vielen Diskussionen und die darin aufgeworfenen kritischen Fragen sowie die unzähligen hilfreichen Tipps haben maßgeblich zu dem Gelingen dieser Arbeit beigetragen.

- Ich danke auch **Prof. Dr. Marika Schleberger** für das Interesse an meiner Arbeit und die Übernahme des Zweitgutachtens.

- Bei **Prof. Dr. Joachim Krug** bedanke ich mich für die Bereitschaft, den Vorsitz der Prüfungskommission zu übernehmen.

- Bei **Dr. Andrea Severing** bedanke ich mich für die Übernahme des Beisitzes.

- Ich danke **Timo Knispel**, **Sabina Simon**, **Philipp Valerius** und **Moritz Will**, die im Rahmen ihrer Bachelor- bzw. Masterarbeit zum Gelingen dieser Arbeit beigetragen haben.

- Für das Korrekturlesen bedanke ich mich bei **Philipp Valerius**, **Ulrike Schröder**, **Wouter Jolie**, **Timm Gerber**, **Stefan Schumacher** sowie **Nadine Herbig**.

This work was in large parts done in the context of cooperations and I want to express my gratitude to all collaborators.

- *I want to thank* ***Arkady V. Krasheninnikov*** *from the Aalto University, Aalto, Finland and the Helmholtz-Zentrum Dresden-Rossendorf, Dresden, Germany, who performed all density functional theory calculations within this work. Thank you for your work, the nice conference in Levi, and all the valuable advice and comments.*

- ***E. Harriet Åhlgren*** *and* ***Jani Kotakoski*** *from the University of Helsinki, Helsinki, Finland, now University of Nottingham, Nottingham, UK and University of Vienna, Vienna, Austria, respectively, who performed the molecular dynamics simulations on the ion irradiation of graphene and contributed a lot to this thesis. Thank you for your great work and special thanks to Harriet for her ongoing efforts and the great time we spent so far off physics.*

- *I would like to thank* ***Jan Knudsen*** *and* ***Alif Arman*** *from the the Division of Synchrotron Radiation Research and the MAX IV Laboratory, Lund, Sweden, who taught me how to acquire XP spectra and how to analyze them. I really appreciate your hospitality during my stay in Lund and the company during shifts at Max-lab. I also want to acknowledge the Max-lab staff for their valuable support during beamtimes.*

- Ein besonderer Dank geht an **Norbert Henn** für das Lösen vieler technischer Probleme und die stets von guter Laune begleitete Hilfe an den Anlagen.

- Bei meinen Kollegen, mit denen ich ein Büro teilen durfte, möchte ich mich für die schöne Atmosphäre und für die zahlreichen Tipps und spannenden Gespräche bedanken. Allen voran Ulrike Schröder, mit der ich auf viele schöne und vorallem lustige Momente zurückblicken kann, Ferdinand Farwick von und zum Hagen für die leider viel zu kurze gemeinsame Zeit im Büro und bei Stefan Kraus, der endlich etwas Ordnung ins Büro gebracht hat - zumindest auf seinem Schreibtisch.

- Desweiteren möchte ich mich bei allen anderen bisher ungenannten Mitgliedern oder ehemaligen Mitgliedern der Arbeitsgruppe Michely für die freundliche und produktive Atmosphäre bedanken sowie bei allen Mitarbeitern des II. Physikalischen Instituts, insbesondere den Werkstätten und Sekretariaten.

- Ich danke der Bonn-Cologne Graduate School of Physics and Astronomy für die eröffneten Möglichkeiten und die finanzielle Unterstützung. Vor allem geht mein Dank hier an Petra Neubauer-Guenther, die mir immer eine große Hilfe war.

- Bei meinen Freunden möchte ich mich für ihre Untersützung und ihr Verständnis bedanken.
- Zu guter Letzt möchte ich mich von ganzem Herzen bei meiner Familie und insbesondere meinen Eltern bedanken, die immer für mich da waren und mich mein ganzes Leben uneingeschränkt untersützt haben. Danke!

APPENDIX G

Bibliography

[1] K. S. Novoselov et al.: "Electric field effect in atomically thin carbon films." *Science* **306** 666–669 (2004). DOI: 10.1126/science.1102896. (Cit. on pp. 3, 7, 8, 14, 143).

[2] A. K. Geim and I. V. Grigorieva: "Van der Waals heterostructures". *Nature* **499** 419–425 (2013). DOI: 10.1038/nature12385. (Cit. on p. 3).

[3] S. Z. Butler et al.: "Progress, challenges, and opportunities in two-dimensional materials beyond graphene." *ACS Nano* **7** 2898–2926 (2013). DOI: 10.1021/nn400280c. (Cit. on p. 3).

[4] M. Xu et al.: "Graphene-like two-dimensional materials." *Chem. Rev.* **113** 3766–3798 (2013). DOI: 10.1021/cr300263a. (Cit. on p. 3).

[5] A. K. Geim and K. S. Novoselov: "The rise of graphene." *Nat. Mater.* **6** 183–91 (2007). DOI: 10.1038/nmat1849. (Cit. on p. 3).

[6] A. H. Castro Neto et al.: "The electronic properties of graphene". *Rev. Mod. Phys.* **81** 109–162 (2009). DOI: 10.1103/RevModPhys.81.109. (Cit. on pp. 3, 8).

[7] A. K. Geim: "Graphene: status and prospects." *Science* **324** 1530–1534 (2009). DOI: 10.1126/science.1158877. (Cit. on pp. 3, 8).

[8] F. Schwierz: "Graphene transistors." *Nat. Nanotechnol.* **5** 487–496 (2010). DOI: 10.1038/nnano.2010.89. (Cit. on pp. 3, 8).

[9] Y. Zhang et al.: "Direct observation of a widely tunable bandgap in bilayer graphene". *Nature* **459** 820–823 (2009). DOI: 10.1038/nature08105. (Cit. on p. 3).

[10] S.-H. Lee et al.: "A graphite foil electrode covered with electrochemically exfoliated graphene nanosheets". *Electrochem. commun.* **12** 1419–1422 (2010). DOI: 10.1016/j.elecom.2010.07.036. (Cit. on p. 3).

[11] S. Nie et al.: "Growth from below: graphene bilayers on Ir(111)." *ACS Nano* **5** 2298–2306 (2011). DOI: 10.1021/nn103582g. (Cit. on pp. 3, 143).

[12] J. Gómez Díaz et al.: "Hexagonal boron nitride on transition metal surfaces". *Theor. Chem. Acc.* **132** 1350 (2013). DOI: 10.1007/s00214-013-1350-z. (Cit. on pp. 3, 10).

[13] K. Watanabe, T. Taniguchi, and H. Kanda: "Direct-bandgap properties and evidence for ultraviolet lasing of hexagonal boron nitride single crystal". *Nat. Mater.* **3** 404–409 (2004). DOI: 10.1038/nmat1134. (Cit. on pp. 3, 10).

[14] M. Liu et al.: "Quasi-freestanding monolayer heterostructure of graphene and hexagonal boron nitride on Ir(111) with a zigzag boundary". *Nano Lett.* **14** 6342–6347 (2014). DOI: 10.1021/nl502780u. (Cit. on pp. 3, 14).

[15] P. S. Goh and A. F. Ismail: "Graphene-based nanomaterial : The state-of-the-art material for cutting edge desalination technology". *Desalination* **356** 115–128 (2015). DOI: 10.1016/j.desal.2014.10.001. (Cit. on p. 3).

[16] M. E. Suk and N. R. Aluru: "Water transport through ultrathin graphene". *J. Phys. Chem. Lett.* **1** 1590–1594 (2010). DOI: 10.1021/jz100240r. (Cit. on p. 3).

[17] Z. Wang et al.: "Modification of defect structures in graphene by electron irradiation: Ab initio molecular dynamics simulations". *J. Phys. Chem. C* **116** 16070–16079 (2012). DOI: 10.1021/jp303905u. (Cit. on pp. 3, 115).

[18] D. Cohen-Tanugi and C. Grossman: "Water desalination across nanoporous graphene". *Nano Lett.* **12** 3602–3608 (2012). DOI: 10.1021/nl3012853. (Cit. on p. 3).

[19] W. Lei et al.: "Porous boron nitride nanosheets for effective water cleaning". *Nat. Commun.* **4** 1777 (2013). DOI: 10.1038/ncomms2818. (Cit. on p. 3).

[20] S. Standop et al.: "Ion impacts on graphene/Ir(111): interface channeling, vacancy funnels, and a nanomesh." *Nano Lett.* **13** 1948–1955 (2013). DOI: 10.1021/nl304659n. (Cit. on pp. 3, 26, 43, 45, 57, 58, 60, 70, 72, 79, 80, 83, 87, 93, 96, 98, 109, 115, 116, 124, 130, 146, 175, 194).

[21] B. M. U. Scherzer: *Sputtering by Particle Bombardment II.* Ed. by R. Behrisch. Vol. 52. Springer Berlin (1983), p. 271. (Cit. on pp. 4, 50, 61).

[22] M. Bruel: "Silicon on insulator material technology". *Electron. Lett.* **31** 1201 (1995). DOI: 10.1049/el:19950805. (Cit. on pp. 4, 50).

[23] V. K. Alimov et al.: "Helium reemission, desorption and microstructure evolution of graphites under helium ion implantation". *J. Appl. Phys.* **78** 137 (1995). DOI: 10.1063/1.360664. (Cit. on pp. 4, 50).

[24] V. N. Chernikov, W. Kesternich, and H. Ullmaier: "Radiation effects and gas cavities in pyrolytic graphite implanted with helium ions". *J. Nucl. Mater.* **227** 157–169 (1996). DOI: 10.1016/0022-3115(95)00157-3. (Cit. on pp. 4, 50).

[25] F. Guinea, M. I. Katsnelson, and A. K. Geim: "Energy gaps and a zero-field quantum Hall effect in graphene by strain engineering". *Nat. Phys.* **6** 30–33 (2010). DOI: 10.1038/nphys1420. (Cit. on pp. 4, 50).

[26] N. Levy et al.: "Strain-induced pseudo-magnetic fields greater than 300 tesla in graphene nanobubbles". *Science* **329** 544–547 (2010). DOI: 10.1126/science.1191700. (Cit. on pp. 4, 50, 80).

[27] J. Lu, A. C. Neto, and K. P. Loh: "Transforming moiré blisters into geometric graphene nano-bubbles". *Nat. Commun.* **3** 823 (2012). DOI: 10.1038/ncomms1818. (Cit. on pp. 4, 50).

[28] T. Georgiou et al.: "Graphene bubbles with controllable curvature". *Appl. Phys. Lett.* **99** 093103 (2011). DOI: 10.1063/1.3631632. (Cit. on pp. 4, 49).

[29] N. G. Boddeti et al.: "Mechanics of adhered, pressurized graphene blisters". *J. Appl. Mech.* **80** 040909 (2013). DOI: 10.1115/1.4024255. (Cit. on pp. 4, 49, 50).

[30] J. M. Macleod and F. Rosei: "Molecular self-assembly on graphene". *small* **10** 1038–1049 (2014). DOI: 10.1002/smll.201301982. (Cit. on p. 4).

[31] H. Dil et al.: "Surface trapping of atoms and molecules with dipole rings". *Science* **319** 1824–1826 (2008). DOI: 10.1126/science.1154179. (Cit. on p. 4).

[32] A. T. N'Diaye et al.: "Two-dimensional Ir cluster lattice on a graphene moiré on Ir(111)". *Phys. Rev. Lett.* **97** 215501 (2006). DOI: 10.1103/PhysRevLett.97.215501. (Cit. on pp. 4, 80).

[33] F. Schulz et al.: "Templated self-assembly and local doping of molecules on epitaxial hexagonal boron nitride". *ACS Nano* **7** 11121–11128 (2013). DOI: 10.1021/nn404840h. (Cit. on p. 4).

[34] I. Brihuega et al.: "Electronic decoupling and templating of Co nanocluster arrays on the boron nitride nanomesh". *Surf. Interface* **602** L95–L99 (2008). DOI: 10.1016/j.susc.2008.04.040. (Cit. on p. 4).

[35] A. K. Geim: "Nobel Lecture : Random walk to graphene". *Rev. Mod. Phys.* **83** 851–862 (2011). DOI: 10.1103/RevModPhys.83.851. (Cit. on p. 7).

[36] P. R. Wallace: "The Band Theory of Graphite". *Phys. Rev.* **71** 622–634 (1947). DOI: 10.1103/PhysRev.71.622. (Cit. on p. 7).

[37] K. S. Novoselov et al.: "Two-dimensional atomic crystals." *Proc. Natl. Acad. Sci. U. S. A.* **102** 10451–10453 (2005). DOI: 10.1073/pnas.0502848102. (Cit. on p. 8).

[38] Y. Zhang et al.: "Experimental observation of the quantum Hall effect and Berry's phase in graphene." *Nature* **438** 201–204 (2005). DOI: 10.1038/nature04235. (Cit. on p. 8).

[39] M. I. Katsnelson, K. S. Novoselov, and A. K. Geim: "Chiral tunnelling and the Klein paradox in graphene". *Nat. Phys.* **2** 620–625 (2006). DOI: 10.1038/nphys384. (Cit. on p. 8).

[40] R. R. Nair et al.: "Fine structure constant defines". *Science* **320** 1308 (2008). DOI: 10.1126/science.1156965. (Cit. on p. 8).

[41] S. Bae et al.: "Roll-to-roll production of 30-inch graphene films for transparent electrodes". *Nat. Nanotechnol.* **5** 574–578 (2010). DOI: 10.1038/nnano.2010.132. (Cit. on p. 8).

[42] B. X. Li et al.: "Graphene-on-silicon Schottky junction solar cells". *Adv. Mater.* **22** 2743–2748 (2010). DOI: 10.1002/adma.200904383. (Cit. on p. 8).

[43] C. Berger et al.: "Ultrathin epitaxial graphite : 2D electron gas properties and a route toward graphene-based nanoelectronics". *J. Phys. Chem. B* **108** 19912–19916 (2004). DOI: 10.1021/jp040650f. (Cit. on p. 8).

[44] M. I. Katsnelson: "Graphene : carbon in two dimensions". *Mater. today* **10** 20–27 (2007). DOI: 10.1016/S1369-7021(06)71788-6. (Cit. on p. 8).

[45] C. Berger et al.: "Electronic confinement and coherence in patterned epitaxial graphene". *Science* **312** 1191–1196 (2006). DOI: 10.1126/science.1125925. (Cit. on p. 8).

[46] A. T. N'Diaye et al.: "Structure of epitaxial graphene on Ir(111)". *New J. Phys.* **10** 043033 (2008). DOI: 10.1088/1367-2630/10/4/043033. (Cit. on p. 8).

[47] C. Busse et al.: "Graphene on Ir(111): Physisorption with chemical modulation". *Phys. Rev. Lett.* **107** 36101–36104 (2011). DOI: 10.1103/PhysRevLett.107.036101. (Cit. on pp. 8, 9, 61).

[48] F. Farwick zum Hagen et al.: "Structure and growth of hexagonal boron nitride on Ir(111)". *ACS Nano* (2016). DOI: 10.1021/acsnano.6b05819. (Cit. on pp. 9–13, 27, 106, 109, 111, 113, 127).

[49] D. Usachov et al.: "Quasifreestanding single-layer hexagonal boron nitride as a substrate for graphene synthesis". *Phys. Rev. B* **82** 075415 (2010). DOI: 10.1103/PhysRevB.82.075415. (Cit. on p. 10).

[50] Y. Wang et al.: "Electrochemical delamination of CVD-grown graphene film: toward the recyclable use of copper catalyst." *ACS Nano* **5** 9927–9933 (2011). DOI: 10.1021/nn203700w. (Cit. on p. 10).

[51] F. Withers et al.: "Light-emitting diodes by band-structure engineering in van der Waals heterostructures". *Nat. Mater.* **14** 301–306 (2015). DOI: 10.1038/NMAT4205. (Cit. on p. 10).

[52] W. Auwärter et al.: "Defect lines and two-domain structure of hexagonal boron nitride films on Ni (1 1 1)". *Surf. Sci.* **545** 735–740 (2003). DOI: 10.1016/j.susc.2003.08.046. (Cit. on pp. 10, 111).

[53] H. Cun et al.: "Immobilizing individual atoms beneath a corrugated single layer of boron nitride." *Nano Lett.* **13** 2098–2103 (2013). DOI: 10.1021/nl400449y. (Cit. on pp. 10, 50, 101, 137).

[54] F. Orlando et al.: "Epitaxial growth of hexagonal boron nitride on Ir(111)". *J. Phys. Chem. C* **116** 157–164 (2012). DOI: 10.1021/jp207571n. (Cit. on pp. 10, 127).

[55] A. B. Preobrajenski et al.: "Monolayer h-BN on lattice-mismatched metal surfaces : On the formation of the nanomesh". *Chem. Phys. Lett.* **446** 119–123 (2007). DOI: 10.1016/j.cplett.2007.08.028. (Cit. on p. 10).

[56] F. Schulz et al.: "Epitaxial hexagonal boron nitride on Ir (111): A work function template". *Phys. Rev. B* **89** 235429 (2014). DOI: 10.1103/PhysRevB.89.235429. (Cit. on p. 10).

[57] A. T. N'Diaye et al.: "In situ observation of stress relaxation in epitaxial graphene". *New J. Phys.* **11** 113056 (2009). DOI: 10.1088/1367-2630/11/11/113056. (Cit. on pp. 12, 13, 128, 152).

[58] H. Hattab et al.: "Interplay of wrinkles, strain, and lattice parameter in graphene on iridium." *Nano Lett.* **12** 678–682 (2012). DOI: 10.1021/nl203530t. (Cit. on p. 13).

[59] H. Hattab et al.: "Growth temperature dependent graphene alignment on Ir(111)". *Appl. Phys. Lett.* **98** 141903 (2011). DOI: 10.1063/1.3548546. (Cit. on pp. 13, 144).

[60] M. Petrovic et al.: "Wrinkles of graphene on Ir (1 1 1): Macroscopic network ordering and internal multi-lobed structure". *Carbon* **94** 856–863 (2015). DOI: 10.1016/j.carbon.2015.07.059. (Cit. on p. 13).

[61] M. Petrović et al.: "The mechanism of caesium intercalation of graphene." *Nat. Commun.* **4** 2772 (2013). DOI: 10.1038/ncomms3772. (Cit. on pp. 13, 14, 153).

[62] G. L. Doll et al.: "Intercalation of hexagonal boron nitride with potassium". *J. Appl. Phys.* **66** 2554–2558 (1989). DOI: 10.1063/1.344219. (Cit. on p. 14).

[63] M. Dresselhaus and G. Dresselhaus: "Intercalation compounds of graphite". *Adv. Phys.* **30** 139–326 (1981). DOI: 10.1080/00018738100101367. (Cit. on p. 14).

[64] N. R. Gall' et al.: "Intercalation of two-dimensional graphite films on metals by atoms and molecules". *Tech. Phys.* **44** 1066–1068 (1999). DOI: 10.1134/1.1259472. (Cit. on p. 14).

[65] W. Auwärter et al.: "Co on h-BN / Ni (1 1 1): From island to island-chain formation and Co intercalation". *Surf. Sci.* **511** 379–386 (2002). DOI: 10.1016/S0039-6028(02)01545-5. (Cit. on p. 14).

[66] E. Grånäs et al.: "CO intercalation of graphene on Ir(111) in the millibar regime". *J. Phys. Chem. C* **117** 16438–16447 (2013). DOI: 10.1021/jp4043045. (Cit. on p. 14).

[67] E. Grånäs et al.: "Oxygen intercalation under graphene on Ir(111): energetics, kinetics, and the role of graphene edges." *ACS Nano* **6** 9951–9963 (2012). DOI: 10.1021/nn303548z. (Cit. on p. 14).

[68] C. Riedl et al.: "Quasi-free-standing epitaxial graphene on SiC obtained by hydrogen intercalation". *Phys. Rev. Lett.* **103** 246804 (2009). DOI: 10.1103/PhysRevLett.103.246804. (Cit. on p. 14).

[69] A. Varykhalov et al.: "Electronic and magnetic properties of quasifreestanding graphene on Ni". *Phys. Rev. Lett.* **101** 157601 (2008). DOI: 10.1103/PhysRevLett.101.157601. (Cit. on p. 14).

[70] R. Drost et al.: "Electronic states at the graphene–hexagonal boron nitride zigzag interface". *Nano Lett.* **14** 5128–5132 (2014). DOI: 10.1021/nl501895h. (Cit. on p. 14).

[71] C. Herbig et al.: "Mechanical exfoliation of epitaxial graphene on Ir(111) enabled by Br2 intercalation." *J. Phys. Condens. Matter* **24** 314208 (2012). DOI: 10.1088/0953-8984/24/31/314208. (Cit. on pp. 14, 194).

[72] U. A. Schröder et al.: "Core level shifts of intercalated graphene". *2D Mater.* **4** 015013 (2017). DOI: 10.1088/2053-1583/4/1/015013. (Cit. on pp. 14, 119, 194).

[73] J. L. McChesney et al.: "Extended van Hove singularity and superconducting instability in doped graphene". *Phys. Rev. Lett.* **104** 136803 (2010). DOI: 10.1103/PhysRevLett.104.136803. (Cit. on p. 14).

[74] R. Mu et al.: "Visualizing chemical reactions confined under graphene". *Angew. Chemie Int. Ed.* **51** 4856–4859 (2012). DOI: 10.1002/anie.201200413. (Cit. on p. 14).

[75] Y. Zhang et al.: "Enhanced reactivity of graphene wrinkles and their function as nanosized gas inlets for reactions under graphene". *Phys. Chem. Chem. Phys.* **15** 19042–19048 (2013). DOI: 10.1039/c3cp52115j. (Cit. on p. 14).

[76] Y. Yao et al.: "Graphene cover-promoted metal-catalyzed reactions". *Proc. Natl. Acad. Sci. U. S. A.* **111** 17023–17028 (2014). DOI: 10.1073/pnas.1416368111. (Cit. on p. 14).

[77] C. Herbig et al.: "Xe irradiation of graphene on Ir(111): From trapping to blistering". *Phys. Rev. B* **92** 085429 (2015). DOI: 10.1103/PhysRevB.92.085429. (Cit. on pp. 14, 39, 49, 80, 86, 137, 193).

[78] M. Batzill: "The surface science of graphene: Metal interfaces, CVD synthesis, nanoribbons, chemical modifications, and defects". *Surf. Sci. Rep.* **67** 83–115 (2012). DOI: 10.1016/j.surfrep.2011.12.001. (Cit. on p. 15).

[79] P. Feibelman: "Pinning of graphene to Ir(111) by flat Ir dots". *Phys. Rev. B* **77** 165419 (2008). DOI: 10.1103/PhysRevB.77.165419. (Cit. on pp. 15, 158).

[80] J. Knudsen et al.: "Clusters binding to the graphene moiré on Ir(111): X-ray photoemission compared to density functional calculations". *Phys. Rev. B* **85** 035407 (2012). DOI: 10.1103/PhysRevB.85.035407. (Cit. on pp. 15, 119, 158, 159).

[81] A. T. N'Diaye et al.: "A versatile fabrication method for cluster superlattices". *New J. Phys.* **11** 103045 (2009). DOI: 10.1088/1367-2630/11/10/103045. (Cit. on p. 15).

[82] M. Nastasi and J. W. Mayer: *Ion Implantation and Synthesis of Materials.* Berling Heidelberg New York: Springer-Verlag (2006). (Cit. on pp. 19, 21).

[83] E. Friedland: "Radiation damage in metals". *Crit. Rev. Solid State Mater. Sci.* **26** 87–143 (2001). DOI: 10.1080/20014091104170. (Cit. on pp. 19, 22, 23).

[84] W. Schilling and H. Ullmaier: "Physics of radiation damage in metals". In: *Mater. Sci. Technol.* Weilheim: Wiley-VCH Verlag GmbH & Co. KGaA (1993). Chap. 9, pp. 180–241. DOI: 10.1002/9783527603978.mst0113 (cit. on p. 20).

[85] A. Redinger: "Surface damage through grazing incidence ions investigated by scanning tunneling microscopy". PhD thesis. Universität zu Köln (2009). (Cit. on p. 21).

[86] H. Gnaser: *Low-energy ion irradiation of solid surfaces.* Berlin Heidelberg New York: Springer-Verlag (1999). (Cit. on pp. 22, 24, 98).

[87] S. Donnelly: "The density and pressure of helium in bubbles in implanted metals : A critical review". *Radiat. Eff.* **90** 1–47 (1985). DOI: 10.1080/00337578508222514. (Cit. on p. 23).

[88] J. H. Evans: "The formation of high pressure precipitation phases during the implantation of inert gas and other insoluble atom species in metals". *Nucl. Instruments Methods Phys. Res. B* **18** 16–23 (1986). DOI: 10.1016/S0168-583X(86)80007-6. (Cit. on p. 23).

[89] K. Oura et al.: *Surface Science: An Introduction.* Berlin Heidelberg New York: Springer-Verlag (2003). (Cit. on pp. 24, 35).

[90] H. Winter: "Collisions of atoms and ions with surfaces under grazing incidence". *Phys. Rep.* **367** 387–582 (2002). DOI: 10.1016/S0370-1573(02)00010-8. (Cit. on p. 24).

[91] A. Redinger et al.: "Trails of kilovolt ions created by subsurface channeling". *Phys. Rev. Lett.* **104** 075501 (2010). DOI: 10.1103/PhysRevLett.104.075501. (Cit. on p. 24).

[92] A. Redinger et al.: "Making channeling visible: keV noble gas ion trails on Pt(111)". *New J. Phys.* **13** 013002 (2011). DOI: 10.1088/1367-2630/13/1/013002. (Cit. on p. 24).

[93] Y. Li et al.: "Stone - Wales defects in single-walled boron nitride nanotubes: Formation energies, electronic structures, and reactivity". *J. Phys. Chem. C* **112** 1365–1370 (2008). DOI: 10.1021/jp077115a. (Cit. on p. 26).

[94] Y. Lin et al.: "Defect functionalization of hexagonal boron nitride nanosheets". *J. Phys. Chem. C* **114** 17434–17439 (2010). DOI: 10.1021/jp105454w. (Cit. on p. 26).

[95] A. Pakdel, Y. Bando, and D. Golberg: "Nano boron nitride flatland". *Chem. Soc. Rev.* **43** 934–959 (2014). DOI: 10.1039/c3cs60260e. (Cit. on p. 26).

[96] M. M. Ugeda et al.: "Missing atom as a source of carbon magnetism". *Phys. Rev. Lett.* **104** 096804 (2010). DOI: 10.1103/PhysRevLett.104.096804. (Cit. on pp. 26, 61, 63).

[97] J. C. Meyer et al.: "Direct imaging of lattice atoms and topological defects in graphene membranes." *Nano Lett.* **8** 3582–3586 (2008). DOI: 10.1021/nl801386m. (Cit. on p. 26).

[98] F. Banhart, J. Kotakoski, and A. V. Krasheninnikov: "Structural defects in graphene". *ACS Nano* **5** 26–41 (2011). DOI: 10.1021/nn102598m. (Cit. on pp. 26, 115).

[99] C. Jin et al.: "Fabrication of a freestanding boron nitride single layer and its defect assignments". *Phys. Rev. Lett.* **102** 195505 (2009). DOI: 10.1103/PhysRevLett.102.195505. (Cit. on p. 27).

[100] A. Zobelli et al.: "Vacancy migration in hexagonal boron nitride". *Phys. Rev. B* **75** 094104 (2007). DOI: 10.1103/PhysRevB.75.094104. (Cit. on pp. 27, 124).

[101] Y. H. Lee, S. G. Kim, and D. Tománek: "Catalytic growth of single-wall carbon nanotubes: An ab initio study". *Phys. Rev. Lett.* **78** 2393 (1997). DOI: 10.1103/PhysRevLett.78.2393. (Cit. on p. 27).

[102] P. O. Lehtinen et al.: "Magnetic properties and diffusion of adatoms on a graphene sheet". *Phys. Rev. Lett.* **91** 017202 (2003). DOI: 10.1103/PhysRevLett.91.017202. (Cit. on pp. 27, 148, 152).

[103] J. Li et al.: "Magnetism of C adatoms on BN nanostructures: Implications for functional nanodevices". *J. Am. Chem. Soc.* **131** 1796–1801 (2009). DOI: 10.1021/ja805632p. (Cit. on p. 27).

[104] O. Cretu et al.: "Migration and localization of metal atoms on strained graphene". *Phys. Rev. Lett.* **105** 196102 (2010). DOI: 10.1103/PhysRevLett.105.196102. (Cit. on p. 27).

[105] L. Ci et al.: "Atomic layers of hybridized boron nitride and graphene domains". *Nat. Mater.* **9** 430–435 (2010). DOI: 10.1038/nmat2711. (Cit. on p. 28).

[106] D. W. Boukhvalov and M. I. Katsnelson: "Chemical functionalization of graphene with defects." *Nano Lett.* **8** 4373–4379 (2008). DOI: 10.1021/nl802234n. (Cit. on p. 28).

[107] J. Coraux et al.: "Structural coherency of graphene on Ir(111)." *Nano Lett.* **8** 565–570 (2008). DOI: 10.1021/nl0728874. (Cit. on pp. 28, 96).

[108] O. V. Yazyev et al.: "Early stages of radiation damage in graphite and carbon nanostructures: A first-principles molecular dynamics study". *Phys. Rev. B* **75** 115418 (2007). DOI: 10.1103/PhysRevB.75.115418. (Cit. on p. 29).

[109] J. Kotakoski et al.: "Electron knock-on damage in hexagonal boron nitride monolayers". *Phys. Rev. B* **82** 113404 (2010). DOI: 10.1103/PhysRevB.82.113404. (Cit. on pp. 29, 116).

[110] C. Gong et al.: "Thermally induced dynamics of dislocations in graphene at atomic resolution". *ACS Nano* **9** 10066–10075 (2015). DOI: 10.1021/acsnano.5b05355. (Cit. on pp. 29, 152).

[111] O. Lehtinen et al.: "Effects of ion bombardment on a two-dimensional target: Atomistic simulations of graphene irradiation". *Phys. Rev. B* **81** 153401 (2010). DOI: 10.1103/PhysRevB.81.153401. (Cit. on pp. 29, 79).

[112] O. Lehtinen et al.: "Cutting and controlled modification of graphene with ion beams." *Nanotechnology* **22** 175306 (2011). DOI: 10.1088/0957-4484/22/17/175306. (Cit. on pp. 29, 79).

[113] O. Lehtinen et al.: "Production of defects in hexagonal boron nitride monolayer under ion irradiation". *Nucl. Instruments Methods Phys. Res. Sect. B Beam Interact. with Mater. Atoms* **269** 1327–1331 (2011). DOI: 10.1016/j.nimb.2010.11.027. (Cit. on p. 29).

[114] S. Akcöltekin et al.: "Unzipping and folding of graphene by swift heavy ions". *Appl. Phys. Lett.* **98** 103103 (2011). DOI: 10.1063/1.3559619. (Cit. on pp. 29, 79).

[115] G. Binnig and H. Rohrer: "Scanning tunneling microscopy". *Surf. Sci.* **126** 236–244 (1983). DOI: 10.1016/0039-6028(83)90716-1. (Cit. on pp. 33, 34).

[116] J. Bardeen: "Tunnelling from a many-particle point of view". *Phys. Rev. Lett.* **6** 57 (1961). DOI: 10.1103/PhysRevLett.6.57. (Cit. on p. 33).

[117] C. J. Chen: *Introduction to scanning tunneling microscopy.* 2nd ed. Oxford University Press New York (1993). (Cit. on p. 34).

[118] S. Donnelly: "A thermal evolution study of the trapping and release of inert gases in nickel". *Vacuum* **28** 163–171 (1978). DOI: 10.1016/S0042-207X(78)80418-7. (Cit. on pp. 36, 51).

[119] S. E. Donnelly, D. C. Ingram, and D. G. Armour: "An experimental study of the trapping and release of krypton in nickel". *Radiat. Eff.* **42** 179–184 (1979). DOI: 10.1080/00337577908209135. (Cit. on p. 36).

[120] C. Herbig et al.: "Interfacial carbon nanoplatelet formation by ion irradiation of graphene on iridium(111)". *ACS Nano* **8** 12208–12218 (2014). DOI: 10.1021/nn503874n. (Cit. on pp. 39, 49, 57, 59, 137, 143, 194).

[121] C. Herbig et al.: "Comment on "Interfacial carbon nanoplatelet formation by ion irradiation of graphene on iridium(111)"". *ACS Nano* **9** 4664–4665 (2015). DOI: 10.1021/acsnano.5b02303. (Cit. on pp. 39, 49, 137, 194).

[122] C. Herbig and T. Michely: "Graphene: the ultimately thin sputtering shield". *2D Mater.* **3** 025032 (2016). DOI: 10.1088/2053-1583/3/2/025032. (Cit. on pp. 39, 89, 93, 193).

[123] T. Michely, M. Kaiser, and M. J. Rost: "Plug 'n' play scanning probe microscopy". *Rev. Sci. Instrum.* **71** 4461 (2000). DOI: 10.1063/1.1322587. (Cit. on p. 40).

[124] D. F. Förster: "EuO and Eu on metal crystals and graphene : interface effects and epitaxial films". PhD thesis. University of Cologne (2011). (Cit. on p. 40).

[125] P. Feulner and D. Menzel: "Simple ways to improve "flash desorption" measurements from single crystal surfaces". *J. Vac. Sci. Technol.* **17** 662 (1980). DOI: 10.1116/1.570537. (Cit. on p. 41).

[126] C. Busse: "Nucleation and Stacking-Faults on the Iridium(111) Surface". PhD thesis. RWTH Aachen (2003). (Cit. on p. 41).

[127] R. van Gastel et al.: "Selecting a single orientation for millimeter sized graphene sheets". *Appl. Phys. Lett.* **95** 121901 (2009). DOI: 10.1063/1.3225554. (Cit. on p. 41).

[128] J. Coraux et al.: "Growth of graphene on Ir(111)". *New J. Phys.* **11** 023006 (2009). DOI: 10.1088/1367-2630/11/2/023006. (Cit. on pp. 41, 68, 98, 99, 146).

[129] E. H. Åhlgren et al.: "Ion irradiation tolerance of graphene as studied by atomistic simulations". *Appl. Phys. Lett.* **100** 233108 (2012). DOI: 10.1063/1.4726053. (Cit. on p. 42).

[130] S. Doniach and M. Sunjic: "Many-electron singularity in X-ray photoemission and X-ray line spectra from metals". *J. Phys. C Solid State Phys.* **3** 285–291 (1970). DOI: 10.1088/0022-3719/3/2/010. (Cit. on p. 44).

[131] G. Kresse and J. Furthmüller: "Efficiency of ab-initio total energy calculations for metals and semiconductors using a plane-wave basis set". *Comput. Mater. Sci.* **6** 15–50 (1996). DOI: 10.1016/0927-0256(96)00008-0. (Cit. on p. 44).

[132] G. Kresse and J. Furthmüller: "Efficient iterative schemes for ab initio total-energy calculations using a plane-wave basis set". *Phys. Rev. B* **54** 11169 (1996). DOI: 10.1103/PhysRevB.54.11169. (Cit. on p. 44).

[133] P. E. Blöchl: "Projector augmented-wave method". *Phys. Rev. B* **50** 17953 (1994). DOI: 10.1103/PhysRevB.50.17953. (Cit. on p. 44).

[134] T. Björkman: "van der Waals density functional for solids". *Phys. Rev. B* **86** 165109 (2012). DOI: 10.1103/PhysRevB.86.165109. (Cit. on p. 44).

[135] N. Blanc et al.: "Strains induced by point defects in graphene on a metal". *Phys. Rev. Lett.* **111** 085501 (2013). DOI: 10.1103/PhysRevLett.111.085501. (Cit. on p. 45).

[136] K. Nordlund et al.: "Defect production in collision cascades in elemental semiconductors and fcc metals". *Phys. Rev. B* **57** 7556 (1998). DOI: 10.1103/PhysRevB.57.7556. (Cit. on p. 45).

[137] K. Albe, K. Nordlund, and R. Averback: "Modeling the metal-semiconductor interaction: Analytical bond-order potential for platinum-carbon". *Phys. Rev. B* **65** 195124 (2002). DOI: 10.1103/PhysRevB.65.195124. (Cit. on p. 45).

[138] H. J. C. Berendsen et al.: "Molecular dynamics with coupling to an external bath". *J. Chem. Phys.* **81** 3684 (1984). DOI: 10.1063/1.448118. (Cit. on p. 45).

[139] P. Sutter, J. T. Sadowski, and E. Sutter: "Graphene on Pt(111): Growth and substrate interaction". *Phys. Rev. B* **80** 245411 (2009). DOI: 10.1103/PhysRevB.80.245411. (Cit. on pp. 45, 143).

[140] D. W. Brenner et al.: "A second-generation reactive empirical bond order (REBO) potential energy expression for hydrocarbons". *J. Phys. Condens. Matter* **14** 783–802 (2002). DOI: 10.1088/0953-8984/14/4/312. (Cit. on p. 45).

[141] J. F. Ziegler, J. P. Biersack, and U. Littmark: "The stopping and range of ions in matter". In: *Treatise heavy-ion sci.* Ed. by D. Bromley. New York: Springer US (1985), pp. 93–129. DOI: 10.1007/978-1-4615-8103-1_3 (cit. on p. 45).

[142] H. Ulbricht et al.: "Thermal desorption of gases and solvents from graphite and carbon nanotube surfaces". *Carbon* **44** 2931–2942 (2006). DOI: 10.1016/j.carbon.2006.05.040. (Cit. on p. 46).

[143] W. Widdra et al.: "Rare-gas thermal desorption from flat and stepped platinum surfaces: Lateral interactions and the influence of dimensionality". *Phys. Rev. B* **57** 4111 (1998). DOI: 10.1103/PhysRevB.57.4111. (Cit. on pp. 46, 51, 55).

[144] J. Scott Bunch et al.: "Impermeable atomic membranes from graphene sheets." *Nano Lett.* **8** 2458–2462 (2008). DOI: 10.1021/nl801457b. (Cit. on p. 49).

[145] S. P. Koenig et al.: "Ultrastrong adhesion of graphene membranes." *Nat. Nanotechnol.* **6** 543–546 (2011). DOI: 10.1038/nnano.2011.123. (Cit. on pp. 49, 61).

[146] J. Zabel et al.: "Raman spectroscopy of graphene and bilayer under biaxial strain: bubbles and balloons." *Nano Lett.* **12** 617–621 (2012). DOI: 10.1021/nl203359n. (Cit. on p. 49).

[147] S. P. Koenig et al.: "Selective molecular sieving through porous graphene." *Nat. Nanotechnol.* **7** 728–732 (2012). DOI: 10.1038/nnano.2012.162. (Cit. on p. 49).

[148] E. Stolyarova et al.: "Observation of graphene bubbles and effective mass transport under graphene films." *Nano Lett.* **9** 332–337 (2009). DOI: 10.1021/nl803087x. (Cit. on pp. 49, 61).

[149] C. H. Y. X. Lim et al.: "A hydrothermal anvil made of graphene nanobubbles on diamond." *Nat. Commun.* **4** 1556 (2013). DOI: 10.1038/ncomms2579. (Cit. on pp. 49, 50).

[150] W. Pan et al.: "Biaxial compressive strain engineering in graphene/boron nitride heterostructures." *Sci. Rep.* **2** 893 (2012). DOI: 10.1038/srep00893. (Cit. on p. 49).

[151] J. M. Yuk et al.: "High-resolution EM of colloidal nanocrystal growth using graphene liquid cells". *Science* **336** 61–64 (2012). DOI: 10.1126/science.1217654. (Cit. on p. 49).

[152] U. Bangert et al.: "Ion implantation of graphene–toward IC compatible technologies". *Nano Lett.* **13** 4902–4907 (2013). DOI: 10.1021/nl402812y. (Cit. on pp. 50, 79).

[153] M. Telychko et al.: "Achieving high-quality single-atom nitrogen doping of graphene/SiC(0001) by ion implantation and subsequent thermal stabilization". *ACS Nano* **8** 7318–7324 (2014). DOI: 10.1021/nn502438k. (Cit. on pp. 50, 79).

[154] H. Cun et al.: "Implantation length and thermal stability of interstitial ar atoms in boron nitride nanotents." *ACS Nano* **8** 1014–1021 (2013). DOI: 10.1021/nn405907a. (Cit. on pp. 50, 137).

[155] H. Cun et al.: "Two-nanometer voids in single-layer hexagonal boron nitride: formation via the can-opener effect and annihilation by self-healing." *ACS Nano* **8** 7423–7431 (2014). DOI: 10.1021/nn502645w. (Cit. on pp. 50, 101, 102, 113, 116, 137).

[156] H. Cun et al.: "Ar implantation beneath graphene on Ru(0001): Nanotents and can-opener effect". *Surf. Sci.* **634** 95–102 (2015). DOI: 10.1016/j.susc.2014.11.004. (Cit. on pp. 50, 102, 116, 117, 137).

[157] Y. Baba, H. Yamamoto, and T. Sasaki: "Core-level electronic structures of rare-gas atoms implanted in transition metals studied by XPS and XAES". *Surf. Sci.* **287-288** 806–810 (1993). DOI: 10.1016/0039-6028(93)91077-3. (Cit. on p. 51).

[158] R. J. Behm, C. R. Brundle, and K. Wandelt: "The underlayer influence on photoemission and thermal desorption of xenon adsorbed on Ag(111)". *J. Chem. Phys.* **85** 1061 (1986). DOI: 10.1063/1.451299. (Cit. on p. 51).

[159] A. R. Lahrood et al.: "X-ray photoelectron spectroscopy on implanted argon as a tool to follow local structural changes in thin films". *Thin Solid Films* **520** 1625–1630 (2011). DOI: 10.1016/j.tsf.2011.07.040. (Cit. on p. 51).

[160] K. Kern et al.: "Registry effects in the thermodynamic quantities of Xe adsorption on Pt(111)". *Surf. Sci.* **195** 353–370 (1988). DOI: 10.1016/0039-6028(88)90347-0. (Cit. on pp. 52, 60, 80, 97).

[161] J. L. F. Da Silva and C. Stampfl: "Nature of Xenon adsorption on graphite: On-top versus hollow site preference". *Phys. Rev. B* **76** 085301 (2007). DOI: 10.1103/PhysRevB.76.085301. (Cit. on p. 55).

[162] L. Sheng, Y. Ono, and T. Taketsugu: "Ab initio study of Xe adsorption on graphene". *J. Phys. Chem. C* **114** 3544–3548 (2010). DOI: 10.1021/jp907861c. (Cit. on p. 55).

[163] P. L. Silvestrelli and A. Ambrosetti: "van der Waals corrected DFT simulation of adsorption processes on transition-metal surfaces: Xe and graphene on Ni(111)". *Phys. Rev. B* **91** 195405 (2015). DOI: 10.1103/PhysRevB.91.195405. (Cit. on p. 55).

[164] K. He et al.: "Extended Klein edges in graphene." *ACS Nano* **8** 12272–12279 (2014). DOI: 10.1021/nn504471m. (Cit. on p. 57).

[165] T. Michely and G. Comsa: "Temperature dependence of the sputtering morphology of Pt(111)". *Surf. Sci.* **256** 217–226 (1991). DOI: 10.1016/0039-6028(91)90865-P. (Cit. on pp. 59, 75, 112).

[166] G. M. Rutter et al.: "Scattering and interference in epitaxial graphene." *Science* **317** 219–222 (2007). DOI: 10.1126/science.1142882. (Cit. on p. 61).

[167] S. J. Altenburg et al.: "Local gating of an Ir(111) surface resonance by graphene islands". *Phys. Rev. Lett.* **108** 206805 (2012). DOI: 10.1103/PhysRevLett.108.206805. (Cit. on p. 63).

[168] A. Varykhalov et al.: "Ir(111) surface state with giant rashba splitting persists under graphene in air". *Phys. Rev. Lett.* **108** 066804 (2012). DOI: 10.1103/PhysRevLett.108.066804. (Cit. on p. 63).

[169] Y. Zhang et al.: "Giant phonon-induced conductance in scanning tunnelling spectroscopy of gate-tunable graphene". *Nat. Phys.* **4** 627–630 (2008). DOI: 10.1038/nphys1022. (Cit. on p. 63).

[170] Y. Li et al.: "Absence of edge states in covalently bonded zigzag edges of graphene on Ir(111)." *Adv. Mater.* **25** 1967–1972 (2013). DOI: 10.1002/adma.201204539. (Cit. on pp. 68, 143).

[171] A. V. Krasheninnikov et al.: "Toward stronger Al–BN nanotube composite materials: Insights into bonding at the Al/BN interface from first-principles calculations". *J. Phys. Chem. C* **118** 26894–26901 (2014). DOI: 10.1021/jp509505j. (Cit. on p. 75).

[172] C. Herbig, E. H. Åhlgren, and T. Michely: "Blister-free ion beam patterning of supported graphene". *Nanotechnology* **28** 055304 (2017). DOI: 10.1088/1361-6528/aa527c. (Cit. on pp. 79, 193).

[173] E. P. Bellido and J. M. Seminario: "Molecular dynamics simulations of ion-bombarded graphene". *J. Phys. Chem. C* **116** 4044–4049 (2012). DOI: 10.1021/jp208049t. (Cit. on p. 79).

[174] S. Bubin et al.: "Simulation of high-energy ion collisions with graphene fragments". *Phys. Rev. B* **85** 235435 (2012). DOI: 10.1103/PhysRevB.85.235435. (Cit. on p. 79).

[175] C. J. Russo and J. A. Golovchenko: "Atom-by-atom nucleation and growth of graphene nanopores." *Proc. Natl. Acad. Sci. U. S. A.* **109** 5953–5957 (2012). DOI: 10.1073/pnas.1119827109. (Cit. on p. 79).

[176] S. C. O'Hern et al.: "Selective ionic transport through tunable subnanometer pores in single-layer graphene membranes". *Nano Lett.* **14** 1234–1241 (2014). DOI: 10.1021/nl404118f. (Cit. on p. 79).

[177] O. Lehtinen et al.: "Non-invasive transmission electron microscopy of vacancy defects in graphene produced by ion irradiation." *Nanoscale* **6** 6569–6576 (2014). DOI: 10.1039/c4nr01918k. (Cit. on pp. 79, 93).

[178] Z. Bai, L. Zhang, and L. Liu: "Bombarding graphene with oxygen ions: Combining effects of incident angle and ion energy to control defect generation". *J. Phys. Chem. C* **119** 26793–26802 (2015). DOI: 10.1021/acs.jpcc.5b09620. (Cit. on p. 79).

[179] G. López-Polín et al.: "Increasing the elastic modulus of graphene by controlled defect creation". *Nat. Phys.* **11** 26–31 (2015). DOI: 10.1038/nphys3183. (Cit. on p. 79).

[180] D. C. Bell et al.: "Precision cutting and patterning of graphene with helium ions." *Nanotechnology* **20** 455301 (2009). DOI: 10.1088/0957-4484/20/45/455301. (Cit. on p. 79).

[181] M. C. Lemme et al.: "Etching of graphene devices with a helium ion beam". *ACS Nano* **3** 2674–2676 (2009). DOI: 10.1021/nn900744z. (Cit. on p. 79).

[182] Y. Naitou, T. Iijima, and S. Ogawa: "Direct nano-patterning of graphene with helium ion beams". *Appl. Phys. Lett.* **106** 033103 (2015). DOI: 10.1063/1.4906415. (Cit. on p. 79).

[183] J. Sforzini et al.: "Structural and electronic properties of nitrogen-doped graphene". *Phys. Rev. Lett.* **116** 126805 (2016). DOI: 10.1103/PhysRevLett.116.126805. (Cit. on p. 79).

[184] A. Redinger et al.: "Step-edge sputtering through grazing incidence ions investigated by scanning tunneling microscopy and molecular dynamics simulations". *Phys. Rev. B* **77** 195436 (2008). DOI: 10.1103/PhysRevB.77.195436. (Cit. on pp. 86, 90).

[185] T. Michely and C. Teichert: "Adatom yields, sputtering yields, and damage patterns of single-ion impacts on Pt(111)". *Phys. Rev. B* **50** 11156 (1994). DOI: 10.1103/PhysRevB.50.11156. (Cit. on pp. 86, 95).

[186] H. Gades and H. M. Urbassek: "Molecular-dynamics simulation of adatom formation under keV-ion bombardment of Pt(111)". *Phys. Rev. B* **50** 11167 (1994). DOI: 10.1103/PhysRevB.50.11167. (Cit. on pp. 86, 97).

[187] M. Morgenstern, T. Michely, and G. Comsa: "Collective effects in the adatom production by 4.5 keV rare-gas impacts on Pt(111): A low-temperature scanning tunnelling microscopy analysis". *Philos. Mag. A* **79** 775–794 (1999). DOI: 10.1080/01418619908210331. (Cit. on p. 86).

[188] M. Ghaly, K. Nordlund, and R. S. Averback: "Molecular dynamics investigations of surface damage produced by kiloelectronvolt self-bombardment of solids". *Philos. Mag. A* **79** 795–820 (1999). DOI: 10.1080/01418619908210332. (Cit. on p. 86).

[189] J. F. Ziegler, M. Ziegler, and J. Biersack: "SRIM – The stopping and range of ions in matter (2010)". *Nucl. Instruments Methods Phys. Res. Sect. B Beam Interact. with Mater. Atoms* **268** 1818–1823 (2010). DOI: 10.1016/j.nimb.2010.02.091. (Cit. on pp. 86, 96).

[190] J. Roth et al.: "Recent analysis of key plasma wall interactions issues for ITER". *J. Nucl. Mater.* **390-391** 1–9 (2009). DOI: 10.1016/j.jnucmat.2009.01.037. (Cit. on p. 93).

[191] G. Algara-Siller et al.: "The pristine atomic structure of MoS2 monolayer protected from electron radiation damage by graphene". *Appl. Phys. Lett.* **103** 203107 (2013). DOI: 10.1063/1.4830036. (Cit. on p. 93).

[192] R. Zan et al.: "Control of radiation damage in MoS(2) by graphene encapsulation." *ACS Nano* **7** 10167–10174 (2013). DOI: 10.1021/nn4044035. (Cit. on p. 93).

[193] K. Morita et al.: "Suppression of sputtering of nickel by coverage with self-sustaining thin segregated carbon layers". *J. Nucl. Mater.* **116** 63–68 (1983). DOI: 10.1016/0022-3115(83)90292-1. (Cit. on p. 93).

[194] A. Dahal and M. Batzill: "Graphene-nickel interfaces: a review." *Nanoscale* **6** 2548–2562 (2014). DOI: 10.1039/c3nr05279f. (Cit. on p. 93).

[195] E. H. Åhlgren et al.: "Structural manipulation of the graphene/metal interface with Ar^+ irradiation". *Phys. Rev. B* **88** 155419 (2013). DOI: 10.1103/PhysRevB.88.155419. (Cit. on pp. 93, 98, 99).

[196] T. Michely and G. Comsa: "The scanning tunneling microscope as a means for the investigation of ion bombardment effects on metal surfaces". *Nucl. Instruments Methods Phys. Res. Sect. B Beam Interact. with Mater. Atoms* **82** 207–219 (1993). DOI: 10.1016/0168-583X(93)96023-6. (Cit. on p. 95).

[197] A. Petersen et al.: "From erosion to bombardment-induced growth on Ir(111)". *Phys. Rev. B* **68** 245410 (2003). DOI: 10.1103/PhysRevB.68.245410. (Cit. on pp. 95, 96).

[198] M. P. Seah et al.: "An accurate semi-empirical equation for sputtering yields I: for argon ions". *Surf. Interface Anal.* **37** 444–458 (2005). DOI: 10.1002/sia.2032. (Cit. on p. 96).

[199] M. P. Seah: "An accurate semi-empirical equation for sputtering yields, II: for neon, argon and xenon ions". *Nucl. Instruments Methods Phys. Res. Sect. B Beam Interact. with Mater. Atoms* **229** 348–358 (2005). DOI: 10.1016/j.nimb.2004.12.129. (Cit. on p. 96).

[200] National Physics Laboratory: *Sputter Yield Values.* URL: http://www.npl.co.uk/science-technology/surface-and-nanoanalysis/services/sputter-yield-values (cit. on p. 96).

[201] A. V. Krasheninnikov, Y. Miyamoto, and D. Tománek: "Role of Electronic Excitations in Ion Collisions with Carbon Nanostructures." *Phys. Rev. Lett.* **99** 016104 (2007). DOI: 10.1103/PhysRevLett.99.016104. (Cit. on p. 98).

[202] J. C. Meyer et al.: "Accurate measurement of electron beam induced displacement cross sections for single-layer graphene." *Phys. Rev. Lett.* **108** 196102 (2012). DOI: 10.1103/PhysRevLett.108.196102. (Cit. on p. 98).

[203] J. C. Meyer et al.: "Erratum: Accurate Measurement of Electron Beam Induced Displacement Cross Sections for Single-Layer Graphene [Phys. Rev. Lett. 108 , 196102 (2012)]". *Phys. Rev. Lett.* **110** 239902 (2013). DOI: 10.1103/PhysRevLett.110.239902. (Cit. on p. 98).

[204] M. W. Thompson: "II. The energy spectrum of ejected atoms during the high energy sputtering of gold". *Philos. Mag.* **18** 377–414 (1968). DOI: 10.1080/14786436808227358. (Cit. on p. 98).

[205] C. Oshima and A. Nagashima: "Ultra-thin epitaxial films of graphite and hexagonal boron nitride on solid surfaces". *J. Phys. Condens. Matter* **9** 1–20 (1997). DOI: 10.1088/0953-8984/9/1/004. (Cit. on p. 99).

[206] M. Sasaki et al.: "Moiré contrast in the local tunneling barrier height images of monolayer graphite on Pt(111)". *Phys. Rev. B* **61** 15653 (2000). DOI: 10.1103/PhysRevB.61.15653. (Cit. on p. 99).

[207] J. Wintterlin and M.-L. Bocquet: "Graphene on metal surfaces". *Surf. Sci.* **603** 1841–1852 (2009). DOI: 10.1016/j.susc.2008.08.037. (Cit. on p. 99).

[208] X. Li et al.: "Large-area synthesis of high-quality and uniform graphene films on copper foils". *Science* **324** 1312–1314 (2009). DOI: 10.1126/science.1171245. (Cit. on p. 99).

[209] L. Gao, G. J. R, and N. P. Guisinger: "Epitaxial graphene on Cu(111)". *Nano Lett.* **10** 3512–3516 (2010). DOI: 10.1021/nl1016706. (Cit. on p. 99).

[210] E. Kim et al.: "Growth of few-layer graphene on a thin cobalt film on a Si/SiO 2 substrate". *Chem. Vap. Depos.* **17** 9–14 (2011). DOI: 10.1002/cvde.201004296. (Cit. on p. 99).

[211] N. A. Vinogradov et al.: "Formation and structure of graphene waves on Fe(110)". *Phys. Rev. Lett.* **109** 026101 (2012). DOI: 10.1103/PhysRevLett.109.026101. (Cit. on p. 99).

[212] S. Nie, A. Bostwick, and N. C. Bartelt: "Extraordinary epitaxial alignment of graphene islands on Au(111)". *New J. Phys.* **14** 053008 (2012). DOI: 10.1088/1367-2630/14/5/053008. (Cit. on p. 99).

[213] Y. Xue et al.: "Synthesis of large-area , few-layer graphene on iron foil by chemical vapor deposition". *Nano Res.* **4** 1208–1214 (2011). DOI: 10.1007/s12274-011-0171-4. (Cit. on p. 99).

[214] Z. Zou et al.: "Uniform single-layer graphene growth on recyclable". *Nano Res.* **8** 592–599 (2015). DOI: 10.1007/s12274-015-0727-9. (Cit. on p. 99).

[215] P. Valerius: "A Hexagonal Boron Nitride Layer on Ir(111): Trapping of Xe Underneath and Growth of C Clusters on Top". Master thesis. Universität zu Köln (2016). (Cit. on p. 101).

[216] P. Valerius et al.: "From amorphization to a triangular 2D world: annealing of ion irradiated hexagonal boron nitride on Ir(111)". *in preparation* (2017). (Cit. on pp. 101, 108, 115, 193).

[217] G. Zamborlini et al.: "Nanobubbles at GPa pressure under graphene". *Nano Lett.* **15** 6162–6169 (2015). DOI: 10.1021/acs.nanolett.5b02475. (Cit. on pp. 101, 137, 138).

[218] S. Wang and G. Ehrlich: "Structure, stability, and surface diffusion of clusters: Ir_x on Ir(111)". *Surf. Sci.* **239** 301–332 (1990). DOI: 10.1016/0039-6028(90)90232-W. (Cit. on p. 106).

[219] P. R. Granfors, A. T. Macrander, and R. O. Simmons: "Crystalline xenon: Lattice parameters, thermal expansion, thermal vacancies, and equation of state". *Phys. Rev. B* **24** 4753 (1981). DOI: 10.1103/PhysRevB.24.4753. (Cit. on p. 111).

[220] D. A. Young: *Phase Diagrams of the Elements.* University of California Press (1991), p. 280. (Cit. on p. 111).

[221] K. Schubert: "Ein Modell für die Kristallstrukturen der chemischen Elemente". *Acta Crystallogr. Sect. B Struct. Crystallogr. Cryst. Chem.* **30** 193–204 (1974). DOI: 10.1111/j.1600-5740.1974.tb00037.x. (Cit. on p. 111).

[222] S. P. Surwade et al.: "Water desalination using nanoporous single-layer graphene". *Nat. Nanotechnol.* **10** 459–464 (2015). DOI: 10.1038/nnano.2015.37. (Cit. on p. 115).

[223] L. Vicarelli et al.: "Controlling defects in graphene for optimizing the electrical properties of graphene nanodevices". *ACS Nano* **9** 3428–3435 (2015). DOI: 10.1021/acsnano.5b01762. (Cit. on p. 115).

[224] J. Kotakoski et al.: "Toward two-dimensional all-carbon heterostructures via ion beam patterning of single-layer graphene". *Nano Lett.* **15** 5944–5949 (2015). DOI: 10.1021/acs.nanolett.5b02063. (Cit. on p. 115).

[225] J. Kotakoski et al.: "From point defects in graphene to two-dimensional amorphous carbon". *Phys. Rev. Lett.* **106** 105505 (2011). DOI: 10.1103/PhysRevLett.106.105505. (Cit. on p. 115).

[226] F. R. Eder et al.: "A journey from order to disorder - Atom by atom transformation from graphene to a 2D carbon glass". *Sci. Rep.* **4** 4060 (2014). DOI: 10.1038/srep04060. (Cit. on p. 115).

[227] C. Pan et al.: "In-situ observation and atomic resolution imaging of the ion irradiation induced amorphisation of graphene". *Sci. Rep.* **4** 6334 (2014). DOI: 10.1038/srep06334. (Cit. on p. 116).

[228] K. Yoon et al.: "Atomistic-scale simulations of defect formation in graphene under noble gas ion irradiation". *ACS Nano* **10** 8376–8384 (2016). DOI: 10.1021/acsnano.6b03036. (Cit. on p. 116).

[229] R. Zan et al.: "Graphene reknits its holes." *Nano Lett.* **12** 3936–3940 (2012). DOI: 10.1021/nl300985q. (Cit. on p. 116).

[230] J. Chen et al.: "Self healing of defected graphene". *Appl. Phys. Lett.* **102** 103107 (2013). DOI: 10.1063/1.4795292. (Cit. on p. 116).

[231] J. Goma and M. Oberlin: "Graphitization of thin carbon films". *Thin Solid Films* **65** 221–232 (1980). DOI: 10.1016/0040-6090(80)90256-4. (Cit. on p. 116).

[232] Y.-B. Zhou et al.: "Ion irradiation induced structural and electrical transition in graphene." *J. Chem. Phys.* **133** 234703 (2010). DOI: 10.1063/1.3518979. (Cit. on p. 116).

[233] P. Jacobson et al.: "Disorder and defect healing in graphene on Ni(111)". *J. Phys. Chem. Lett.* **3** 136–139 (2012). DOI: 10.1021/jz2015007. (Cit. on pp. 116, 121).

[234] S. Karoui et al.: "Nickel-assisted healing of defective graphene." *ACS Nano* **4** 6114–6120 (2010). DOI: 10.1021/nn101822s. (Cit. on pp. 116, 121).

[235] S. Rey and F. Le Normand: "Surface transformations of carbon (graphene, graphite, diamond, carbide), deposited on polycrystalline nickel by hot filaments chemical vapour deposition". *Thin Solid Films* **519** 4426–4428 (2011). DOI: 10.1016/j.tsf.2011.01.331. (Cit. on p. 119).

[236] S. T. Jackson and R. G. Nuzzo: "Determining hybridization differences for amorphous carbon from the XPS C 1s envelope". *Appl. Surf. Sci.* **90** 195–203 (1995). DOI: 10.1016/0169-4332(95)00079-8. (Cit. on p. 119).

[237] J. Díaz et al.: "Separation of the sp3 and sp2 components in the C1s photoemission spectra of amorphous carbon films". *Phys. Rev. B* **54** 8064 (1996). DOI: 10.1103/PhysRevB.54.8064. (Cit. on p. 119).

[238] P. Mérel et al.: "Direct evaluation of the sp3 content in diamond-like-carbon films by XPS". *Appl. Surf. Sci.* **136** 105–110 (1998). DOI: 10.1016/S0169-4332(98)00319-5. (Cit. on p. 119).

[239] A. Nagashima et al.: "Electronic structure of monolayer graphite on some transition metal carbide surfaces". *Surf. Sci.* **287/288** 609–613 (1993). DOI: 10.1016/0039-6028(93)91037-P. (Cit. on p. 119).

[240] A. B. Preobrajenski et al.: "Controlling graphene corrugation on lattice-mismatched substrates". *Phys. Rev. B* **78** 073401 (2008). DOI: 10.1103/PhysRevB.78.073401. (Cit. on p. 119).

[241] P. Lacovig et al.: "Growth of dome-shaped carbon nanoislands on Ir(111): The intermediate between carbidic clusters and quasi-free-standing graphene". *Phys. Rev. Lett.* **103** 166101 (2009). DOI: 10.1103/PhysRevLett.103.166101. (Cit. on p. 121).

[242] A. A. El-Barbary et al.: "Structure and energetics of the vacancy in graphite". *Phys. Rev. B* **68** 144107 (2003). DOI: 10.1103/PhysRevB.68.144107. (Cit. on pp. 124, 130).

[243] W. E. Moddeman et al.: "Surface oxides of boron and B12O2 as determined by XPS". *Surf. Interface Anal.* **14** 224–232 (1989). DOI: 10.1002/sia.740140503. (Cit. on p. 128).

[244] M. Corso et al.: "Boron nitride nanomesh". *Science* **303** 217–220 (2004). DOI: 10.1126/science.1091979. (Cit. on p. 130).

[245] L. H. de Lima et al.: "Note : An ion source for alkali metal implantation beneath graphene and hexagonal boron nitride monolayers on transition metals". *Rev. Sci. Instrum.* **84** 126104 (2013). DOI: 10.1063/1.4848936. (Cit. on p. 137).

[246] R. Larciprete et al.: "Self-assembly of graphene nanoblisters sealed to a bare metal surface". *Nano Lett.* **16** 1808–1817 (2016). DOI: 10.1021/acs.nanolett.5b04849. (Cit. on pp. 137, 138).

[247] F. Späth et al.: "Keeping argon under a graphene lid–Argon intercalation between graphene and nickel(111)". *Surf. Sci.* **643** 222–226 (2016). DOI: 10.1016/j.susc.2015.05.009. (Cit. on pp. 137, 138).

[248] M. Iannuzzi: "Ar implantation at the hBN/Rh(111) nanomesh by ab initio molecular dynamics". *J. Phys. Chem. C* **119** 22198–22207 (2015). DOI: 10.1021/acs.jpcc.5b06774. (Cit. on p. 137).

[249] T. Ohta et al.: "Controlling the electronic structure of bilayer graphene". *Science* **313** 951–954 (2006). DOI: 10.1126/science.1130681. (Cit. on p. 143).

[250] S. Lee, K. Lee, and Z. Zhong: "Wafer scale homogeneous bilayer graphene films by chemical vapor deposition". *Nano Lett.* **10** 4702–4707 (2010). DOI: 10.1021/nl1029978. (Cit. on p. 143).

[251] E. McCann: "Asymmetry gap in the electronic band structure of bilayer graphene". *Phys. Rev. B* **74** 161403 (2006). DOI: 10.1103/PhysRevB.74.161403. (Cit. on p. 143).

[252] J. B. Oostinga et al.: "Gate-induced insulating state in bilayer graphene devices". *Nat. Mater.* **7** 151–157 (2008). DOI: 10.1038/nmat2082. (Cit. on p. 143).

[253] S. Nie et al.: "Growth from below: bilayer graphene on copper by chemical vapor deposition". *New J. Phys.* **14** 093028 (2012). DOI: 10.1088/1367-2630/14/9/093028. (Cit. on p. 143).

[254] Y. Hao et al.: "Oxygen-activated growth and bandgap tunability of large single-crystal bilayer graphene". *Nat. Nanotechnol.* **11** 426–431 (2016). DOI: 10.1038/nnano.2015.322. (Cit. on p. 143).

[255] Y. Cui, Q. Fu, and X. Bao: "Dynamic observation of layer-by-layer growth and removal of graphene on Ru (0001)". *Phys. Chem. Chem. Phys.* **12** 5053–5057 (2010). DOI: 10.1039/c000719f. (Cit. on p. 143).

[256] Y. Que et al.: "Epitaxial growth of large-area bilayer graphene on Ru (0001)". *Appl. Phys. Lett.* **104** 093110 (2014). DOI: 10.1063/1.4868021. (Cit. on p. 143).

[257] A. Y. Tontegode and E. V. Rut: "Intercalation by atoms of a two-dimensional graphite film on a metal Intercalation by atoms of a two-dimensional graphite film on a metal". *Phys. - Uspekhi* **36** 1053–1067 (1993). DOI: 10.1070/PU1993v036n11ABEH002180. (Cit. on pp. 143, 155).

[258] M. I. Katsnelson and A. K. Geim: "Electron scattering on microscopic corrugations in graphene". *Philos. Trans. R. Soc. A* **366** 195–204 (2008). DOI: 10.1098/rsta.2007.2157. (Cit. on p. 144).

[259] W. Zhu et al.: "Structure and electronic transport in graphene wrinkles". *Nano Lett.* **12** 3431–3436 (2012). DOI: 10.1021/nl300563h. (Cit. on p. 144).

[260] L. Tsetseris and S. T. Pantelides: "Adatom complexes and self-healing mechanisms on graphene and single-wall carbon nanotubes". *Carbon* **47** 901–908 (2009). DOI: 10.1016/j.carbon.2008.12.002. (Cit. on p. 148).

[261] Y. Ma: "Simulation of interstitial diffusion in graphite". *Phys. Rev. B* **76** 075419 (2007). DOI: 10.1103/PhysRevB.76.075419. (Cit. on p. 149).

[262] J. Drowart et al.: "Mass spectrometric study of carbon vapor". *J. Chem. Phys.* **31** 1131 (1959). DOI: 10.1063/1.1730519. (Cit. on p. 148).

[263] S. A. Krasnokutski and F. Huisken: "A simple and clean source of low-energy atomic carbon". *Appl. Phys. Lett.* **105** 113506 (2014). DOI: 10.1063/1.4895806. (Cit. on p. 148).

[264] P. Wu et al.: "Bilayer graphene growth via a penetration mechanism". *J. Phys. Chem. C* **118** 6201–6206 (2014). DOI: 10.1021/jp4108156. (Cit. on pp. 148, 167, 169).

[265] G. Henkelman, B. P. Uberuaga, and H. Joï¿½nsson: "A climbing image nudged elastic band method for finding saddle points and minimum energy paths". *J. Chem. Phys.* **113** 9901 (2000). DOI: 10.1063/1.1329672. (Cit. on p. 150).

[266] S. Riikonen et al.: "The role of stable and mobile carbon adspecies in copper-promoted graphene growth". *J. Phys. Chem. C* **116** 5802–5809 (2012). DOI: 10.1021/jp211818s. (Cit. on p. 150).

[267] D. E. Bradley: "A simple adaptation of the carbon replica technique for the examination of selected areas in the electron microscope". *Br. J. Appl. Phys.* **6** 430–432 (1955). DOI: 10.1088/0508-3443/6/12/305. (Cit. on p. 155).

[268] A. J. Lakin et al.: "Recovering molecular orientation from convoluted orbitals". *Phys. Rev. B* **88** 035447 (2013). DOI: 10.1103/PhysRevB.88.035447. (Cit. on p. 156).

[269] R. Pawlak et al.: "Local detection of nitrogen-vacancy centers in a nanodiamond monolayer". *Nano Lett.* **13** 5803–5807 (2013). DOI: 10.1021/nl402243s. (Cit. on p. 156).

[270] P. J. Feibelman: "Onset of three-dimensional Ir islands on a graphene/Ir (111) template". *Phys. Rev. B* **80** 085412 (2009). DOI: 10.1103/PhysRevB.80.085412. (Cit. on p. 158).

[271] M. Bianchi et al.: "Surface core level shifts of clean and oxygen covered Ir(111)". *New J. Phys.* **11** 063002 (2009). DOI: 10.1088/1367-2630/11/6/063002. (Cit. on p. 158).

[272] T. Gerber et al.: "Stability and reactivity of graphene-templated nanoclusters". *J. Phys. Chem. C* **120** 26290–26299 (2016). DOI: 10.1021/acs.jpcc.6b07828. (Cit. on p. 158).

[273] U. A. Schröder: "Interaction of Molecular Oxygen with Graphene on Ir(111): Intercalation and Etching". Masterthesis. Universität zu Köln (2012). (Cit. on p. 159).

[274] U. A. Schröder et al.: "Etching of graphene on Ir(111) with molecular oxygen". *Carbon* **96** 320 –331 (2016). DOI: 10.1016/j.carbon.2015.09.063. (Cit. on pp. 187, 188).

[275] C. Herbig et al.: "From permeation to cluster arrays: graphene on Ir(111) exposed to carbon vapor". *under review* (2017). (Cit. on p. 193).

APPENDIX H

Offizielle Erklärung

Ich versichere, dass ich die von mir vorgelegte Dissertation selbstständig angefertigt, die benutzten Quellen und Hilfsmittel vollständig angegeben und die Stellen der Arbeit - einschließlich Tabellen, Karten und Abbildungen -, die anderen Werken im Wortlaut oder dem Sinn nach entnommen sind, in jedem Einzelfall als Entlehnung kenntlich gemacht habe; dass diese Dissertation noch keiner anderen Fakultät oder Universität zur Prüfung vorgelegen hat; dass sie - abgesehen von den angegebenen Teilpublikationen - noch nicht veröffentlicht worden ist, sowie, dass ich eine solche Veröffentlichung vor Abschluss des Promotionsverfahrens nicht vornehmen werde. Die Bestimmungen der Promotionsordnung sind mir bekannt.
Die von mir vorgelegte Dissertation ist von Prof. Dr. Thomas Michely betreut worden.

Köln, den 10.03.2017

Charlotte Herbig